ScuDo
Scuola di Dottorato ~ Doctoral School
WHAT YOU ARE, TAKES YOU FAR

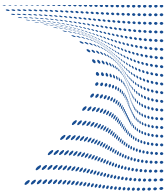

Doctoral Dissertation
Doctoral Program in Physics (32^{th} cycle)

Strange and non-strange D-meson production in pp, p–Pb, and Pb–Pb collisions with ALICE at the LHC

Fabrizio Grosa
* * * * * *

Supervisors
Prof. Stefania Bufalino, Supervisor
Dr. Francesco Prino, Co-supervisor

Doctoral Examination Committee:
Prof. Klaus Werner, Referee, Laboratoire de Physique Subatomique et des Technologies Associées de Nantes
Prof. Raphaël Granier de Cassagnac, Referee, Laboratoire Leprince-Ringuet, École polytechnique de Paris
Prof. Michela Chiosso, Universitá degli Studi di Torino
Prof. Ernesto Migliore, Universitá degli Studi di Torino
Prof. Michelangelo Agnello, Politecnico di Torino

Politecnico di Torino
February 4, 2020

I hereby declare that the contents and organisation of this dissertation constitute my own original work and does not compromise in any way the rights of third parties, including those relating to the security of personal data.

. . . . . .

Fabrizio Grosa

Turin, February 4, 2020

Abstract

The ALICE experiment at the CERN LHC was designed to study the colour-deconfined state of the nuclear matter created in heavy-ion collisions, called Quark-Gluon Plasma (QGP). Heavy flavours (i.e. charm and beauty quarks) represent an ideal probe of the QGP, since they are produced via hard-scattering processes in short time scales and hence experience the full system evolution, loosing energy via elastic and inelastic scatterings with the medium constituents. The measurement of open-heavy flavour hadrons represents also an important test for the understanding of the hadronisation mechanism in the hot environment created in heavy-ion collisions. In fact, if a fraction of heavy quarks hadronises via recombination with the medium constituents, the relative abundance of open heavy-flavour hadrons containing strange quarks with respect to those without strange-quark content is expected to be larger in heavy-ion collisions compared to proton–proton (pp) collisions, due to the enhanced production of strange quarks in the QGP.

The aim of the studies presented in this Thesis is the precise measurement of charmed mesons with and without strange-quark content, reconstructed in the three-body decay channels $\mathrm{D_s^+} \to \phi\pi^+ \to \mathrm{K^-K^+}\pi^+$ and $\mathrm{D^+} \to \mathrm{K^-}\pi^+\pi^+$.

The measurement of the $\mathrm{D_s^+}$-meson production in pp collisions at a centre-of-mass energy of $\sqrt{s} = 5.02$ TeV is described by perturbative QCD calculations. The abundance of $\mathrm{D_s^+}$ mesons relative to that of non-strange D mesons is found to be compatible with that measured in e^+e^- collisions, indicating that the charm-quark hadronisation mechanism is not significantly modified in pp collisions.

The multiplicity-dependent nuclear modification factor of $\mathrm{D^+}$ mesons Q_{pA} measured in p–Pb collisions at a centre-of-mass-energy per nucleon pair of $\sqrt{s_{\mathrm{NN}}} = 5.02$ TeV was found compatible with unity, with a hint of enhancement for the transverse-momentum interval $2 < p_{\mathrm{T}} < 10$ GeV/c. A strong suppression of the p_{T}-differential yields of $\mathrm{D^+}$ and $\mathrm{D_s^+}$ mesons, increasing with the collision centrality, is observed in Pb–Pb collisions at $\sqrt{s_{\mathrm{NN}}} = 5.02$ TeV. The nuclear modification factor R_{AA} of $\mathrm{D^+}$ mesons is found to be higher than that of charged particles for $p_{\mathrm{T}} < 8$ GeV/c. The central values of the $\mathrm{D_s^+}$-meson R_{AA} are found to be higher than those of non-strange D mesons, as expected in case of hadronisation via recombination in a strangeness-rich medium, but still compatible within uncertainties.

The measurement of the azimuthal anisotropies in the momentum distribution of $\mathrm{D^+}$ mesons in Pb–Pb collisions at $\sqrt{s_{\mathrm{NN}}} = 5.02$ TeV, quantified by the second-harmonic coefficient of the Fourier decomposition, denoted elliptic flow v_2, indicates that the charm quarks participate in the collective motions of the system. The comparison with the v_2 of charged pions and J/ψ mesons suggests a contribution to the $\mathrm{D^+}$-meson v_2 originated by the hadronisation of the charm quark via recombination with flowing light-quarks in the medium. A positive correlation between the v_2 of $\mathrm{D^+}$ mesons and that of light-flavour hadrons is observed thanks to the first application of the event-shape engineering (ESE) technique to the measurement of the D-meson azimuthal anisotropies.

The perspectives of improved measurements with the application of machine-learning techniques for the selection of the D-meson signal and with the upgrade of the ALICE Inner Tracking System (ITS), planned for the LHC Run3 in 2020, are discussed.

The results presented in this Thesis were approved by the ALICE Collaboration and presented in various conferences. The measurement of the $\mathrm{D_s^+}$-meson production in pp collisions was published in Ref. [1], the measurement of the $\mathrm{D^+}$-meson nuclear modification factors in p–Pb and Pb–Pb collisions in Refs. [2, 3], and the measurement of the $\mathrm{D^+}$-meson azimuthal anisotropies in Refs. [4, 5]. The perspectives for the ESE measurements with the upgraded ITS were included in Ref. [6]. The measurement of the $\mathrm{D_s^+}$-meson R_{AA} and the improved measurements of the $\mathrm{D^+}$-meson azimuthal anisotropies were approved as preliminary results and will be published soon.

Key words: high-energy nuclear physics, ALICE experiment, quark-gluon plasma, heavy flavours, D mesons, strangeness enhancement, nuclear modification factor, elliptic flow, event-shape engineering, machine learning

Preface

My Ph.D. project within the ALICE group of Torino started in November 2016. I was already involved in the activities of the Torino group and the the physics analysis group of the ALICE Collaboration devoted to the measurement of charmed hadrons via the full reconstruction of their hadronic decays (D2H) for my Master Thesis, therefore I was immediately introduced in the analysis of the sample of Pb–Pb collisions at $\sqrt{s_{\rm NN}} =$ 5.02 TeV during the Run2 of LHC in 2015.

I started with the measurement of the $\rm D^+$-meson nuclear modification factor and azimuthal anisotropy in semi-central Pb–Pb collisions. With the help of the other members of the Torino group and the D2H involved in the analyses of D mesons in Pb–Pb collisions, we adapted the code used for the Run1 analyses. In particular, we introduced in the code for the D-meson analyses the the so-called ALICE Q_n-framework, useful to compute the calibrations needed for the measurements of the azimuthal anisotropies. In the meantime, following the idea of my supervisor Francesco, I started developing the measurement of the D-meson azimuthal anisotropies and $p_{\rm T}$-differential yields with the event-shape engineering (ESE) technique. This technique was never applied to the heavy-flavour sector before. These measurements were approved as preliminary results, and I presented them in a poster at Quark Matter 2017. The D-meson anisotropy was shortly published in PRL (Phys. Rev. Lett. **120** no. 10), while the $R_{\rm AA}$ was first complemented with the measurements in the central and peripheral classes of events and it was published later in 2018 in JHEP (JHEP **10** (2018) 174). I was included in the paper writing committee of both manuscripts. I also had the chance to present these new results in a talk at Strangeness in Quark Matter 2017. In 2017 I also started working at the measurement of the $\rm D^+$-meson production in p–Pb collisions $\sqrt{s_{\rm NN}} =$ 5.02 TeV. Together with the other members of the analysis group, we performed the first measurement of the central-to-peripheral ratio which turned out to be more precise than the more common nuclear modification factor, thanks to the cancelation of most sources of systematic uncertainties. These results were published only in 2019, since it was decided to wait for the run of pp collisions at $\sqrt{s} =$ 5.02 TeV of 2017, in order to include the measurements of the nuclear modification factors computed with a more precise measured pp reference. The paper is currently on arXiv and it was accepted by JHEP (arXiv:1906.03425). In 2018 I performed the measurement of the $\rm D_s^+$-meson production in pp collisions at $\sqrt{s} =$ 5.02 TeV, which is currently the most precise measurement at mid-rapidity at the LHC energies. For this analysis, I developed a new procedure for the evaluation of the systematic uncertainty related to the efficiency of the particle identification selection, which was then used for

all the D-meson analyses. I was included in the paper writing committee of this measurements and the analysis was published in 2019 in EPJC (Eur. Phys. J **C79** no. 5, (2019) 388), just before the paper on the D-meson production in p–Pb collisions. Moreover, I presented the results obtained in pp and p–Pb collisions in a poster at Quark Matter 2018. Always during my second year of Ph.D., after several iterations with experts of the flow analyses, I finalised the first measurements with the ESE technique and I contributed to write the related article as chair of the paper committee. The first paper about these kind of measurements in the heavy-flavour sector was then published in JHEP (JHEP **02** (2019) 150). I also had the opportunity to present these results in a talk at Hard Probes 2018. In the context of the ESE measurements, I also performed a study for the expected precision with the upgrade of the ALICE detector planned for the LHC Run3, that was included in the document for the future perspectives of the heavy-ion physics at the LHC (arXiv:1812.06772). During my last year of Ph.D., I analysed the Pb–Pb data sample collected at the end of 2018. To accomplish this measurements, I had the chance to spend four months at CERN. The size of this data sample was 9 (4) times the one collected in 2015 for central (semi-central) collisions. Hence, I focused my activity to the improvement of the measurements of the D^+-meson azimuthal anisotropies in semi-central collisions, with and without the ESE technique, and to the measurement of the D_s^+-meson production in central collisions. For the first analysis, I developed a new code able to manage different Q_n-vector calibrations. Then, I developed a post-calibration procedure for the particle-identification response of the TPC detector, that was necessary to correct the non-perfect calibration available. This correction was used by all the analyses of the Pb–Pb sample collected in 2018 performed by the D2H group. Finally, together with my colleague of Ph.D. in Torino, Fabio, we started the investigation of machine-learning techniques for the measurement of the D_s^+ meson in Pb–Pb collisions. These analyses were approved as preliminary results and I had the chance to present them in a talk at the European Conference for High-Energy Physics 2019.

In parallel to the activities of data analysis for the measurement of charmed mesons, I was also involved in the development and the production of the upgraded Inner Tracking System (ITSU), the new silicon-tracker detector that will be installed in ALICE at the beginning of 2020. I started attending the laboratory during my first year of Ph.D. and I took over the activity related to the positioning and the assembly of the units that make up the outer barrel of the ITSU (called staves). I developed a software for the coordinate measuring machines used for the assembly, and I became responsible for the automatisation of the assembly procedures. The software that I developed was adopted in all the production sites, and therefore I had the opportunity to visit four of them (Berkeley, Daresbury, Frascati, and of course Torino) for the preparation of the assembly tools, for the training of the people involved, and to provide support for the procedures that I developed. Between the second and the third year of my Ph.D. I also actively participated in the production of the staves for the outer barrel of the ITSU in Torino.

List of Publications

1. **Measurement of prompt D^0, D^+, D^{*+} and D_s^+ production in p–Pb collisions at $\sqrt{s_\mathrm{NN}} = 5.02$ TeV**
   ALICE Collaboration
   PC members: Anastasia Maria Barbano, Annelies Marianne Veen, Cristina Bedda (chair), Cristina Terrevoli, Francesco Prino, Julien Charles Hamon, Renu Bala, Zaida Conesa Del Valle
   DOI: 10.1007/JHEP12(2019)092
   arXiv:1906.03425

2. **Measurement of D^0, D^+, D^{*+} and D_s^+ production in pp collisions at $\sqrt{s} = 5.02$ TeV with ALICE**
   ALICE Collaboration
   PC members: Cristina Terrevoli (chair), Fabrizio Grosa, Francesco Prino, Luuk Vermunt
   DOI: 10.1140/epjc/s10052-019-6873-6
   arXiv:1901.07979

3. **Event-shape engineering for the D-meson elliptic flow in Pb–Pb collisions at $\sqrt{s_\mathrm{NN}} = 5.02$ TeV**
   ALICE Collaboration
   PC members: Andrea Festanti, Fabrizio Grosa (chair), Francesco Prino, Grazia Luparello
   DOI: 10.1007/JHEP02(2019)150
   arXiv:1809.09371

4. **Measurement of D^0, D^+, D^{*+} and D_s^+ production in Pb–Pb collisions at $\sqrt{s_\mathrm{NN}} = 5.02$ TeV**
   ALICE Collaboration
   PC members: Anastasia Maria Barbano (chair), Andrea Dainese, Andrea Rossi, Elena Bruna, Fabrizio Grosa, Syaefudin Jaelani, Xinye Peng
   DOI: 10.1007/JHEP10(2018)174
   arXiv:1804.09083

5. **D-meson azimuthal anisotropy in mid-central Pb–Pb collisions at $\sqrt{s_\mathrm{NN}} = 5.02$ TeV**
   ALICE Collaboration

PC members: Anastasia Maria Barbano, Andrea Festanti (chair), Andrea Dainese, Fabrizio Grosa, Francesco Prino, Grazia Luparello
DOI: 10.1103/PhysRevLett.120.102301
arXiv:1707.01005

6. **Future physics opportunities for high-density QCD at the LHC with heavy-ion and proton beams**
Authors: Z. Citron *et al.* (Fabrizio Grosa)
arXiv:1812.06772

7. **Study of R_{AA} and v_2 of non-strange D mesons and D-jet production in Pb–Pb collisions with ALICE**
Fabrizio Grosa (for the ALICE Collaboration)
Submitted to Proceedings of Science
arXiv:1909.06562

8. **Measurement of D-meson nuclear modification factor and flow in Pb–Pb collisions with ALICE at the LHC**
Fabrizio Grosa (for the ALICE Collaboration)
DOI: 10.22323/1.345.0138
arXiv:1812.06188

9. **Measurement of the D-meson nuclear modification factor and elliptic flow in Pb–Pb collisions at $\sqrt{s_{\mathrm{NN}}} = 5.02$ TeV with ALICE at the LHC**
Fabrizio Grosa (for the ALICE Collaboration)
DOI: 10.1051/epjconf/201817118007
arXiv:1710.05644

Acknowledgements

I would like to acknowledge all the people that during these three years of Ph.D. contributed to my personal and professional development. First and foremost, I would like to acknowledge my supervisors Stefania Bufalino and Francesco Prino, who always provided an extraordinary support in all my activities and who gave me a lot of insight of Physics and analysis techniques. A special thank goes also to Stefania Beolé, who introduced me in the laboratory activities. Then, I would like to thank Elena Bruna and Anastasia Barbano who, together with Francesco Prino, passed on their passion for the HF Physics to me, and Fabio Catalano for the very positive collaboration for the analyses of the last year. Thanks to the laboratory colleagues, Yasser Corrales Morales, Silvia Coli, Jochen Klein, Bruno Alessandro, Franco Benotto, Antonio Zampieri, Floarea Dumitrache, and Riccardo Panero for all the days spent in the laboratory for the construction of the ITS. My thanks goes also to all those who are and have been colleagues in the groups at Politecnico and Universitá di Torino and have not been mentioned yet: Michelangelo Agnello, Massimo Masera, Mario Sitta, Luciano Ramello, Luca Barioglio, Maximiliano Puccio, Matteo Concas, Ivan Ravasenga, Pietro Fecchio, Stefano Trogolo and our new entries, Alessandro Balbino, Francesco Mazzaschi, and Lorenzo de Cilladi. Finally, I would like to thank all the colleagues of the D2H, especially Cristina Terrevoli, Andrea Festanti, and Andrea Rossi, for the constructive collaboration and discussions.

Thanks!

Contents

Chapter 1

High-energy nuclear physics

The strong interaction between the elementary constituents of the hadronic matter (quarks and gluons) is described by the Quantum Chromodynamics (QCD) field theory. The QCD theory predicts a transition of the strongly interacting matter under extreme conditions of high temperature and energy density from the hadronic phase to a colour-deconfined medium, called Quark–Gluon Plasma (QGP) [7–10]. This state of the nuclear matter is created and studied in the laboratory via ultra-relativistic heavy ion collisions. In this Chapter, a brief introduction to the high-energy nuclear physics, and a selection of the main experimental results obtained in this field and their interpretation are presented.

1.1 Quantum Chromodynamics

Quantum Chromodynamics (QCD) is a non-Abelian quantum gauge field theory, based on the invariance under local $\mathrm{SU}(3)_c$ group transformations. The conserved charge of QCD is called *colour charge* and can assume three values, commonly referred as *red*, *green*, and *blue*. The colour charge is carried by elementary particles, called quarks, which can be of six different flavours: *up*, *down*, *strange*, *charm*, *beauty*, and *top*. The interaction is exchanged by eight mass-less vector gauge bosons named gluons, which carry a colour and an anti-colour charge.

The QCD Lagrangian can be written as [11]:

$$\mathcal{L}_{\mathrm{QCD}} = \sum_f \bar{q}_i^f (i\gamma_\mu D_{ij}^\mu - m_f \delta_{ij}) q_j^f - \frac{1}{4} G_a^{\mu\nu} G_{\mu\nu}^a, \tag{1.1}$$

where q_i^f is the field of a quark with flavour f, colour charge i, and mass m_f. The covariant derivative D_{ij}^μ is written as a function of the gluon fields G_a^μ (with $a = 1, ...,8$) and the strong coupling constant g_s,

$$D_{ij}^\mu = \partial^\mu \delta_{ij} - i g_s \left(\frac{\lambda_{ij}^a}{2} \right) G_a^\mu, \tag{1.2}$$

where λ_{ij}^a are the Gell-Mann matrices. The second term of Eq. 1.1 describes the kinematics and the dynamics of the gluons and, if we make explicit the gluon tensor

$$G_{\mu\nu}^a = \partial_\mu G_\nu^a - \partial_\nu G_\mu^a + i g_s f_{abc} G_\mu^b G_\nu^c, \tag{1.3}$$

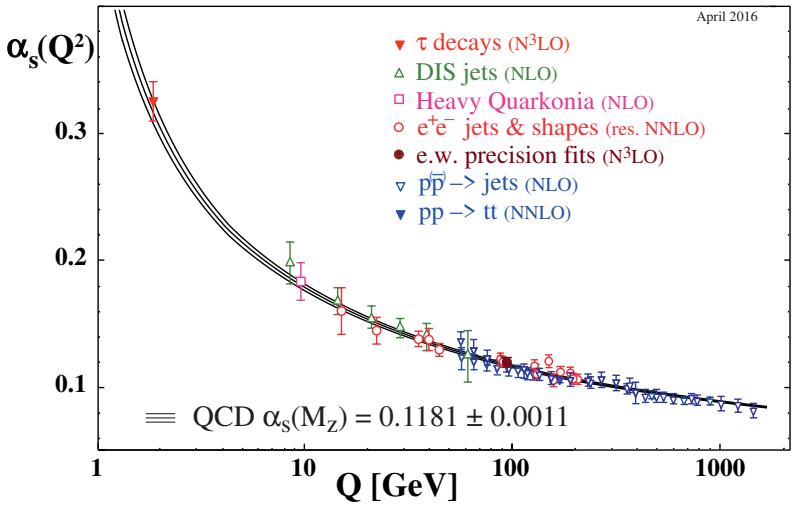

Figure 1.1: Collection of experimental values of the strong coupling constant α_s as a function of the transferred momentum of the measured process. Figure taken from [13].

we find that the non-Abelian term ($ig_s f_{abc} G^b_\mu G^c_\nu$, where f_{abc} are the structure constants of SU(3)) produces self-interactions among gluons. These self interactions among gluon fields results in the so-called anti-screening in colour interaction. As a result, the QCD coupling constant evolves with the transferred momentum $\mathcal{Q}$ [12]:

$$\alpha_s = \frac{g_s^2}{4\pi} = \frac{\alpha_s(\mu^2)}{1 + \alpha_s(\mu^2)\frac{33-2n_f}{12\pi} \ln \frac{\mathcal{Q}^2}{\mu^2}}, \tag{1.4}$$

where μ is the mass scale of the renormalisation and $2n_f$ is the number of flavours. Therefore, α_s decreases with increasing $\mathcal{Q}^2$, as confirmed by the experimental results shown in Fig. 1.1. For decreasing $\mathcal{Q}^2$ (increasing distances) α_s diverges. This means that quarks are strongly bound in hadrons and they cannot be separated. This phenomenon is called *confinement*. For large values of $\mathcal{Q}^2$, the coupling constant becomes very small, therefore in this energy region the hadron constituents can be considered free and weakly interacting. This property of the strong interaction is addressed as the *asymptotic freedom*.

For $\mathcal{Q}^2 \gtrsim 1\ \mathrm{GeV}^2/c^2$, a perturbative expansion in α_s can be used to calculate transition elements of the scattering matrix (perturbative QCD, pQCD). For smaller values of $\mathcal{Q}$, α_s becomes too large and a perturbative approach cannot be applied anymore. In this case, the Green's functions of the QCD Lagrangian can still be evaluated on a discrete space-time grid. This method is called lattice QCD (lQCD) [14].

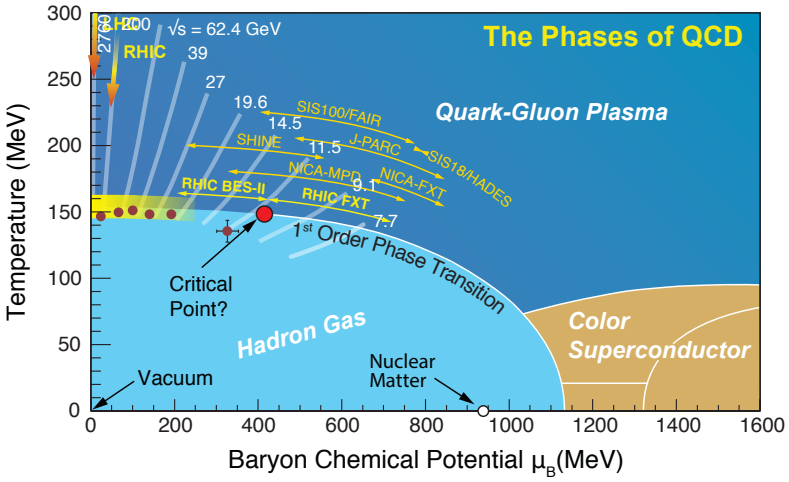

Figure 1.2: The QCD phase diagram. Figure taken from [15].

1.2 Deconfinement and Quark–Gluon Plasma

As a consequence of the large variation of α_s, the properties of the strongly-interacting matter can be very different, depending on the transferred momentum in the interactions among its constituents. A critical behaviour is expected to appear in case of very high temperature and/or density. In particular, a phase transition from the ordinary hadronic matter to a colour-deconfined state in which the quark and gluons are no longer bound into the hadrons - the Quark–Gluon Plasma (QGP) - was predicted [16].

The states of the strongly-interacting matter under different conditions can be represented in a phase diagram. In Fig. 1.2, this phase diagram is reported in terms of temperature T on the y-axis, and baryon-chemical potential μ_{B} on the x-axis, both expressed in MeV. The baryo-chemical potential is defined as the energy needed to increase by one unity the total baryon number and it is proportional to the net baryon density. The ordinary nuclear matter is located at approximately $T \approx 0$ and $\mu_{\mathrm{B}} \approx 1$ GeV. Increasing the baryo-chemical potential by about 5–10 times a transition to the QGP is expected to happen [17]; this high-μ_{B} QGP has been hypothesised to be present in the core of neutron stars [18]. A further increase of μ_{B} should lead to the formation of Cooper pairs and therefore of a colour-superconductive state [19, 20]. In the limit of $\mu_{\mathrm{B}} = 0$ the transition is expected to occur at $T \approx 145 - 165$ MeV ($\approx 1.7 \times 10^{12}$ K), corresponding to a energy density of about $\epsilon \approx 0.18 - 0.5$ GeV/fm^3. In this case, a crossover between the hadronic and the deconfined states is predicted by lQCD simulations [21]. The nature of the phase transition is controlled by global symmetries of the QCD Lagrangian and, in particular, the crossover is a consequence of the chiral symmetry, which is restored in case of vanishing quark masses. This crossover is believed to hold in the low-μ_{B} region, while at higher μ_{B} the transition is expected to be of the first order. Therefore, a critical point is predicted in the phase diagram, as shown in Fig. 1.2.

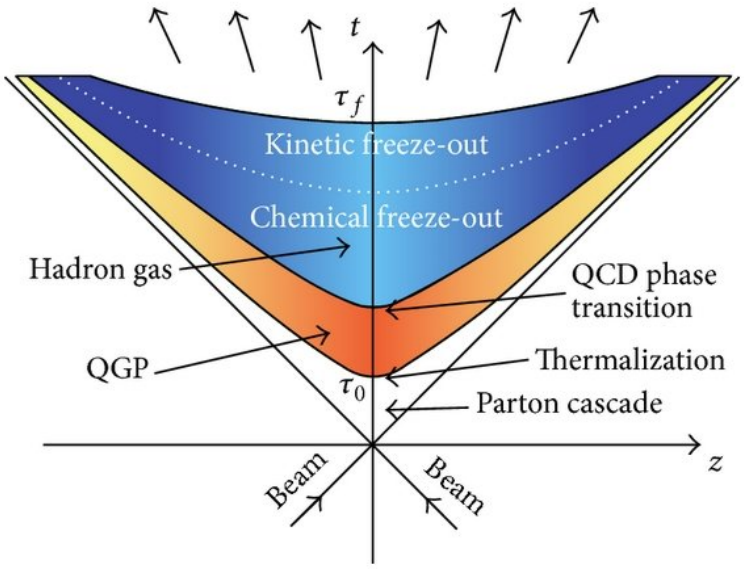

Figure 1.3: Space-time evolution of a heavy-ion collision. Figure taken from [23].

1.3 Heavy-ion collisions

Experimentally, the QGP is recreated in laboratory via ultra-relativistic heavy ion collisions.

The first heavy-ion experiments started in the second half of the 1980s at the Super Proton Synchrotron (SPS) at CERN and at the Alternating Gradient Synchrotron (AGS) at Brookhaven National Laboratory (BNL). There, several fixed-target experiments were operating at a centre-of-mass energy per nucleon-pair $\sqrt{s_{\mathrm{NN}}}$ in the range $7.7 - 17.3$ GeV, probing the μ_{B} interval $200 - 500$ MeV. At these energies the nucleons are stopped in the collision region, hence the net baryon density is high. This condition is called *stopping regime*. The heavy-ion physics moved then to the colliders, first with the Relativistic Heavy Ion Collider (RHIC) at BNL in 2000 and then with the Large Hadron Collider (LHC) at CERN in 2010. The top centre-of-mass energies of the two accelerators are 200 GeV and 5.5 TeV for Au and Pb ions, respectively, which permits to explore the QCD phase diagram in the region of μ_{B} close to zero. In this case one refers to the *Bjorken regime* or the *transparency regime* [22].

The collision between two heavy nuclei is an event with a complex space-time evolution. Assuming to satisfy the Bjorken condition, it is possible to describe the stages of this evolution in terms of the light-cone variables t (time) and z (direction of the colliding beams), as shown in Fig. 1.3. The following phases of the system evolution can be defined:

- Collision: the collision takes place in a very short time, e.g. at RHIC energies $\tau_{\mathrm{coll}} = 2R/\gamma \sim 0.1$ fm/c, being γ the Lorentz factor and R the radius of the gold

ions.

- Pre-equilibrium: after a time $\tau_{\rm f} > \tau_{\rm coll}$ particles are produced from the energy deposited in the interaction region by the colliding ions. In the mid-rapidity region, where the net baryon density is zero, according to the Bjorken regime, it is possible to estimate the energy density using the following relation

$$\epsilon_{\rm BJ} = \frac{\langle m_{\rm T} \rangle}{\tau_{\rm f} A} \frac{{\rm d}N}{{\rm d}y}\bigg|_{y=0} (\tau_{\rm f}) \tag{1.5}$$

  where A is transverse surface of the collision region, $m_{\rm T}$ is the transverse mass defined as $m_{\rm T} = \sqrt{m^2 + p_{\rm T}^2}$, being $p_{\rm T} = \sqrt{p_x^2 + p_y^2}$ the transverse momentum, ${\rm d}N/{\rm d}y$ the particle multiplicity per unit of rapidity ($y = \frac{1}{2}\ln(\frac{E-p_z}{E+p_z})$) and $\tau_{\rm f}$ the formation time. Assuming $\tau_{\rm f} \sim 1$ fm/c and considering the ${\rm d}N/{\rm d}y$ values measured at the centre-of-mass energy of RHIC, the energy density obtained is well above the critical value obtained in Sec. 1.2. In particular at RHIC energies it results to be $\epsilon_{\rm BJ} \sim 5.4$ GeV/fm^3, while at LHC ~ 15 GeV/fm^3.

- QGP formation: the system of produced particles reaches the thermal equilibrium through binary scatterings, the QGP forms and the system starts the expansion. From hydrodynamic studies the time needed to reach the thermal equilibrium is evaluated to be $0.6 \leq \tau_{\rm eq} \leq 1$ fm/c at RHIC.

- Hadronisation: when the temperature decreases below the pseudo-critical value for the transition crossover, the QGP cannot longer exist and its constituents hadronise. A gas of interacting hadrons, which continues to expand, is formed.

- Freeze-out: below a certain temperature the interactions among the hadrons stop. First the inelastic interactions cease (*chemical freeze-out*) and the relative abundances of hadronic species are fixed. Then, the elastic interactions cease (*thermal freeze-out*), defining the momentum spectra of all the particle species.

1.3.1 The Glauber model

The finite size of the colliding atomic nuclei implies the necessity of a description of the collision geometry. This description can be obtained via the Glauber Model [24], which also provides estimates of useful variables, such as the interaction probability, the number of nucleons that takes part in the collision (*participant nucleons*, $N_{\rm part}$), and the number of binary nucleon–nucleon collisions ($N_{\rm coll}$).

In the Glauber-Model formulation the collision between two nuclei is described as incoherent superposition of binary nucleon–nucleon interactions. Moreover, the nucleons inside the nuclei are considered indistinguishable (protons from neutrons) and point-like, the nucleus and the nucleons inside it are not deflected in the interaction, and the cross section for the elementary interaction between two nucleons does not vary through all the collision. Under these assumptions, also known as *optical limit*, the collision between two nuclei can be analytically described using the nuclear density function ρ (typically

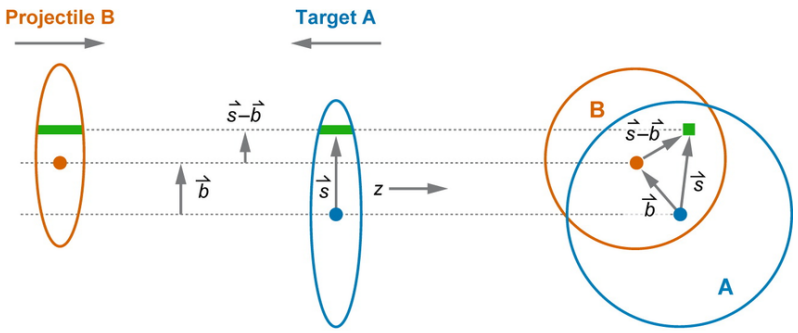

Figure 1.4: Schematic representation of two nuclei before a collision together with the coordinate system for the nucleons. Figure taken from [24].

parametrised with a Wood-Saxon function [24]) and the inelastic nucleon–nucleon cross section $\sigma_{\text{inel}}^{\text{NN}}$ as inputs.

The coordinate system used to describe the collision of a nucleus A (with A nucleons) and a nucleus B (with B nucleons) is shown in Fig. 1.4. The origin of the coordinate system is placed in the centre of A, and the position in the transverse plane of the nucleons inside A expressed by the vector $\vec{s}$. The same position with respect to the centre of the nucleus B is then given by $\vec{b}-\vec{s}$, where $\vec{b}$ is the vector that connects the centres of the two nuclei and it is called *impact parameter*. The probability to find a nucleon of the nucleus A at the transverse coordinate $\vec{s}$ is given by the *nuclear thickness function*

$$T_{\text{A}}(\vec{s}) = \int_{-\infty}^{+\infty} \mathrm{d}z_A \cdot \rho_{\text{A}}(\vec{s}, z_i^A). \tag{1.6}$$

The probability to have an elementary collision between two nucleons is then given by

$$p(\vec{b}) = \sigma_{\text{inel}}^{\text{NN}} \cdot \int d^2s \cdot T_{\text{A}}(\vec{s}) \cdot T_{\text{B}}(\vec{b}-\vec{s}) = \sigma_{\text{inel}}^{\text{NN}} \cdot T_{\text{AB}}(\vec{b}), \tag{1.7}$$

where $T_{\text{AB}}(\vec{b})$ is defined as the *nuclear overlap function*. The probability to have n nucleon–nucleon interactions is given by the binomial distribution:

$$P_{n,\text{AB}}(\vec{b}) = \begin{pmatrix} AB \\ n \end{pmatrix} \cdot \left[\sigma_{\text{inel}}^{\text{NN}} \cdot T_{\text{AB}}(\vec{b})\right]^n \cdot \left[1 - \sigma_{\text{inel}}^{\text{NN}} \cdot T_{\text{AB}}(\vec{b})\right]^{AB-n}. \tag{1.8}$$

The average number of binary nucleon–nucleon collisions is obtained as the mean value of the binomial probability distribution:

$$\langle N_{\text{coll}}(\vec{b})\rangle = AB \cdot \sigma_{\text{inel}}^{\text{NN}} \cdot T_{\text{AB}}(\vec{b}). \tag{1.9}$$

Similarly, it is possible to estimate the number of nucleons that participate in the collision as:

$$\begin{aligned}\langle N_{\mathrm{part}}(\vec{b})\rangle = A \cdot \int \mathrm{d}^2 s \cdot T_{\mathrm{A}}(\vec{s}) \cdot \left[1 - (1 - \sigma_{\mathrm{inel}}^{\mathrm{NN}} \cdot T_{\mathrm{B}}(\vec{b} - \vec{s}))^B\right] + \\ + B \cdot \int \mathrm{d}^2 s \cdot T_{\mathrm{B}}(\vec{b} - \vec{s}) \cdot \left[1 - (1 - \sigma_{\mathrm{inel}}^{\mathrm{NN}} \cdot T_{\mathrm{A}}(\vec{s}))^A\right].\end{aligned} \tag{1.10}$$

The inelastic nucleus–nucleus interaction cross section can be obtained as the probability to have at least one binary nucleon–nucleon collision:

$$\frac{\mathrm{d}\sigma_{\mathrm{AB}}^{\mathrm{inel}}}{\mathrm{d}\vec{b}} = 1 - P_{0,\mathrm{AB}}(\vec{b}) = 1 - \left[1 - \sigma_{\mathrm{inel}}^{\mathrm{NN}} \cdot T_{\mathrm{AB}}(\vec{b})\right]^{AB}. \tag{1.11}$$

In case of hard processes, for which the cross section is small, Eq. 1.11 with σ_{inel} substituted by σ_{hard} can be expanded in Fourier series:

$$\frac{\mathrm{d}\sigma_{\mathrm{AB}}^{\mathrm{hard}}}{\mathrm{d}\vec{b}} \simeq 1 - \left[1 - AB \cdot \sigma_{\mathrm{hard}}^{\mathrm{NN}} \cdot T_{\mathrm{AB}}(\vec{b})\right] = AB \cdot \sigma_{\mathrm{hard}}^{\mathrm{NN}} \cdot T_{\mathrm{AB}}(\vec{b}) \propto \sigma_{\mathrm{hard}}^{\mathrm{NN}} \cdot \langle N_{\mathrm{coll}}(\vec{b})\rangle, \tag{1.12}$$

where Eq. 1.9 was used in the last step. As a consequence, the Glauber Model predicts that the yield of particles produced via hard processes in nucleus–nucleus collisions is proportional to the one in proton-proton collisions, with proportionality constant $\langle N_{\mathrm{coll}}\rangle$. This property is typically addressed as *binary-scaling* or N_{coll}-*scaling*.

Glauber Monte Carlo simulations

Despite the Glauber Model in the approach of the optical limit can be very useful to compute relevant quantities related to the geometry of a heavy-ion collision, it has as limitation the usage of continuous density functions for quantities that are discrete in nature and that can fluctuate event by event. This is for example the case of the position of the nucleons inside the nuclei, which are discrete and therefore event-by-event give rise to a lumpy distribution, which can be approximated to a continuous distribution only on average.

The event-by-event fluctuations can be taken into account using Glauber Monte Carlo simulations [24]. In this approach, the nucleon position in the two colliding nuclei are randomly generated according to their nuclear density distributions and a random impact parameter is assigned according to the differential cross section $\mathrm{d}\sigma/\mathrm{d}b \propto 2\pi b$. The collision between the two nuclei is then treated as a superposition of independent binary nucleon–nucleon collisions. A collision between two nucleons being distant d from each other in the plane orthogonal to the beam axis takes place if

$$d < \sqrt{\sigma_{\mathrm{NN}}^{\mathrm{inel}}/\pi}. \tag{1.13}$$

Using this description, the N_{part} and N_{coll} values are obtained for each genrated event.

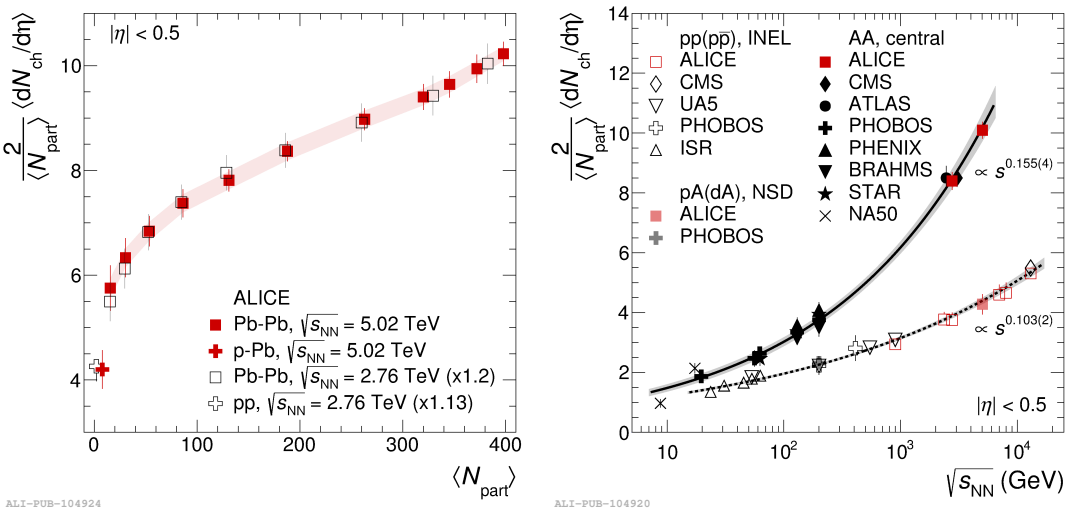

Figure 1.5: Pseudorapidity density of charged particles per participant-nucleon pair $\frac{2}{\langle N_{\rm part}\rangle}\langle {\rm d}N_{\rm ch}/{\rm d}\eta\rangle$ as a function of $N_{\rm part}$ (left panel) and $\sqrt{s_{\rm NN}}$ (right panel), measured at mid rapidity in different colliding systems. Figures taken from Ref. [25].

1.4 Observables in heavy-ion physics

This Section is devoted to the description of a selection of the main observables of the heavy-ion physics and the experimental results that contributed to the current understanding of the hot and dense medium created in ultra-relativistic heavy-ion collisions.

1.4.1 Particle multiplicity and energy density

The measurement of the particle multiplicity produced in heavy-ion collisions provides important information about the properties of the created medium.

This observable is typically expressed in terms of pseudorapidity density of charged particles per pair of participant nucleons, $\frac{2}{\langle N_{\rm part}\rangle}\langle {\rm d}N_{\rm ch}/{\rm d}\eta\rangle$. The division by $\langle N_{\rm part}\rangle/2$ is introduced to compare different colliding systems. The pseudorapidity ($\eta = -\ln(\theta/2)$, being θ the polar angle), can be used as an approximation of the rapidity ($\eta \approx y$ for $p_{\rm T} \gg m$) when the mass of the measured particles is not known. Therefore, ${\rm d}N_{\rm ch}/{\rm d}\eta$ measured at mid-rapidity can be used to have an estimate of the energy density of the medium created in heavy-ion collisions using the Bjorken formula reported in Eq. 1.5.

The left panel of Fig. 1.5 shows the charged-particle pseudorapidity density per participant pair measured by the ALICE Collaboration in pp, p–Pb, and Pb–Pb collisions as a function of $N_{\rm part}$ [25]. The charged-particle density per participant pair increases steeply from pp and p–Pb collisions to peripheral Pb–Pb collisions, while the slope is reduced from $N_{\rm part} \approx 50$. This behaviour is similar for different energies described by models that include gluon saturation in the initial stage. The right panel of the same Figure shows $\frac{2}{\langle N_{\rm part}\rangle}\langle {\rm d}N_{\rm ch}/{\rm d}\eta\rangle$ as a function of $\sqrt{s_{\rm NN}}$, measured in different collision systems by

several experiments. The charged-particle density per participant pair increases with the centre-of-mass energy of the collision, with a different slope in A–A collisions with respect to that observed in pp collisions. The measurements in p–A and d–A collisions lie on the curve of pp collisions, indicating that the difference observed in A–A collisions is not only due to the multiple interactions among the participating nucleons, present also in p–A collisions. The two series of points were fitted with a power low function, as^b, and b was found to be 0.155 ± 0.004 for Pb–Pb collisions and 0.103 ± 0.002 for the smaller systems. In case of A–A collisions, the energy density obtained applying the Bjorken formula 1.5 is larger than the critical energy density for the deconfinement.

1.4.2 Hadro-chemical composition

The measurement of identified hadron yields can provide an estimation of the chemical freeze-out temperature $T_{\rm ch}$, the baryo-chemical potential $\mu_{\rm B}$ and the volume of the system V at the chemical freeze-out. Those parameters can be in fact evaluated by comparing the measured abundances of different hadron species with the predictions of the statistical hadronisation model (SHM), which assumes that the system is in the thermal and chemical equilibrium at the chemical freeze-out. In particular, considering the system exchanging energy and particles with the outside (*grand-canonical ensemble*), the abundance of a defined particle species i is

$$N_i(T, V, \mu_i) = \frac{g_i V}{2\pi^2} \int_0^\infty \frac{p^2 \mathrm{d}p}{e^{(E-\mu_i)/T} \pm 1} \tag{1.14}$$

where g_i are the degrees of freedom of the species i and μ_i the chemical potential, which guarantees the conservation on average of the quantum numbers (baryon number, isospin, and strangeness). Variations from the grand-canonical description can be applied by introducing additional parameters to account for an incomplete thermalisation for the strange ($\gamma_{\rm s}$) or charm ($\gamma_{\rm c}$) quarks. In case of non-equilibrium these parameters are smaller than unity. This is typically needed in peripheral A–A collisions or in small systems, such as pp and p–Pb collisions. An additional parameter $\gamma_{\rm q}$ is used in the SHARE model, which describes an expanding, super-cooled QGP which is in non-equilibrium and undergoes a sudden hadronisation without further re-interactions.

The temperatures obtained from the thermal fits is close to the value expected for the pseudo-critical temperature of the crossover transition and the measured abundances of the hadron species at the equilibrium follow a distribution which is governed by their mass, spin, by the temperature, and by the $\mu_{\rm B}$.

In Fig. 1.6, the results of the fits with the SHARE model to the yields of the different particle species measured by the ALICE Collaboration in the 10% most central Pb–Pb collisions at $\sqrt{s_{\rm NN}} = 5.02$ TeV, are shown. A chemical freeze-out temperature of $T_{\rm ch} = (154 \pm 3)$ MeV, with a $\chi^2/\mathrm{ndf} = 6.4$ (5) is found in case of $\gamma_{\rm s}$ and $\gamma_{\rm q}$ equal (close) to unity. A smaller value of $T_{\rm ch} = (139 \pm 1)$ MeV and a lower $\chi^2/\mathrm{ndf} = 2.6$ are obtained when $\gamma_{\rm s}$ and $\gamma_{\rm q}$ are both let free in the fits. In this case the values of $\gamma_{\rm s}$ and $\gamma_{\rm q}$ are found to be larger than unity. When also the light (hyper-) nuclei are included in the fit, the temperature increases again to $T_{\rm ch} = (160 \pm 10)$ MeV and $\gamma_{\rm s}$ and $\gamma_{\rm q}$ are found to be smaller than unity, although the χ^2/ndf increase again to a value of 4.8.

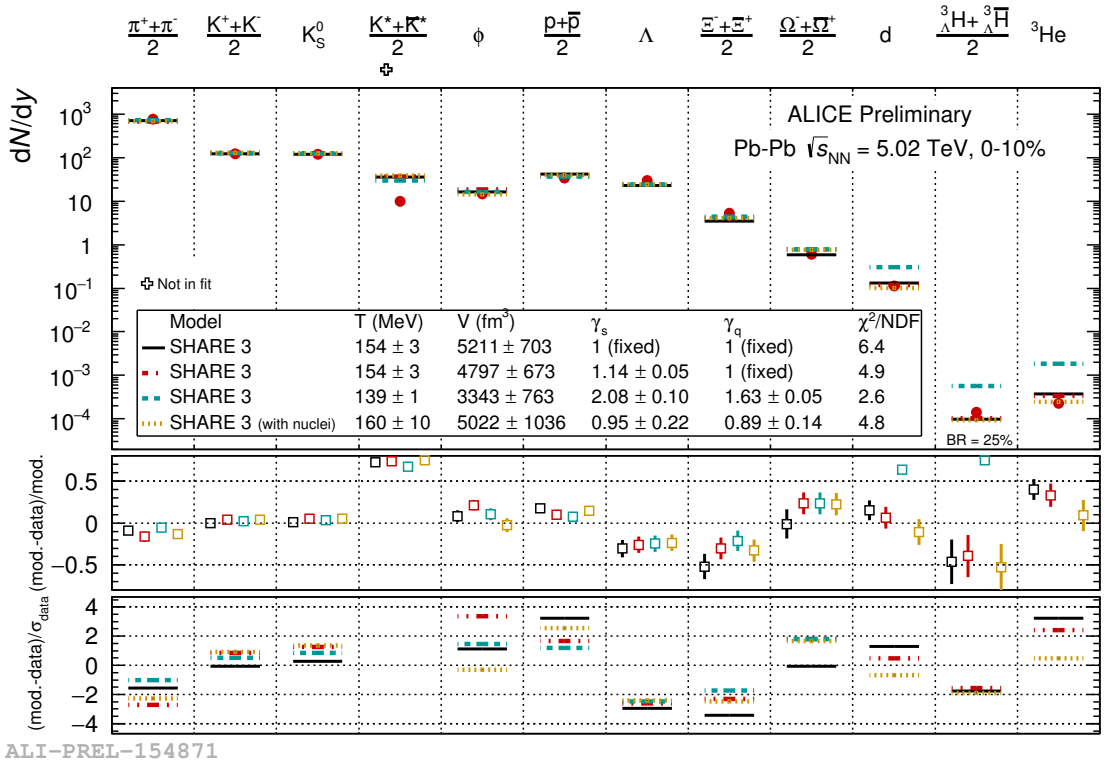

Figure 1.6: Thermal fit to the particle yields measured by the ALICE Collaboration in the 10% most central Pb–Pb collisions at $\sqrt{s_{\mathrm{NN}}} = 5.02$ TeV. Figure taken from the ALICE figure repository ©.

1.4.3 Strangeness enhancement

The first evidences of the enhanced production of hadrons containing strange quarks in A–A collisions with respect to those measured in pp collisions was observed by the NA35, WA97, and NA57 Collaborations in the 1990s [26–28]. The more strange quarks were contained in the hadron, the larger was the measured enhancement. These observations were consistent with the prediction by Rafelski and Müller, that proposed the strangeness enhancement as a signature of the deconfinement [29]. Since no valence strange quarks are present in the colliding nuclei, they must be produced in the collision or in the QGP. When the temperature is below the critical temperature of the phase transition, the production of strange quarks is disfavoured since the effective mass of the strange quark is larger than the temperature. When the system reaches the critical temperature, the phase transition occurs and the mass of the strange quark decrease to the current value of ≈ 100 MeV/c^2 due to the restoration of the chiral symmetry [30]. Hence, strange quark-antiquark pairs are expected to be abundantly produced in gluon-fusion processes, owing to the high density of gluons in the QGP, leading to an increase of the relative abundance of particles with strange-quark content.

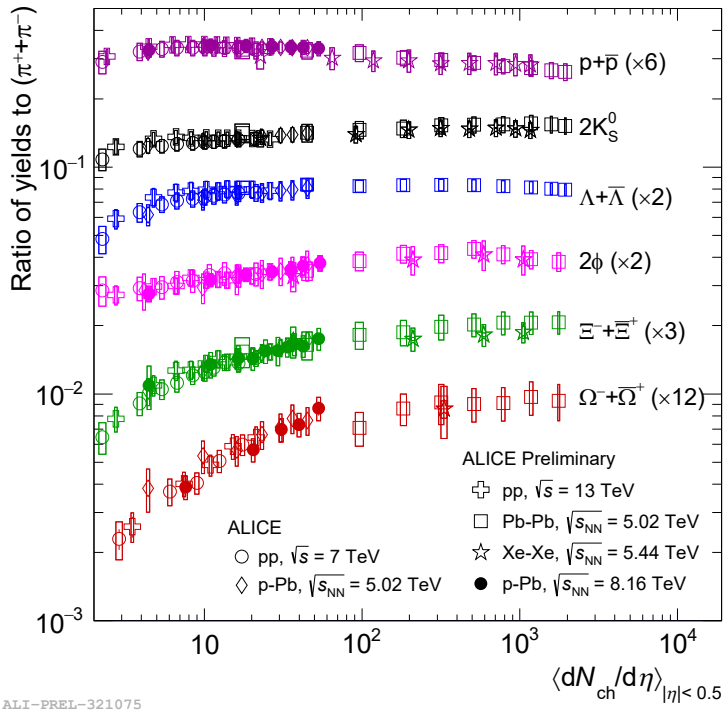

Figure 1.7: Ratios of p_{T}-integrated yields of hadrons with strange-quark content and those of charged pions as a function of the charged-particle multiplicity at mid-rapidity, measured by the ALICE Collaboration in several colliding systems. Figure taken from the ALICE figure repository ©.

An enhanced production of strange hadrons was also observed at RHIC [31] and LHC energies [32]. Recently the ALICE Collaboration published the first observation of an enhancement of strangeness production in high-multiplicity pp collisions [33]. Figure. 1.7 shows the ratios of the p_{T}-integrated yields of strange and multi-strange hadrons with respect to those of charged pions as a function of the charged-particle multiplicity at mid-rapidity in different colliding systems. A smooth increase is observed from low-multiplicity pp collisions to central Pb–Pb collisions. The increasing trend is more steep for hadrons with multiple strange-quark content. This behaviour is not reproduced by event generators such as PYTHIA [34], DIPSY [35], and EPOS [36], and therefore it is still a challenge for the models that describe the particle production in pp collisions. A possible explanation of this behaviour is provided by the statistical hadronisation model. In fact, in small collisions systems, such as pp and p–A, the grand-canonical formulation cannot be adopted due to the small number of produced particles and the canonical formulation must be used. In a grand-canonical ensamble, the quantum numbers (i.e. strangeness) are conserved on average, while in a canonical ensamble they must be exactly conserved. This conservation law reduces the phase space available for particle production [37], causing a suppression of the strange hadron production in small systems. This effect is denoted as *canonical suppression*.

1.4.4 Radial flow

After the chemical freeze-out, the abundances of the particle species are defined, but the particles still interact among themselves through elastic scatterings. Only after the thermal freeze-out all the interactions cease and the momentum spectra of primary particles become fixed. If the system is in thermal equilibrium, the transverse-momentum spectrum at low p_{T} can described by approximated by a Maxwell-Boltzmann distribution, where the slope parameter T_{fo} represents the thermal freeze-out temperature:

$$\frac{1}{p_{\mathrm{T}}}\frac{\mathrm{d}N}{\mathrm{d}p_{\mathrm{T}}} \propto e^{-\sqrt{m^2+p_{\mathrm{T}}^2}/T_{\mathrm{fo}}}. \tag{1.15}$$

However, in A–A collisions a different slope for particles with different masses was observed [38]. This is the effect of a collective motion in the transverse plane, called *radial flow*, which is due to the internal pressure generated by the QGP and is superimposed to the thermal random motion. Hence, the slope parameter (T_{slope}) is the sum of the thermal freeze-out temperature and the radial flow terms:

$$T_{\mathrm{slope}} = T_{\mathrm{fo}} + \frac{m}{2}\langle\beta_{\mathrm{T}}\rangle^2, \tag{1.16}$$

where $\langle\beta_{\mathrm{T}}\rangle$ is the collective transverse average velocity of the medium. An additional complication is represented by the fact that the system is expanding and therefore the velocity is not the same along the radial direction. This was developed within the Blast-Wave model [39], where the radial expansion velocity $\beta_{\mathrm{T}}(r)$ distribution was parametrised as

$$\beta_{\mathrm{T}}(r) = \beta_s\left(\frac{r}{R}\right), \tag{1.17}$$

where β_s is the velocity at the surface of the expanding system and R is the maximum radius. Within this model, the observed particle spectrum results from the sum of the spectra of individual thermal sources each boosted with the boost angle $\rho = \tanh^{-1}[\beta_{\mathrm{T}}(r)]$ [39].

This model can be used to estimate the kinetic freeze-out temperature and the average radial expansion velocity via fits to the measured p_{T}-differential distributions of different hadron species. Figure 1.8 shows these fits to the p_{T} spectra of charged pions, kaons, and protons measured in the 5% most central Pb–Pb collisions at $\sqrt{s_{\mathrm{NN}}} = 2.76$ TeV by the ALICE Collaboration [38]. The spectra measured by the STAR and PHENIX Collaborations in Au–Au collisions at $\sqrt{s_{\mathrm{NN}}} = 200$ GeV [40, 41] are also superimposed to appreciate the difference in the slope at lower collision energy. The expansion velocity is found to increase from about 0.35 to 0.65, while the freeze-out temperature to decrease from about 160 MeV to 100 MeV, going from peripheral to central Pb–Pb collisions at the LHC energies [38].

Surprisingly, at LHC energies a mass-dependent shift of the p_{T} distributions of identified hadrons was also observed in smaller systems, such as p–Pb collisions [42–44]. This observation can be explained by models including an hydrodynamical expansion [45], which provide a description of other observables that were found to exhibit a collective-like behaviour [46–50]. This could be attributed to the formation of QGP droplets in smaller systems, however this interpretation is currently debated.

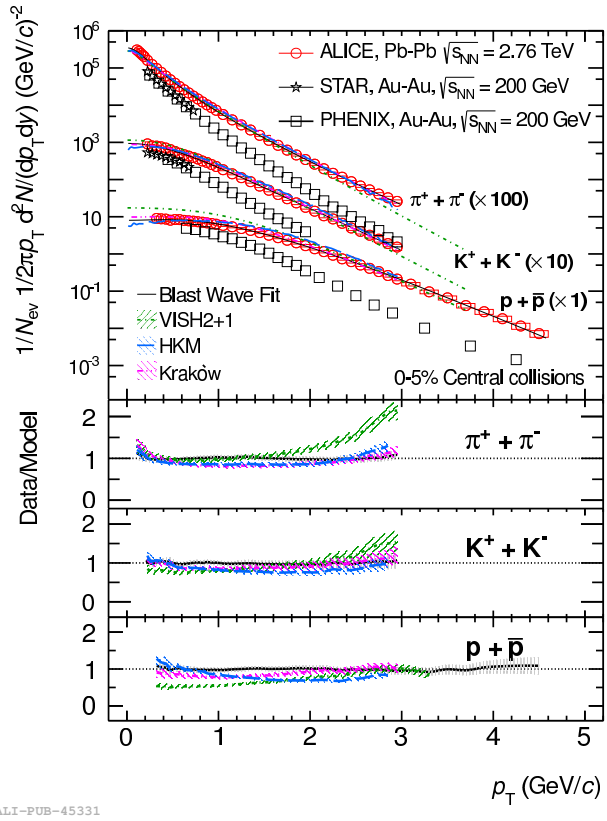

Figure 1.8: Transverse-momentum spectra of charged pions, kaons, and protons in central (0–5%) Au–Au collisions at $\sqrt{s_{\mathrm{NN}}} = 200$ GeV measured by the STAR and PHENIX Collaborations and in central (0–5%) Pb–Pb collisions at $\sqrt{s_{\mathrm{NN}}} = 2.76$ TeV by the ALICE Collaboration. Figure taken from Ref. [38].

1.4.5 Anisotropic flow

The initial geometry of a nucleus–nucleus collision shows an anisotropy in the azimuthal plane due to the finite size of the colliding objects (see Sec. 1.3.1), which increases with the impact parameter between the two colliding nuclei. This initial geometrical anisotropy is converted to an anisotropy in the momentum distribution of the produced particles due to the anisotropic pressure gradients, and therefore it can be measured through the azimuthal angle distributions of the particles in the final state. The anisotropy is characterised via a Fourier series expansion of the azimuthal angle φ with respect to the symmetry-plane angles Ψ_n,

$$\frac{\mathrm{d}^2N}{\mathrm{d}(\varphi - \Psi_n)\mathrm{d}p_{\mathrm{T}}} = \frac{\mathrm{d}N}{2\pi \mathrm{d}p_{\mathrm{T}}}\left\{1 + 2\sum_{n=0}^{\infty} v_n(p_{\mathrm{T}})\cos[n(\varphi - \Psi_n)]\right\}, \tag{1.18}$$

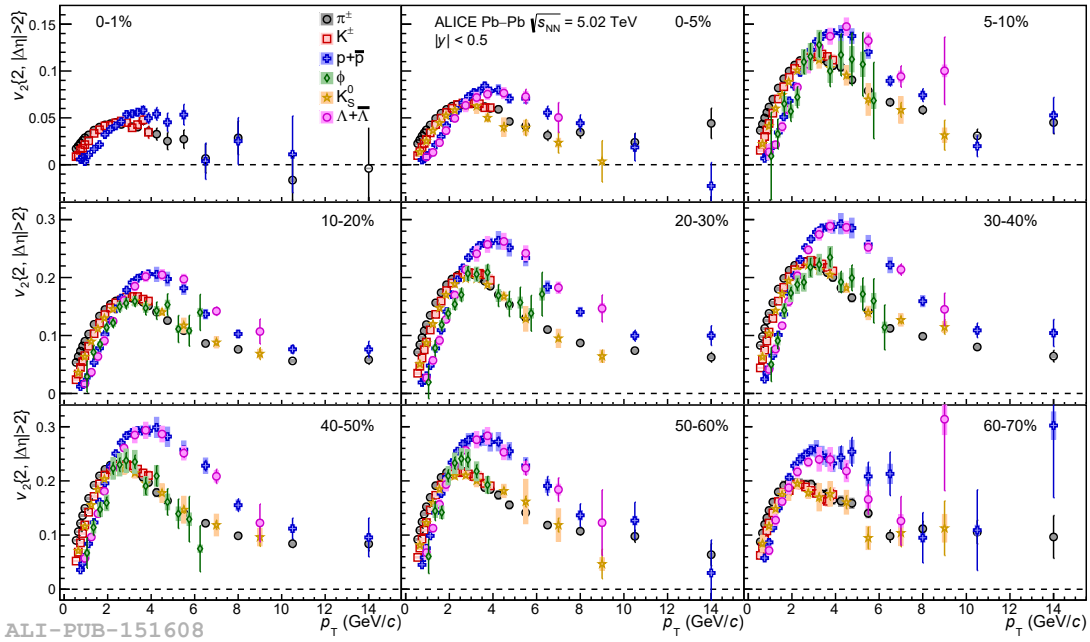

Figure 1.9: Elliptic flow coefficient v_2 of charged pions, charged and neutral kaons, protons, ϕ mesons, and hyperons as a function of p_{T}, measured by the ALICE Collaboration for several centrality classes in Pb–Pb collisions at $\sqrt{s_{\mathrm{NN}}} = 5.02$ TeV. Figure taken from Ref. [52].

where n is the order of the harmonic and $v_n(p_{\mathrm{T}})$ are the p_{T}-dependent Fourier (flow) coefficients defined as

$$v_n(p_{\mathrm{T}}) = \langle \cos[n(\varphi - \Psi_n)] \rangle. \tag{1.19}$$

The brackets denote an average over particles in a given p_{T} interval and over the events in a given centrality class. The symmetry-plane angles for the n^{th} harmonic Ψ_n are defined by the geometrical distribution of the nucleons participating in the collision [51]. In case of no fluctuations in the initial geometry, they correspond to the reaction-plane angle Ψ_{RP}, which is defined by the beam direction and the impact parameter.

The dominant term in non-central collisions is the second-harmonic coefficient v_2, called *elliptic flow*, originating from the almond shape of the interaction region. Figure 1.9 shows the elliptic flow coefficient of charged pions, charged and neutral kaons, protons, ϕ mesons, and hyperons as a function of p_{T}, measured by the ALICE Collaboration for several centrality classes in Pb–Pb collisions at $\sqrt{s_{\mathrm{NN}}} = 5.02$ TeV. The v_2 increases from central (0–1%) to semi-central (30–40%) collisions, due to the increased initial geometrical anisotropy. For more peripheral collisions it decreases because of the reduction of the pressure gradients due to the smaller density of the medium. The v_2 of the different species follows a mass ordering for $p_{\mathrm{T}} < 3$ GeV/c. This is expected from the collective radial flow imparted by an hydrodynamically expanding source, because particles with larger mass are pushed to higher p_{T} by the common flow velocity β_{T}. For $3 < p_{\mathrm{T}} < 8$ GeV/c,

the v_2 of the different hadron species are grouped according to the number of their valence quarks rather than their mass, as expected in case of hadron production via quark recombination [53]. The comparison of the measured v_n harmonics with viscous hydrodynamic models provide information of medium properties, such as equation of state, sound velocity or shear viscosity η/s. In particular, a value of η/s of about 0.12 and 0.2 allows for a good parametrisation of the measurements in Au–Au collisions at top of RICH energy and for Pb–Pb collisions at $\sqrt{s_{\mathrm{NN}}} = 2.76$ TeV, respectively [54].

Recently, a long-range correlations in the transverse plane were found at the LHC in high-multiplicity pp collisions [46, 47] and subsequently in high-multiplicuty p–Pb collisions [48–50] by studying the two-dimensional $\Delta\varphi - \Delta\eta$ correlation function. Moreover, the PHENIX collaboration measured positive second and third harmonic coefficients v_2 and v_3 in p–Au, d–Au, and ^{3}He–Au collisions, which were found to be dependent on the initial geometry [55]. The measured v_n coefficients in small systems were found to be described both by Color-Glass Condensate (CGC) models based on initial state non-linear gluon interactions [56, 57], and by hydrodynamical models, which include the formation of a short-lived QGP droplet [58–60].

1.4.6 High-p_{T} hadrons and jet quenching

High-p_{T} partons are produced in hard-scattering processes in the early stage of the collision. They subsequently propagate in the QGP losing energy interacting with the medium constituents via inelastic (gluon radiation) and elastic (scattering) processes. This energy loss causes a shift of the energy distribution of partons traversing the medium, which results in a softening of the p_{T} distributions of the hadrons measured in the final state, called *jet quenching*.

As demonstrated in Sec. 1.3.1, the yield of particles produced in hard processes in heavy-ion collisions is expected to scale with the average number of binary nucleon–nucleon collisions $\langle N_{\mathrm{coll}} \rangle$. This scaling rule is typically tested via the measurement of the *nuclear modification factor* R_{AA}, defined as

$$R_{\mathrm{AA}}(p_{\mathrm{T}}, y) = \frac{1}{\langle N_{\mathrm{coll}} \rangle} \frac{\mathrm{d}^2 N_{\mathrm{AA}}/\mathrm{d}p_{\mathrm{T}}\mathrm{d}y}{\mathrm{d}^2 N_{\mathrm{pp}}/\mathrm{d}p_{\mathrm{T}}\mathrm{d}y}, \tag{1.20}$$

where $\mathrm{d}^2 N_{\mathrm{pp(AA)}}/\mathrm{d}p_{\mathrm{T}}\mathrm{d}y$ are the p_{T}- and y-differential yields of hadrons measured in pp (AA) collisions. The R_{AA} is expected to be equal to unity in absence of medium effects, while a difference from unity implies modifications of the p_{T} distributions of the produced hadrons. Other effects not related to the presence of the QGP, the *cold nuclear matter* (CNM) effects, can cause a deviation from unity. These effects can be assessed by studying the nuclear modification factor in p–A collisions.

The left panel of Fig. 1.10 shows the nuclear modification factor of charged particles as a function of p_{T} measured by the ALICE [61] and CMS [65] Collaborations in p–Pb and central (0–5%) Pb–Pb collisions at $\sqrt{s_{\mathrm{NN}}} = 5.02$ TeV. For high-p_{T} particles ($p_{\mathrm{T}} \gtrsim 3$ GeV/c) the nuclear modification factor is compatible with unity for p–Pb collisions, while it is significantly suppressed for Pb–Pb collisions, as a consequence of the energy loss. In addition, the nuclear modification factor of electroweak probes, such as photons and Z and W bosons, in Pb–Pb collisions is found to be compatible with

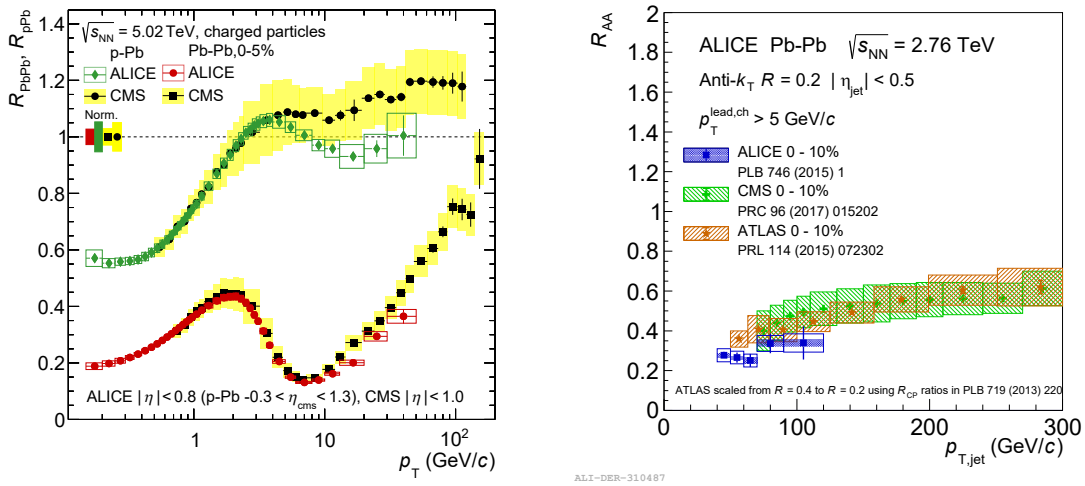

Figure 1.10: Left: nuclear modification factor as a function of p_{T} for charged particles in p–Pb and 0–5% Pb–Pb collisions at $\sqrt{s_{\mathrm{NN}}} = 5.02$ TeV by the ALICE and CMS Collaborations. Figure taken from Ref. [61]. Right: nuclear modification factor of charged jets in the 10% most central Pb–Pb collisions at $\sqrt{s_{\mathrm{NN}}} = 2.76$ TeV measured by the ALICE Collaboration [62], compared to that of inclusive jets measured by the ATLAS [63] and CMS [64] Collaborations at the same energy and centrality class. Figure taken from the ALICE figure repository ©.

unity [66–70]. For $p_{\mathrm{T}} \gtrsim 10$ GeV/c the charged-particle R_{AA} increases and approaches unity for $p_{\mathrm{T}} \approx 100$ GeV/c. This is not observed in the R_{AA} of jets, which is approximately flat in this p_{T} region, as shown in the right panel of Fig. 1.10, where the R_{AA} of charged jets measured by the ALICE Collaboration in the 10% most central Pb–Pb collisions at $\sqrt{s_{\mathrm{NN}}} = 2.76$ TeV [62] is compared to that of inclusive jets measured by the ATLAS [63] and CMS [64] Collaborations at the same energy and in the same centrality class. The rise of the charged-particle R_{AA} could be therefore due to a modification of the fragmentation functions in Pb–Pb collisions with respect to pp collisions, which would modify the shape of the p_{T} distributions. For $p_{\mathrm{T}} \lesssim 3$ GeV/c both the nuclear modification factors measured in p–Pb and Pb–Pb collisions are lower than unity, however in this p_{T} region the binary scaling is not expected to occur even in absence of medium effects because particle production is dominated by soft processes, for which the yield of produced particles is expected to scale with $\langle N_{\mathrm{part}} \rangle$.

The measurement of the R_{AA} is therefore a sensitive probe to the formation of the QGP and the comparison with the model predictions can be used to extract the transport properties of the medium [71].

Chapter 2

Open heavy-flavour physics

Open-heavy flavour hadrons, i.e. particles made of at least a heavy (charm or beauty) quark and other lighter quarks, are excellent probes of the Quark–Gluon Plasma created in heavy-ion collisions [72]. In fact, heavy quarks are produced in hard-scattering processes occurring in the early stage of the collision and subsequently experience the full system evolution, interacting with the medium constituents via elastic and inelastic processes. This Chapter is dedicated to the introduction to open-heavy flavours as a probe of the Quark-Gluon Plasma created in heavy-ion collisions, which is presented following the various stages of their evolution, starting from the production, going through the interaction with the medium, ending up with the hadronisation.

2.1 Open heavy-flavour production

Because of their large masses, $m_{\mathrm{c}} \simeq 1.3$ GeV/c^2 and $m_{\mathrm{b}} \simeq 4.2$ GeV/c^2 [13], heavy quarks are always produced in scattering processes with large momentum transfer ($\mathcal{Q}^2 \gtrsim 4m^2_{\mathrm{b,c}}$). Since the strong coupling constant is significantly smaller than unity in this $\mathcal{Q}^2$ region (see section 1.1), the elementary cross section for the production of the heavy quark-antiquark pair $\sigma_{\mathrm{ij}\to\mathrm{Q\overline{Q}}}$ can be calculated with a perturbative expansion of α_s, which depends on the energy scale of the process, encoded in the renormalisation scale, μ_{R}. The two processes that contribute to the heavy-quark production cross section at leading order in the perturbation theory ($\mathcal{O}(\alpha_s^2)$) are the quark-antiquark annihilation $\mathrm{q\overline{q}} \to \mathrm{Q\overline{Q}}$ and the gluon fusion $\mathrm{gg} \to \mathrm{Q\overline{Q}}$ [73].

The production cross section of open heavy-flavour hadrons in pp collisions can be obtained from the elementary heavy quark-antiquark production cross section by applying the *factorisation theorem*:

$$\sigma_{\mathrm{pp}\to\ \mathrm{H_Q+X}} = \sum_{\mathrm{i,j=q,\overline{q},g}} f(x_{\mathrm{i}};\mathcal{Q}^2) \otimes f(x_{\mathrm{j}};\mathcal{Q}^2) \otimes \sigma_{\mathrm{ij}\to\mathrm{Q\overline{Q}}} \otimes D(z_{\mathrm{Q}};\mathcal{Q}^2), \tag{2.1}$$

where $f(x_{\mathrm{i}};\mathcal{Q}^2)$ is the *parton distribution function* (PDF), describing the probability to find a parton i in the colliding proton which carries a fraction x_{i} of the proton momentum, and $D(z_{\mathrm{Q}};\mathcal{Q}^2)$ is the *fragmentation function* (FF), which describes the probability that the heavy quark Q hadronises in the hadron $\mathrm{H_Q}$, carrying a fraction z_{Q} of the

original quark momentum. Both the PDFs and the FFs describe non-perturbative processes and therefore cannot be obtained with pQCD calculations. The PDFs are typically parametrised using measurements of deep-inelastic scattering [74–76], while the FFs from measurements in e^+e^- collisions [77]. Both the PDFs and the FFs are parametrised at a given energy scale $\mathcal{Q}_0^2$ and are subsequently evolved to the desired $\mathcal{Q}^2$ using the DGLAP equations [78]. Since the PDFs and the FFs depend on the energy scale of the considered process, they are expressed as a function of the factorisation scale, μ_F. The μ_F and μ_R scales are usually chosen of the same order of the momentum transfer of the hard process $\mu_\mathrm{R} \sim \mu_\mathrm{F} \sim \sqrt{m_\mathrm{Q}^2 + p_\mathrm{T,Q}^2}$ or $\sim \sqrt{4m_\mathrm{Q}^2 + p_\mathrm{T,Q}^2}$.

The state-of-the-art perturbative calculations that provide predictions for the production cross sections of open heavy flavours using the collinear factorisation approach are FONLL [79, 80] and GM-VFNS [81–83]. They are computed with a next-to-leading order (NLO) accuracy with all-order resummation of next-to-leading logarithms. In Fig. 2.1, the p_T-differential production cross sections of D^0 (top-left panel), D^+ (top-right panel), and B^0 (bottom panel) mesons measured in pp collisions at $\sqrt{s} = 5.02$ TeV and $\sqrt{s} = 7$ TeV by the ALICE and LHCb Collaborations, respectively, are compared to FONLL and GM-VFNS(mod-$\mu_\mathrm{R,F}$) [81, 82] calculations. The pQCD calculations are compatible within their uncertainties with the measured beauty and charm production at the LHC. Nevertheless, for the charm mesons, the measurements systematically lay on the upper edge of FONLL uncertainty band. This was observed at RHIC ($\sqrt{s} = 200$ GeV), Tevatron ($\sqrt{s} = 1.96$ TeV), and LHC ($\sqrt{s} = 2.76 - 13$ TeV) energies.

Calculations at the leading order (LO) approximation, with the factorisation implemented in terms of the partonic transverse momentum k_T, are available within the k_T-FACTORISATION model [85]. The k_T-FACTORISATION predictions describe the data at low and intermediate p_T, but overshoots them for $p_\mathrm{T} \gtrsim 7$ GeV/c.

Another approach for the description of the production of heavy-flavour hadrons alternative to pQCD calculations is represented by general purpose Monte Carlo generators, such as PYTHIA [86] and HERWIG [87]. These generators have the advantage of providing a more complete description of the final state, including hard and soft interactions, parton distributions, initial- and final-state parton showers, multiple parton interactions, fragmentation and decays. However, they implement exactly only LO processes, while higher order calculations are included only in an approximate approach. For example, the PYTHIA generator includes also flavour-excitation processes, such as $\mathrm{qQ} \rightarrow \mathrm{qQ}$, $\mathrm{gQ} \rightarrow \mathrm{gQ}$, and $\mathrm{g} \rightarrow \mathrm{Q\overline{Q}}$. These processes diverges for the transverse momentum of the outgoing quarks of the hard interaction ($p_\mathrm{T}^\mathrm{hard}$) going to zero, Therefore, a lower cut-off on $p_\mathrm{T}^\mathrm{hard}$, which influences the low-p_T region of the heavy-flavour hadron production, is applied. Monte Carlo generators with NLO accuracy, such as POWHEG [88] and MC@NLO [89], are also available and can be matched to the parton shower of PYTHIA and HERWIG. They provide predictions for more differential observables (e.g. correlations) and jets.

2.2 Modifications in the cold nuclear matter

The presence of nuclei in the collision implies a modification in the production of open-heavy flavours also in absence of a colour-deconfined medium, due to the CNM

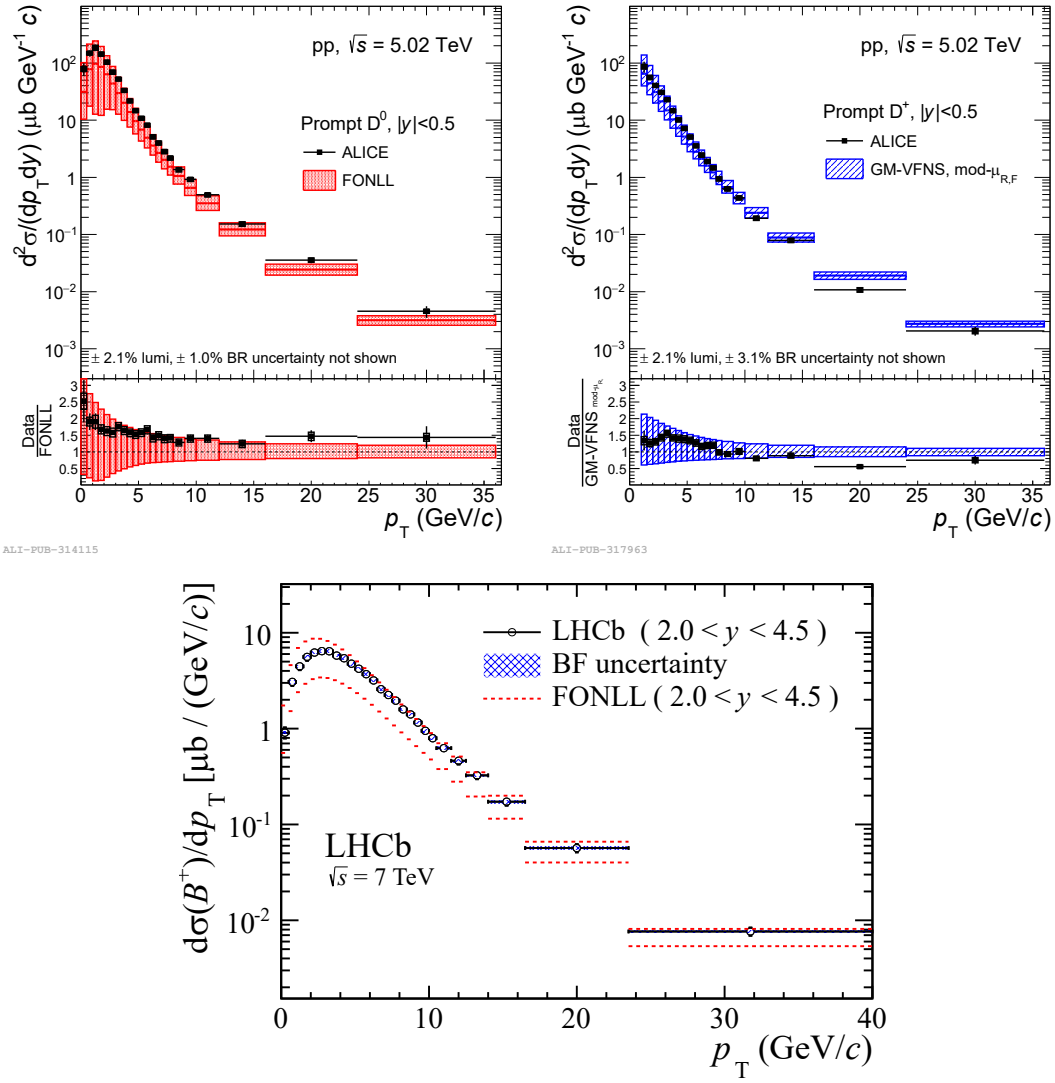

Figure 2.1: Top: p_{T}-differential production cross section of D^0 (left panel) and D^+ (right panel) mesons at mid-rapidity ($|y| < 0.5$) measured by the ALICE Collaboration in pp collisions at $\sqrt{s} = 5.02$ TeV compared to FONLL [79, 80] and GM-VFNS(mod-$\mu_{\mathrm{R,F}}$) [81, 82] calculations, respectively. Figures taken from Ref. [1]. Bottom: p_{T}-differential production cross section of B^+ mesons at forward rapidity ($2.0 < y < 4.5$) measured by the LHCb Collaboration in pp collisions at $\sqrt{s} = 7$ TeV compared to FONLL calculations. Figure taken from Ref. [84].

effects (see Sec. 1.4.6). It is important to factorise these effects from those induced by the creation of the QGP, in order to properly interpret the measurements in A–A collisions. This is typically performed by studying p–A or d–A collisions.

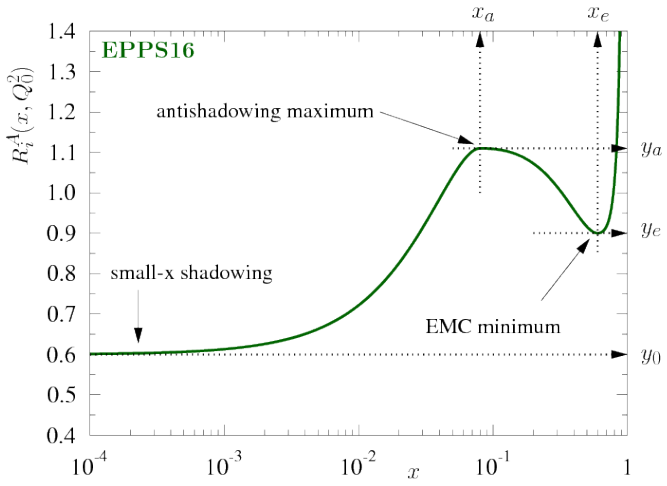

Figure 2.2: Representation of the nuclear PDFs modification as a function of x. Figure taken from Ref. [93].

The dominant effect at LHC energies is the modification of the PDFs. If the nuclei were a simple collection of free nucleons, the only modification expected for the PDFs would be due to the Fermi motion of the protons and neutrons inside the nucleus, which leads to a modification of the distribution of the nucleon momentum fraction (Bjorken x) carried by the partons. However, experiments of deep-inelastic scattering with nuclei observed other effects, which depend on the range of x considered. The modification of the PDFs is usually quantified by the ratio

$$R(x; \mathcal{Q}^2) = \frac{f^{\mathrm{A}}(x; \mathcal{Q}^2)}{\mathrm{A} \cdot f^{\mathrm{p}}(x; \mathcal{Q}^2)}, \tag{2.2}$$

where $f^{\mathrm{p}}(x; \mathcal{Q}^2)$ is the PDF in the free nucleon, while $f^{\mathrm{A}}(x; \mathcal{Q}^2)$ that in a nucleon bounded inside a nucleus with A nucleons. Figure 2.2 shows the modification of the PDFs as a function of x. For $x \lesssim 0.05$ a suppression of the PDFs called *shadowing* is observed [90]. This effect can be described by the high density of gluons at low x, which implies a high gluon-fusion probability. This is taken to the extreme in the Color Glass Condensate (CGC) model, which predicts a saturation of the gluon density at very low x. An enhancement called *anti-shadowing* is instead found in the $0.05 \lesssim x \lesssim 0.3$ interval. For $0.3 \lesssim x \lesssim 0.8$ the ratio is lower than unity, reaching a minimum around $x \simeq 0.7$. This suppression is addressed as the *EMC effect* [91]. Finally, the ratio $R(x; \mathcal{Q}^2)$ increases above unity because of the Fermi motion for $0.8 \lesssim x \lesssim 1$. As the proton PDFs (see Sec. 2.1), the nuclear PDFs are parametriesd via global fits to several sets of experimental data [92, 93].

At LHC energies, the heavy-flavour production is expected to be influenced mostly by the shadowing, since $\mathrm{c\overline{c}}$ and $\mathrm{b\overline{b}}$ pairs at mid-rapidity are produced in hard scatterings with values of Bjorken x around $\sim 10^{-4}$ for charm and $\sim 10^{-3}$ for beauty, increasing

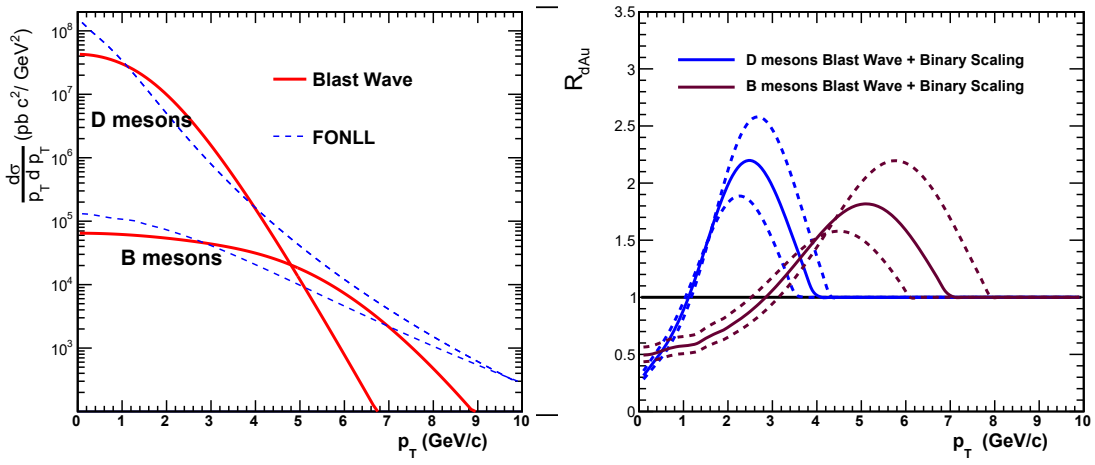

Figure 2.3: Left: p_{T} distributions of D and B mesons from FONLL [79, 80] (dashed lines) and from the blast-wave prediction obtained from fits to pion, kaon, and proton spectra (solid lines). Right: R_{dAu} obtained by dividing the p_{T} distributions from the Blast-Wave and FONLL models and assuming the binary scaling at high p_{T}. Figure taken from Ref. [95].

with increasing p_{T} [94].

Another important effect that contributes to the modification of the open heavy-flavour production in p–A collisions compared to that in pp collisions. is the *Cronin enhancement*, which was observed for the first time in p–A experiments at Fermilab [96]. It consists in an increase of the nuclear modification factor above unity, due to a shift of the p_{T} distribution in p–A collisions toward higher values of transverse momentum. The interpretation of this effect is based on the idea that the partons inside the projectile particle go through multiple elastic collisions with the constituents of the target nucleus, before the hard scattering. These elastic interactions transfer an initial transverse momentum to the partons, which is responsible of the p_{T}-spectrum shift (k_{T} *broadening*) for the particles produced in hard scatterings, such as heavy-quarks. In recent years, collective-like behaviours were observed at LHC and RHIC energies in small systems, suggesting also the presence of final-state effects in p–A collisions (see Sec. 1.4.4 and 1.4.5), that may lead to a similar effect. The radial flow observed via the measurement of light-flavour hadrons may also influence the shape of the p_{T} distributions of open-heavy flavours. In Ref. [95], the effect of the radial flow for B and D mesons in d–Au collisions was investigated using the Blast-Wave model. The left panel of Fig. 2.3 shows the comparison of the p_{T} distributions for D and B mesons obtained with FONLL calculations and those obtained with the Blast-Wave model, where the parameters were fixed to those extracted via simultaneous fits of pion, kaon, and proton spectra measured by the PHENIX Collaboration in the 20% most central d–Au collisions at $\sqrt{s_{\mathrm{NN}}} = 200$ GeV [97]. The right panel of the same Figure shows the nuclear modification factor obtained by dividing the p_{T} distributions from the Blast-Wave and FONLL models, assuming the binary scaling to be satisfied at

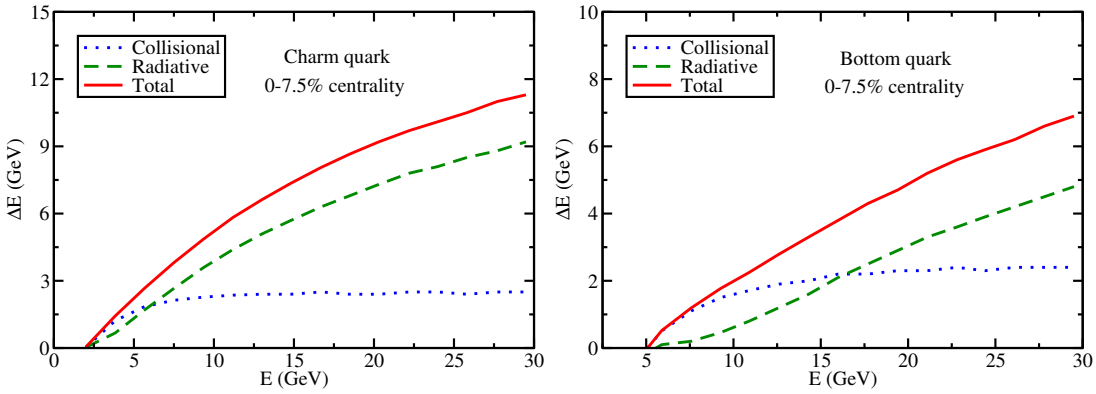

Figure 2.4: Comparison of radiative and collisional energy loss for charm (left panel) and beauty (right panel) quarks as a function of the quark energy as obtained from the calculations in Ref. [101]. Figure taken from Ref. [101].

high p_{T}. A large enhancement up to a factor 2 (1.8) is observed around $p_{\mathrm{T}} \approx 2$ (5) GeV/c for D (B) mesons. The same study performed for the 5% most central p–Pb collisions at $\sqrt{s_{\mathrm{NN}}} = 5.02$ TeV [42] leads to a 20% enhancement of the D-meson nuclear modification factor around $p_{\mathrm{T}} \approx 3$ GeV/c [95]. A similar effect is also obtained by the POWLANG [98] and DUKE [99] model calculations that include the formation of the QGP, but differently from the Blast-Wave model, only a partial thermalisation of the charm quarks. These models include also a suppression of about 20% for $p_{\mathrm{T}} > 3-5$ GeV/c, due to the energy loss of the charm quark in the QGP, that will be described in the next sections.

2.3 Interactions with the hot deconfined medium

Heavy quarks traversing the QGP interact with the medium constituents via elastic (collisional) and inelastic (gluon radiation) processes. The typical momentum exchange with the heat bath which of the order of the medium temperature $\mathcal{Q}^2 \approx T$, and thus typically small compared to their thermal momentum, $p_{\mathrm{Q}}^{\mathrm{th}} = \sqrt{2m_{\mathrm{Q}}T}$. Hence, low-$p_{\mathrm{T}}$ heavy quarks execute a *Brownian motion* in the medium, undergoing several momentum kicks. The interactions with the medium constituents cause a loss of energy of the parton that traverse the medium, but they also provide a push to low-p_{T} quarks due to the radial flow of the bulk. Moreover, the heavy-quark thermalisation time is of the order of the medium lifetime or more [100], and therefore the momentum spectra of heavy-flavour hadrons carry the memory of the interaction history, making them excellent probes of the medium properties. For high momenta, their mass becomes negligible ($m_{\mathrm{Q}} \ll p$) and they behave like light particles, which lose energy mainly via gluon radiation. Figure 2.4 shows the energy loss via collisional and gluon radiation processes as a function of the quark energy for charm (left panel) and beauty (right panel) quarks, as calculated in Ref. [101].

2.3.1 Gluon radiation

High-momentum partons traversing the QGP interact with the free colour charges of the deconfined medium and lose energy mainly for gluon radiation (*gluonsstralhung*), which is the analogous process of the electromagnetic *bremsstralhung*.

The energy loss calculations are performed by several theoretical groups that adopts different approximations. In the BDMPS model [102], the medium is modelled with static scattering centres, which implies that the hard parton undergoes multiple scatterings, picking up transverse momentum k_{T}. A gluon in the hard parton wave function can be emitted due to multiple scatterings, when the transferred transverse momentum k_{T} is enough to decohere it from the partonic projectile. The characteristic energy of the emitted gluons ω_c for a finite path length L traversed by the parton is

$$\omega_c = \frac{1}{2}\hat{q}L^2, \tag{2.3}$$

where $\hat{q}$ is the transport coefficient, defined as the average squared transverse momentum transferred to the projectile per unit of path length $\hat{q} = \langle k_{\mathrm{T}}^2 \rangle / L$. The energy distribution of the radiated gluons with $\omega \ll \omega_c$ can be obtained as

$$\omega \frac{\mathrm{d}I_{\mathrm{rad}}}{\mathrm{d}\omega} = \frac{2\alpha_s C_R}{\pi}\sqrt{\frac{\omega_c}{2\omega}}. \tag{2.4}$$

where C_R is the *Casimir factor* for the QCD vertices, which is equal to 4/3 for quark-gluon coupling and to 3 for gluon-gluon coupling. The average energy loss $\langle \Delta E_{\mathrm{rad}} \rangle$ can be expressed as

$$\langle \Delta E_{\mathrm{rad}} \rangle = \int_0^{\omega_c} \omega \frac{\mathrm{d}I_{\mathrm{rad}}}{\mathrm{d}\omega}\mathrm{d}\omega \propto \alpha_s C_R \omega_c \propto \alpha_s C_R \hat{q} L^2. \tag{2.5}$$

The average energy loss is independent from the energy of the hard parton that traverse the QGP, is proportional to the transport coefficient $\hat{q}$ and to $\alpha_s C_R$, hence larger by a factor 9/4 for gluons than for quarks.

Moreover, the *dead cone effect* [103] predicts that the energy loss decreases with increasing mass of the travelling parton, since the gluon emission is forbidden at angles smaller than

$$\Theta_c = m_{\mathrm{Q}}/E_{\mathrm{Q}}, \tag{2.6}$$

where m_{Q} and E_{Q} are respectively the mass and the energy of the quark.

A simple observable which has sensitivity to the energy loss is the nuclear modification factor R_{AA} (see Sec. 1.4.6). Figure 2.5 shows the average R_{AA} of prompt D^0, D^+, and D^{*+} mesons measured as a function of p_{T} (left panel) and centrality, expressed in terms of N_{part}, (right panel) by the ALICE Collaboration in Pb–Pb collisions at $\sqrt{s_{\mathrm{NN}}} = 2.76$ TeV [104, 105]. Prompt D mesons come directly from the hadronisation of a charm quark, or from the decay of excited open charm or charmonium states. A large suppression up to a factor 5-6 (2-3) is observed for central (semi-central) collisions for $p_{\mathrm{T}} > 6$ GeV/c, where the dominant process is the radiative energy loss. In the same p_{T} region, the nuclear modification factor measured in p–Pb collisions at

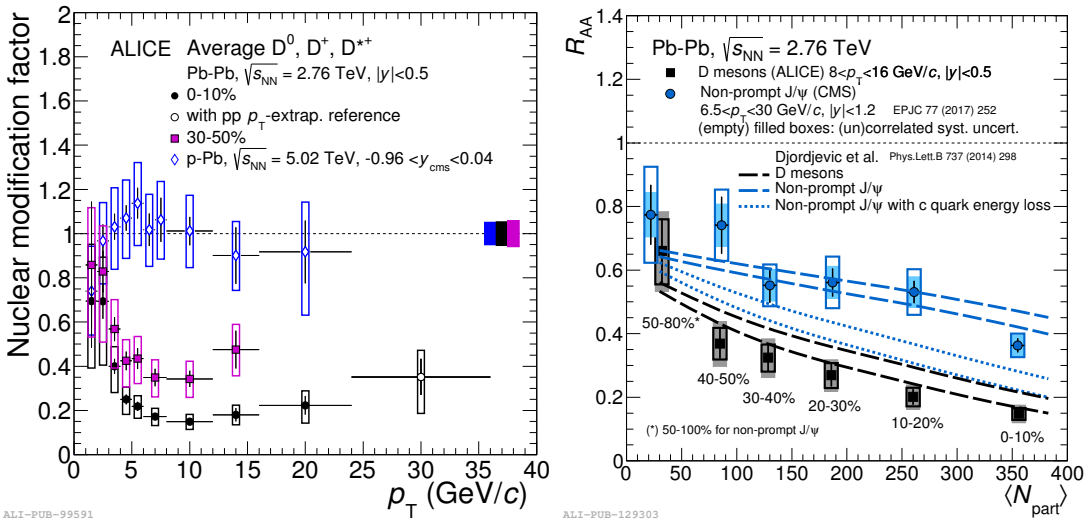

Figure 2.5: Left: average R_{AA} of prompt D^0, D^+, and D^{*+} mesons as a function of p_{T} in central (0–10%) and semi-central (30–50%) Pb–Pb collisions at $\sqrt{s_{\mathrm{NN}}} = 2.76$ TeV compared to that in p–Pb collisions at $\sqrt{s_{\mathrm{NN}}} = 5.02$ TeV. Figure taken from Ref. [104]. Right: average R_{AA} of prompt D^0, D^+, and D^{*+} mesons as a function of centrality (expressed in terms of N_{part}) in Pb–Pb collisions at $\sqrt{s_{\mathrm{NN}}} = 2.76$ TeV measured by the ALICE Collaboration [105] compared to that of non-prompt J/ψ mesons measured by the CMS Collaboration at the same centre-of-mass energy [106] and to model calculations [103]. Figure taken from Ref. [105].

$\sqrt{s_{\mathrm{NN}}} = 5.02$ TeV is consistent with unity. The R_{AA} of J/ψ mesons coming from beauty-hadron decays (non-prompt J/ψ) measured by the CMS Collaboration in Pb–Pb collisions at $\sqrt{s_{\mathrm{NN}}} = 2.76$ TeV [106] is found to be higher than that of prompt D mesons, as expected by the dead cone effect. The two measurements are performed in the intervals $8 < p_{\mathrm{T}} < 16$ GeV/c and $6 < p_{\mathrm{T}} < 30$ GeV/c, for prompt D mesons and non-prompt J/ψ mesons respectively, and therefore in a region where the dominant contribution to the energy loss is given by the radiative processes.

2.3.2 Collisional processes

The dominant interaction processes for low-p_{T} heavy quarks are the elastic scatterings with the medium constituents [107]. These processes lead to a energy loss that can be expressed as [108]:

$$\langle \Delta E_{\mathrm{coll}} \rangle \approx \frac{1}{\sigma T} \int t \frac{\mathrm{d}\sigma}{\mathrm{d}t} \mathrm{d}t \tag{2.7}$$

where t is the transferred momentum, σ the integrated cross section of the particle-medium interaction, T the temperature of the medium, and $\mathrm{d}\sigma/\mathrm{d}t$ the parton–parton differential elastic cross section. Considering as dominant contribution to the elastic

cross section

$$\frac{\mathrm{d}\sigma}{\mathrm{d}t} \approx \frac{4\pi C_i \alpha_s^2}{t^2}, \tag{2.8}$$

where C_i is the colour factor for gg, gq and qq scatterings, in the limit $E_\mathrm{Q} \gg m_\mathrm{Q}^2/T$, the collisional energy loss $\langle \Delta E_\mathrm{coll} \rangle$ is found to be linearly dependent on the medium thickness L and logarithmically dependent on the initial parton energy [109].

The scatterings with the medium constituents transfer to the heavy quarks the radial and anisotropic flows of the QGP. The anisotropic flow will be discussed in Sec. 2.3.3. The space-time evolution of heavy quarks undergoing multiple elastic scatterings in the QGP can be described by the Boltzmann equation [72]:

$$\left[\frac{\partial}{\partial t} + \frac{1}{E_\mathrm{Q}}\frac{\partial}{\partial \vec{x}} + \vec{F}\frac{\partial}{\partial \vec{p}}\right] f_\mathrm{Q}(t, \vec{x}, \vec{p}) = C[f_\mathrm{Q}], \tag{2.9}$$

where f_Q is the phase-space distribution function, $\vec{F}$ is the force induced by the external field (e.g. chromo and electromagnetic fields), and $C[f_\mathrm{Q}]$ is the collisional integral, which contain the parton–parton scattering amplitude. In the limit of Brownian motion, which can be assumed since $m_\mathrm{Q} \gg T$ and therefore the momentum transfers between the heavy quark and the constituents are small, the Boltzmann equation can be approximated by the Fokker-Planck equation, which is often further reduced into the Langevin equation [101]:

$$\frac{\mathrm{d}\vec{p}}{\mathrm{d}t} = -\eta_D(p)\vec{p} + \vec{\xi}. \tag{2.10}$$

In the right-hand side of Eq. 2.10, the first term represents the drag force, while the second one the stochastic thermal force. The η_D coefficient is the inverse of the relaxation (thermalisation) time of the heavy quarks τ_Q, and it is related to the spatial diffusion coefficient D_s, which describes the broadening of the spatial distribution with time:

$$D_s = \frac{T}{\eta_D m_\mathrm{Q}} = \frac{T}{m_\mathrm{Q}}\tau_\mathrm{Q}. \tag{2.11}$$

Typical values of τ_Q are $5-15$ fm/c, which are of the order of the QGP lifetime in central heavy-ion collisions at RHIC and LHC energies ($5-10$ fm/c [72, 110]).

2.3.3 Azimuthal anisotropy

The initial spatial eccentricity in the azimuthal plane of a heavy-ion collision is transferred to the particle momenta via the pressure gradients produced by the hot and deconfined medium, as discussed in Sec. 1.4.5.

The dynamics of heavy quarks, however, is very different from that of the light partons that constitute the bulk of the medium, since they are produced in the initial hard scattering processes. Therefore, heavy quarks are not expected to be in equilibrium with the light partons at the formation time of the QGP, and thus they only marginally take part in the build-up of the collective motions of the bulk in the early stage of the system evolution. However, the bulk flow is transferred to the heavy quarks via the multiple interactions of the heavy quarks with the medium constituents discussed in the previous

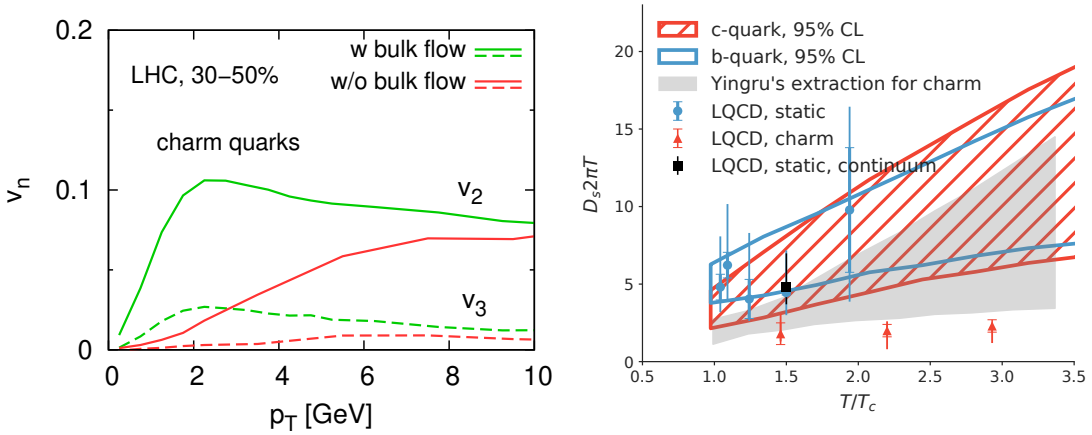

Figure 2.6: Left: v_2 and v_3 coefficients of charm quarks obtained with and without the contribution of the bulk flow. Figure taken from Ref. [113]. Right: Posterior range of the heavy quark spatial diffusion coefficient for charm (red) and beauty (blue) quarks as a function of the temperature compared to lattice QCD calculations. Figure taken from Ref. [114].

Sections, which impart non-vanishing elliptic and triangular flows to charm and beauty quarks [111, 112].

The contribution of the bulk flow to the heavy quark flow can be investigated with model calculations that implement the heavy-quark transport in an hydrodynamically expanding medium. In the left panel of Fig. 2.6 the v_2 and v_3 coefficients of charm quarks obtained in Ref. [113], with and without the contribution of the bulk flow, are compared. A large difference is observed for $p_{\mathrm{T}} \lesssim 4-6$ GeV/c, indicating that the anisotropic flow of charm quarks in this p_{T} interval is mostly imparted by the interactions with the bulk particles. At higher p_{T} this difference is reduced, indicating that the azimuthal anisotropy is governed by the path-length dependence of the in-medium parton energy loss.

The large contribution to the heavy-quark flow coming from the bulk flow, makes the measurement of the azimuthal anisotropy an important ingredient to quantify the strength of the interaction between the heavy quarks and the medium constituents. In Ref. [4], the D-meson elliptic flow measured in semi-central Pb–Pb collisions at $\sqrt{s_{\mathrm{NN}}} = 5.02$ TeV by the ALICE Collaboration was compared to the model predictions to infer the spatial diffusion coefficient of the charm quark. It was found that models that describe the data use values of the charm quark diffusion coefficient $2\pi T D_s$ in the range 1.5–7 at the critical temperature T_{c}, which corresponds to a thermalisation time of about $3-14$ fm/c. More quantitative estimations include the data-to-model comparison of different observables, such as the Bayesian analysis proposed in Ref. [114]. The resulting posterior range of the heavy-quark spatial diffusion coefficient is shown as a function of the temperature in the right panel of Fig. 2.6. The values obtained are consistent with those predicted by lQCD calculations and are significantly smaller than those predicted by pQCD calculations ($2\pi T D_s \approx 40$).

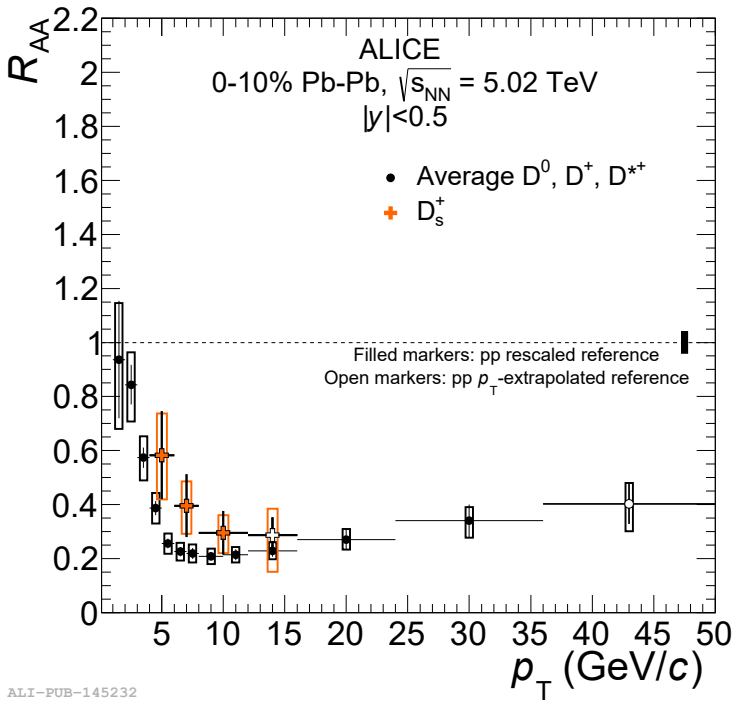

Figure 2.7: Top: Comparison between the R_{AA} of $\mathrm{D_s^+}$ and that of non-strange D mesons measured in Pb–Pb collisions at $\sqrt{s_{\mathrm{NN}}} = 5.02$ TeV by the ALICE Collaboration. Figure taken from Ref. [3].

2.4 Hadronisation mechanisms

In heavy-ion collisions, heavy quarks are expected to hadronise via two different mechanisms. On the one hand, heavy quarks can hadronise via fragmentation into a jet of lower-momentum hadrons as in the vacuum, on the other hand they can recombine with other quarks in the medium, giving rise to a hadron with momentum higher than that of the initial quark. The recombination (coalescence) mechanism gives an important contribution at low p_{T}, while the independent fragmentation is expected to dominate at high p_{T} [101, 115]. The recombination mechanism is supported by the measurements of the v_2 of identified particles (see Sec. 1.4.5), p_{T}-differential baryon-over-meson ratios [116], and the R_{AA} and v_2 of J/ψ mesons [117, 118].

The production of the strange charm meson $\mathrm{D_s^+}$ represents a sensitive probe of the coalescence mechanisms. In fact, if a fraction of charm quarks hadronise via coalescence, the relative abundance of $\mathrm{D_s^+}$ mesons with respect to non-strange D mesons is expected to be larger in heavy-ion collisions compared to pp collisions, due to the enhanced production of strange quarks in the QGP (see Sec. 1.4.3). In Fig. 2.7, the R_{AA} of $\mathrm{D_s^+}$ and non-strange D mesons measured in Pb–Pb collisions at $\sqrt{s_{\mathrm{NN}}} = 5.02$ TeV by the ALICE Collaboration [3] are compared. As expected from the coalescence mechanism, the central values of the $\mathrm{D_s^+}$-meson R_{AA} are higher than those of the non-strange D mesons, however

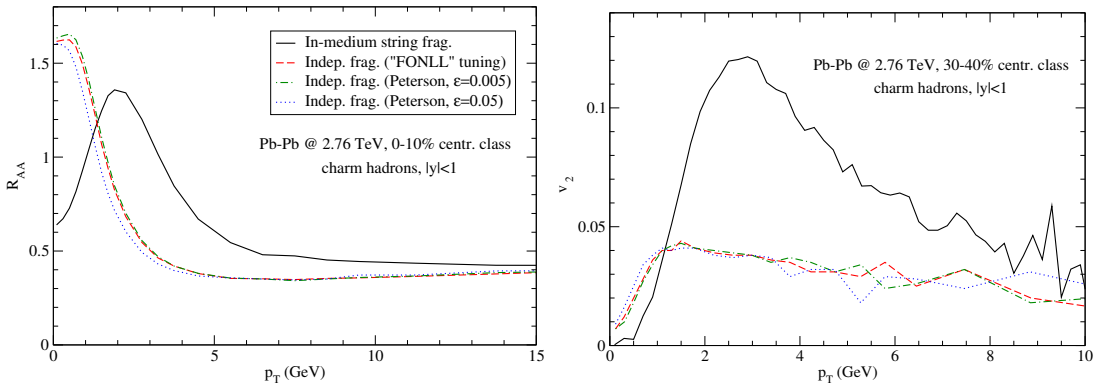

Figure 2.8: D-meson R_{AA} (left panel) and v_2 (right panel) resulting from different hadronisation schemes, as calculated in Ref. [120]. In case of fragmentation of strings formed via recombination with light thermal quarks from the medium, the R_{AA} shows a bump at intermediate p_{T} and the v_2 is significantly enhanced. Figures taken from Ref. [120].

the current precision does not allow to draw a final conclusion. Recently, the ALICE Collaboration measured an enhanced production of Λ_{c} baryons with respect to D^0 mesons in pp and p–Pb collisions compared to the relative abundance measured in e^+e^- collisions, which suggests the hadronisation via coalescence also in smaller systems [119].

The measurement of the anisotropic flow of open heavy-flavour hadrons can also provide insight of the hadronisation mechanism in heavy-ion collisions. The effect of the hadronisation via coalescence on the D-meson R_{AA} and v_2 according to the calculations from Ref. [120] is shown in Fig. 2.8. In case of hadronisation via coalescence, the R_{AA} shows a bump at intermediate p_{T}. Since the elliptic flow of light-flavour quarks is expected to be larger than that of charm quarks, the v_2 of D mesons is also expected to be larger in case of hadronisation of the charm quark via recombination with flowing light-flavour quarks.

Chapter 3

ALICE: A Large Ion Collider Experiment

The ALICE (A Large Ion Collider Experiment) detector is one of the four major experiments operating at the most powerful particle collider in the world, the Large Hadron Collider (LHC). ALICE is focused on the investigation of the properties of the strongly interacting matter at extreme energy densities reached in ultra-relativistic heavy-ion collisions. In this Chapter a description of the current ALICE experimental setup is given.

3.1 The Large Hadron Collider

The Large Hadron Collider (LHC) is a hadron accelerator and collider made of two rings of superconductive magnets installed at the European Organisation for Nuclear Research (CERN) laboratories [121]. The LHC with its circumference of 26.7 kilometers is the world largest circular particle accelerator. It is situated in the 3.8-meter-wide tunnel located 50 to 175 meters underground, that previously housed the Large Electron Positron (LEP) collider. The LHC was constructed to accelerate protons with a maximum centre-of-mass energy of $\sqrt{s} = 14$ TeV at a peak luminosity of $\mathcal{L} = 10^{34}$ cm^{-2} s^{-1} as well as Pb ions at a centre-of-mass energy per nucleon of $\sqrt{s_{\rm NN}} = 5.52$ TeV at a peak luminosity of $\mathcal{L} = 10^{27}$ cm^{-2} s^{-1}.

During the Run1 and Run2 physics programs, from 2009 to 2013 and from 2015 to 2018 respectively, the LHC delivered pp collisions at $\sqrt{s} = 0.9$, 2.76, 5.02, 7, 8 and 13 TeV, Pb–Pb collisions at $\sqrt{s_{\rm NN}} = 2.76$ and 5.02 TeV, p–Pb collisions at $\sqrt{s_{\rm NN}} = 5.02$ and 8.16 TeV, and Xe–Xe collisions at $\sqrt{s_{\rm NN}} = 5.44$ TeV to the four large CERN experiments, which are placed on four of the eight LHC beam intersections, as illustrated in figure 3.1. The CMS (Compact Muon Solenoid) and ATLAS (A Toroidal LHC Apparatus) experiments are general purpose detectors designed to measure the Higgs boson, which was discovered in 2012 [122, 123], and to search for physics beyond the Standard Model. The LHCb experiment was built to investigate the physics of beauty quark, especially the CP violation in the B-meson sector, and to study the matter-antimatter asymmetry. Finally, the ALICE experiment is the one designed for the physics of ultra-relativist

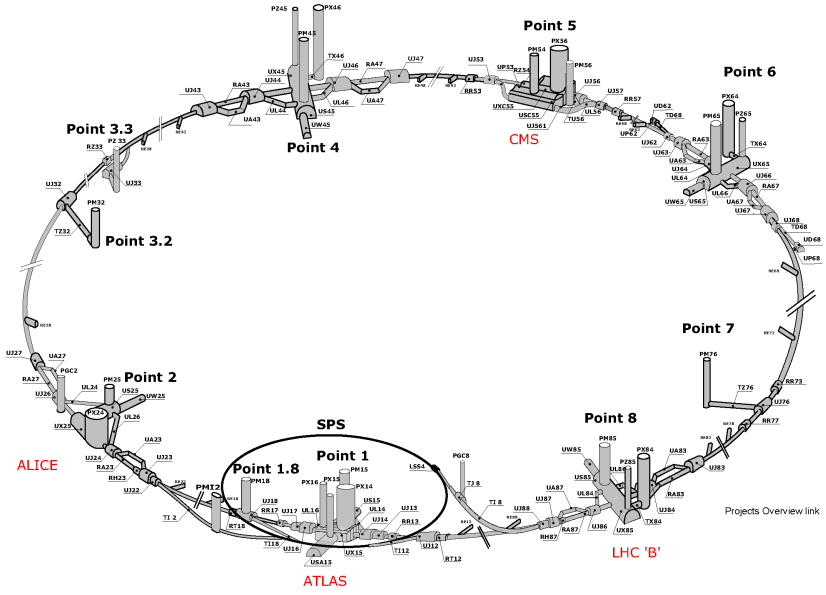

Figure 3.1: Schematic of the LHC layout, including each of the main experiments and all other beam interaction points. Figure taken from [124]

heavy-ion collisions, although all the four experiments have nowadays a dedicated heavy-ion program.

3.2 The ALICE apparatus

ALICE is a general-purpose detector built for the study of ultra-relativistic heavy-ion collisions [125]. It is designed to address the physics of strongly-interacting matter and the QGP at extreme values of energy density and temperature to investigate the phase diagram of the QCD phase. The study of the QGP properties requires to track charged particles down to very low momenta (about 80 MeV/c for pions [126]) in an environment characterised by a large charged particle multiplicity (original estimates of the charged-particle multiplicity density at mid-rapidity in a central Pb–Pb event ranged from $\mathrm{d}N/\mathrm{d}\eta = 2000$ up to $\mathrm{d}N/\mathrm{d}\eta = 8000$). For these reasons detectors with high granularity and low material budget, such as the Time Projection Chamber (TPC) [127] and the Inner Tracking System [128], were adopted. In addition, a key feature of ALICE is the possibility to identify particles in a wide momentum range, using the information provided by different particle-identification (PID) detectors.

The ALICE apparatus, shown in Fig. 3.2, is 26 m long, 16 m high, 16 m wide and weights more than 10000 tons. The ALICE coordinate system is a right-handed Cartesian system. The z axis identifies the beam direction, pointing towards the ATLAS experiment (see figure 3.1), while the transverse plane is defined by the x and y coordinates. In particular the x axis is aligned with the horizontal and points toward the accelerator

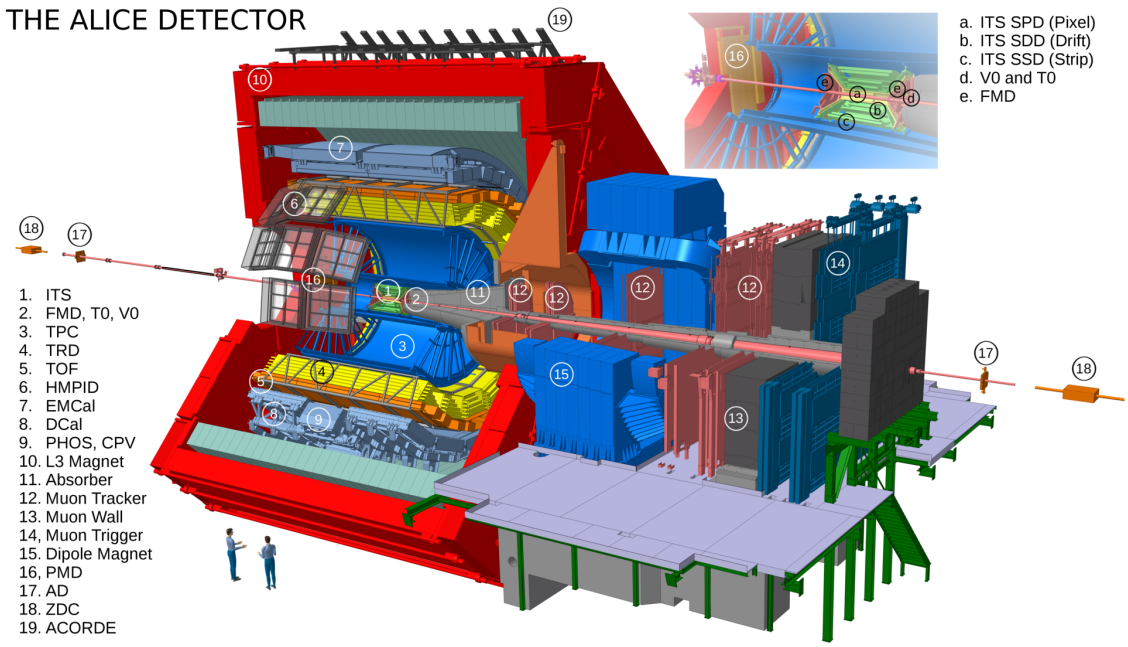

Figure 3.2: The ALICE experimental apparatus. The top right inset shows a zoom of V0, T0, FMD, and ITS detectors. Figure from ALICE figure repository ©.

centre, while the y axis is oriented upward. Furthermore, the polar angle θ is defined with respect to the z direction and φ, the azimuthal angle, increases counter-clockwise starting from the x axis towards the CMS side.

The ALICE apparatus is composed by two main parts: the *central barrel*, which consists of all the detectors located inside and outside the ALICE solenoid (L3 magnet in Fig. 3.1) in the pseudorapidity region $|\eta| < 0.9$ and the *muon spectrometer* that covers the pseudorapidity interval $-4 < \eta < -2.5$ and the full azimuth.

The central barrel is embedded in a large solenoid magnet reused from the L3 experiment at LEP, which generates a maximum magnetic field of $B = 0.5$ T parallel to the beam direction. From the inside out, the central barrel is composed of the Inner Tracking System (ITS), which is made of two silicon pixel detector layers (SPD), two silicon drift detector layers (SDD) and two silicon strip detector layers (SSD), a large cylindrical Time Projection Chamber (TPC), the Transition Radiation Detector (TRD), the Time Of Flight (TOF) detector, the Ring Imaging Cherenkov (HMPID) detector, and two electromagnetic calorimeters (PHOS and EMCal). All these detectors cover the full azimuth, except for PHOS, HMPID and EMCal.

The forward muon arm consists of a complex arrangement of absorbers, a large dipole magnet and fourteen planes of tracking and triggering Resistive Plate Chambers (RPC).

ALICE includes also several smaller detectors for global event characterisation and triggering (ZDC, PMD, FMD, T0, V0A and V0C) located at forward and backward rapidity and an array of scintillators (ACORDE) located on top of L3 magnet used to

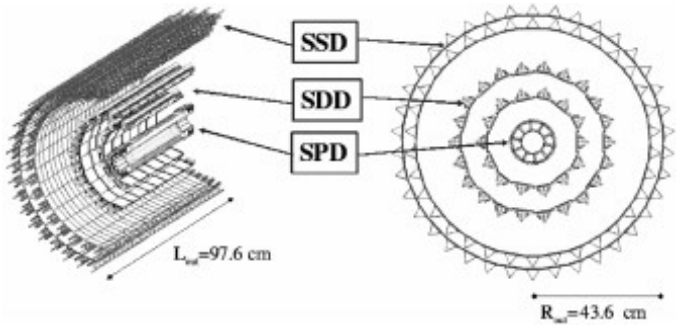

Figure 3.3: Schematic layout of the ALICE Inner Tracking System. Figure taken from [125]

trigger on cosmic rays. In the next section, a more detailed description of the subdetectors used for the analyses of my thesis project is provided.

3.2.1 Inner tracking system

The Inner Tracking System is the ALICE detector closest to the interaction point. As shown in Fig. 3.3, it is a cylindrical silicon tracker composed of six layers with three different technologies: the two innermost layers are silicon pixel detectors (SPD), the third and the fourth ones are silicon drift detectors (SDD) and the last two layers are double sided silicon strip detectors (SSD). The details about the spatial resolution and the material budget for each ITS subdetector is reported in Table 3.1. The total material traversed by a particle crossing the ITS, at $\eta = 0$, is around 7.2% of an interaction length X_0 including the thermal shields and support structures.

Silicon Pixel Detectors

The SPD detector is fundamental for the determination of the position of the point of interaction between the two incoming beams (also called *primary vertex*), decay (secondary) vertices, as well as for the measurement of the impact parameter (defined as the distance of closest approach between the track trajectory and the primary vertex), which

Detector	material budget ($\%X_0$)	spatial resolution (μm)		two-track resolution (μm)	
		$r\varphi$	z	$r\varphi$	z
SPD	$1.14 - 1.14$	12	100	100	850
SDD	$1.13 - 1.26$	35	25	200	600
SSD	$0.83 - 0.86$	20	830	300	2400

Table 3.1: Details about the spacial resolution and material budget of the ITS subdetectors.

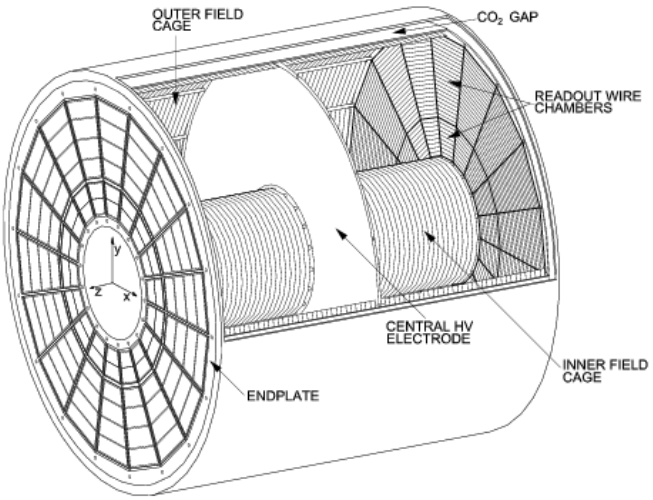

Figure 3.4: Schematic layout of the ALICE Time Projection Chamber. Figure taken from [127]

is crucial for the measurement of secondary tracks originating from the weak decays of strange, charm and beauty particles. Thanks to its fast response, it can also provide a fast trigger signal. The sensor matrix includes 256 x 160 cells, corresponding to a sensor area of 12.8 mm ($r\varphi$) x 70.7 mm (z). The thickness of the sensor is 200 μm.

Silicon Drift Detectors

The ALICE SDD detector has very good multi-track capability and provides two out of the four $\mathrm{d}E/\mathrm{d}x$ samples needed for the ITS particle identification (PID). The sensors have a thickness of 300 μm and a sensitive area of 70.17 mm ($r\varphi$) x 75.26 mm (z). The $r\varphi$ coordinate of the crossing particle is obtained from the drift time of the electrons originated from the transition of the crossing particle through the detector, with respect to the trigger time.

Silicon Strip Detectors

The SSD detector is crucial for the prolongation of tracks from the TPC to the ITS. SSDs also provide $\mathrm{d}E/\mathrm{d}x$ information that is used for the PID of low-momentum particles. The basic SSD module is a double-sided strip detector. The sensors are 300 μm thick and have 768 strips on each side with 95 μm pitch. The stereo angle between the strips of the two sides is 35 mrad, which is a compromise between the best resolution on $r\varphi$ direction and the minimisation of ambiguous measurement resulting from high particle densities.

3.2.2 Time Projection Chamber

The TPC is the main tracking detector of the central barrel and it is optimised to provide charged particle momentum measurements with good two-track separation and PID via $\mathrm{d}E/\mathrm{d}x$.

The TPC, shown in figure 3.4, is a cylindrical detector that covers the full azimuthal angle, having an active radial range from about 85 cm to 250 cm and and overall length along the beam direction of 500 cm. It covers the pseudorapidity range $|\eta| < 0.9$ for tracks with full radial track length (matches in ITS, TRD and TOF), and up to $|\eta| = 1.5$ for reduced track length. The TPC also allows charged particle reconstruction in a wide range of transverse momentum, from low p_{T} of about 100 MeV/c (for pions) up to 100 GeV/c. Each end plate is divided in 18 trapezoidal sectors, where multi-wire proportional chambers are mounted. The field cage is based on a design with a central high-voltage electrode and two opposite axial resistive potential dividers, which create a highly uniform electrostatic field in the common gas volume. The drift gas mixture $\mathrm{Ne/CO_2/N_2}$ was initially chosen and used during Run1 data taking, while at the beginning of the Run2 phase the Ne was replaced with the Ar. The mixture was changed again to the Ne mixture in 2017, owing to the larger space-charge distortions observed when using the Ar mixture.

Thanks to this design, the detector provides more than 90% efficiency in track finding, with a resolution up to about 2% in charge particle momentum measurement at $p_{\mathrm{T}} \approx$ 10 GeV/c. The relative $\mathrm{d}E/\mathrm{d}x$ resolution in pp (Pb–Pb) collisions was measured to be 5% (6%) for particle crossing the entire detector.

3.2.3 Time of Flight

The TOF detector is a large area detector arranged around the TRD that covers the same pseudorapidity range of ITS, TPC and TRD ($|\eta| < 0.9$). Its main purpose is the particle identification in the intermediate momentum range, up to 2.5 GeV/c (4 GeV/c) for the separation of pions (protons) from kaons by more than 3 times the time-of-flight resolution. The TOF is made of Multi-gap Resistive Plate Chambers (MRPC) which cover an area of about 160 m^2. Each multi gap is made of 10 layer double-stack strip detectors with a time resolution of about 40 ps. The time of flight (t_{flight}) for each particle is given by the information of the time in which the particle hits the detector (t_{hit}) and the start time of the event, t_0 ($t_{\mathrm{flight}} = t_{\mathrm{hit}} - t_0$). The start time t_0 is determined with the T0 detector or using the particle arrival times at the TOF, as described in [129]. The overall TOF resolution is around 60–80 ps in Pb–Pb events and 100 ps in proton-proton collisions, where there is a larger uncertainty on the determination of the event time zero.

3.2.4 V0

The V0 detector consists of two arrays of 32 scintillators located on both sides of the interaction point (V0A and V0C), which are segmented in 4 rings and 8 sectors in the radial and azimuthal directions, respectively. The V0A detector is 340 cm away from the nominal interaction point on the opposite side of the muon spectrometer, while the V0C is in front of the hadronic absorber at 90 cm from the nominal interaction

point. They cover the full azimuth and the pseudorapidity intervals $2.8 < \eta < 5.1$ and $-3.7 < \eta < -1.7$, respectively. The AND logic between the V0A and V0C signals defines the Minimum Bias (MB) trigger. In addition, the V0 time information is also used to reject background events due to beam-gas interactions. In Pb–Pb collisions the V0 signals are used to define the centrality of the collision and to estimate the plane of the reaction.

3.2.5 T0

The T0 detector is composed of two arrays of Cherenkov counters (T0A, T0C), which cover the full azimuth and the pseudorapidity intervals $4.61 < \eta < 4.92$ and $-3.28 < \eta < -2.97$, respectively. It is used for the determination of the start time for the TOF detector and as primary online luminosity monitoring detector.

3.2.6 ZDC

The ALICE Zero Degree Calorimeter (ZDC) detector includes two electromagnetic calorimeters (ZEM), two hadronic calorimeters for the detection of protons (ZP) and two for the detection of neutrons (ZN). The ZN and ZP calorimeters, detect spectator nucleons that emerge at 0° from the heavy-ion collisions. Both are located at $z = \pm 112$ m from the interaction point; the ZN calorimeters are placed between the two beam pipes, while the ZP calorimeters are located outside the two beam pipes on the side where positive particles are deviated by the LHC magnetic field. The ZEM calorimeters are located at 7.25 m distance from the interaction point and are used to distinguish between central and peripheral Pb–Pb collisions by measuring the energy deposited by π^0 decays and photons produced at forward rapidity.

The ZDC is mainly used to veto on the parasitic beam-gas background interactions and to determine the centrality in p–Pb and Pb–Pb collisions by measuring the energy deposited by spectator nucleons [130], which decreases with increasing centrality. For peripheral Pb–Pb collisions (centrality $> 50\%$) however the behaviour of the energy deposited by nuclear fragments is no more monotonic, since some nuclear fragments can be deviated by the LHC magnets outside the acceptance of the ZDC leading to a energy signature similar to that of central collisions. This ambiguity can be solved by correlating the ZDC energy deposit with the energy deposit in the ZEM [130]. The ZDC detectors are also fundamental for the determination of the spectator plane for the measurement of the directed flow in Pb–Pb collisions [131].

3.3 The ALICE offline framework

The ALICE offline software, called `AliRoot` [132], is based on `ROOT` [133], a scientific software designed for high-energy physics experiments, to deal with big data processing, statistical analysis, data visualisation, and storage. It is mainly written in `C++`, but it is integrated with other languages such as `Python` and `R` [134].

The `AliRoot` framework is used in ALICE for simulation, alignment, calibration,

reconstruction, and analysis of the experimental data collected by the experiment. Simulated events are generated with Monte Carlo generators, such as PYTHIA [86] and HERWIG [87] for pp collisions, and HIJING [135] and DPMJET [136] for proton–nucleus and nucleus–nucleus collisions. Furthermore, `AliRoot` includes a detailed description of the detector geometry, divided in independent modules that contain the code for simulation and reconstruction for each subdetector. In these packages the detector material budget is simulated in detail, including support structures and the beam pipe. To simulate the detector response to the passage of the particles, `AliRoot` makes use of different transport packages like GEANT3 [137], GEANT4 [138], and FLUKA [139].

The reconstructed data, both real and simulated, are stored in files containing all the physical information needed for the analysis and for checking the quality of the reconstruction for each sub-detector in a format called ESD (*Event Summary Data*). In order to reduce the size of the files and the computational time needed for the analysis, the AOD (*Analysis Object Data*) files, which contains only the information needed for the analysis, are produced.

The simulations, the reconstruction of the collected data, and the analyses are performed using the Worldwide LHC Computing Grid (WLCG) [140]. The Grid is a geographically distributed infrastructure that connects several computing centres from more than 40 countries. These computing centres have a hierarchical structure and are organised in 3 tiers. The Tier 0 is constituted by the CERN computing centre and the computing centre at the Wigner Research Centre for Physics in Budapest, which keep the first copy and perform the first reconstruction of all the raw data. A second replica of the raw and reconstructed data is stored in the Tier 1 centres, which are also involved in the re-processing of the data and in part of the reconstruction. Finally, the Tier 2 centres are dedicated to the production of Monte Carlo simulations and the processing of the analyses.

`AliRoot` also provides a user interface to access the grid, via the *AliEn* (ALICE Environment) [141] system. The AliEn user interface is used by ALICE users to access the data available everywhere on the grid, send analysis tasks and simulations, and monitor their status.

3.4 Centrality determination

An important quantity for the characterisation of a heavy-ion collision is the impact parameter b (already introduced in Sec. 1.3.1). However this quantity is not accessible experimentally, consequently the centrality of the collision is estimated using the produced particle multiplicity (N_{ch}) or the energy deposited in the ZDC (E_{ZDC}) by the spectator nucleons, which are then connected to the value of the impact parameter using the Glauber Model [24]. The centrality percentile is typically expressed as a fraction of the total hadronic cross sections σ_{AA},

$$c(b) = \frac{\int_0^b \frac{\mathrm{d}\sigma}{\mathrm{d}b'}\mathrm{d}b'}{\int_0^\infty \frac{\mathrm{d}\sigma}{\mathrm{d}b'}\mathrm{d}b'} = \frac{1}{\sigma_{\mathrm{AA}}}\int_0^b \frac{\mathrm{d}\sigma}{\mathrm{d}b'}\mathrm{d}b'. \tag{3.1}$$

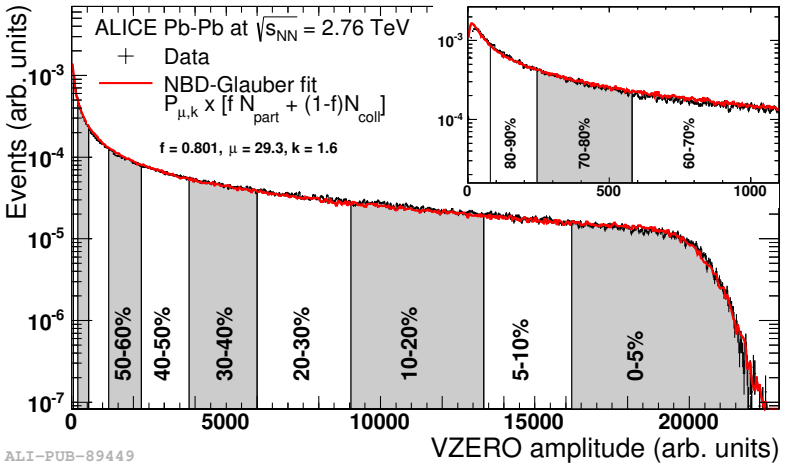

Figure 3.5: distribution of the sum of amplitudes in the V0 scintillators for Pb–Pb collisions at $\sqrt{s_{\mathrm{NN}}} = 2.76$ TeV. The distribution is fitted with the NBD-Glauber function, shown as a red curve. The inset shows a zoom of the low V0-signal region. Figure taken from [130]

Under the assumption that the particle multiplicity (energy deposited in the ZDC) increases (decreases) monotonically with centrality, the centrality can be experimentally computed as

$$c \approx \frac{1}{\sigma_{\mathrm{AA}}} \int_{N_{\mathrm{ch}}}^{\infty} \frac{\mathrm{d}\sigma}{\mathrm{d}N'_{\mathrm{ch}}} \mathrm{d}N'_{\mathrm{ch}} \approx \frac{1}{\sigma_{\mathrm{AA}}} \int_{0}^{E_{\mathrm{ZDC}}} \frac{\mathrm{d}\sigma}{\mathrm{d}E'_{\mathrm{ZDC}}} \mathrm{d}E'_{\mathrm{ZDC}} \tag{3.2}$$

where $\mathrm{d}\sigma$ can be replaced by the number of observed events $\mathrm{d}n$ with a given multiplicity/energy deposit and σ_{AA} with the total number of events, N_{ev}, corrected for the trigger efficiency and for the non-hadronic interaction background. The assumption of monotonic decrease of the energy deposit in the ZN and ZP detectors for increasing centrality does not hold anymore for peripheral heavy-ion collisions and therefore the information from the ZEM has to be used to determine the centrality (see 3.2.6).

In ALICE, several centrality estimators are used in different colliding systems [130]. The centrality estimators used in the analyses presented in this thesis are listed and described in more details below.

3.4.1 Centrality determination in Pb–Pb collisions

The centrality determination via particle multiplicity in Pb–Pb collisions is typically performed with the V0 detectors. The percentile of the hadronic cross section is obtained for each measured value of amplitude of the V0 (sum of V0A and V0C) signals by integrating the distribution of the V0 signal normalised at an *anchor point*, corresponding to 90% of the total hadronic cross section. The events with multiplicity lower than that of the anchor point are contaminated by background electromagnetic events and are therefore not considered for the centrality determination. The V0-signal distribution is then fitted with a parameterisation based on a Glauber Monte Carlo simulation and an

Ansatz on the particle production. In particular, the Glauber model is used to generate the number of participant nucleons $N_{\rm part}$ and the number of binary collisions $N_{\rm coll}$, while the multiplicity per nucleon–nucleon collision is parametrised with a Negative Binomial Distribution (NBD)

$$P_{\mu,k}(n) = \frac{\Gamma(n+k)}{\Gamma(n+1)+\Gamma(k)} \cdot \frac{(\mu/k)^n}{(\mu/k+1)^{n+k}} \tag{3.3}$$

which gives the probability of measuring n hits per independent emitting source of particles (called *ancestor*), where μ is the mean multiplicity per ancestor, and k is the parameter that governs the width of the distribution. The number of ancestors ($N_{\rm ancestors}$) is parametrised as a linear combination of a soft component (scaling with $N_{\rm part}$) and a hard component (scaling with $N_{\rm coll}$) [130]. Figure 3.5 shows the distribution of the sum of the V0A and V0C signals fitted with the NBD-Glauber function in Pb–Pb collisions at $\sqrt{s_{\rm NN}} = 2.76$ TeV. The slices represent the limits of the centrality classes defined in terms of percentiles of the total integral of the distribution. The resolution on the centrality determination ranges from 0.5% in central events to 2% in peripheral events.

3.4.2 Centrality determination in p–Pb collisions

The centrality determination in p–Pb collisions is affected by several biases that could lead to a nuclear modification factor (see Sec. 1.4.6) different from unity also in absence of nuclear effects [142]. In particular, the sources of bias observed include (i) the sizeable multiplicity fluctuations at fixed $N_{\rm part}$ compared to Pb–Pb collisions (*multiplicity bias*), (ii) the bias induced by the presence of high-$p_{\rm T}$ particles (*jet-veto bias*), and (iii) the dependence of the nucleon–nucleon impact parameter on the centrality of the p–Pb collision (*geometrical bias*).

The multiplicity bias originates from the consideration that the range of multiplicities used to select a centrality class is of similar magnitude as the fluctuations, with the consequence that a centrality selection based on multiplicity may select a sample of nucleon–nucleon collisions which is biased compared to a sample defined by the impact parameter. By selecting high (low) multiplicity one chooses not only large (small) average $N_{\rm coll}$, but also positive (negative) multiplicity fluctuations leading to deviations from the binary scaling of hard processes.

The jet-veto bias arises from the trivial correlation between the centrality estimator and the presence of a high-$p_{\rm T}$ particle in the event; the more energetic was the parton that originated the jet, the more is the particle multiplicity inside the jet. Therefore, for very peripheral collisions, the multiplicity range that governs the centrality is dominated by the bulk of soft collisions that represents an effective veto on hard processes, leading to a nuclear modification factor smaller than unity.

Finally, the impact parameter between two nucleons in p–Pb collisions depends on the centrality, leading to a pure geometrical bias. As illustrated in the left panel of Fig. 3.6 the mean impact parameter between two nucleons obtained from a Glauber Monte Carlo simulation is almost constant for central collisions, while it is significantly larger for $N_{\rm part} < 6$. This translates in a reduction of the average number of multi-parton

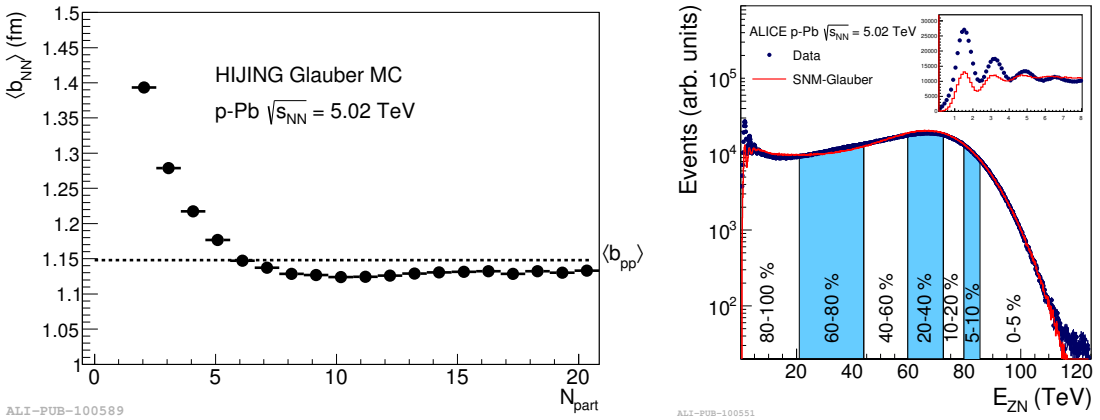

Figure 3.6: Left: Average nucleon–nucleon impact parameter as a function of the number of participants in p–Pb collisions at $\sqrt{s_{\rm NN}} = 5.02$ TeV from a Glauber MC simulation. Right: distribution of the energy spectrum measured in the ZNA neutron calorimeter in p–Pb collisions at $\sqrt{s_{\rm NN}} = 5.02$ TeV. The distribution is fitted with the SNM-Glauber function, shown as a red curve. The inset shows a zoom of the low ZNA-signal region. Figure taken from [142]

interactions (MPIs) for most peripheral events, resulting in a nuclear modification factor less than (greater than) one for peripheral (central) collisions.

In light of these considerations, the centrality in p–Pb is evaluated with the so called *hybrid method* that aims to provide an unbiased centrality estimator [142]. This method relies on the assumptions that (i) the estimation of the centrality with the ZN detectors, which is based on the measurement of the nucleon spectators, is free from the multiplicity and jet-veto biases and (ii) the charged-particle multiplicity measured at mid-rapidity scales with $N_{\rm part}$. Under these assumptions, the centrality intervals are classified using the Pb-going side of the ZN detector (ZNA) by slicing the energy distribution. Then, the scaling law of particle production in different pseudorapidity regions is studied as a function of several centrality classes defined by the ZNA energy distribution. Finally, the average number of binary nucleon–nucleon collisions $\langle N_{\rm coll}\rangle_{\rm i}$ in the i-*th* ZNA centrality class is obtained as

$$\langle N_{\rm coll}\rangle_{\rm i} = \langle N_{\rm part}\rangle_{\rm i} - 1 = \langle N_{\rm part}\rangle_{\rm MB} \cdot \left(\frac{\langle {\rm d}N_{\rm ch}/{\rm d}\eta\rangle_{\rm i}}{\langle {\rm d}N_{\rm ch}/{\rm d}\eta\rangle_{\rm MB}} \right)_{-1<\eta<0} - 1 \qquad (3.4)$$

where $\langle {\rm d}N_{\rm ch}/{\rm d}\eta\rangle$ is the average charged particle multiplicity.

The centrality determined with the hybrid method is consistent with that obtained by fitting the ZNA energy distribution using a Glauber MC coupled to a slow-nucleon emission (SNM) model (right panel of Fig. 3.6), that describes the nucleons emitted during a proton–nucleus interaction [143], and has the advantage of being model independent.

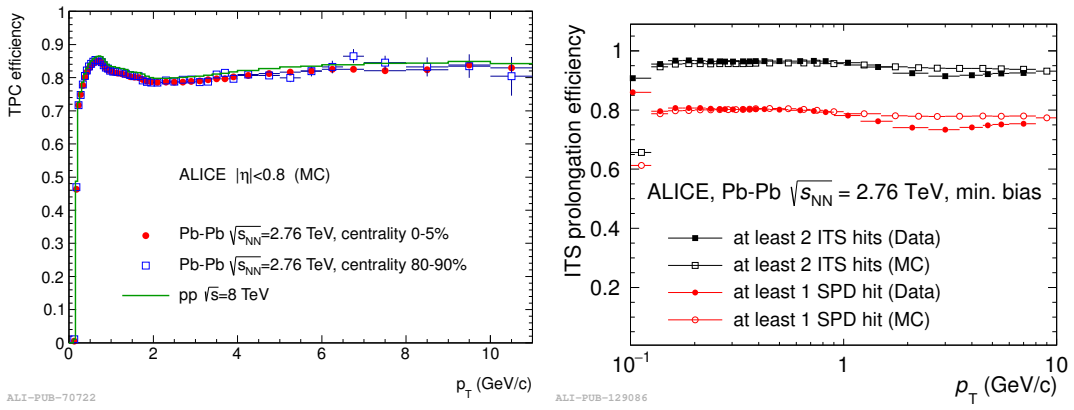

Figure 3.7: Left: reconstruction efficiency for TPC tracks in pp collisions at $\sqrt{s} = 8$ TeV and in central and peripheral Pb–Pb collisions at $\sqrt{s_{\rm NN}} = 2.76$ TeV. Right: matching efficiency of tracks from ITS to TPC in real (full markers) and simulated (open markers) Pb–Pb collisions at $\sqrt{s_{\rm NN}} = 2.76$ TeV. Figure taken from [126].

3.5 Track and vertex reconstruction

In ALICE the track-reconstruction and the vertex-finding procedures are performed offline. The tracking procedure starts with the conversion of the detector hits in clusters, characterised by several quantities, such as position, signal amplitude and signal time, with their associated errors. Then, a first evaluation of the primary vertex is performed as the space point that minimise the distance among the *tracklets*, track segments reconstructed by associating pairs of clusters in the two layers of the SPD within an azimuthal acceptance window. In low multiplicity events, if it is not possible to find a single point of convergence, the algorithm performs a one-dimensional minimisation to reconstruct the position of the interaction point along the beam direction (z axis) by using the distances of closest approach of the tracklets to the average position of the beam in the transverse plane.

After this procedure the tracks are reconstructed and fitted in TPC and ITS using the Kalman Filter algorithm [144] and subsequently prolonged to the other central barrel detectors and fitted again. As a first step, the track seeds are built from the clusters in the two outermost pad rows of the TPC and the primary vertex estimated with the SPD tracklets. Then, the seeds are propagated inward and updated with every nearest cluster found by Kalman Filter algorithm until the inner radius of the TPC is reached. The efficiency of reconstructed tracks in the TPC is shown in the left panel of Fig. 3.7 as a function of $p_{\rm T}$, in pp at $\sqrt{s} = 8$ TeV and Pb–Pb collisions at $\sqrt{s_{\rm NN}} = 2.76$ TeV. The efficiency drops for $p_{\rm T} \lesssim 500$ MeV/c due to the energy loss in the material of the detector, since the trajectory of particles that lose energy deviates from the helicoidal path of a charged track in a magnetic field. The observed shape of the efficiency at higher $p_{\rm T}$ is due to the loss of clusters in the dead zones between the TPC sectors.

The tracks reconstructed in the TPC are matched to the hits in the outermost SSD

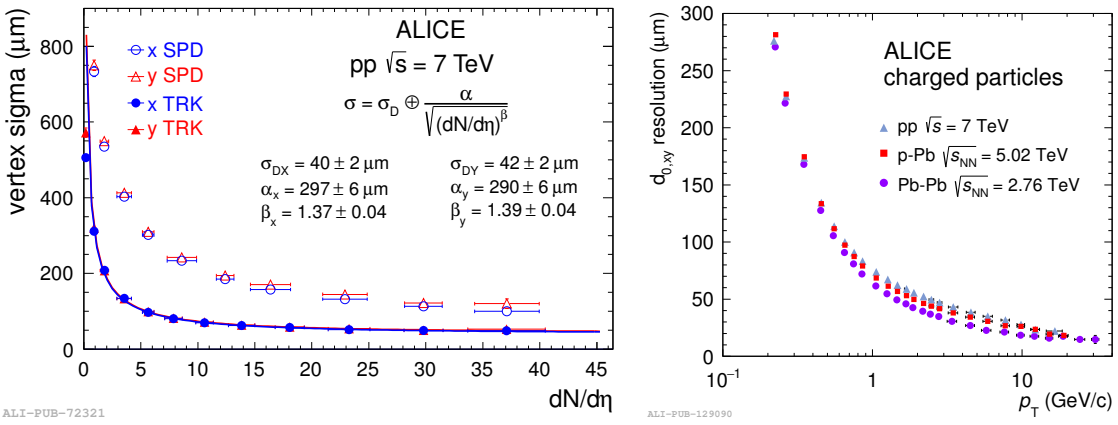

Figure 3.8: Left: resolution on the primary-vertex position using the SPD and the track algorithms as a function of the charged-particle multiplicity in pp collisions at $\sqrt{s} = 7$ TeV. Right: resolution on the impact parameter in the transverse plane for charged particles in pp, p–Pb, and Pb–Pb collisions as a function of p_{T}. Figure taken from [126].

layer and become the seed for the track finding in the ITS. Similarly to the previous step, the seed is propagated inward and updated at each ITS layer attaching all the clusters within a proximity cut. Therefore, for each TPC track, a corresponding tree of track hypotheses in the ITS is produced. The candidates are then selected according to their χ^2. The right panel of Fig. 3.7 shows the comparison between the fraction of tracks in TPC that have a prolongation in the ITS (matching efficiency) in data and in the simulation for Pb–Pb collisions at $\sqrt{s_{\mathrm{NN}}} = 2.76$ TeV, for different requirements on ITS points [126].

In order to increase the efficiency for tracks with low transverse momentum ($p_{\mathrm{T}} < 200$ MeV/c) and to reconstruct tracks of particles traversing dead zones of the TPC or which decay before entering in the TPC, the hits in the ITS not attached to tracks propagated from the TPC are used to perform an ITS stand-alone reconstruction.

The tracks obtained with clusters in both the ITS and TPC detectors are then back-propagated in the outward direction to match the clusters in the TRD and TOF, and the signals in EMCal, PHOS and HMPID. Finally, the tracks are re-fitted inward using all the previously found clusters and propagated to the point of distance of closest approach to the beam line.

After the full tracking procedure, if two or more tracks are reconstructed, the position of the primary vertex is recomputed using global tracks. From the left panel of Fig. 3.8 the improvement of the resolution on the primary-vertex position obtained with global tracks with respect to that obtained with SPD tracklets can be appreciated. The resolution depends on the charged-particle multiplicity, and in particular is around 200 μm for low-multiplicity ($\mathrm{d}N/\mathrm{d}\eta \approx 2$) pp collisions, 50 μm for high multiplicity ($\mathrm{d}N/\mathrm{d}\eta \approx 30 - 40$) pp collisions, and 10 μm for Pb–Pb collisions. The right panel of the same figure shows the resolution on the impact parameter projected on the transverse plane for all charged-particle tracks in pp, Pb–Pb and p–Pb collisions. The impact-parameter resolution for

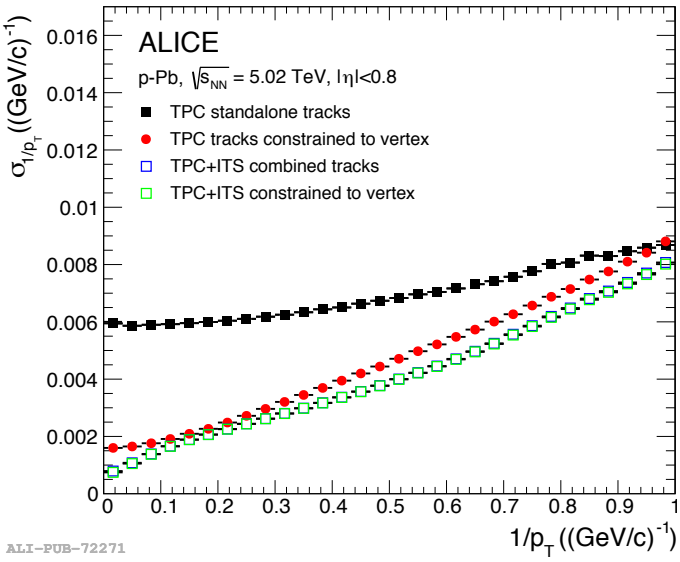

Figure 3.9: Resolution on $1/p_{\mathrm{T}}$ as a function of $1/p_{\mathrm{T}}$ in p–Pb collisions at $\sqrt{s_{\mathrm{NN}}} = 5.02$ TeV. The resolution is quoted for TPC tracks and for ITS+TPC tracks with and without vertex constraint. Figure taken from [126].

tracks with $p_{\mathrm{T}} = 1$ GeV/c is around 75 μm in pp collisions and 60 GeV/c in Pb–Pb collisions. The improvement in heavier systems is due to the large multiplicities that allow for a more precise determination of the primary vertex.

Figure 3.9 shows the resolution on $1/p_{\mathrm{T}}$ for TPC stand-alone tracks and tracks reconstructed with both TPC and ITS clusters, with and without vertex constrain, in p–Pb collisions at $\sqrt{s_{\mathrm{NN}}} = 5.02$ TeV. The resolution on the parameter $1/p_{\mathrm{T}}$ is directly connected to that on the p_{T} by the relation

$$\frac{\sigma_{p_{\mathrm{T}}}}{p_{\mathrm{T}}} = \frac{\sigma_{1/p_{\mathrm{T}}}}{1/p_{\mathrm{T}}}. \tag{3.5}$$

The resolution is quoted for $1/p_{\mathrm{T}}$ because this can be extracted directly from the covariance matrix of the Kalman Filter fit. The resolution on reconstructed track vary from 1% to 10% in the p_{T} range between 0.1 and 100 GeV/c.

3.6 Particle identification

One of the distinctive features of the ALICE detector is the excellent PID capability, which can be performed in a wide range of momentum, exploiting different techniques. In particular, the ITS and TPC detectors can be used to identify charged particles via the measurement of their specific energy loss, the TOF via the measurement of the particle time-of-flight measurement, the HMPID via the Cherenkov angle measurement of the light produced by the charged particle that traverses the detector. In addition, electrons and positrons can be identified by the TRD detector, via the measurement of

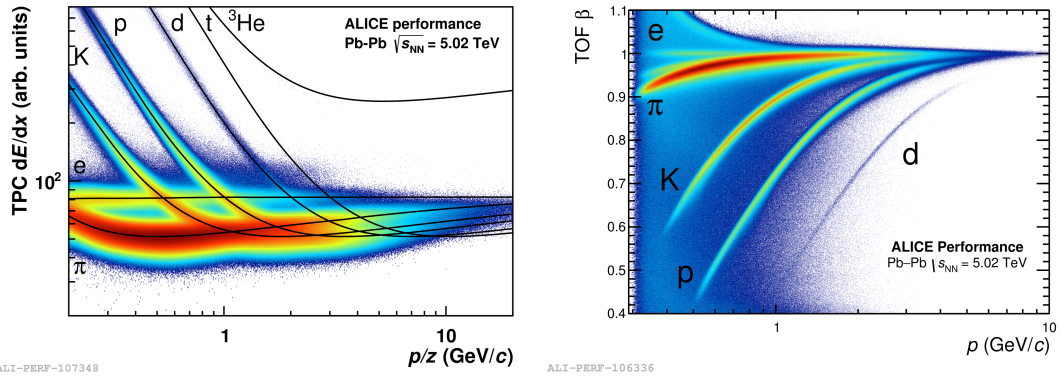

Figure 3.10: Left: specific energy loss ($\mathrm{d}E/\mathrm{d}x$) in the TPC as a function of the particle momentum in p–Pb collisions at $\sqrt{s_{\mathrm{NN}}} = 5.02$ TeV. The lines show the parametrisation of the expected mean energy loss. Right: velocity β as measured with the TOF detector as a function of momentum for particles reaching the TOF in Pb–Pb collisions at $\sqrt{s_{\mathrm{NN}}} = 5.02$ TeV. Figure from ALICE figure repository ©.

their transition radiation, and by the PHOS and EMCAL calorimeters via the energy deposited compared to their momentum (E/p). The techniques used for charged-hadron PID in the analyses presented in this thesis, based on the TPC and TOF detectors, are described in more details in the following sections.

3.6.1 TPC particle identification

The PID with the TPC is performed by simultaneously measuring the specific energy loss via the measurement of the charge deposited on up to 159 pad rows, the charge, and the momentum of each particle traversing the detector gas. A truncated mean of the $\mathrm{d}E/\mathrm{d}x$ samples is calculated using the 65% of the lowest-amplitude clusters. The particle identification is based on the comparison of the measured $\mathrm{d}E/\mathrm{d}x$ with the expectation for a specific particle species with a certain momentum p. The expected $\mathrm{d}E/\mathrm{d}x$ is obtained with a data-driven procedure that employs spline parameterisations, or with a function originally proposed by the ALEPH collaboration [145],

$$f(\beta\gamma) = \frac{P_1}{\beta^{P_4}}\left[P_2 - \beta^{P_4} - \ln\left(P_3 + \frac{1}{(\beta\gamma)^{P_5}}\right)\right]. \tag{3.6}$$

In the above formula β and γ are the relativistic factors and P_{1-5} are free parameters that can be determined by fitting the data distribution. The relative $\mathrm{d}E/\mathrm{d}x$ resolution achieved is of about 6% for particles crossing the entire detector. In the left panel of Fig. 3.10 the specific energy loss measured with the TPC in Pb–Pb collisions at $\sqrt{s_{\mathrm{NN}}} = 5.02$ TeV is shown as a function of the track momentum, with the curves of the expected $\mathrm{d}E/\mathrm{d}x$ of electrons, pions, kaons, protons, deuterium, tritium, and ^{3}He nuclei superimposed. The particle identification of pions and kaons can be performed on

a track-by-track basis for $p \lesssim 0.7$ GeV/c, where the largest separation is achieved (see left panel of Fig. 3.10). The separation is typically expressed in number of σ, where σ is the expected $\mathrm{d}E/\mathrm{d}x$ resolution for a track with a given momentum.

In the relativistic rise region ($2 \lesssim p \lesssim 20$ GeV/c) the relative particle abundances can still be extracted with a statistical approach.

3.6.2 TOF particle identification

The TOF is a dedicated PID detector, which measures the arrival time of charged particles. In order to obtain the flight time of the charged particles, the start time for the TOF detector can be provided either by the T0 detector or via a combinatorial analysis of the particle arrival times at the TOF detector. The overall TOF resolution, including the uncertainty on the start time of the event, and the tracking and momentum resolution contributions, is around $\sim 60 - 80$ ps for tracks with $p \approx 1$ GeV/c in Pb–Pb collisions [126]. As shown in the right panel of figure 3.10, where the particle velocity is plotted as a function of momentum, the TOF detector provides a proton-kaon separation at more than 3σ level up to $p \simeq 4$ GeV/c.

Chapter 4

D^+ and D_s^+ reconstruction strategy in pp, p–Pb and Pb–Pb collisions

In this Chapter, the data samples used in this thesis are introduced and the general strategy adopted to measure D^+ and D_s^+ mesons and their antiparticles in the central rapidity region of the ALICE detector is presented. The D^+ (D_s^+) mesons, composed by a charm quark and a down (strange) antiquark, cannot be directly revealed because of their mean proper decay length of few hundred microns that prevents them to reach the detector. Hence, they are measured via the exclusive reconstruction of their hadronic decays. In particular, the decay channels $D^+ \to K^-\pi^+\pi^+$ and $D_s^+ \to \phi\pi^+ \to K^-K^+\pi^+$ and their charge conjugates are considered in this thesis. The spatial resolution of the ALICE detector [126, 146] allows the separation of the secondary decay vertices of D mesons from the primary interaction vertex, therefore the analysis is based on the reconstruction and selection of secondary-vertex topologies with relatively large separation from the primary interaction vertex. The PID capabilities are also exploited to improve the selection of the D_s^+ and D^+ decay products and thus to reduce the background.

4.1 Data samples and event selection

The analyses presented in this thesis are performed on the data samples reported in Table 4.1, which include pp collisions at $\sqrt{s} = 5.02$ TeV, p–Pb and Pb–Pb collisions at $\sqrt{s_{\rm NN}} = 5.02$ TeV. All the data samples were collected with a MB trigger that required coincident signals in the V0A and V0C detectors. In addition, for the Pb–Pb samples collected in 2018, a further online selection on the sum of the V0 detector amplitudes was applied to enhance the most central (0–10%) and semi-central (30–50%) events.

System	$\sqrt{s_{NN}}$ (TeV)	Trigger	N_{events}	$\mathcal{L}_{int}$ (μb^{-1})	Year
pp	5.02	minimum bias	990×10^6	19300 ± 400	2017
p–Pb	5.02	minimum bias	623×10^6	292 ± 11	2016
Pb–Pb	5.02	minimum bias	104×10^6	13 ± 1	2015
	5.02	central	89×10^6	49 ± 1	2018
	5.02	semi-central	76×10^6	114 ± 1	2018

Table 4.1: Summary of data samples used for the analyses presented in this thesis. The centre-of-mass energy, the trigger strategy (see text for details), the number of events after the quality selections, and the integrated luminosity are reported.

4.1.1 Offline event selections

In p–Pb and Pb–Pb collisions, background events from machine-induced beam-gas interactions were rejected using the timing information from the V0 and the ZDC detectors. In pp collisions, the timing information from the V0 and the correlation between the number of hits and tracklets in the SPD detector were used for the same purpose.

As explained in Sec. 3.5, the primary vertex can be reconstructed using global tracks or SPD tracklets. Considering that the D^+ and D_s^+ mean-proper decay lengths are about 312 μm and 150 μm respectively [13], it is crucial to have a primary vertex position measured as precisely as possible to reconstruct the full decay topology. Therefore, only the events with a primary vertex reconstructed with global tracks were used for the analysis. In addition, to obtain a symmetric geometrical acceptance and to guarantee the pseudorapidity coverage of $|\eta| < 0.8$ in each ITS layer, the selected events were required to have a reconstructed primary vertex within ± 10 cm from the nominal position along the beam axis ($|z_{vtx}| < 10$ cm). This requirement also helps to reject satellite collisions. The SPD was also used to identify the presence of multiple interaction vertices in the same bunch crossing (in-bunch *pile-up* events) in pp and p–Pb collisions. In particular, the vertex-finding algorithm is run on the SPD tracklets not associated to the main vertex, which is the one with largest associated multiplicity; pile-up events are identified and rejected whenever another vertex with at least 5 contributors is found to be at least 0.8 cm away from the main vertex. The probability of in-bunch pile-up events was found to be negligible in Pb–Pb, given the lower interaction rate [3].

The number of events after the aforementioned selections (N_{events}) and the corresponding integrated luminosity ($\mathcal{L}_{int}$) are reported in Table 4.1 for each data sample. Further selections on the centrality were applied for each specific analysis and will be discussed in the dedicated Chapters.

4.1.2 Vertex-reconstruction efficiency

The selections reported in Sec. 4.1.1 reduce the reconstruction efficiency of the primary vertex. This efficiency is taken into account in the reconstruction efficiency of D mesons

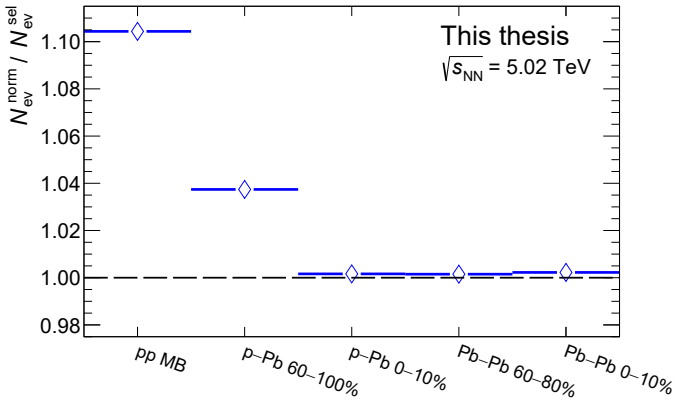

Figure 4.1: Ratio between the normalisation factor ($N_{\mathrm{ev}}^{\mathrm{norm}}$, see text for details) and the number of selected events ($N_{\mathrm{ev}}^{\mathrm{sel}}$) in pp, p–Pb, and Pb–Pb collisions at $\sqrt{s_{\mathrm{NN}}} = 5.02$ TeV.

(see Sec. 4.3.1), however the number of events with a primary vertex within $|z_{\mathrm{vtx}}| < 10$ cm has also to be considered for the normalisation of a production cross section. For this reason, these events were taken into account computing a corrected number of events for the normalisation

$$\begin{aligned} N_{\mathrm{ev}}^{\mathrm{norm}} &= N^{\text{reco vtx}}(|z_{\mathrm{vtx}}| < 10 \text{ cm}) + N^{\text{no vtx}}(|z_{\mathrm{vtx}}| < 10 \text{ cm}) = \\ &= N^{\text{reco vtx}}(|z_{\mathrm{vtx}}| < 10 \text{ cm}) + N^{\text{no vtx}} - N^{\text{no vtx}}(|z_{\mathrm{vtx}}| > 10 \text{ cm}) = \\ &= N^{\text{reco vtx}}(|z_{\mathrm{vtx}}| < 10 \text{ cm}) + N^{\text{no vtx}} - N^{\text{no vtx}} \cdot \frac{N^{\text{reco vtx}}(|z_{\mathrm{vtx}}| > 10 \text{ cm})}{N^{\text{reco vtx}}} \end{aligned} \tag{4.1}$$

where $N^{\text{reco vtx}}$ and $N^{\text{no vtx}}$ are the number of events with and without reconstructed primary vertex, respectively. The number of events with reconstructed vertex within 10 cm from the nominal position ($N^{\text{reco vtx}}(|z_{\mathrm{vtx}}| < 10$ cm)) corresponds to the number of selected events ($N_{\mathrm{ev}}^{\mathrm{sel}}$).

As shown in Fig. 4.1, the correction factor computed from $N_{\mathrm{ev}}^{\mathrm{sel}}$ to obtain $N_{\mathrm{ev}}^{\mathrm{norm}}$ is about 10.5% in pp collisions, 4% in peripheral (60–100%, estimated with the hybrid method described in Sec. 3.4.2) p–Pb collisions, while it is negligible for high-multiplicity (0–10%) p–Pb collisions and Pb–Pb collisions. This is motivated by the increase of the primary-vertex reconstruction efficiency as a function of the charged-particle multiplicity.

4.2 $\mathrm{D_s^+}$ and $\mathrm{D^+}$ decay-vertex reconstruction and selection

The $\mathrm{D_s^+}$ and $\mathrm{D^+}$ mesons (and their charge conjugates) are reconstructed in the hadronic decay channels $\mathrm{D^+ \to K^-\pi^+\pi^+}$ and $\mathrm{D_s^+ \to \phi\pi^+ \to K^-K^+\pi^+}$, using an analysis based on the selection of fully reconstructed decay topologies displaced from the primary interaction vertex. The main properties of these two particles [13] are reported in Table 4.2.

The candidate D mesons are built by combining triplets of tracks with proper charge-sign combination, $(+,-,+)$ for $\mathrm{D^+}$ and $\mathrm{D_s^+}$, and $(-,+,-)$ for their antiparticles. The

Particle	Mass (MeV/c^2)	$c\tau$ (μm)	Decay channel	BR (%)
D^+ ($c\bar{d}$)	1869.65 ± 0.05	311.8	$K^-\pi^+\pi^+$	8.98 ± 0.28
D_s^+ ($c\bar{s}$)	1968.34 ± 0.07	150.2	$\phi(1020)[\rightarrow K^+K^-]\pi^+$	2.27 ± 0.08
B^+ ($u\bar{b}$)	5279.33 ± 0.13	491.1	$D^+ + X$	2.5 ± 0.5
			$D^- + X$	9.9 ± 1.2
			$D_s^+ + X$	$7.9^{+1.4}_{-1.3}$
			$D_s^- + X$	$1.10^{+0.40}_{-0.32}$
B^0 ($d\bar{b}$)	5279.64 ± 0.13	455.4	$D^+ + X$	< 3.9
			$D^- + X$	36.9 ± 3.3
			$D_s^+ + X$	$10.3^{+2.1}_{-1.8}$
			$D_s^- + X$	< 2.6
B_s^0 ($s\bar{b}$)	5366.88 ± 0.17	452.7	$D_s^- + X$	93 ± 25
Λ_b^0 (udb)	5619.60 ± 0.17	441.0	$\Lambda_c^+ D^-$	0.46 ± 0.06
			$\Lambda_c^+ D_s^-$	1.10 ± 0.10

Table 4.2: Main properties of charmed mesons studied in this thesis (D^+, D_s^+) and main beauty hadrons that can decay to D^+ and D_s^+ mesons [13].

decay-vertex position is reconstructed as the space point that minimise the distance D between the three considered tracks and calculated as:

$$D = \sqrt{\sum_{i=1}^{3} \left[\left(\frac{x_i - x_0}{\sigma_{x_i}} \right)^2 + \left(\frac{y_i - y_0}{\sigma_{y_i}} \right)^2 + \left(\frac{z_i - z_0}{\sigma_{z_i}} \right)^2 \right]} \tag{4.2}$$

where (x_i, y_i, z_i) are the coordinates of the i-th track at the point of closest approach to the reconstructed decay vertex (x_0, y_0, z_0), and $(\sigma_{x_i}, \sigma_{y_i}, \sigma_{z_i})$ are their uncertainties.

The momentum associated to the decay vertex is computed as the sum of the momenta of the three tracks evaluated in the point along each track closest to the decay vertex. The invariant mass of each D-meson candidate is computed using the energy and the momentum of the decay tracks

$$M_{\rm inv}^2 = (\sqrt{m_{\rm OS}^2 + \vec{p}_{\rm OS}^2} + \sqrt{m_{\rm LS,1}^2 + \vec{p}_{\rm LS,1}^2} + \sqrt{(m_{\rm LS,2}^2 + \vec{p}_{\rm LS,2}^2)})^2 - (\vec{p}_{\rm OS} + \vec{p}_{\rm LS,1} + \vec{p}_{\rm LS,2})^2. \tag{4.3}$$

In the computation of the invariant mass, the mass of the kaon is unambiguously assigned to the track having charge with opposite sign (OS) with respect to the candidate. For $D^\pm$ mesons, the pion mass is assigned to the remaining two decay tracks having the same charge sign of the candidate (like sign, LS), and hence to each D^+ candidate only one mass hypothesis is assigned. For the two LS tracks of the $D_s^\pm$ candidates, the two possible mass-hypothesis assignments are considered (i.e. one being a pion and the other one a

kaon and viceversa). With this procedure a large number of candidates is obtained, most of them being combinatorial background. In order to increase the signal-to-background ratio and the statistical significance of the measurement, strict selections are therefore needed. In particular, the selections applied can be divided in three main categories:

1. Track-quality selections
2. Selections based on the decay topology and kinematics
3. Particle identification of the decay products

4.2.1 Track-quality selections

Tracks used to build D_s^+ and D^+ candidates are required to satisfy several track-quality and kinematics criteria. In particular, only tracks successfully fitted in both TPC and ITS, with a minimum of 70 (out of 159) associated space points in the TPC were considered. A $\chi^2/\mathrm{ndf} < 2$ of the momentum fit in the TPC (where ndf is the number of degrees of freedom involved in the tracking procedure) and a ratio of crossed rows (total number of hit TPC pad rows) over findable clusters (pad rows which, based on the geometry of the track, are possible clusters) in the TPC larger than 0.8 were required. The requirement of two hits in the ITS, with at least one of the two in the first two layers, ensures a good compromise between impact-parameter and decay-vertex resolution, which are crucial for the measurement of heavy-flavoured hadrons, and high reconstruction efficiency.

For tracks that fulfil the aforementioned requirements, the transverse-momentum resolution in pp collisions was found to be better than 1% for $p_{\mathrm{T}} = 1$ GeV/c and about 2% for $p_{\mathrm{T}} = 10$ GeV/c, while the impact-parameter resolution is better than 75 μm for tracks with $p_{\mathrm{T}} > 1$ GeV/c (see Figs. 3.9 and 3.8). In addition, in pp and p–Pb (Pb–Pb) collisions only tracks having $p_{\mathrm{T}} > 0.3$ GeV/c ($p_{\mathrm{T}} > 0.4$ GeV/c) and $|\eta| < 0.8$ were selected to build the candidates. In Pb–Pb collisions, a selection on the impact parameter of tracks with $p_{\mathrm{T}} < 2$ GeV/c of $|d_0| > 60$ μm is applied to select tracks displaced from the primary vertex.

These selections limits the rapidity acceptance of D mesons, which decreases steeply for $|y| > 0.5$ at low p_{T} and for $|y| > 0.8$ for $p_{\mathrm{T}} > 5$ GeV/c. In order to avoid border effects, only D_s^+ and D^+ candidates having $|y| < y_{\mathrm{fid}}(p_{\mathrm{T}})$ were selected. The p_{T}-dependent fiducial acceptance factor $y_{\mathrm{fid}}(p_{\mathrm{T}})$ was defined by a second-order polynomial function

$$y_{\mathrm{fid}}(p_{\mathrm{T}}) = 0.5 + \frac{1.9}{15} p_{\mathrm{T}} - \frac{0.2}{15} p_{\mathrm{T}}^2, \tag{4.4}$$

as shown in Fig. 4.2.

4.2.2 Topological and kinematical selections

The main criteria used to discriminate the D^+ and D_s^+ signal from the combinatorial background are based on the displaced topology of reconstructed decay vertices. This is possible since the candidates that form the combinatorial background are predominantly

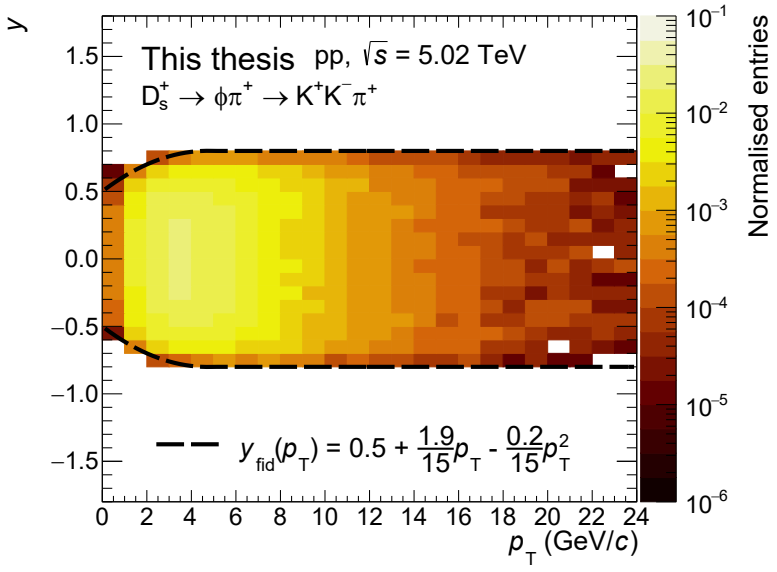

Figure 4.2: Rapidity as a function of transverse momentum of reconstructed D_s^+ mesons in pp collisions at $\sqrt{s} = 5.02$ TeV. The fiducial acceptance region is defined as $|y| < y_{\rm fid}$.

built using tracks that are produced at the primary vertex and therefore exhibit a non-zero displacement only due to the detector resolution. In addition, the decay topology is different for promptly produced D mesons (which come directly from the hadronisation of a charm quark or from the decay of open or hidden charm excited states), and D mesons coming from beauty-hadron decays, denoted as *feed-down*, because of the longer mean proper decay length of beauty hadrons (see Table 4.2). The variables used in the analyses presented in this thesis are sketched in Fig. 4.3 and described below. In Figs. 4.4, 4.5, 4.6, and 4.7 the distributions of prompt and feed-down D mesons are obtained from Monte Carlo simulations (see Sec. 4.3), while the distributions of the combinatorial background from data, excluding the invariant-mass region of the signal.

- **Decay length (L)**

  The decay length is defined as the distance between the reconstructed interaction and decay. For prompt D^+ and D_s^+ mesons it is an approximation of the real decay length because of the curvature of their trajectory in the magnetic field, which however leads only to a negligible effect considering the mean proper decay length of D^+ and D_s^+ mesons of few hundred microns. For feed-down D mesons it includes also the distance covered by the beauty hadron before decaying to the D meson and it is therefore on average larger than that of prompt D mesons, as shown in the left panel of Fig. 4.4 for D^+ mesons and background candidates with $4 < p_{\rm T} < 5$ GeV/c. The middle panel of the same figure shows the dependence of the decay length distribution on the transverse momentum of D_s^+ mesons, which

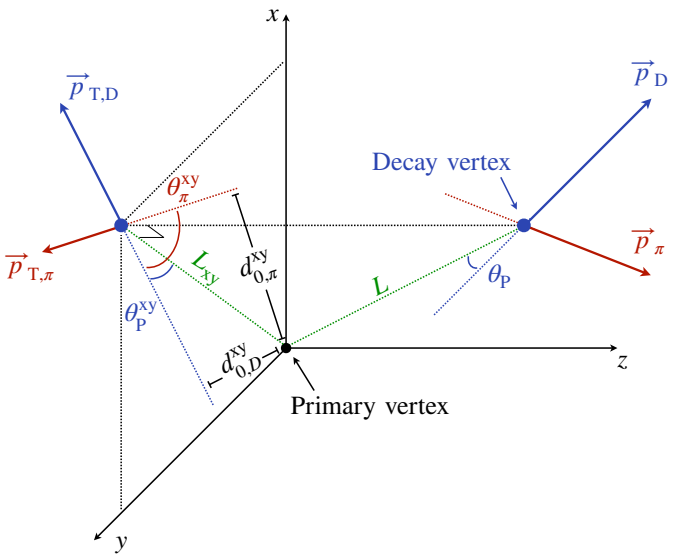

Figure 4.3: Sketch of the D-meson decay with the main topological variables used to improve the selection of D^+ and D_s^+ mesons.

is due to the Lorentz boost that enlarges the decay length of high momentum D mesons. Since the $c\tau$ of D^+ mesons is larger than that of D_s^+ mesons (see Table 4.2), the decay-length distribution of D^+ mesons is shifted towards higher values than that of D_s^+ mesons in the same p_T interval. Nevertheless, both distributions are larger than that of the combinatorial background which is different from zero only

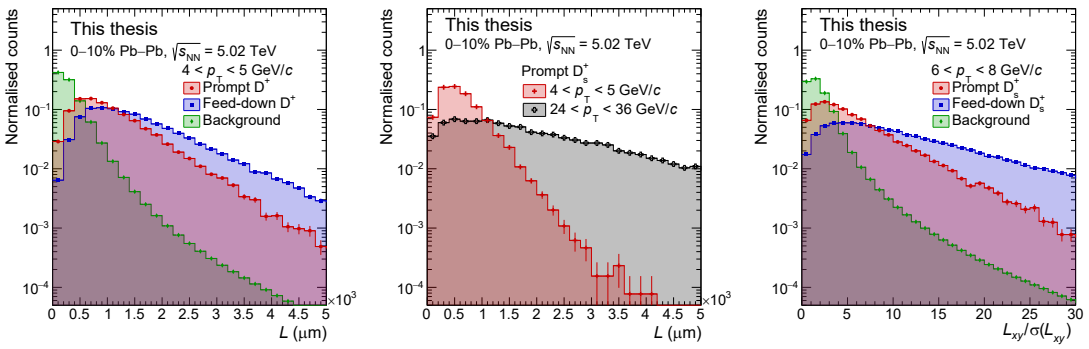

Figure 4.4: Left: decay-length distribution of prompt D^+, feed-down D^+ mesons and combinatorial-background candidates for $4 < p_T < 5$ GeV/c. Middle: decay-length distribution of prompt D_s^+ mesons with $4 < p_T < 5$ GeV/c and $24 < p_T < 36$ GeV/c. Right: normalised decay-length xy distribution of prompt D_s^+, feed-down D_s^+ mesons and combinatorial-background candidates for $6 < p_T < 8$ GeV/c.

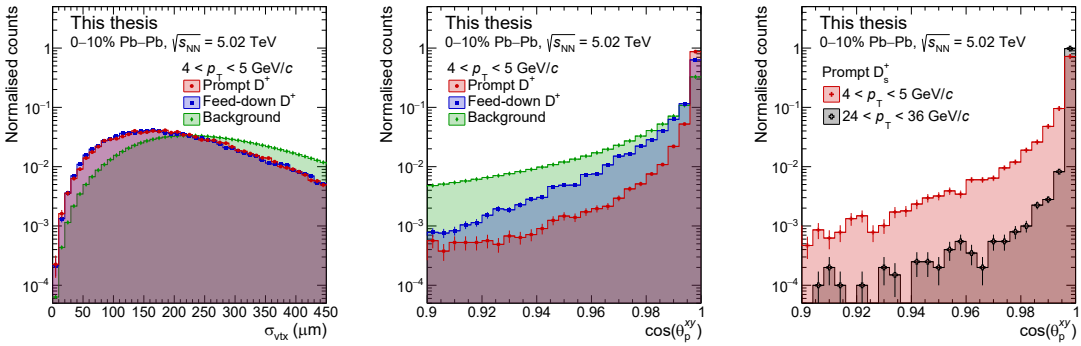

Figure 4.5: Left: distribution of track dispersion at the secondary vertex for prompt D^+, feed-down D^+ mesons and combinatorial-background candidates having $4 < p_T < 5$ GeV/c. Middle: $\cos(\theta_P^{xy})$ distribution of prompt D^+, feed-down D^+ mesons and combinatorial-background candidates for $4 < p_T < 5$ GeV/c. Right: $\cos(\theta_P^{xy})$ distribution of prompt D_s^+ mesons with $4 < p_T < 5$ GeV/c and $24 < p_T < 36$ GeV/c.

due to the finite impact-parameter resolution.

- **Normalised decay length in the transverse plane ($L_{xy}/\sigma(L_{xy})$)**

  It is the decay length projected in the transverse plane with respect to the beam direction and divided by its uncertainty. The projection in the transverse plane is considered to exploit the better detector resolution in the x and y coordinates than in the z coordinate. The right panel of Fig. 4.4 shows a comparison among the normalised decay-length-xy distributions of prompt D_s^+, feed-down D_s^+ and combinatorial background candidates with $6 < p_T < 8$ GeV/c.

- **Dispersion of the tracks at the decay vertex (σ_{vertex})**

  This variable is defined as

$$\sigma_{\mathrm{vtx}} = \sqrt{\sum_{i=1}^{3} d_i^2} \tag{4.5}$$

  where d_i are the distances of closest approach between the decay tracks and the reconstructed secondary vertex. For a true D meson it assumes non-zero values only because of the tracking and vertexing resolution, while it is on average larger for the combinatorial background, as shown in the left panel of Fig. 4.5.

- **Cosine of pointing angle ($\cos\theta_P$, $\cos\theta_P^{xy}$)**

  The pointing angle θ_P is defined as the angle between the line connecting the primary and secondary vertices and the direction of the reconstructed D meson momentum. This variable is also defined using only the transverse components of these

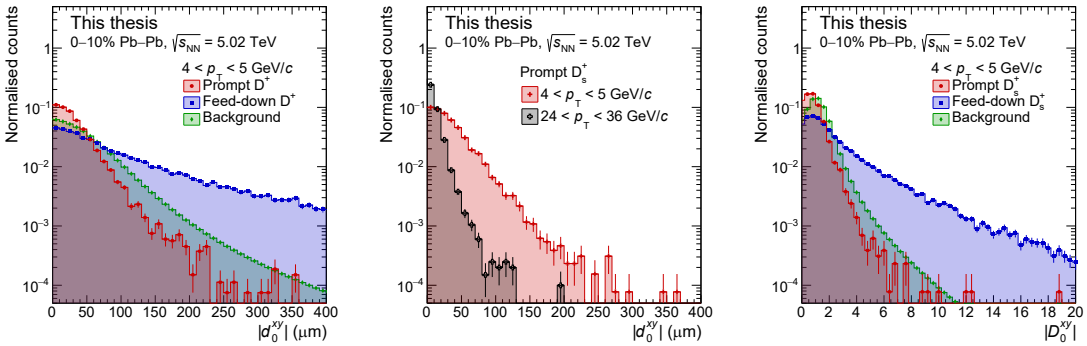

Figure 4.6: Left: impact-parameter distributions of prompt $\mathrm{D^+}$, feed-down $\mathrm{D^+}$ mesons and combinatorial-background candidates having $4 < p_{\mathrm{T}} < 5$ GeV/c. Middle: impact-parameter distributions of prompt $\mathrm{D_s^+}$ mesons with $4 < p_{\mathrm{T}} < 5$ GeV/c and $24 < p_{\mathrm{T}} < 36$ GeV/c. Right: distribution of D_0^{xy} of prompt $\mathrm{D_s^+}$, feed-down $\mathrm{D_s^+}$ mesons and combinatorial-background candidates with $4 < p_{\mathrm{T}} < 5$ GeV/c.

two directions (θ_{xy}), as shown in the sketch reported in Fig. 4.3, to exploit the better resolution in the x and y coordinates than in the z coordinate. Without resolution effects it should be exactly 0 for prompt D mesons and close to 0 for feed-down D mesons. The distribution of its cosine is therefore peaked at 1, as shown for $\mathrm{D^+}$ mesons in the middle panel of Fig. 4.5. For the combinatorial background θ_{P} can assume any value with the same probability. The distribution The right panel of the same figure shows the difference of the $\cos(\theta_{\mathrm{P}}^{xy})$ distribution for low and high p_{T} $\mathrm{D_s^+}$ mesons, due to the different momentum and vertexing resolution.

- **Impact parameter in the transverse plane (d_0^{xy})**

  The impact parameter of D-meson candidates in the transverse plane is defined as the distance of closest approach between the reconstructed flight line of the D-meson and the primary vertex, projected in the transverse plane. For promptly produced D mesons it is different from zero only because of the detector resolution and therefore it becomes narrower at high p_{T}, thanks to the better momentum and vertexing resolution (see middle panel of Fig. 4.6). Besides the rejection of the combinatorial background, it is also useful to suppress the feed-down contribution, which has a much broader distribution, as shown in the left panel of Fig. 4.6 for $\mathrm{D^+}$ mesons with $4 < p_{\mathrm{T}} < 5$ GeV/c.

- **Maximum normalised difference between the measured and the expected daughter-track impact parameters in the transverse plane (D_0^{xy})**

  As the D-meson impact parameter, this variable is efficient in rejecting combinatorial background as well as feed-down D mesons. It is defined as

  $$D_0^{xy} = \max_i \left\{ \frac{d_{0,i}^{xy}(\text{meas}) - d_{0,i}^{xy}(\text{exp})}{\sqrt{\sigma^2_{d_{0,i}^{xy}(\text{meas})} + \sigma^2_{d_{0,i}^{xy}(\text{exp})}}} \right\} \tag{4.6}$$

  where $d_{0,i}^{xy}(\text{meas})$ is the measured impact parameter of the *i-th* daughter track in the xy plane, $\sigma_{d_{0,i}^{xy}(\text{meas})}$ its uncertainty. The expected value $d_{0,i}^{xy}(\text{exp})$ is estimated from L_{xy} and the angle θ_{xy}^i between the reconstructed D-meson momentum and that of the i-th daughter track in the xy plane

  $$d_{0,i}^{xy}(\text{exp}) = L_{xy} \cdot \sin(\theta_{xy}^i). \tag{4.7}$$

  Its uncertainty $\sigma_{d_{0,i}^{xy}(\text{exp})}$ is computed neglecting the uncertainty on θ_{xy}^i, and therefore

  $$\sigma_{d_{0,i}^{xy}(\text{exp})} = \sigma_{L_{xy}} \cdot \sin(\theta_{xy}^i). \tag{4.8}$$

  An example of D_0^{xy} distribution for prompt D_s^+, feed-down D_s^+ mesons and combinatorial-background candidates with $4 < p_\mathrm{T} < 5$ GeV/c is shown in the right panel of Fig. 4.6.

4.2.3 Kinematical selections for the $\mathrm{D}_\mathrm{s}^+ \to \phi\pi^+ \to \mathrm{K}^-\mathrm{K}^+\pi^+$ decay

In addition to the selections on the decay topology, for D_s^+ also kinematic variables related to the decay chain can help to improve the selection of the signal. In particular for the analyses presented in this thesis, the variables listed in the following were used.

- **Difference between the invariant mass of the kaon pair and the ϕ-meson mass ($\Delta M(\mathrm{KK})$)**

  In order to exploit the narrow width of the $\phi(1020)$-meson resonance, one of the pairs of opposite-sign tracks is required to have a reconstructed $\mathrm{K}^+\mathrm{K}^-$ invariant mass ($M(\mathrm{KK})$) compatible with respect to the PDG world average of the ϕ-meson mass ($M_\phi = 1019.461 \pm 0.016$) [13]. This is achieved by applying a selection on the absolute value of their difference

  $$\Delta M(KK) = |M(\mathrm{KK}) - M_\phi| \tag{4.9}$$

  which is typically smaller than 20 MeV/c^2 for the signal (considering the ϕ-meson width convoluted with the detector resolution), while it is almost uniformly distributed over a wide range for background candidates, as illustrated in the left

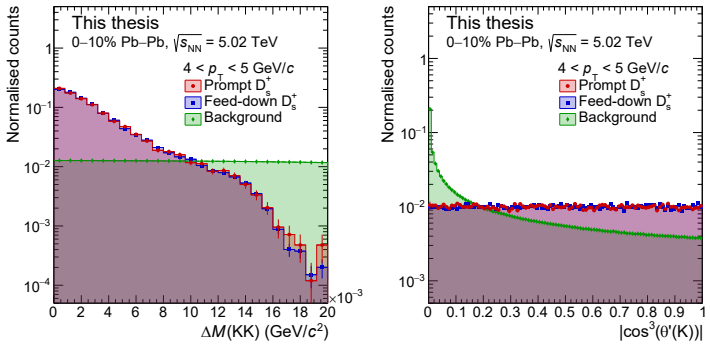

Figure 4.7: Left: distribution of difference between the invariant mass of the kaon pair and the ϕ-meson mass of prompt $\mathrm{D_s^+}$, feed-down $\mathrm{D_s^+}$ mesons and combinatorial-background candidates with $4 < p_\mathrm{T} < 5$ GeV/c. Right: distribution of $|\cos^3(\theta'(\mathrm{K}))|$ of prompt $\mathrm{D_s^+}$, feed-down $\mathrm{D_s^+}$ mesons and combinatorial-background candidates with $4 < p_\mathrm{T} < 5$ GeV/c.

panel of Fig. 4.7. As explained in Sec. 4.2, for each $\mathrm{D_s^+}$ candidate, two mass hypotheses can be assigned to the LS decay tracks. This selection therefore is tested against both the possible kaon pairs and is useful to discriminate the correct mass hypothesis from the wrong one, and hence to reduce the number of $\mathrm{D_s^+}$ candidates with the wrong-mass assignment.

- $(|\cos^3(\theta'(\mathrm{K}))|)$

  The $\theta'(\mathrm{K})$ angle is defined as the angle between one of the kaons and the pion in the $\mathrm{K^+K^-}$ rest frame. In the $\mathrm{D_s^+} \to \phi\pi^+ \to \mathrm{K^-K^+}\pi^+$ decay, the spin of the ϕ-meson is aligned to its direction of motion relative to the $\mathrm{D_s^+}$ meson, and as a consequence it can be shown that $\cos^3(\theta'(\mathrm{K}))$ is uniformly distributed in $[-1, +1]$ for signal candidates. On the contrary, for the combinatorial background is peaked at zero, as shown in the right panel of Fig. 4.7.

4.2.4 Particle identification

Further rejection of the combinatorial background was achieved via the PID of the decay tracks. As introduced in Sec. 3.6, the PID selection criteria adopted are based on the measurement of the specific energy loss ($\mathrm{d}E/\mathrm{d}x$) in the TPC detector and the time-of-flight measured with the TOF detector. A track is considered compatible with a mass hypothesis (i.e. kaon, pion or proton) depending on the difference between the measured signal S_meas and the expected signal $S_\mathrm{exp}^{\pi,\mathrm{K,p}}$ for the given hypothesis. In particular this is expressed in units of resolution

$$N_\sigma(\pi, \mathrm{K}, \mathrm{p}) = \left| \frac{S_\mathrm{meas} - S_\mathrm{exp}(\pi, \mathrm{K}, \mathrm{p})}{\sigma(\pi, \mathrm{K}, \mathrm{p})} \right| \tag{4.10}$$

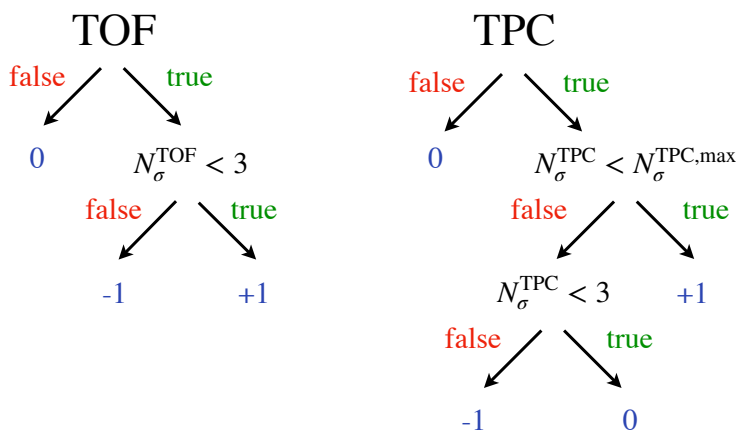

Figure 4.8: PID selection logic of a decay track for a given mass hypothesis. More details are reported in the text.

where $\sigma(\pi, \mathrm{K}, \mathrm{p})$ is the resolution of the $\mathrm{d}E/\mathrm{d}x$ or the time-of-flight signals for each hadron species. For both D^+ and D_s^+ mesons, the OS track has to be compatible with the kaon hypothesis. For D^+ mesons the two LS tracks have to be compatible with the pion hypothesis, while for D_s^+ mesons one LS track has to be compatible with the kaon hypothesis and the other one with the pion hypothesis or viceversa. A D_s^+ or D^+ candidate is discarded if at least one of the decay tracks is rejected as kaon and as pion. The logic adopted to combine the information from the TPC and TOF signals is sketched in Fig. 4.8. The measured value of $N_{\mathrm{sigma}}^{\mathrm{TPC}}$ is compared to a threshold value $N_\sigma^{\mathrm{TPC,max}}$, which depends on the p_{T} of the considered track and on the PID strategy adopted, namely the *conservative PID* and *strong PID* strategies reported in Table 4.3. For each detector, a response of -1, 0 or +1 is assigned to each mass hypothesis. In each detector, a response value of -1 is given if $N_\sigma > 3$. If the signal in one of the two detectors is not available, a response value of 0 is assigned. This choice is motivated by the large fraction of low-momentum tracks that do not reach the TOF detector (up to 30%-40% for $p_{\mathrm{T}} \lesssim 1$ GeV/c) and therefore have no TOF signal. A D^+ or D_s^+ candidate is accepted if the sum of the two response values is larger or equal to 0. This PID selection criteria preserve around

	$N_\sigma^{\mathrm{TPC,max}}$	
PID strategy	strong	conservative
$p_{\mathrm{T}}^{\mathrm{trk}} < 0.6$ GeV/c	2	3
$0.6 < p_{\mathrm{T}}^{\mathrm{trk}} < 0.8$ GeV/c	1	3
$p_{\mathrm{T}}^{\mathrm{trk}} > 0.8$ GeV/c	2	3

Table 4.3: Selection criteria for particle identification with the TPC for different transverse momentum intervals of the decay tracks.

99% (85%) of the signal in case of conservative (strong) PID strategy, while provides a rejection of the combinatorial background up to a factor 10 for D^+ and D_s^+ candidates with $p_\mathrm{T} < 4$ GeV/c. In addition, for the D_s^+ it is also helpful to discriminate between the two mass hypotheses that can be assigned to the LS track (see Sec. 4.2).

4.3 Monte Carlo simulations

Reliable MC simulations with a precise description of the kinematics and topology of the $\mathrm{D}^+ \to \mathrm{K}^-\pi^+\pi^+$ and $\mathrm{D}_\mathrm{s}^+ \to \phi\pi^+ \to \mathrm{K}^-\mathrm{K}^+\pi^+$ decays, as well as the detector conditions, the track-parameter resolution and the PID performance, are an important ingredient for the measurement of D^+- and D_s^+-meson production, to study the selection variables and to compute the efficiency and acceptance corrections.

The simulations used in this thesis were configured with a detailed description of the ALICE apparatus geometry and detector response. They were tuned to reproduce the position and width of the interaction vertex distribution, the number of active electronic channels, gain, noise level and the accuracy of the detector calibration, as well as their time evolution within the pp, p–Pb or Pb–Pb data taking periods considered for the analysis.

The PYTHIA6.4.25 event generator [86] with the Perugia-11 [147] tune was adopted to simulate pp collisions at $\sqrt{s} = 5.02$ TeV. In order to achieve a satisfactory statistical precision, each simulated pp event contained at least a $\mathrm{c\overline{c}}$ or $\mathrm{b\overline{b}}$ pair and D_s^+ and D^+ mesons were forced to decay in the hadronic channel of interest for the analysis. In case of heavy-ion collisions, the HIJING V1.383 generator [135] was used to simulate the underlying Pb–Pb or p–Pb events, while the D-meson signals were injected with PYTHIA events that had to satisfy the same conditions as for pp collisions. For p–Pb collisions, only one PYTHIA event per underlying HIJING event was injected, while for Pb–Pb collisions the number of PYTHIA events injected per HIJING event increased with increasing collision centrality. For all the collision systems, the generated particles were propagated through the ALICE apparatus using the GEANT3 transport package [137]. It was also verified that using GEANT4 [138] the performance was compatible.

4.3.1 Acceptance and efficiency corrections

In order to obtain the number of produced D^+ and D_s^+ at mid-rapidity ($|y| < 0.5$), the measured raw yield extracted after all the selections applied has to be corrected for the efficiency and acceptance factors. These correction factors were evaluated using the MC sample described above. The efficiency was defined as

$$\epsilon = \frac{N_\mathrm{reco}|_{|y|<y_\mathrm{fid}}}{N_\mathrm{gen}^{\text{dau in acc}}|_{|y|<y_\mathrm{fid}}} \tag{4.11}$$

where $N_\mathrm{reco}|_{|y|<y_\mathrm{fid}}$ is the number of reconstructed D^+ (D_s^+) mesons after all the selections, while $N_\mathrm{gen}^{\text{dau in acc}}|_{|y|<y_\mathrm{fid}}$ is the number of generated D^+ (D_s^+) mesons decaying in the decay channel of interest for the analysis, having $|y| < y_\mathrm{fid}$, with the three daughters that fulfil the acceptance requirements of $|\eta| < 0.9$ and $p_\mathrm{T} > 0.1$ GeV/c. Only events

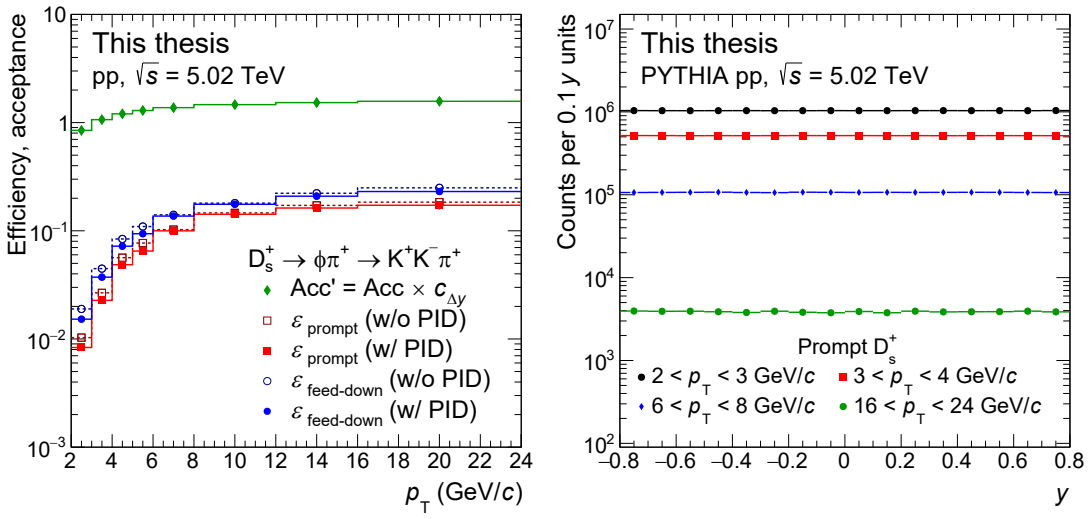

Figure 4.9: Left: efficiency and acceptance factors of D_s^+ mesons in pp collisions at $\sqrt{s} = 5.02$ TeV obtained with the selections described in Sec. 5.1. Right: rapidity distribution of prompt D_s^+ mesons in $|y| < 0.8$ and in different p_T intervals as obtained with PYTHIA6.4.25[86] for pp collisions at $\sqrt{s} = 5.02$ TeV.

with the z coordinate of the generated primary-vertex position within ±10 from the nominal interaction point ($|z_{vtx}^{gen}| < 10$ cm) were considered for $N_{gen}^{dau\ in\ acc}|_{|y|<y_{fid}}$. The efficiency varies as a function of p_T because of the track-reconstruction efficiency and the topological selections applied. In addition, it is in general different for prompt and feed-down D mesons, because of the different decay topology, as shown for D_s^+ mesons in pp collisions at $\sqrt{s} = 5.02$ TeV in the left panel of Fig. 4.9. The efficiency factors are shown with and without the PID selection, are obtained with the selections described in Sec. 5.1. The effect of the PID is the same for prompt and feed-down D_s^+ mesons and it is around 15% for $p_T < 6$ GeV/c where the strong PID strategy is applied, and around 1-2% for $p_T > 6$ GeV/c where the conservative PID is applied.

The acceptance factor was defined as

$$\mathrm{Acc}' = \mathrm{Acc} \cdot c_{\Delta y} = \frac{N_{gen}^{dau\ in\ acc}|_{|y|<y_{fid}}}{N_{gen}|_{y<0.5}} \tag{4.12}$$

where $N_{gen}|_{y<0.5}$ is the number of generated D^+ (D_s^+) mesons in events with $|z_{vtx}^{gen}| < 10$ cm decaying in the decay channel of interest for the analysis with $|y| < 0.5$. The Acc′ factor include also the correction for the rapidity coverage ($c_{\Delta y}$) which is approximately $c_{\Delta y} \simeq y_{fid}/0.5$, since the rapidity distribution of produced D mesons in PYTHIA is nearly flat for $|y| < 0.8$ (see right panel of Fig. 4.9). This is also confirmed by FONLL pQCD calculations [80] and experimental measurements [106, 148]. Therefore $c_{\Delta y}$ varies from 1 to 1.6 as a function of p_T according to Eq. 4.4, and consequently the Acc′ factor can be larger than unity, as shown in the left panel of Fig. 4.9.

Chapter 5

$\mathrm{D_s^+}$ production cross section in pp collisions at $\sqrt{s} = 5.02$ TeV

In this Chapter, the measurement of the production cross section of prompt $\mathrm{D_s^+}$ mesons at mid-rapidity ($|y| < 0.5$) in pp collisions at $\sqrt{s} = 5.02$ TeV is discussed. The D-meson cross section in pp collisions provides a reference for the measurements of the nuclear modification factors in p–Pb and Pb–Pb collisions and constitute an important test for pQCD calculations [80]. The results presented in this Chapter were published in Ref. [1].

The p_{T}-differential production cross section in $|y| < 0.5$ was computed as

$$\left.\frac{\mathrm{d}^2\sigma(\mathrm{D_s^+})}{\mathrm{d}p_{\mathrm{T}}\mathrm{d}y}\right|_{|y|<0.5} = \frac{\frac{1}{2} \cdot f_{\mathrm{prompt}} \cdot N_{\mathrm{raw}}(\mathrm{D_s^\pm})|_{|y|<y_{\mathrm{fid}}}}{\Delta p_{\mathrm{T}} \cdot c_{\Delta y} \cdot (\mathrm{Acc} \times \epsilon)_{\mathrm{prompt}} \cdot \mathrm{BR} \cdot \mathcal{L}_{\mathrm{int}}}, \tag{5.1}$$

where $N_{\mathrm{raw}}(\mathrm{D_s^\pm})|_{|y|<y_{\mathrm{fid}}}$ is the raw yield of $\mathrm{D_s^+}$ mesons and their charged conjugates measured in the p_{T} interval Δp_{T} and in the fiducial acceptance interval defined in Sec. 4.2.1, f_{prompt} is the fraction of prompt $\mathrm{D_s^+}$ in the raw yield, and the factor $\frac{1}{2}$ is introduced to obtain a charged-average yield. The $(\mathrm{Acc} \times \epsilon)_{\mathrm{prompt}}$ factor is the acceptance-times-efficiency of prompt $\mathrm{D_s^+}$ mesons, $c_{\Delta y}$ is the correction for the rapidity coverage (see Sec. 4.3.1), BR is the branching ratio of the decay channel $\mathrm{D_s^+} \to \phi\pi^+ \to \mathrm{K^-K^+}\pi^+$ (see Table 4.2), and $\mathcal{L}_{\mathrm{int}}$ is the integrated luminosity, obtained from the cross section for the MB trigger (σ_{MB}) and the number of events ($N_{\mathrm{ev}}^{\mathrm{norm}}$, see Section 4.1.2) as

$$\mathcal{L}_{\mathrm{int}} = \sigma_{\mathrm{MB}}/N_{\mathrm{ev}}^{\mathrm{norm}}. \tag{5.2}$$

For the analysed data sample of pp collisions at $\sqrt{s} = 5.02$ TeV, σ_{MB} was measured to be (50.9 ± 0.9) mb^{-1} with van der Meer scans [149] and $N_{\mathrm{ev}}^{\mathrm{norm}}$ was 990 millions after all the event selections described in Sec. 4.1.2.

In the following sections the description of the $\mathrm{D_s^+}$-meson selection, raw-yield extraction and correction factors needed to compute the p_{T}-differential cross section is provided. Afterwards, the evaluation of the systematic uncertainties and the results are discussed.

5.1 Topological, kinematical, and PID selections

In order to increase the statistical significance of the extracted $\mathrm{D_s^+}$ raw yields, several selections to the $\mathrm{D_s^+}$-decay topology and to the kinematics of the decay channel were applied. In particular, the variables used to improve the rejection of the combinatorial background are those introduced in Sec. 4.2.2. The selection criteria were tuned to have a large statistical significance ($S/\sqrt{S+B}$) while preserving a relatively high efficiency and signal-to-background ratio (S/B) to keep the systematic uncertainties as low as possible. For this purpose, the effect of the selections was estimated by performing a scan of the threshold values for each variable, varying them simultaneously. For each combination of selections, the expected statistical significance was computed. To avoid biases induced by the statistical fluctuations of the background under the $\mathrm{D_s^+}$ peak, which can artificially enhance the extracted signal and thus the final measurement, the signal S was estimated as

$$S = \frac{\mathrm{d}^2\sigma(\mathrm{D_s^+})}{\mathrm{d}p_\mathrm{T}\mathrm{d}y}\bigg|_{|y|<0.5}^{\text{GM-VFNS(mod-}\mu_\mathrm{R,F}\text{)}} \cdot \frac{2 \cdot \Delta p_\mathrm{T} \cdot c_{\Delta y} \cdot (\mathrm{Acc} \times \epsilon)_\mathrm{prompt} \cdot \mathrm{BR} \cdot \mathcal{L}_\mathrm{int}}{f_\mathrm{prompt}}, \tag{5.3}$$

where $\frac{\mathrm{d}^2\sigma(\mathrm{D_s^+})}{\mathrm{d}p_\mathrm{T}\mathrm{d}y}\Big|_{|y|<0.5}^{\text{GM-VFNS(mod-}\mu_\mathrm{R,F}\text{)}}$ is the p_T-differential cross section predicted by the GM-VFNS(mod-$\mu_\mathrm{R,F}$) pQCD calculations [81, 82]. In particular, the upper band of the prediction uncertainty was used, since the measured data points of the D-meson production cross section in pp collisions typically lie on the upper edge of the uncertainty band of the pQCD predictions [1]. The f_prompt parameter was set to 0.9, which is a typical value obtained for the fraction of prompt $\mathrm{D_s^+}$ mesons in the raw yield [1]. The background B was instead obtained from the data, by fitting the invariant-mass distribution of $\mathrm{D_s^+}$ candidates with an exponential function, after having applied the selections and excluded the invariant-mass region aside the $\mathrm{D_s^+}$ and $\mathrm{D^+}$ peaks (*side-bands* distribution). The background in the signal region was then computed integrating the exponential function in the invariant-mass interval within $\pm 3\sigma$ from the PDG $\mathrm{D_s^+}$ mass [13], where σ is the width of the $\mathrm{D_s^+}$ peak extracted from the MC simulation. Only 10% of the total data sample was used for the background estimation in order to avoid an autocorrelation between the statistical fluctuations in the estimated significance and the measurement.

Figure 5.1 shows the expected significance as a function of the reconstruction efficiency of prompt $\mathrm{D_s^+}$ (left panel) and the signal-to-background ratio (right panel) for the p_T interval between 2 and 3 GeV/c. The red lines represent the chosen set of selections applied in the analysis. The threshold values for all the variables and the p_T intervals of the analysis are reported in Table 5.1. On one hand, at low momentum, where the contribution from the combinatorial background is larger, tighter selections are needed. On the other hand, the decay vertices of low p_T $\mathrm{D_s^+}$ mesons are less displaced with respect to the higher p_T $\mathrm{D_s^+}$ mesons, which are more boosted, and therefore too tight selections on the decay topology (i.e. on the decay length) reduce the efficiency, leading to a lower significance. The threshold values were also smoothened as a function of p_T in order to further reduce biases induced by statistical fluctuations in the estimation of the expected significance.

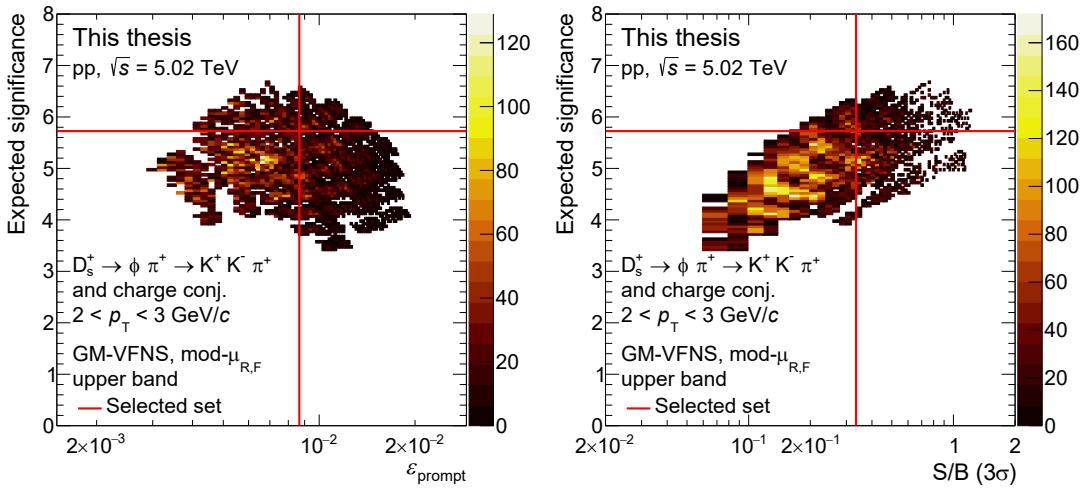

Figure 5.1: Expected significance of D_s^+ signal in $2 < p_T < 3$ GeV/c for different selections as a function of the efficiency of prompt D_s^+ mesons (left panel) and the signal-to-background ratio (right panel) obtained estimating the amount of signal with the GM-VFNS(mod-$\mu_{R,F}$) model [81, 82]. The red lines represent the set of selections chosen for the analysis.

In addition to the topological and kinematical selections, the particle identification of the decay tracks was applied exploiting the TPC and TOF PID information as described in Sec. 4.2.4. For D_s^+ candidates with $p_T < 6$ GeV/c the strong PID strategy was applied, while the conservative PID strategy was applied above 6 GeV/c. This choice was motivated by the large combinatorial background and the higher effectiveness of the PID selections at low p_T.

p_T (GeV/c)	[2,3]	[3,4]	[4,5]	[5,6]	[6,8]	[8,12]	[12,16]	[16,24]
ΔM(KK) (MeV/c^2) <	10	10	10	10	10	10	10	10
L (μm) >	200	200	300	300	300	300	500	500
$L_{xy}/\sigma(L_{xy})$ >	4	4	4	4	4	4	4	4
σ_{vertex} (μm) <	300	300	400	400	400	600	600	600
$\cos\theta_p$ >	0.92	0.92	0.90	0.90	0.90	0.90	0.90	0.90
$\cos\theta_p^{xy}$ >	0.92	0.92	0.92	0.92	0.90	0.90	0.90	0.90
$\lvert\cos^3\theta'(K)\rvert$ >	0.10	0.10	0.05	0.05	0.05	0.00	0.00	0.00
$\lvert d_0^{xy}\rvert$ (μm) <	140	140	120	120	120	120	120	120

Table 5.1: Topological and kinematical selections applied to the D_s^+ candidates in pp collisions at $\sqrt{s} = 5.02$ TeV for the 8 p_T intervals studied in the present analysis.

5.2 Raw-yield extraction

The raw yield (sum of $\mathrm{D_s^+}$ and $\mathrm{D_s^-}$ mesons) was extracted by fitting the invariant-mass distributions $M(\mathrm{KK}\pi)$ of the candidates that passed the topological, kinematical, and PID selections in eight p_T intervals from $p_\mathrm{T} = 2$ GeV/c to $p_\mathrm{T} = 24$ GeV/c. The fits to the invariant-mass spectra are reported in Fig. 5.2; the blue curve represents the total fit function and the red dotted curve is the term describing the combinatorial background. The $\mathrm{D_s^+}$ signal was modelled with a Gaussian function and the combinatorial background with an exponential function. An additional Gaussian term was introduced to describe the peak present on the left side of the $\mathrm{D_s^+}$ signal, arising from the $\mathrm{D^+} \to \phi\pi^+ \to \mathrm{K^-K^+}\pi^+$ decay, having a BR of $(9.51 \pm 0.34) \times 10^{-3}$ [13]. To improve the fit stability, the width of the $\mathrm{D^+}$ peak ($\sigma(\mathrm{D^+})^\mathrm{data}$) was fixed to the width of the $\mathrm{D_s^+}$ peak extracted in data ($\sigma(\mathrm{D_s^+})^\mathrm{data}$) multiplied by the ratio of the $\mathrm{D^+}$ and $\mathrm{D_s^+}$ peak widths obtained from the MC simulation ($\sigma(\mathrm{D^+})^\mathrm{MC}$, $\sigma(\mathrm{D_s^+})^\mathrm{MC}$),

$$\sigma(\mathrm{D^+})^\mathrm{data} = \frac{\sigma(\mathrm{D^+})^\mathrm{MC}}{\sigma(\mathrm{D_s^+})^\mathrm{MC}} \cdot \sigma(\mathrm{D_s^+})^\mathrm{data}, \tag{5.4}$$

under the assumption that the relative variation of the mass resolution of the $\mathrm{D_s^+}$ and $\mathrm{D^+}$ peaks is reproduced in the MC simulation. The typical values of $\sigma(\mathrm{D^+})^\mathrm{MC}/\sigma(\mathrm{D_s^+})^\mathrm{MC}$ in the MC simulation were found to be around 0.9 (see left panel of Fig. 5.3).

The values of raw yield, S/B, and significance are reported in Table 5.2. The best significance is achieved at intermediate p_T, while it is lower at low p_T because of the larger combinatorial background and at high p_T because of the lower signal yield. In Fig. 5.3, the Gaussian mean (left panel) and width (right panel) of the $\mathrm{D_s^+}$ peak extracted from the fits are compared to the values obtained from the MC simulation. The values obtained in data are typically compatible with the simulation within 2 standard deviations, except for the $\mathrm{D_s^+}$ peak position for $p_\mathrm{T} < 4$ GeV/c, which is larger by about $3 - 5$ MeV/c. This

p_T (GeV/c)	Raw yield	S/B (3σ)	Significance (3σ)
[2,3]	147 ± 24	0.341	6.1 ± 0.9
[3,4]	217 ± 23	0.820	9.9 ± 0.8
[4,5]	250 ± 21	1.339	12.0 ± 0.7
[5,6]	143 ± 15	1.650	9.5 ± 0.7
[6,8]	251 ± 23	1.028	11.3 ± 0.8
[8,12]	152 ± 19	0.910	8.5 ± 0.8
[12,16]	53 ± 9	1.891	5.9 ± 0.7
[16,24]	20 ± 5	2.027	3.6 ± 0.7

Table 5.2: Raw yields, signal-to-background ratio (S/B), and statistical significance of the $\mathrm{D_s^+}$ invariant-mass peak in the 8 p_T intervals of the analysis of pp collisions at $\sqrt{s} =$ 5.02 TeV.

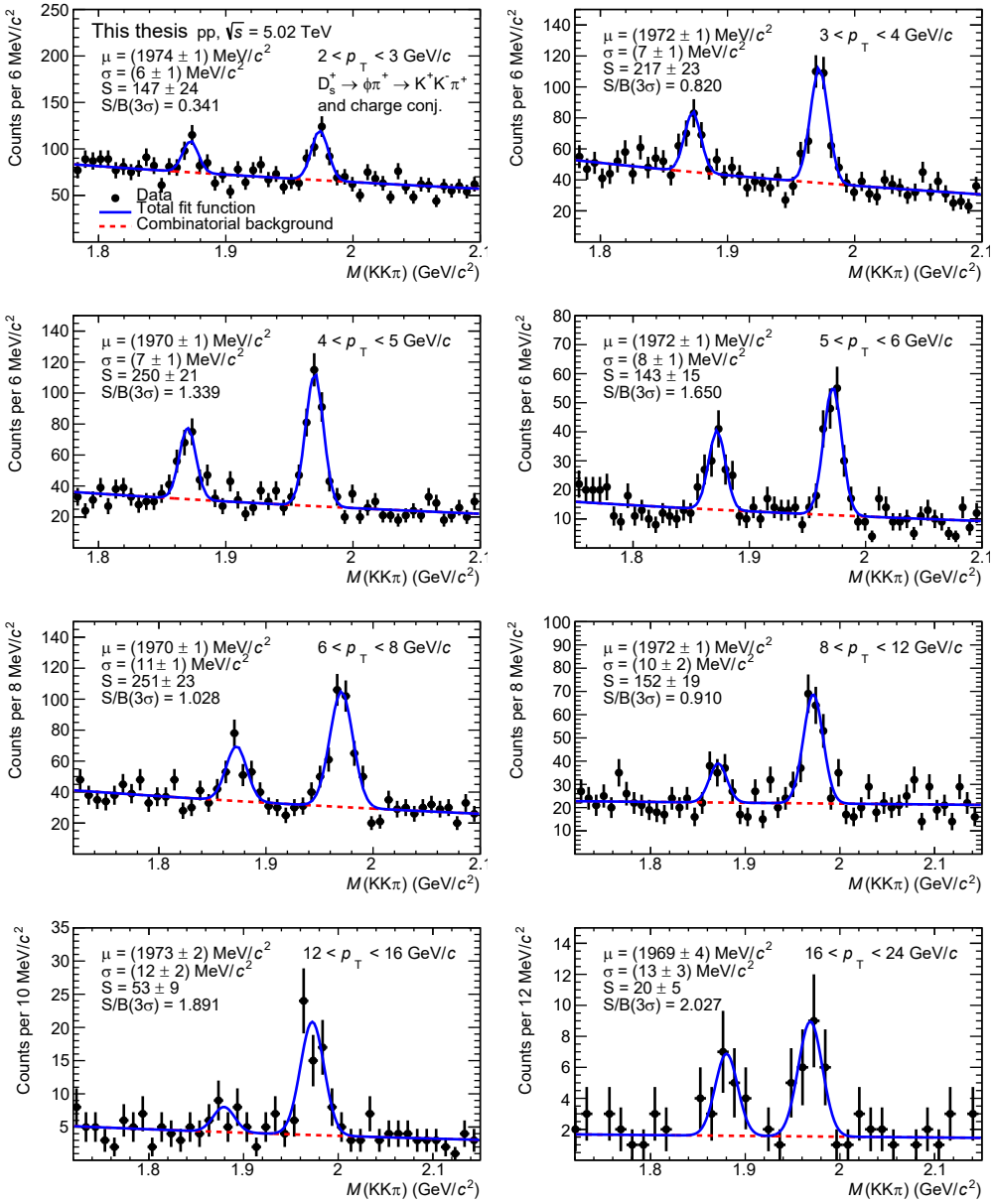

Figure 5.2: Invariant-mass distributions of D_s^+ candidates in pp collisions at $\sqrt{s} = 5.02$ TeV for the 8 p_T intervals of the analysis. The solid blue and the dotted red curves represent the total and the combinatorial-background fit functions, respectively.

discrepancy was taken into account in the evaluation of the systematic uncertainties. The peak width increases with increasing p_T, as expected from the transverse-momentum resolution of the decay tracks. Similarly, the mass resolution of the D^+ peak from the MC simulation is lower than that of the D_s^+ meson by about 10%, as shown in the right

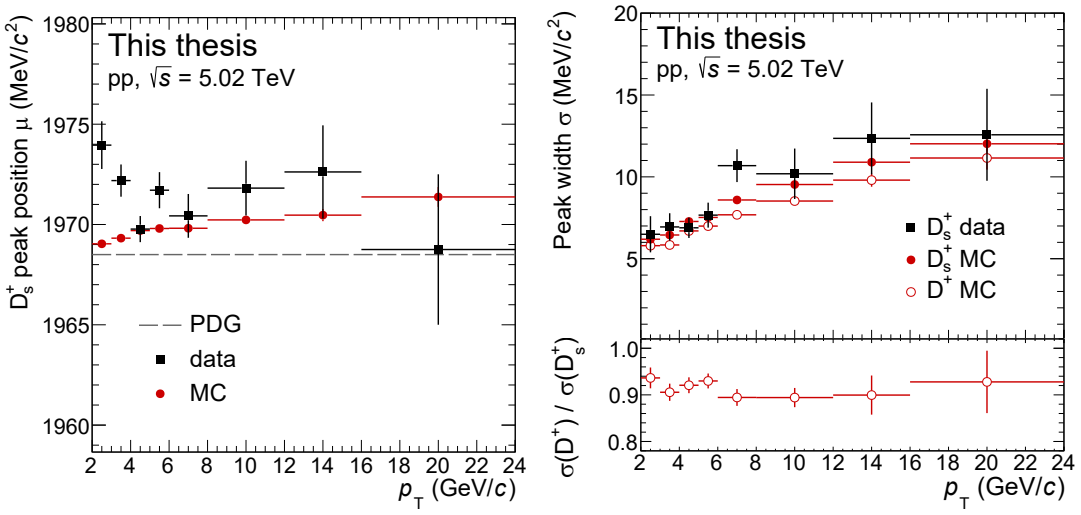

Figure 5.3: Gaussian mean (left panel) and width (right panel) of the D_s^+-meson peak in data and in the MC simulation. The dotted line in the left panel represents the world-average value from the PDG [13]. The D^+-peak width obtained from the MC simulation and its ratio with respect to the D_s^+-peak width is also shown in the right panel.

panel of Fig. 5.3. In fact, for a given p_T of the mother particle, the D^+ daughter tracks have typically a lower p_T than the daughter tracks of the D_s^+ mesons, because of the lower mass of the D^+ meson.

5.2.1 Study of K-π reflected signal

The contribution to the invariant-mass distributions from the D_s^+ candidates with wrong-mass hypothesis assignment to the pion and kaon tracks (K-π reflected signal) having the same charge sign was studied in the MC simulation. In particular, the invariant-mass distribution of the K-π reflected signal is centred at a value close to the D_s^+ mass and has a much broader RMS. Since the candidates with wrong-mass assignment cannot be distinguished from the correct ones, the reflection contribution could modify the background shape and affect the signal extraction enlarging the width of the Gaussian peak. However, the contribution of the K-π reflected signal is strongly suppressed when applying the PID selection on the decay tracks and the requirement of compatibility of the invariant-mass of the kaon pair with the ϕ-meson mass. An example of simulated K-π reflected signal distribution for candidates with $6 < p_T < 8$ GeV/c before and after applying the PID and ΔM(KK) selection reported in Table 5.1 is shown in the left panel of Fig. 5.4. In the right panel of the same Figure, the ratio between the reflected and correct D_s^+ signal (R/S) in the invariant-mass interval within $\pm 5\sigma$ from the D_s^+ peak is shown as a function of p_T. The relative contribution of the K-π reflected candidates to the D_s^+ signal is around $6-8\%$ without PID and ΔM(KK) selections, while it is less than 0.1% for $p_T < 6$ GeV/c and around 0.1% for $p_T > 6$ GeV/c after the application of these selections. The difference between the low and high p_T regions is caused by the different

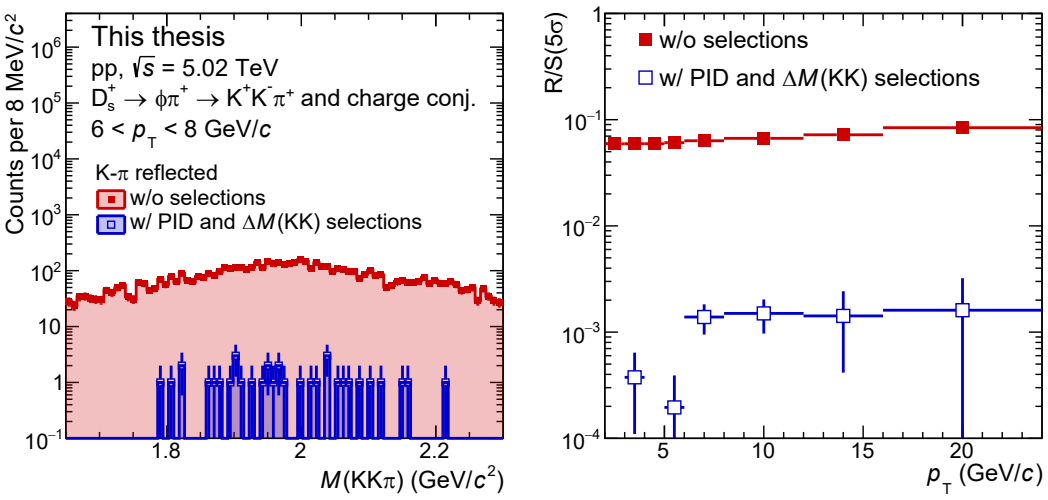

Figure 5.4: Left: invariant-mass distribution of the K-π reflected signal before (in red) and after (in blue) applying the ΔM(KK) and PID selections. Right: ratio between the K-π reflected signal and the D_s^+ signal in the invariant-mass region of the signal before (in red) and after (in blue) applying the ΔM(KK) and PID selections.

PID strategy adopted, which is stronger at low p_T. Since R/S was found to be negligible after the application of the selections used for the analysis, no additional contribution for the K-π reflected was added in the invariant-mass fits.

5.3 Acceptance and efficiency corrections

The acceptance-times-efficiency factor (Acc $\times$ ϵ) was computed using the MC simulation with the PYTHIA event generator described in Sec. 4.3. The (Acc $\times$ ϵ) of prompt and feed-down D_s^+ mesons decaying via the $D_s^+ \to \phi\pi^+ \to K^-K^+\pi^+$ decay channel, obtained applying the topological selections reported in Table 5.1 is shown in the left panel of Fig. 5.5. The efficiency increases with increasing p_T, mostly due to the and the topological selections and slightly for the p_T dependence of the track-reconstruction efficiency (see Sec. 3.5). The efficiency of feed-down D_s^+ mesons is higher than that of prompt D_s^+ mesons by about 30%-80% depending on p_T, because of the average larger displacement from interaction point of D mesons originating from beauty-hadron decays.

5.4 Contamination from other resonant decay channels

The requirement of compatibility of the invariant-mass of the kaon pair with the ϕ-meson mass ensures the selection of the decay channel $D_s^+ \to \phi\pi^+ \to K^-K^+\pi^+$. However, a fraction of D_s^+ mesons decaying into the same final state ($K^+K^-\pi^+$) via other intermediate resonances could be selected. In particular, the $D_s^+ \to \overline{K}^{*0}K^+ \to K^-K^+\pi^+$ (with

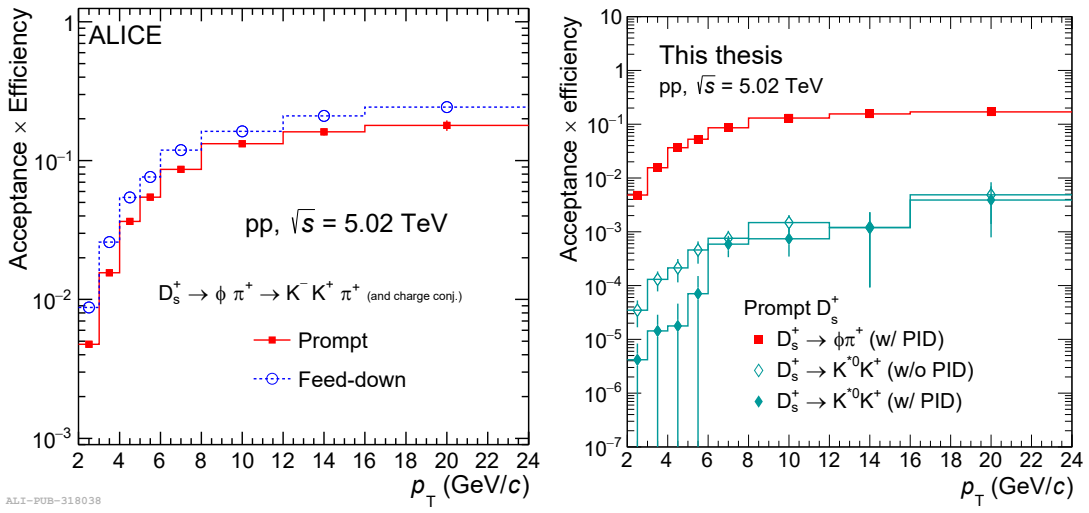

Figure 5.5: Left: Efficiency-times-acceptance as a function of p_T of prompt and feed-down D_s^+ mesons in pp collisions at $\sqrt{s} = 5.02$ TeV; figure taken from Ref. [1]. Right: (Acc $\times\,\epsilon$) factors of prompt D_s^+ mesons decaying via the K^{0*}-meson resonant decay (with and without PID selection) compared to that of prompt D_s^+ mesons decaying via the ϕ-meson resonant decay.

BR= $(2.61 \pm 0.09)\%$) and the $D_s^+ \to f_0\pi^+ \to K^-K^+\pi^+$ (with BR= $(1.15 \pm 0.32)\%$) are expected to give the largest contribution, given the similar mass of the $\phi(1020)$, $K^{0*}(892)$ and $f_0(980)$ mesons [13].

The contamination from the K^{0*}-meson resonant decay was studied in the MC simulation. The (Acc $\times\,\epsilon$) factor of prompt D_s^+ mesons decaying via the K^{*0}-meson resonance is compared to that of prompt D_s^+ mesons decaying via the ϕ-meson resonance in the right panel of Fig. 5.5. The selection efficiency for the K^{0*}-meson resonant decay is lower than that for the ϕ-meson resonant decay of about a factor 100 without the PID selection applied. The PID selection reduces further the efficiency, since it rejects the D_s^+-meson candidates that have the invariant-mass of the kaon pair compatible with that of the ϕ meson in case of the wrong-mass hypothesis of one LS track. The contamination from this resonant decay was hence found to be smaller than 1%.

Conversely, the $D_s^+ \to f_0\pi^+ \to K^-K^+\pi^+$ decay was not simulated in the MC production described in Sec. 4.3, owing to the large uncertainty on the f_0 mass ($M(f_0)$) and width ($\Gamma(f_0)$) that, according to the PDG, can vary from 970 to 1010 MeV/c^2 and from 10 to 100 MeV/c^2, respectively [13]. This uncertainty on the f_0-meson line shape could lead to a different contamination, ranging from 1–2% to about 26% depending on the values of the $M(f_0)$ and $\Gamma(f_0)$, as shown in the left panel of Fig. 5.6. It is however worthwhile mentioning that a recent preliminary measurement of f_0-meson production at mid-rapidity ($|y| < 0.5$) in pp collisions at $\sqrt{s} = 5.02$ TeV performed by the ALICE Collaboration indicates that $M(f_0) \approx 974$ MeV/c^2 and $\Gamma(f_0) \approx 38$ MeV/c^2, corresponding to a relatively small contamination of about 2.9%. The right panel of Fig. 5.6 shows an example of fit

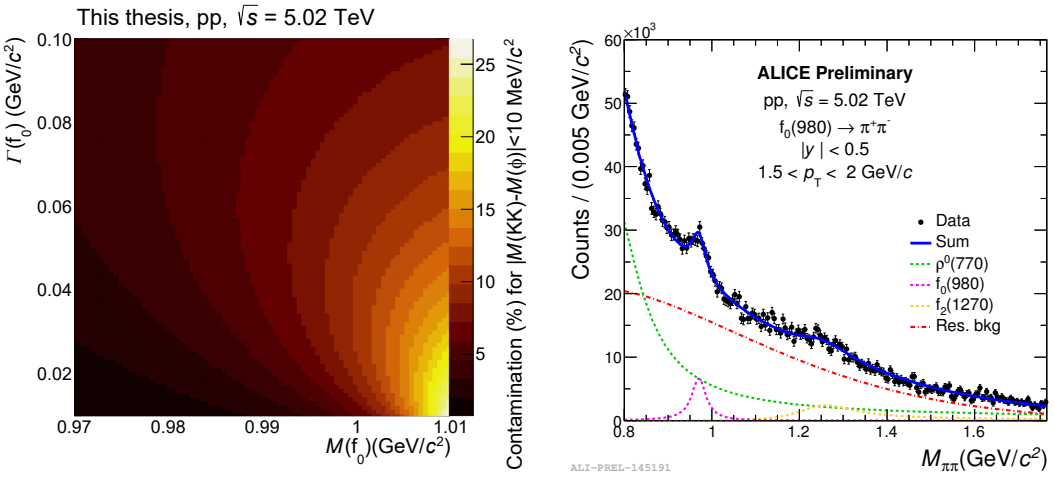

Figure 5.6: Left: contamination from the $D_s^+ \to f_0\pi^+ \to K^-K^+\pi^+$ resonant decay as a function of the mass and the width of the f_0 meson. Right: example of fit to the invariant-mass distribution of opposite-sign pion pairs for the preliminary measurement of the f_0 meson performed by the ALICE Collaboration ©.

to the invariant-mass distribution of opposite-sign pion pairs with $1.5 < p_T < 2$ GeV/c used to extract the f_0-meson signal.

In addition, to confirm that the bias from the contamination of the resonant decays via the K^{0*} and f_0 mesons is small, the normalisation adopted in this analysis was compared to the one suggested by the CLEO Collaboration in Ref. [150], which was adopted by the LHCb Collaboration for the measurement of the D_s^+-production cross section at forward rapidity [151–153]. The CLEO Collaboration measured partial branching ratios for D_s^+ mesons decaying to $K^+K^-\pi^+$ for different $\Delta M(KK)$ selections ($\mathcal{B}_{\Delta M}$), that include the contribution of all resonant decays in the considered $\Delta M(KK)$ range. The values provided by the CLEO Collaboration are reported in Table 5.3 with the BR of the $D_s^+ \to \phi\pi^+ \to K^-K^+\pi^+$ decay from the PDG [13] multiplied by the selection efficiency of

$\Delta M(KK)$ (MeV/c^2)	$\mathcal{B}_{\Delta M}$ (%)	BR (%) $\times\, \epsilon(D_s^+ \to \phi\pi^+ \to K^-K^+\pi^+)$
5	$1.69 \pm 0.08 \pm 0.06$	1.75 ± 0.06
10	$1.99 \pm 0.10 \pm 0.05$	2.07 ± 0.07
15	$2.14 \pm 0.10 \pm 0.05$	2.17 ± 0.08
20	$2.24 \pm 0.11 \pm 0.06$	2.27 ± 0.08

Table 5.3: Partial branching ratios ($\mathcal{B}_{\Delta M}$) provided by the CLEO Collaboration [150] and the BR of the $D_s^+ \to \phi\pi^+ \to K^-K^+\pi^+$ decay from the PDG [13] multiplied by the selection efficiency of D_s^+ mesons decaying via the f_0-meson resonant decay for different $\Delta M(KK)$ selections.

$\mathrm{D_s^+}$ mesons decaying via the ϕ-meson resonant decay evaluated with the MC simulation described in Sec. 4.3, for different $\Delta M(\mathrm{KK})$ selections. For each $\Delta M(\mathrm{KK})$ selection, the two values are compatible within uncertainties, therefore no uncertainty in addition to the one on the BR of the $\mathrm{D_s^+} \to \phi\pi^+ \to \mathrm{K^-K^+}\pi^+$ decay channel was added for the contamination of the other resonant decay channels.

5.5 Fraction of prompt $\mathrm{D_s^+}$

The fraction of prompt $\mathrm{D_s^+}$ mesons in the measured raw yield (f_{prompt}) was estimated with a theory-driven method that exploits the beauty-hadron cross sections obtained from FONLL calculations [79, 80] and the (Acc$\times\epsilon$) of feed-down $\mathrm{D_s^+}$ mesons from the simulations. In addition, the estimated f_{prompt} was cross-checked with a data-driven approach that exploits the different shapes of the impact-parameter distributions of prompt and feed-down $\mathrm{D_s^+}$ mesons.

5.5.1 Theory-driven estimation

The f_{prompt} parameter was evaluated by subtracting the calculated raw yield of feed-down $\mathrm{D_s^+}$ mesons ($N_{\mathrm{raw}}^{\text{feed-down}}(\mathrm{D_s^\pm})$) from the inclusive raw yield ($N_{\mathrm{raw}}(\mathrm{D_s^\pm})$) in each p_{T} interval of the analysis:

$$\begin{aligned} f_{\mathrm{prompt}} &= 1 - \frac{N_{\mathrm{raw}}^{\text{feed-down}}(\mathrm{D_s^\pm})}{N_{\mathrm{raw}}(\mathrm{D_s^\pm})} = \\ &= 1 - \left(\frac{\mathrm{d}^2\sigma}{\mathrm{d}p_{\mathrm{T}}\mathrm{d}y}\right)_{\text{FONLL, EvtGen}}^{\text{feed-down}} \cdot \frac{(\mathrm{Acc}\times\epsilon)_{\text{feed-down}} \cdot c_{\Delta y}\ \Delta p_{\mathrm{T}} \cdot \mathrm{BR} \cdot \mathcal{L}_{\mathrm{int}}}{\frac{1}{2} \cdot N_{\mathrm{raw}}(\mathrm{D_s^\pm})} \,. \end{aligned} \tag{5.5}$$

In the above formula, the cross section of feed-down $\mathrm{D_s^+}$ mesons is obtained by folding the beauty-hadron cross section estimated with FONLL calculations with the beauty-hadron $\to \mathrm{D} + \mathrm{X}$ decay kinematics from the EvtGenpackage [154]. The f_{prompt} values depend on the topological selections applied and it decreases from 0.94 to 0.89 with increasing p_{T} for the selections reported in Table 5.1. A systematic uncertainty on the estimation of f_{prompt} was evaluated by varying the FONLL parameters, which include the factorisation (μ_{F}) and renormalisation (μ_{R}) scales, as well as the mass of the beauty quark, as explained in Ref. [80]. In particular, the renormalisation and factorisation scales were varied independently in the range $0.5 < \mu_{\mathrm{R}}\ (\mu_{\mathrm{F}})/\mu_0 < 2$, being $\mu_0 = \sqrt{p_{\mathrm{T}}^2 + m_{\mathrm{b}}^2}$ the default value of μ_{R} and μ_{F} in the central FONLL prediction. The mass of the beauty quark m_{b} was varied between 4.5 and 5 GeV/c^2. Finally the uncertainty on the PDFs used in the FONLL calculations (CTEQ6.6 PDFs [74]) was also taken into account.

5.5.2 Data-driven estimation

The f_{prompt} factor obtained with the theory-driven approach was cross-checked with the measurement of the fraction of prompt $\mathrm{D_s^+}$ mesons in the raw yield performed via fits to the d_0^{xy} distributions of $\mathrm{D_s^+}$ candidates. In particular, f_{prompt} was extracted from an

unbinned log-likelihood fit of the d_0^{xy} distributions of $\mathrm{D_s^+}$ candidates in the invariant-mass interval of the signal ($|M(\mathrm{KK}\pi) - M(\mathrm{D_s^+})| < 2\sigma$), using the function

$$F(d_0^{xy}) = S \cdot [f_{\mathrm{prompt}} \cdot F^{\mathrm{prompt}}(d_0^{xy}) + (1 - f_{\mathrm{prompt}}) \cdot F^{\text{feed-down}}(d_0^{xy})] + (N - S) \cdot F^{\mathrm{bkg}}(d_0^{xy}), \tag{5.6}$$

where N is the total number of counts fitted, S is the amount of signal candidates in the selected invariant-mass interval, fixed to the values extracted from the invariant-mass fits, while F^{prompt}, $F^{\text{feed-down}}$, and F^{bkg} are the functions describing the d_0^{xy} distributions of prompt $\mathrm{D_s^+}$ mesons, feed-down $\mathrm{D_s^+}$ mesons, and combinatorial background, respectively.

The d_0^{xy} of prompt $\mathrm{D_s^+}$ mesons assumes non-zero values only because of the detector resolution, and therefore F^{prompt} was modelled with a Gaussian function plus a symmetric exponential term to describe the non-Gaussian term of the distribution:

$$\begin{aligned} F^{\mathrm{prompt}}(d_0^{xy}) &= F^{\mathrm{gaus+exp}}(d_0^{xy};\ f_{\mathrm{gaus}}, \mu_{\mathrm{prompt}}, \sigma_{\mathrm{prompt}}, \lambda_{\mathrm{prompt}}) = \\ &= \frac{f_{\mathrm{gaus}}}{\sqrt{2\pi}\sigma_{\mathrm{prompt}}} e^{-\frac{(d_0^{xy} - \mu_{\mathrm{prompt}})^2}{2\sigma^2_{\mathrm{prompt}}}} + \frac{1 - f_{\mathrm{gaus}}}{2\lambda_{\mathrm{prompt}}} e^{-\frac{|d_0^{xy} - \mu_{\mathrm{prompt}}|}{\lambda_{\mathrm{prompt}}}}, \end{aligned} \tag{5.7}$$

where f_{gaus} is the fraction of the integral contained in the Gaussian function, μ_{prompt} the common mean value for the two contributions, $\lambda_{\mathrm{prompt}}$ is the slope of the exponential function and σ_{prompt} is the width of the Gaussian function, which represents the resolution of the detector. The $F^{\text{feed-down}}$ function was obtained by the convolution of the function describing the intrinsic impact-parameter distribution of feed-down $\mathrm{D_s^+}$ mesons ($F^{\text{feed-down}}_{\mathrm{true}}$) and the detector-resolution term which coincides with the prompt distribution (F^{prompt}):

$$F^{\text{feed-down}}(d_0^{xy}) = \int_{d_{0,\mathrm{min}}^{xy}}^{d_{0,\mathrm{max}}^{xy}} \left[F^{\text{feed-down}}_{\mathrm{true}}(d_0^{xy\prime}) \cdot F^{\mathrm{prompt}}(d_0^{xy} - d_0^{xy\prime}) \right] \mathrm{d}d_0^{xy\prime}. \tag{5.8}$$

The intrinsic impact parameter of the feed-down $\mathrm{D_s^+}$ mesons is different from zero since in general the momentum of the $\mathrm{D_s^+}$ meson is not parallel to the one of the beauty hadron, and therefore it does not point to the interaction vertex. Its distribution was modelled with a double symmetric exponential function

$$F^{\text{feed-down}}_{\mathrm{true}}(d_0^{xy}) = \frac{f^{\mathrm{FD}}_{\lambda_1}}{2\lambda_1^{\mathrm{FD}}} e^{-\frac{|d_0^{xy} - \mu_{\mathrm{FD}}|}{\lambda_1^{\mathrm{FD}}}} + \frac{1 - f_{\lambda_1^{\mathrm{FD}}}}{2\lambda_2^{\mathrm{FD}}} e^{-\frac{|d_0^{xy} - \mu_{\mathrm{FD}}|}{\lambda_2^{\mathrm{FD}}}}, \tag{5.9}$$

where $\lambda^{\mathrm{FD}}_{1,2}$ are the slopes of the two symmetrised exponential functions, $f^{\mathrm{FD}}_{\lambda_1}$ is the fraction of integral contained in the first function and μ_{FD} is the common mean value. Finally the combinatorial-background function was modelled with the sum of two Gaussian functions with exponential tails and different means:

$$\begin{aligned} F^{\mathrm{bkg}}(d_0^{xy}) = F^{\mathrm{gaus+exp}}(d_0^{xy};\ f^{\mathrm{bkg}}_{\mathrm{gaus}}, \mu_1^{\mathrm{bkg}}, \sigma_{\mathrm{bkg}}, \lambda_{\mathrm{bkg}}) + \\ + F^{\mathrm{gaus+exp}}(d_0^{xy};\ f^{\mathrm{bkg}}_{\mathrm{gaus}}, \mu_2^{\mathrm{bkg}}, \sigma_{\mathrm{bkg}}, \lambda_{\mathrm{bkg}}). \end{aligned} \tag{5.10}$$

The parameters of the aforementioned functions, except for the detector-resolution parameter σ_{prompt} and the prompt fraction f_{prompt} of Eq. 5.6, were fixed by fitting the

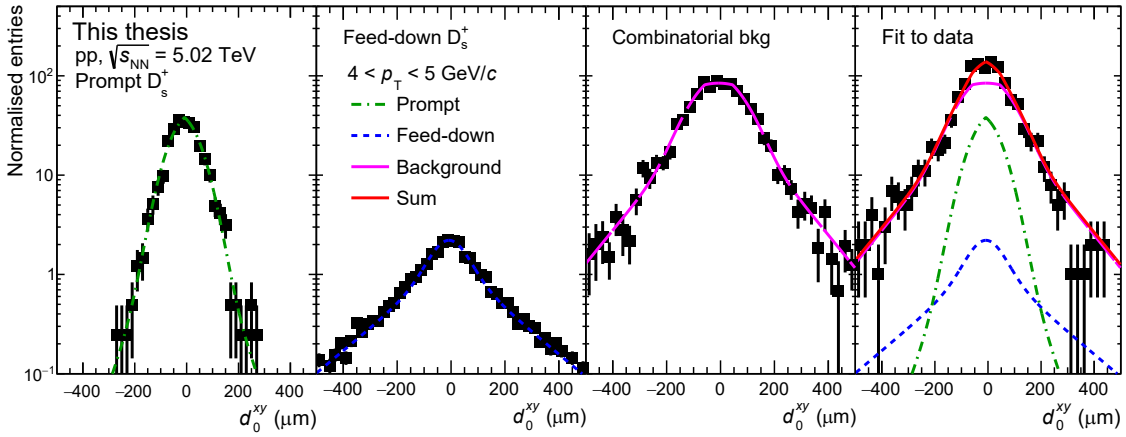

Figure 5.7: Fits to the template d_0^{xy} distributions of prompt $\mathrm{D_s^+}$ mesons from MC simulations (left panel), feed-down $\mathrm{D_s^+}$ mesons from MC simulations (middle-left panel), combinatorial background candidates from data (middle-right panel), and fit to the d_0^{xy} distribution of $\mathrm{D_s^+}$ candidates in data (right panel) for the interval $4 < p_{\mathrm{T}} < 5$ GeV/c.

d_0^{xy} distributions of each contribution (*template* distributions) separately. For prompt and feed-down $\mathrm{D_s^+}$ mesons, the template distributions were obtained from the MC sample described in section 4.3. The distribution of the combinatorial background was instead taken from data, in particular from the d_0^{xy} distribution of $\mathrm{D_s^+}$ candidates in the side-band distributions, defined by two invariant-mass windows of 100 MeV/c^2 away from the the $\mathrm{D_s^+}$ and $\mathrm{D^+}$ peaks ($M(\mathrm{KK}\pi) \in [1.73,1.83]$ GeV/c^2 and $M(\mathrm{KK}\pi) \in [2.02,2.12]$ GeV/c^2). Examples of fit to the template distributions of prompt $\mathrm{D_s^+}$ mesons, feed-down $\mathrm{D_s^+}$ mesons and combinatorial background candidates with $4 < p_{\mathrm{T}} < 5$ GeV/c are reported in the left, middle-left, and right-left panels of Fig. 5.7, respectively. The right panel of the same Figure shows the fit to the d_0^{xy} distribution of $\mathrm{D_s^+}$ candidates with $|M(\mathrm{KK}\pi) - M(\mathrm{D_s^+})| < 2\sigma$ used to extract the fraction of prompt $\mathrm{D_s^+}$ mesons in the same p_{T} interval.

Systematic uncertainties

The systematic uncertainties associated to the fitting procedure were evaluated by (i) varying the d_0^{xy} fit range, (ii) varying the invariant-mass intervals used to define the side-band distribution, (iii) taking into account the uncertainty on the signal and background yields extracted from the invariant-mass fit. In particular, six alternatives fit ranges, from ± 400 μm to ± 900 μm, being the default range the largest possible (± 1000 μm), were tested. Four different invariant-mass intervals were considered to define the template distribution of the combinatorial background, moving the invariant-mass region used to define the side-band distributions closer and further from the $\mathrm{D_s^+}$ and $\mathrm{D^+}$ peaks. The S parameter in Eq. 5.6 was varied considering both the statistical and systematic uncertainty of the $\mathrm{D_s^+}$ raw yield extracted from the invariant-mass fits. Moreover, the fits were repeated by selecting the $\mathrm{D_s^+}$ candidates in four alternatives invariant-mass

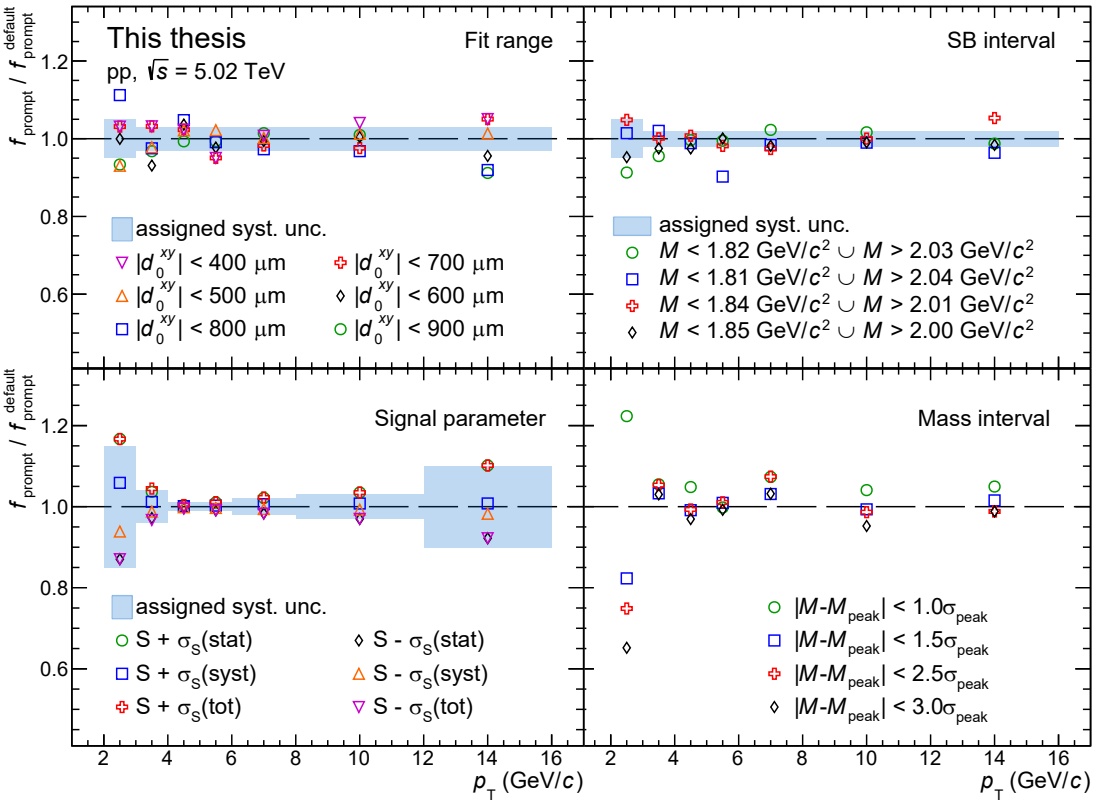

Figure 5.8: Ratio of f_{prompt} obtained varying the d_0^{xy} fit range (top-left panel), the invariant-mass range used to define the background distribution (top-right panel), the signal parameter S within its uncertainties (bottom-left panel), and the invariant-mass range considered to obtain the d_0^{xy} distribution (bottom-left panel), compared to the reference value $f_{\mathrm{prompt}}^{\mathrm{default}}$. The systematic uncertainty assigned for each variation is also displayed.

windows from $|M(\mathrm{KK}\pi) - M(\mathrm{D_s^+})| < 1\sigma$ to $|M(\mathrm{KK}\pi) - M(\mathrm{D_s^+})| < 3\sigma$. Since the sample of candidates differs for each invariant-mass window and no trend was observed among the extracted f_{prompt} values, no additional systematic uncertainty was assigned for this check. The ratio of f_{prompt} with respect to the default value for each variation is reported in Fig. 5.8 together with the assigned systematic uncertainty for each source shown as a filled box. The total systematic uncertainty ranged from 4% to 17% depending on p_{T}.

Result

The fraction of prompt $\mathrm{D_s^+}$ mesons obtained with the theory-driven and data-driven methods is reported in Fig. 5.9, together with the same quantities extracted for the $\mathrm{D^0}$ mesons published in Ref. [1]. The d_0^{xy} fit was not applicable in the $16 < p_{\mathrm{T}} < 24$ GeV/c interval, because of the small number of $\mathrm{D_s^+}$ candidates available. The two

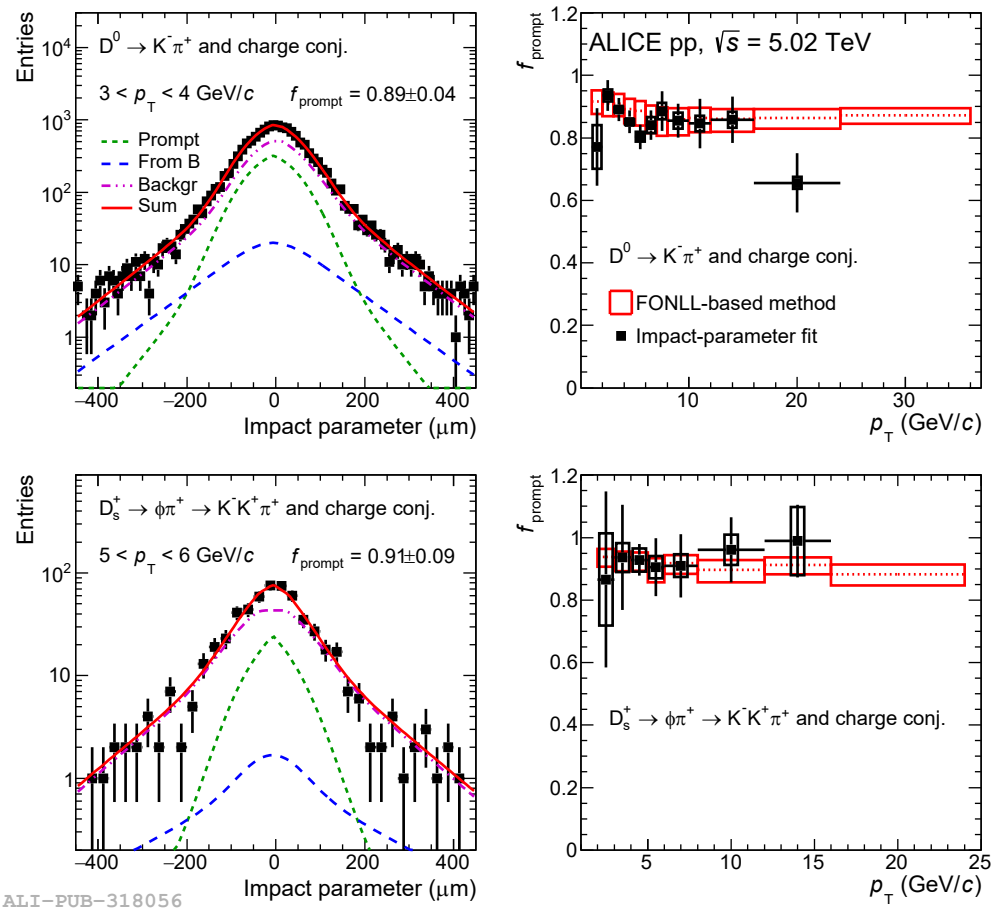

Figure 5.9: Left: examples of d_0^{xy} fits for D^0 (top panel) and D_s^+ (bottom panel) mesons. The green and blue curves represent the contributions of the prompt and feed-down D_s^+ mesons, the magenta curve the combinatorial background, and the red curve the total fit function. Right: comparison between the $f_{\rm prompt}$ parameter as a function of $p_{\rm T}$ obtained with the FONLL-based method and from the d_0^{xy} fits for D^0 (top panel) and D_s^+ (bottom panel) mesons. Figure taken from Ref. [1].

results are compatible within uncertainties, although the $f_{\rm prompt}$ parameter evaluated with the theory-driven method has smaller uncertainties, because of the poorer statistical precision of the one extracted from the d_0^{xy} fits. For this reason, the fraction of prompt D_s^+ mesons estimated with Eq. 5.5 was used to correct the raw yield in Eq. 5.1, while the other one was kept as a cross check of the theory-driven method.

5.6 Systematic uncertainties

In this Section, the sources of systematic uncertainties considered for the measurement of the $\mathrm{D_s^+}$ p_T-differential cross section are presented. They include (i) the extraction of the raw $\mathrm{D_s^+}$ yield, (ii) the topological and kinematical selection efficiency, (iii) the PID selection efficiency, (iv) the tracking efficiency, (v) the p_T shape of generated $\mathrm{D_s^+}$ mesons in the MC simulation, and (vi) the subtraction of the feed-down contribution described in Sec. 5.5.

5.6.1 Raw-yield extraction

The systematic uncertainty due to the raw-yield extraction was evaluated with a multi-trial approach, repeating the fits to the invariant-mass distributions, varying the invariant-mass fit range (five different lower and five different upper limits) and the functional form of the combinatorial background (linear, parabolic, and exponential); the fits were performed both as leaving the peak position as a free parameter and by fixing it to the value extracted from the MC simulation. In particular, all the combinations of the aforementioned fit configurations were considered. As additional stability check, the fits were repeated using different invariant-mass bin widths (from 2 to 10 MeV/c^2) and the result were compared to the ones obtained with a bin-counting method. This last approach consisted in integrating the invariant-mass distribution within $\pm3\sigma$ and $\pm5\sigma$ the mass of the $\mathrm{D_s^+}$ meson, after subtracting the combinatorial background estimated from a fit to the side-band distributions. This latter test was performed to have an estimation of the raw yield independent of the signal shape chosen for the fit.

The systematic uncertainty was then evaluated by considering the RMS and the shift from the central value of the raw-yield distribution obtained with the multi-trial study, for the fits having $\chi^2/\mathrm{ndf} < 2$. The left panel of Fig. 5.10 shows an example of raw-yield distribution for the interval $2 < p_\mathrm{T} < 3$ GeV/c, evaluated with the multi-trial study from the fit and the bin-counting method. The right panel of the same Figure shows the mean of the raw-yield distribution divided by the raw yield extracted with the default fit configuration as a function of p_T. The error bars represent the RMS of the raw-yield distribution and the blue band the assigned systematic uncertainty. The values assigned as relative systematic uncertainty range from 3% to 7%.

5.6.2 Topological and kinematical selection efficiency

If the distributions of the topological and kinematical variables used for the selection of $\mathrm{D_s^+}$ candidates were exactly reproduced in the MC simulation, the result would be independent of the selection criteria used in the analysis. However, a possible imperfect description of these variables in the simulation could lead to a systematic bias in the result. For this reason, the cross section was recomputed applying several different sets of selections. For each variable adopted in the analysis, two tighter and two looser selection criteria were tested keeping the other fixed, resulting in a maximum variation of the selection efficiency of about ±50%. The systematic uncertainty was assigned considering the RMS and the shift with respect to unity of the distribution of the ratio between the

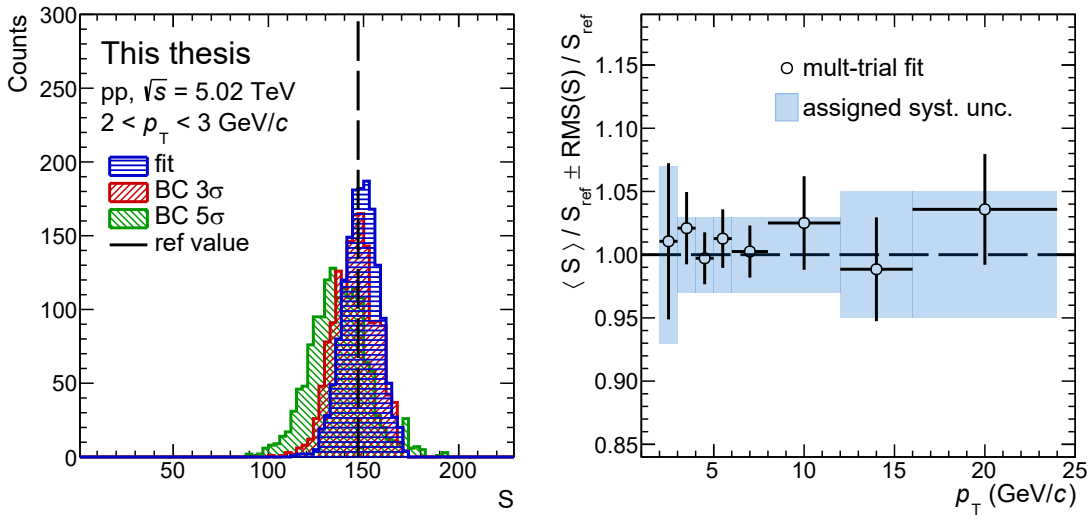

Figure 5.10: Left: raw-yield distribution obtained with the multi-trial study from the fit and the bin-counting (BC) methods in the interval $2 < p_{\mathrm{T}} < 3$ GeV/c. Right: mean $\pm$ RMS of the distributions of the raw yield divided by the reference value as a function of p_{T}. The blue band represents the assigned systematic uncertainty.

cross section obtained with each set of selections and the default one.

Figure 5.11 shows the study performed for the transverse momentum interval $2 < p_{\mathrm{T}} < 3$ GeV/c as an example. The variation of the extracted raw yield (top-left panel), the statistical significance (top-middle panel), the signal-to-background ratio (top-right panel), and the variation of the selection efficiency (bottom-left panel) are reported as a function of the different sets of selections adopted. The bottom-middle panel shows the variation of the cross section as a function of the set of selections, compared to the default value and the assigned systematic uncertainty. The largest variation of the cross section is observed for the trials for the sets of selections between the sixth and the twentieth, which correspond to the variation of $L_{xy}/\sigma(L_{xy})$, and the following four, which correspond to the variation of σ_{vtx}. However, for these selections also the S/B and the statistical significance vary more and therefore a worse raw-yield extraction could influence the result. Finally, in the bottom-right panel of Fig. 5.11 the distribution of the ratio between the cross section obtained with each set of selections and the default one is reported; the blue band represents the sum in quadrature of the RMS and the shift with respect to unity of the distribution, while the red band the assigned systematic uncertainty. The relative systematic uncertainty ranges from 5% to 8%, depending on the p_{T} intervals of the analysis.

Analysis without decay-vertex reconstruction

To test the stability of the result with an extreme approach, the analysis was also repeated without applying any selection on the D_s^+ decay-vertex topology. In this case,

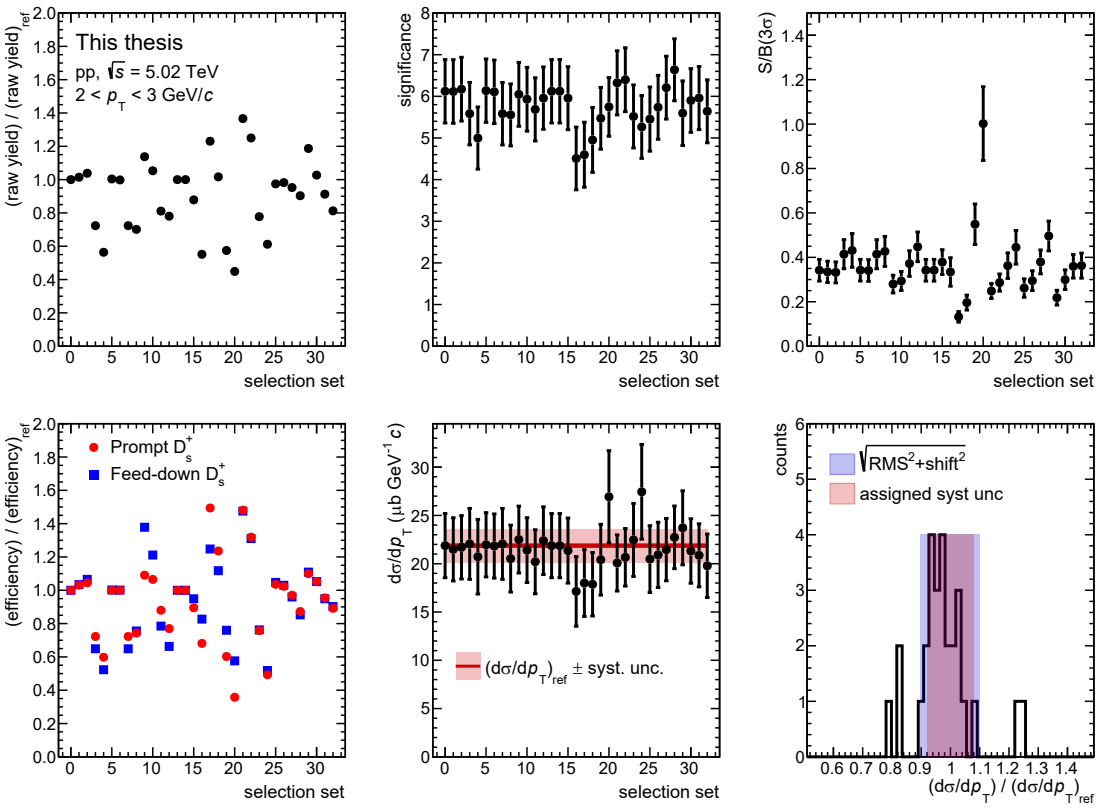

Figure 5.11: Variation of the extracted raw yield (top-left panel), statistical significance (top-middle panel), signal-to-background ratio (top-right panel), variation of the selection efficiency (bottom-left panel), and variation of the cross section (bottom-middle panel) as a function of the set of selections applied for the interval $2 < p_{\mathrm{T}} < 3$ GeV/c. The distribution of the ratio between the cross section obtained with each set of selections and the default one is reported in the bottom right panel. The blue band represents the sum in quadrature of the shift and the RMS of the distribution, while the red band the assigned systematic uncertainty.

the analysis strategy is similar to the one previously adopted by the ALICE Collaboration to measure low-p_{T} D^0 mesons (see Ref. [1, 2, 148]) and is based on the estimation and subtraction of the combinatorial background.

For this analysis, candidates were selected by requiring $|M(\mathrm{KK}) - M(\phi)| < 5$ MeV/c^2 and a minimum p_{T} of 300 MeV/c for the decay tracks. In addition, the same PID selection strategy as the one adopted for the analysis with the decay-topology selections was applied to the decay tracks. The invariant-mass distribution of the combinatorial background was estimated with the track-rotation technique, which consists in rotating on of the decay tracks by a given angle to obtain uncorrelated background candidates. In particular, the track of the pion was rotated up to 19 times around the tracks of the kaon pair by an angle between $\frac{\pi}{10}$ and $\frac{19\pi}{10}$ radians in the azimuthal plane. This

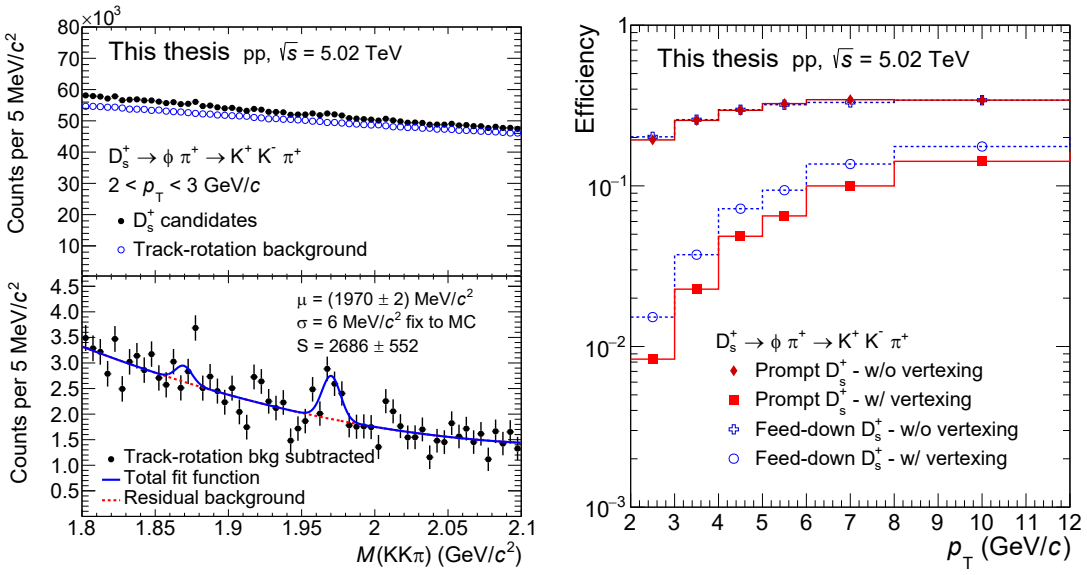

Figure 5.12: Left: invariant-mass distribution of D_s^+ candidates and estimated combinatorial background (top panel) and fit to the invariant-mass distribution after the background subtraction (bottom panel). Right: selection efficiency of prompt and feed-down D_s^+ mesons for the analyses with and without decay-vertex topology selections.

rotation was performed to mimic the combinatorial-background candidates formed by two kaons coming from the same ϕ meson and an uncorrelated pion, which is the dominant contribution given the requirement on the invariant-mass of the kaon pair. The top-left panel of Fig. 5.12 shows the invariant-mass distribution of D_s^+ candidates with $2 < p_T < 3$ GeV/c with the estimated combinatorial background normalised to the right side-band of the invariant-mass distribution in order to obtain positive entries after the background subtraction. The fit to the invariant-mass distribution after the subtraction of the combinatorial background is shown in the bottom-left panel of the same Figure. The residual background was modelled with a second-order polynomial function, while the signal with a Gaussian function. In order to improve the stability of the fit, the width of the Gaussian function was fixed to the value extracted from the MC simulation (see Fig. 5.3). The selection efficiency obtained without applying selections to the decay-vertex topology is compared to the one obtained for the analysis with topological selections in the right panel of Fig. 5.12. Unlike the analysis with topological selections, the efficiency is the same for prompt and feed-down D_s^+ mesons, and it is higher up to a factor 30 at low p_T with respect to that obtained with the topological analysis.

Figure 5.13 shows the ratio between the cross section obtained without and with decay-vertex topology selections. Different PID and ΔM(KK) selections were tested in case of no topological selections. Given the large difference in the reconstruction efficiency and the amount of combinatorial background, the statistical uncertainty in the ratio was propagated as uncorrelated between the two measurements. All the ratios were found to be compatible with unity within the large uncertainties, confirming that the selections

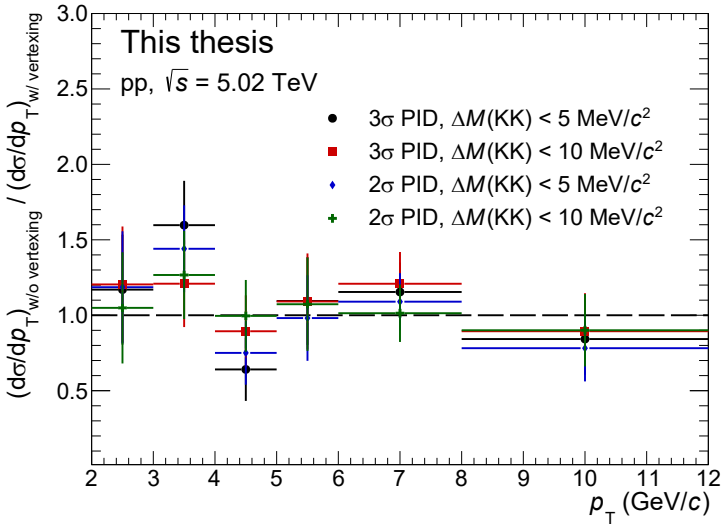

Figure 5.13: Ratio between the cross section obtained without and with decay-vertex topology selections. Four different PID and $\Delta M(\mathrm{KK})$ selections were tested in case of no topological selections.

on the decay topology do not introduce a large bias in the measurement.

5.6.3 PID selection efficiency

Similarly to the distributions of the topological and kinematical variables, also a difference in the $N_\sigma^{\mathrm{TPC,\ TOF}}$ distributions of pions and kaons between data and the MC simulation could introduce a bias in the measurement. The analysis was therefore repeated with the two PID selection strategies described in Sec. 4.2.4 (labelled as conservative and strong PID) and applied in the full p_T range and without any PID selection. The signal extraction was however only possible for $p_\mathrm{T} > 4$ GeV/c in absence of PID selection, because of the too large background. The ratio between the cross sections obtained with the strong and conservative PID strategies and the ratio between the cross section obtained with the conservative PID strategy and no PID selection applied are shown in Fig. 5.14. The large uncertainties prevent to asses whether there is a systematic difference among the three results, or the difference is only due to statistical fluctuations.

For this reason, the systematic uncertainty arising from a possible difference in the $N_\sigma^{\mathrm{TPC,\ TOF}}$ distributions in data and in the simulation was evaluated with a per-track study, based on the selection of relatively pure samples of pions and kaons. Pions were selected from V^0 (K^0_s and Λ) decays, applying tight selections on the decay topology and kinematics. Two examples of N_σ distributions for the pion $\mathrm{d}E/\mathrm{d}x$ in the TPC detector and the pion time-of-flight signal in the TOF detector are shown in Fig. 5.15 for the MC simulation (top row) and the data (bottom row) for two different transverse-momentum intervals. The contamination in the selected sample of pions is below 0.1% for $p_\mathrm{T} <$ 5 GeV/c and around 0.5% for higher p_T, both in the data and the MC simulation. The

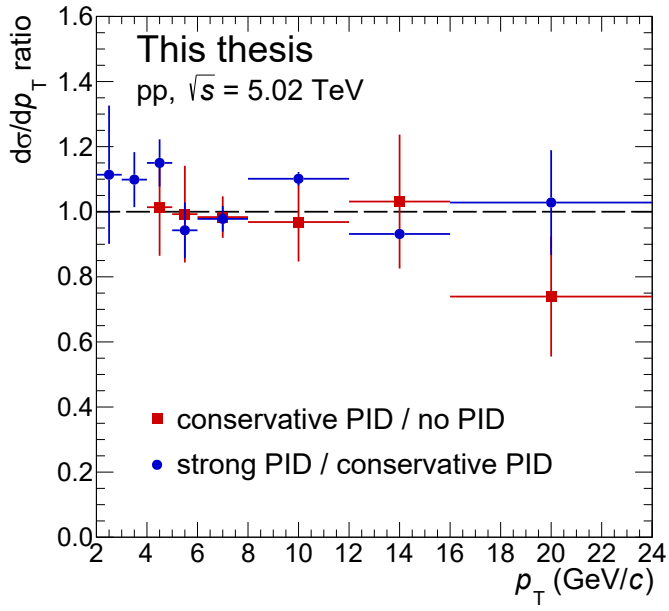

Figure 5.14: The ratio between the D_s^+ cross section obtained with the strong and conservative PID strategies and the ratio between the cross section obtained with the conservative PID strategy and no PID selection applied.

$N_\sigma^{\mathrm{TPC}}(\pi)$ distributions in data were fitted with a Gaussian function for each contribution in order to isolate the pion distribution (red curve in Fig. 5.15). The shape of the $N_\sigma^{\mathrm{TOF}}(\pi)$ distribution instead cannot be simply parametrised because of the non-Gaussian tails, and therefore in this case the contamination was considered negligible.

To obtain a relatively pure sample of kaons in the TPC detector, tracks were selected applying a tight selection on the time-of-flight signal in the TOF detector of $|N_\sigma^{\mathrm{TOF}}(\mathrm{K})| < 0.2$. The contamination, mainly consisting of pions, was estimated with the MC simulation to be around 1% for $p_{\mathrm{T}} \lesssim 3$ GeV/c, increasing up to 30% for $1 \lesssim p_{\mathrm{T}} \lesssim 3$ GeV/c. For $p_{\mathrm{T}} \gtrsim 3$ GeV/c the π/K separation provided by the TOF detector is not efficient and the contamination in the kaon sample becomes larger than 50%. As in the case of the pions, the kaon distribution was then extracted by fitting the total $N_\sigma^{\mathrm{TPC}}(\mathrm{K})$ distributions with a Gaussian function for each contribution, as shown in the bottom left panels of Fig. 5.16. Similarly, for the TOF detector, a sample of kaons was identified by requiring $|N_\sigma^{\mathrm{TPC}}(\mathrm{K})| < 0.2$. In this case, the contamination was found to be around 1% for $p_{\mathrm{T}} \lesssim 0.3$ GeV/c, increasing from 30% to 80% for $0.3 \lesssim p_{\mathrm{T}} \lesssim 1.5$ GeV/c and decreasing again down to 5% for $p_{\mathrm{T}} \approx 5-10$ GeV/c. Unlike the case of the pions, the contamination cannot be considered negligible and therefore the $N_\sigma^{\mathrm{TOF}}(\mathrm{K})$ distributions from data were fitted with the template distributions for each contribution obtained from the MC simulation, taking into account both data and MC statistical uncertainties, and varying the MC templates within the statistics [155]. Finally, to reduce as much as possible the dependency on the shape of the MC template, the $N_\sigma^{\mathrm{TOF}}(\mathrm{K})$ distribution

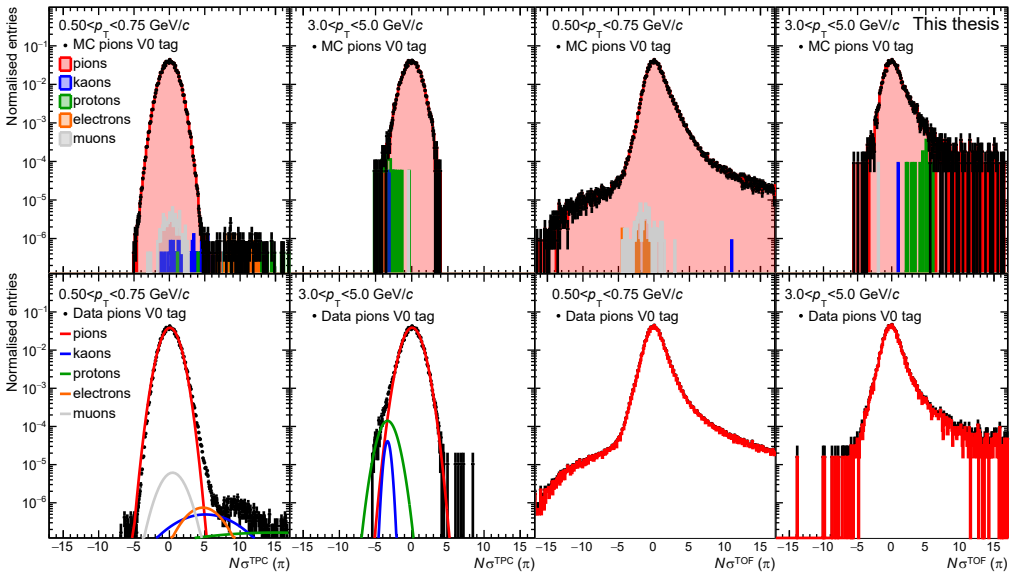

Figure 5.15: Examples of $N_\sigma^{\mathrm{TPC}}(\pi)$ (left panels) and $N_\sigma^{\mathrm{TOF}}(\pi)$ (right panels) distributions of selected pions from V0 decays in the MC simulations (top panels) and data (bottom panels) for two transverse-momentum intervals.

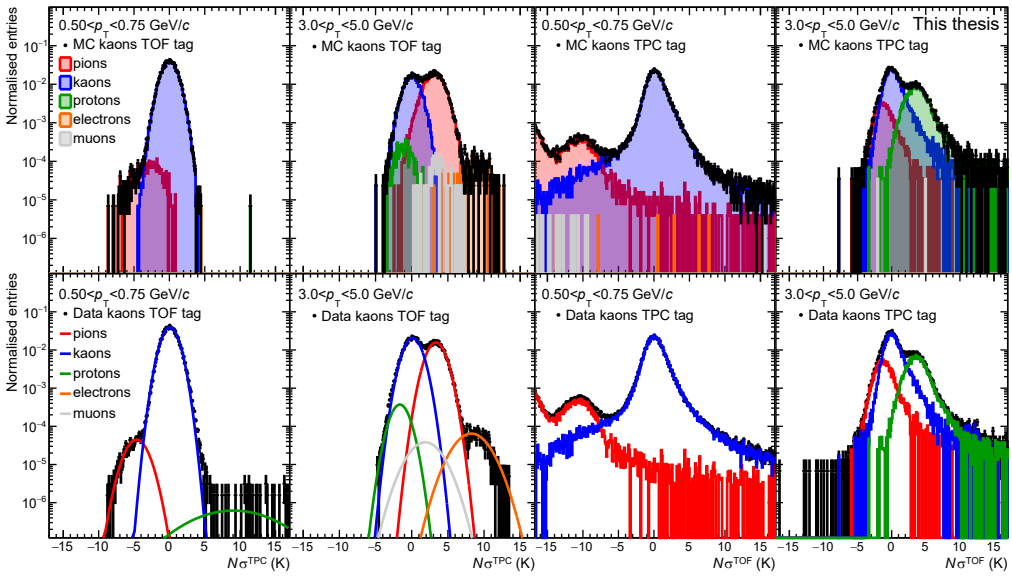

Figure 5.16: Examples of $N_\sigma^{\mathrm{TPC}}(\mathrm{K})$ (left panels) and $N_\sigma^{\mathrm{TOF}}(\mathrm{K})$ (right panels) distributions of selected pions from TOF and TPC PID selections respectively in the MC simulations (top panels) and data (bottom panels) for two transverse-momentum intervals.

of the kaons was obtained by subtracting the distributions of the other particle species obtained from the fit to the total distribution.

The efficiency of the N_σ selection for the pions (kaons) in data and in the simulation was then evaluated by integrating the red (blue) distributions of Fig. 5.15 (Fig. 5.16) within 1σ, 2σ, and 3σ and normalising the obtained values to the integral of the same distributions in the full range. A p_T-dependent per-track systematic uncertainty for the selection of pions and kaons was defined as the relative difference between the efficiencies of the N_σ selection in data and in the MC simulation. Figure 5.17 shows the data-to-MC ratios of the PID efficiencies of pions and kaons in the TPC (top-left panel) and TOF (top-right panel) detectors for the N_σ selections applied in the $\mathrm{D_s^+}$-meson analysis. The per-track systematic uncertainties were then propagated to the $\mathrm{D_s^+}$ mesons, via the kinematics of the $\mathrm{D_s^+}$ daughter tracks. For each $\mathrm{D_s^+}$ meson in the MC simulation, a systematic uncertainty was assigned by summing linearly the PID uncertainty of the three daughter tracks, which depends on their p_T according to the logic described in Sec. 4.2.4 for the conservative and strong PID strategies.

The bottom-left panel of Fig. 5.17 shows the correlation between the p_T of the daughter tracks and the parent $\mathrm{D_s^+}$ meson. The propagated systematic uncertainty to each $\mathrm{D_s^+}$ meson in the MC simulation is reported together with the average value as a function of p_T in the bottom-right panel of the same Figure. The discontinuity at $p_\mathrm{T} = 6$ GeV/c is due to the change from the strong PID to the conservative PID selection strategies. The values assigned as systematic uncertainty are reported in Table 5.4.

5.6.4 Track-reconstruction efficiency

The track-finding procedure starts from the outer radius of the TPC detector and continues with the prolongation of the track to the inner radius with the Kalman filter algorithm, where the clusters in TPC are matched to those in the ITS detector.

The systematic uncertainty due to the track-reconstruction efficiency includes the contributions of the track-finding procedure in the TPC detector and prolongation in the ITS detector, and the track-quality selections.

The ITS-TPC matching efficiency was computed as the number of tracks successfully fitted with the Kalman filter in the TPC and ITS, with at least one hit in the SPD layers, divided by the number of reconstructed tracks successfully fitted in the TPC. The systematic uncertainty on its determination arises from discrepancies in the tracking performance between data and the MC simulation. The ITS-TPC matching efficiency is different for particles produced in the collision, including strong decays and weak decays of charm and beauty hadrons, which are considered as primary particles in this study, and secondary particles (i.e. particles produced in the interactions with the material or in decays of strange hadrons). The PYTHIA event generator and the GEANT3 transport package do not reproduce the relative abundance of primary and secondary particles, therefore data-driven corrections for the fraction of primary particles (f_primary) were used to weight the MC simulation and obtain the corrected inclusive MC efficiency ($\epsilon_\mathrm{inclusive}(\mathrm{MC})$), which is computed as:

$$\epsilon_\mathrm{inclusive}(\mathrm{MC}) = f_\mathrm{primary} \cdot \epsilon_\mathrm{primary}(\mathrm{MC}) + (1 - f_\mathrm{primary}) \cdot \epsilon_\mathrm{secondary}(\mathrm{MC}), \tag{5.11}$$

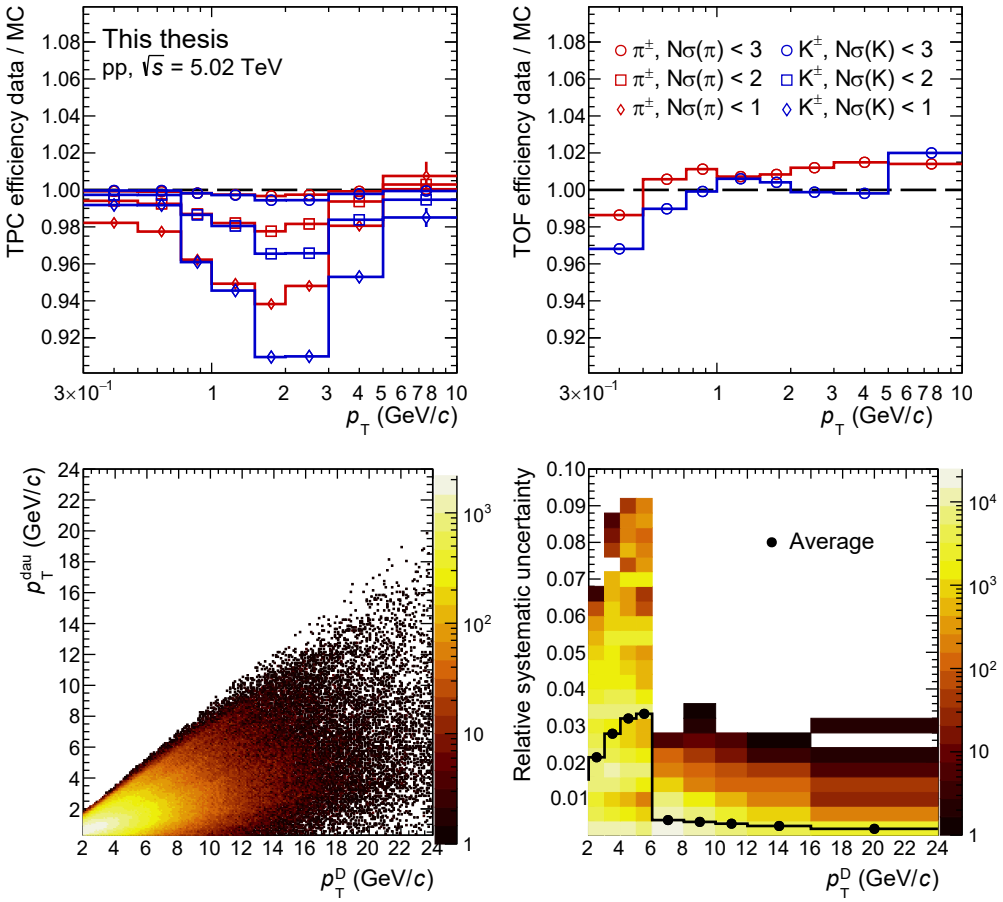

Figure 5.17: Top: data-to-MC ratios of the N_σ selection efficiencies of pions and kaons with the TPC (left panel) and TOF (right panel) detectors as a function of track p_{T}. Bottom: p_{T} of $\mathrm{D_s^+}$ daughter tracks as a function of $\mathrm{D_s^+}$-meson p_{T} (left) and relative systematic uncertainty on the PID selection applied to $\mathrm{D_s^+}$ candidates in the analysis as a function of $\mathrm{D_s^+}$-meson p_{T} (right).

where $\epsilon_{\mathrm{primary}}(\mathrm{MC})$ and $\epsilon_{\mathrm{secondary}}(\mathrm{MC})$ are the ITS-TPC matching efficiencies for primary and secondary particles, which are determined via fits to the d_0^{xy} distributions of the tracks with a similar procedure to the one adopted for prompt and feed-down $\mathrm{D_s^+}$ mesons described in Sec. 5.5.2. More details about the measurement of the fraction of primary particles in data can be found in Ref. [156]. The left panel of Fig. 5.18 shows the ratio of the ITS-TPC matching efficiency in the MC simulation after the correction for the fraction of primary particles and that extracted from the data as a function of p_{T}. The deviation from unity was assigned as per-track systematic uncertainty for the ITS-TPC matching efficiency.

In addition, it was checked if a discrepancy between the efficiency of the track-quality selections in data and in the MC simulation need to be considered. For this purpose, the

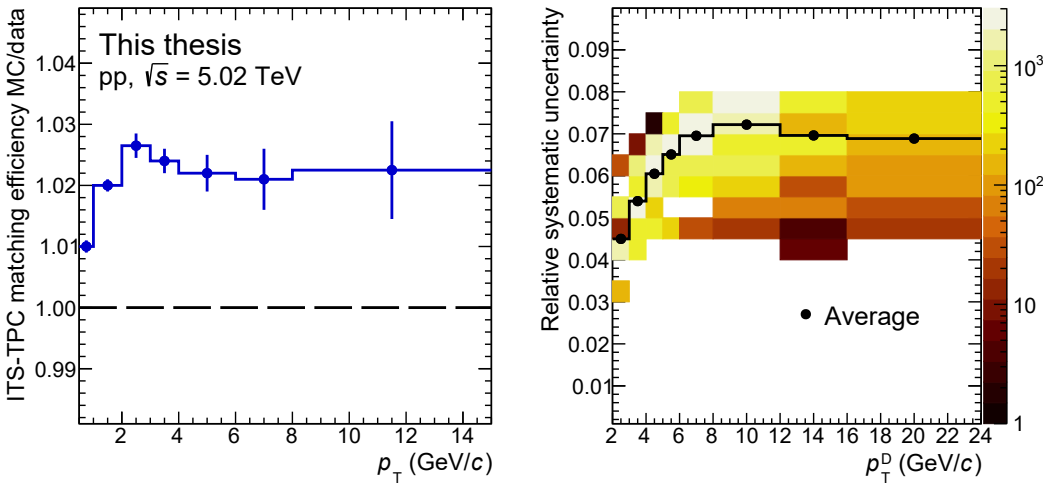

Figure 5.18: Left: MC-to-data ratio of ITS-TPC matching efficiency as a function of the track p_T. Right: relative systematic uncertainty on track-reconstruction efficiency as a function of D_s^+-meson p_T.

D_s^+-meson cross section was re-evaluated with three alternative track-quality selection criteria, which include the selection of tracks with (i) a number TPC crossed rows larger than $120 - 5/(p_T\ [\mathrm{GeV}/c])$ instead of the default value of 70, (ii) the number of TPC clusters at least 0.65 times the number of TPC crossed rows and (iii) a ratio of crossed rows over findable clusters in the TPC larger than 0.9 (being the default 0.8). These variations were also performed for the decay channels $D^0 \to K^-\pi^+$, $D^+ \to K^-\pi^+\pi^+$, and $D^{*+} \to K^-\pi^+\pi^+$ mesons, whose measurement has a higher statistical significance. The variation of the cross section was observed to be around 1% for D^0 (two-body decay) and 1.5% for the other D mesons (three-body decays), therefore a value equal to 0.5% was added to the per-track systematic uncertainty estimated for the ITS-TPC matching efficiency.

Finally, the p_T-dependent per-track systematic uncertainty was propagated to the D_s^+ mesons via the kinematics of the D_s^+ daughter tracks, similarly to the procedure explained in Sec. 5.6.3 for the PID uncertainty. The distribution of the relative systematic uncertainty, together with its average value as a function of the D_s^+-meson p_T is shown in the right panel of Fig. 5.18. The values assigned as systematic uncertainty are also reported in Table 5.4.

5.6.5 Generated Monte Carlo p_T shape

A non-realistic p_T shape of generated D_s^+ mesons in the MC simulation could lead to a bias in the determination of the efficiency because of the finite width of the p_T intervals considered in the analysis and the variation of the efficiency within the p_T intervals. In order to evaluate a systematic uncertainty, the p_T distribution of D_s^+ mesons in the MC simulations was weighted in order to reproduce the p_T shape predicted by

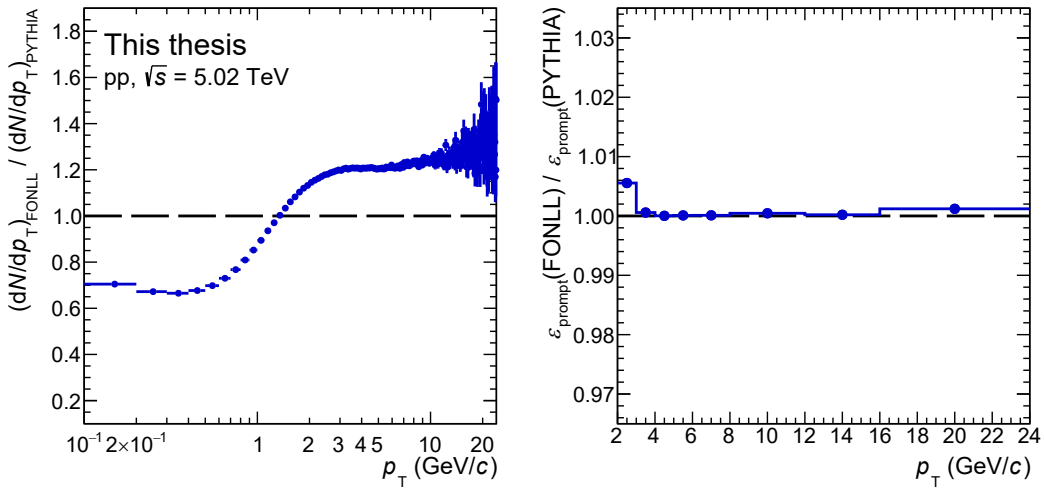

Figure 5.19: Left: ratio between the normalised p_{T} spectra from the PYTHIA simulation and from FONLL calculations. Right: ratio between the efficiency of prompt $\mathrm{D_s^+}$ mesons obtained with the FONLL and PYTHIA p_{T} shapes.

FONLL calculations for $\mathrm{D^0}$ mesons, which well describe the p_{T} shape of the measured D-meson cross sections. The left panel of Fig. 5.19 shows the ratio between the normalised p_{T} spectra from the PYTHIA simulation and FONLL predictions used to weight the p_{T} distribution of $\mathrm{D_s^+}$ mesons in the MC simulation. In the right panel of the same Figure, the ratio of the efficiency obtained with the two p_{T} shapes is shown. A systematic uncertainty of 1% was assigned in the $2 < p_{\mathrm{T}} < 3$ GeV/c interval, which is the one where the efficiency varies more steeply and therefore is more sensitive to the shape of the p_{T} distribution, while the effect was considered negligible in the remaining p_{T} range of the analysis.

5.6.6 Summary of systematic uncertainties

The values assigned as systematic uncertainty for each contribution and the total systematic uncertainty, obtained as the sum in quadrature of the different sources, are reported in Table 5.4 for all the p_{T} intervals of the analysis. The systematic uncertainty on the raw-yield extraction is uncorrelated among the p_{T} intervals, considering that the background invariant-mass shape and the S/B parameter vary substantially as a function of p_{T}, while the uncertainties on the topological, tracking, and PID selection efficiencies are mostly correlated. The total systematic uncertainty includes also a global normalisation uncertainty, which is due to the uncertainties on the BR for the $\mathrm{D_s^+ \to \phi\pi^+ \to K^-K^+\pi^+}$ decay channel and the integrated luminosity.

p_{T} (GeV/c)	[2,3]	[3,4]	[4,5]	[5,6]	[6,8]	[8,12]	[12,16]	[16,24]
Raw-yield extraction (%)	7.0	3.0	3.0	3.0	3.0	3.0	5.0	5.0
Selection efficiency (%)	8.0	5.0	5.0	5.0	5.0	5.0	5.0	5.0
PID efficiency (%)	2.5	2.5	3.0	3.0	negl.	negl.	negl.	negl.
Tracking efficiency (%)	4.5	5.5	6.0	6.5	7.0	7.0	7.0	7.0
MC p_{T} shape (%)	1.0	negl.	negl.	negl.	negl.	negl.	negl.	negl.
B feed-down (%)	$^{+2.7}_{-3.2}$	$^{+2.8}_{-3.5}$	$^{+2.6}_{-3.5}$	$^{+3.3}_{-4.6}$	$^{+2.7}_{-3.6}$	$^{+3.4}_{-4.4}$	$^{+2.6}_{-3.2}$	$^{+2.8}_{-3.6}$
Branching ratio (%)	3.5	3.5	3.5	3.5	3.5	3.5	3.5	3.5
Luminosity (%)	2.1	2.1	2.1	2.1	2.1	2.1	2.1	2.1
Total (%)	$^{+12.9}_{-13.0}$	$^{+9.8}_{-10.1}$	$^{+10.2}_{-10.4}$	$^{+10.6}_{-11.1}$	$^{+10.3}_{-10.6}$	$^{+10.5}_{-10.9}$	$^{+11.1}_{-11.3}$	$^{+11.1}_{-11.4}$

Table 5.4: Summary of relative systematic uncertainties on the p_{T}-differential production cross section of $\mathrm{D_s^+}$ mesons in pp collisions at $\sqrt{s} = 5.02$ TeV.

5.7 Results

Figure 5.20 shows the p_{T}-differential production cross section of $\mathrm{D_s^+}$ mesons in pp collisions at $\sqrt{s} = 5.02$ TeV, compared to that of $\mathrm{D^0}$, $\mathrm{D^+}$, and $\mathrm{D^{*+}}$ mesons at the same centre-of-mass energy. The vertical bars represent the statistical uncertainty, while the boxes the total systematic uncertainty, except for the uncertainty on the integrated luminosity and the branching ratio. Thanks to the large data sample of pp collisions at $\sqrt{s} = 5.02$ TeV, the measurement of the $\mathrm{D_s^+}$-meson production presented in this thesis is more differential in p_{T} and has a wider p_{T} coverage compared to previous ALICE measurements at $\sqrt{s} = 7$ TeV [157, 158]. The visible $\mathrm{D_s^+}$-meson production cross section was computed by integrating the cross section in the p_{T} intervals of the analysis in the full p_{T} range of the measurement, i.e. $2 < p_{\mathrm{T}} < 24$ GeV/c. The systematic uncertainty, except for the yield-extraction uncertainty, was propagated as fully correlated among the various p_{T} intervals. The uncertainty associated to the yield extraction was instead propagated as uncorrelated. The production cross section per unity of rapidity $\mathrm{d}\sigma/\mathrm{d}y$ in $|y| < 0.5$ was computed starting from the visible cross section, with an extrapolation procedure to account for the cross section of $\mathrm{D_s^+}$ mesons with $p_{\mathrm{T}} < 2$ GeV/c and $p_{\mathrm{T}} > 24$ GeV/c. The extrapolation factor was computed using a theoretical prediction to evaluate the ratio between the total production cross section and that in the p_{T} range covered by the measurement. In particular, even if FONLL calculations are not available for the $\mathrm{D_s^+}$ meson, to be consistent with the other D mesons (see Ref. [1]) FONLL calculations for the charm-quark production were used together with the fractions $f(c \to \mathrm{D_s^+})$ and $f(c \to \mathrm{D_s^{*+}})$ from ALEPH [159], and the fragmentation functions from Ref. [160] and the $\mathrm{D_s^{*+}} \to \mathrm{D_s^+}$ decay kinematics from PYTHIA. The uncertainty on the extrapolation procedure was estimated considering (i) the variation of the charm-quark mass, (ii) the renormalisation and factorisation scales in the FONLL calculation, and (iii) the uncertainties of the CTEQ6.6 PDFs [74] and (iv) the fragmentation functions, using those of $\mathrm{D^0}$

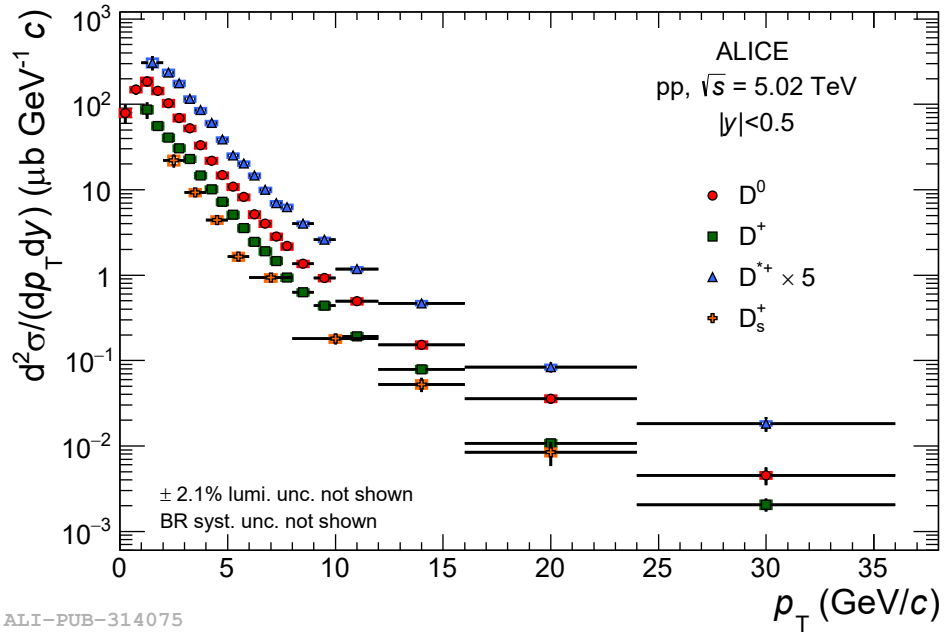

Figure 5.20: p_{T}-differential production cross section of prompt D^0, D^+, D^{*+}, and D_s^+ mesons in pp collisions at $\sqrt{s} = 5.02$ TeV. The D^{*+} cross section is scaled by a factor 5 to improve the visibility. Figure taken from Ref. [1]

and D^{*+} mesons from FONLL instead of the one computed for the D_s^+. The visible cross section in the measured p_{T} range and the extrapolated production cross section of D_s^+ mesons are reported in Table 5.5. From this study, the cross section for $p_{\mathrm{T}} < 2$ GeV/c should account for more than 50% of the total production cross section, leading to a large uncertainty of about 30% in the extrapolated cross section. For this reason, future larger samples of pp collisions would be important to extend the measurement to lower p_{T}, in order to have a more precise determination of the D_s^+-meson production cross section.

The abundance of D_s^+ mesons relative to non-strange D mesons was evaluated by computing ratio between the p_{T}-differential cross sections of D_s^+ and $\mathrm{D}^0(\mathrm{D}^+)$ mesons. The systematic uncertainties on the BR, raw-yield extraction, and selection efficiency were propagated as uncorrelated among the different species, while the other sources as

p_{T} range (GeV/c)	extr. factor	visible/production cross section in $\lvert y\rvert < 0.5$ (μb)
$[2-24]$	–	$40 \pm 4(\mathrm{stat}) \pm 4(\mathrm{syst}) \pm 1(\mathrm{lumi}) \pm 1(\mathrm{BR})$
> 0	$2.35^{+0.78}_{-0.66}$	$95 \pm 9(\mathrm{stat}) \pm 10(\mathrm{syst}) \pm 2(\mathrm{lumi}) \pm 3(\mathrm{BR})^{+31}_{-26}(\mathrm{extr})$

Table 5.5: Visible and extrapolated production cross section of D_s^+ mesons in pp collisions at $\sqrt{s} = 5.02$ TeV.

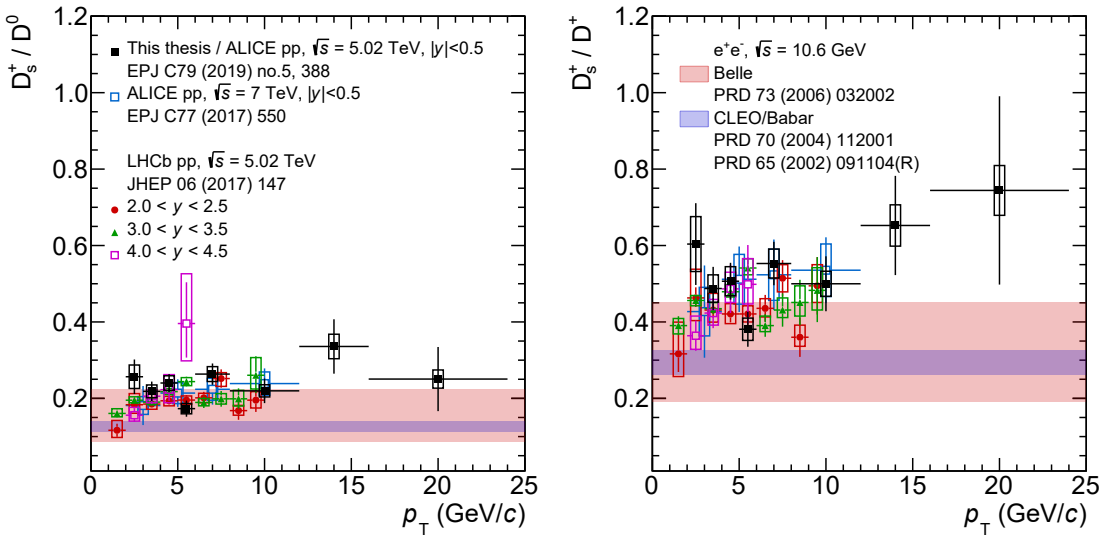

Figure 5.21: D_s^+/D^0 (left panel) and D_s^+/D^+ (right panel) p_T-differential cross-section ratios in pp collisions at $\sqrt{s} = 5.02$ TeV. The measurement is compared to the previous ALICE measurement at $\sqrt{s} = 7$ TeV [158], the measurement performed by the LHCb Collaboration at forward rapidity [153], and the p_T-integrated measurements performed by the Belle, CLEO, and Babar Collaborations in e^+e^- collisions at $\sqrt{s} = 10.6$ GeV [161–163].

fully correlated. The p_T-differential D_s^+/D^0 and D_s^+/D^+ cross-section ratios are shown in the left and right panels of Fig. 5.21, respectively. They were found to be compatible with those measured by the ALICE Collaboration in the same rapidity interval at $\sqrt{s} = 7$ TeV [158] and with those measured at the same centre-of-mass energy at forward rapidity ($2.0 < y < 4.5$) by the LHCb Collaboration [153]. The D_s^+/D^0 and D_s^+/D^+ ratios integrated in the measured p_T interval were also computed from the visible cross sections in Table 5.5 and are reported in Table 5.6. Moreover, the D_s^+/D^0 and D_s^+/D^+ cross-section ratios were found to be compatible with the corresponding p_T-integrated ratios computed using measurements from e^+e^- collider experiments at $\sqrt{s} = 10.6$ GeV [161–163] using the BR reported in Table 4.2, which are depicted as coloured bands in Fig. 5.21, and those measured at LEP [164]. This observation suggests that the fragmentation fractions of charm quarks into charmed mesons are not significantly modified in pp collisions with respect to e^+e^- collisions.

5.7.1 Comparison to theoretical models

The p_T-differential production cross section of D_s^+ mesons was compared to pQCD calculations based on the collinear factorisation in the GM-VFNS scheme [81–83] and on k_T-FACTORISATION [85]. Predictions from FONLL calculations are not available, since the fragmentation functions for the D_s^+ mesons are not included in the FONLL calculations.

Two predictions based on the GM-VFNS scheme with next-to-leading order (NLO)

	$p_{\rm T}$ range (GeV/c)	production cross section ratio in $\lvert y\rvert < 0.5$
$\sigma(\rm D_s^+)/\sigma(\rm D^0)$	$[2-24]$	$0.24 \pm 0.02(\rm stat) \pm 0.02(\rm syst) \pm 0.01(\rm BR)$
$\sigma(\rm D_s^+)/\sigma(\rm D^+)$	$[2-24]$	$0.56 \pm 0.06(\rm stat) \pm 0.05(\rm syst) \pm 0.03(\rm BR)$

Table 5.6: Ratios between $\rm D_s^+$, $\rm D^0$ and $\rm D^+$-meson $p_{\rm T}$-differential cross sections in pp collisions at $\sqrt{s} = 5.02$ TeV in the $p_{\rm T}$ interval of the $\rm D_s^+$-meson measurement.

accuracy with all-order resummation of next-to-leading logarithms are available with different prescriptions to regulate the divergences at low $p_{\rm T}$. In particular, in the GM-VFNS(SACOT-$m_{\rm T}$) [83] schema the divergences are regularised by the heavy-quark mass, while in the GM-VFNS(mod-$\mu_{\rm R,F}$) calculations different values of $\mu_{\rm R}$ and $\mu_{\rm F}$ are used at low $p_{\rm T}$. The charm-quark mass is set to $m_{\rm c} = 1.3$ GeV/c^2 and the CTEQ14 [75] PDFs are used in the GM-VFNS(mod-$\mu_{\rm R,F}$) calculation, while $m_{\rm c} = 1.5$ GeV/c^2 and the NNPDF3.1 [76] PDFs are used in the GM-VFNS(SACOT-$m_{\rm T}$) calculation. Also calculations based on $k_{\rm T}$-FACTORISATION with leading-order (LO) accuracy are available [85]. In this case the mass of the charm quark is set to $m_{\rm c} = 1.5$ GeV/c^2, and the MMHT2014 [166] PDFs are used.

The measured $p_{\rm T}$-differential $\rm D_s^+$-meson production cross section is superimposed to the $k_{\rm T}$-FACTORISATION (top panels) and $k_{\rm T}$-FACTORISATION (bottom-left panel) predictions in Fig. 5.22. In all the cases the experimental data lie on the upper edge of the uncertainty band of the predictions for $p_{\rm T} < 8$ GeV/c, while are closer to the central value for $p_{\rm T} > 8$ GeV/c. The theoretical uncertainties take into account the variation of the renormalisation and factorisation scales in case of GM-VFNS(SACOT-$m_{\rm T}$) and $k_{\rm T}$-FACTORISATION calculations, while only the variation of the renormalisation scale for GM-VFNS(mod-$\mu_{\rm R,F}$) calculations. In the $k_{\rm T}$-FACTORISATION uncertainty the charm-quark mass variation is also included.

The measured $p_{\rm T}$-differential production cross section of $\rm D_s^+$ mesons was also compared to the predictions obtained from the PYTHIA8 MC generator [34] with the Monash 2013 tune [167], with and without another tune that includes a model of string formation beyond the leading-colour approximation, called colour-reconnection (CR) mechanism [165]. The comparison between the experimental cross section and the values obtained with PYTHIA8 is shown in the bottom-right panel of Fig. 5.22. The coloured bands represent the statistical uncertainty on the PYTHIA8 predictions, which is due to the finite number of generated events (10^7 MB events for each configuration). The prediction from PYTHIA8 without CR mechanism is higher than the data by up to a factor 3. When enabling the CR mechanism instead PYTHIA8 describes the measured cross section for $p_{\rm T} < 3$ GeV/c and for $p_{\rm T} > 16$ GeV/c, while it still overestimates the measurement up to factor 2 in the intermediate $p_{\rm T}$ region. The reduction of the $\rm D_s^+$-production cross section when the CR mechanism is included reflects the enhancement of charm-baryon production needed to explain the recent measurements of the $\Lambda_{\rm c}^+$-baryon production in pp and p–Pb collisions by the ALICE and CMS Collaborations [119, 168].

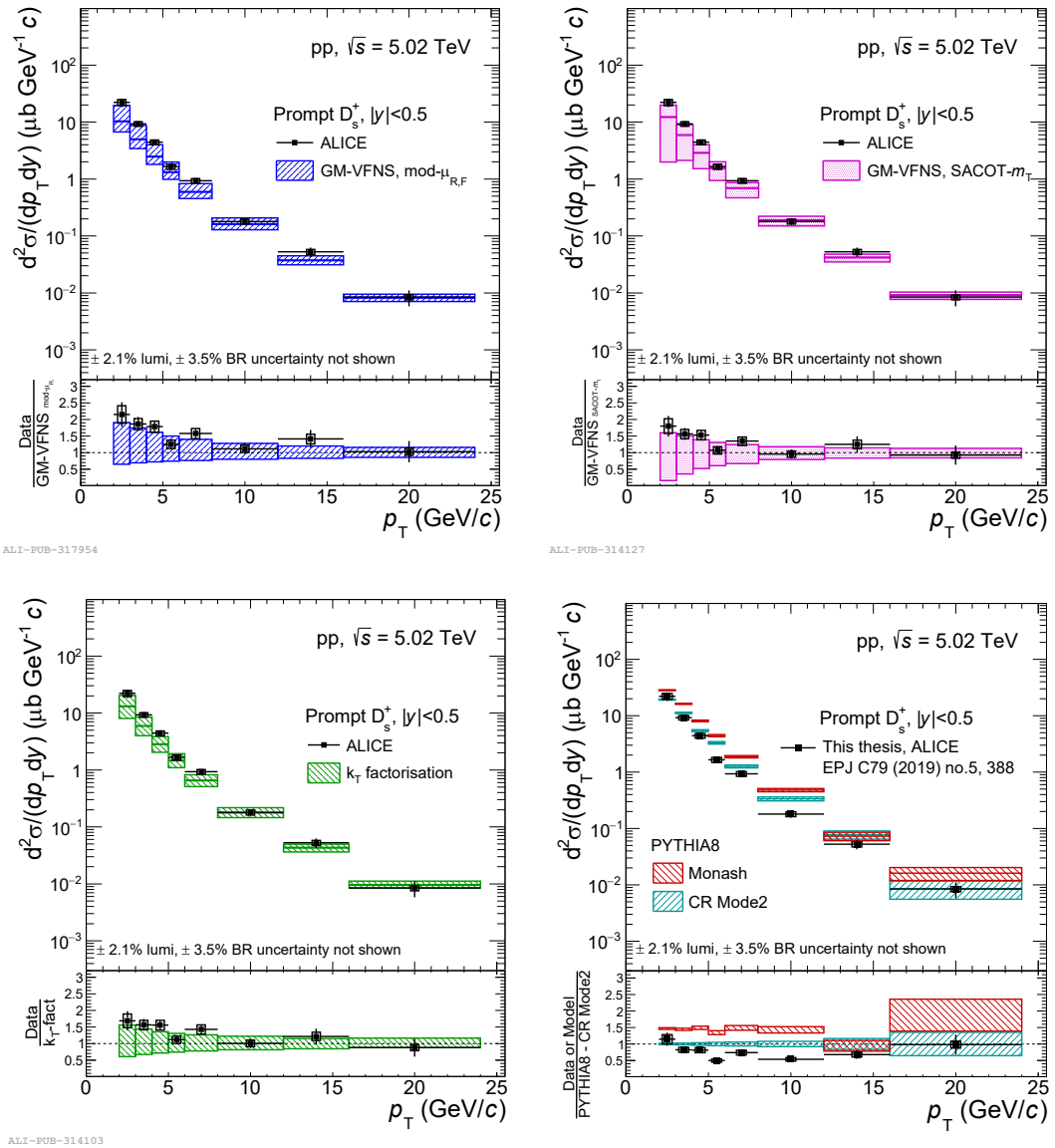

Figure 5.22: p_{T}-differential production cross section of $\mathrm{D_s^+}$ mesons in pp collisions at $\sqrt{s} = 5.02$ TeV compared to the GM-VFNS(mod-$\mu_{\mathrm{R,F}}$) [81, 82] (top-left panel), GM-VFNS(SACOT-m_{T}) [83] (top-right panel), LO k_{T}-FACTORISATION [85] (bottom-left panel) pQCD calculations, and PYTHIA8 simulation (bottom-right panel), with and without colour-reconnection mechanism [165]. The top and bottom-left panels are taken from Ref. [1].

Chapter 6

$\mathrm{D_s^+}$ and $\mathrm{D^+}$ nuclear modification factors in Pb–Pb and p–Pb collisions at $\sqrt{s_{\mathrm{NN}}} = 5.02$ TeV

In this Chapter, the measurement of the nuclear modification factor of prompt $\mathrm{D^+}$ mesons in p–Pb and Pb–Pb collisions at $\sqrt{s_{\mathrm{NN}}} = 5.02$ TeV and that of prompt $\mathrm{D_s^+}$ mesons in central Pb–Pb collisions at $\sqrt{s_{\mathrm{NN}}} = 5.02$ TeV are discussed. For the $\mathrm{D^+}$-meson nuclear modification factor, the sample of Pb–Pb collisions and that of p–Pb collisions collected by the ALICE experiment in 2015 and 2016 (see Sec. 4.1.1) were used. The two results were published in Ref. [3] and in Ref. [2], respectively. For the nuclear modification factor of $\mathrm{D_s^+}$ mesons the larger sample of central Pb–Pb collisions collected during November 2018 was exploited (see Sec. 4.1.1), and the measurement was approved as preliminary result by the ALICE Collaboration.

The nuclear modification factor was computed as

$$R_{\mathrm{AA}}(Q_{\mathrm{pA}}) = \frac{1}{\langle T_{\mathrm{AA(pA)}} \rangle} \cdot \frac{\mathrm{d}^2 N_{\mathrm{AA(pA)}}/\mathrm{d}p_{\mathrm{T}}\mathrm{d}y}{\mathrm{d}^2\sigma_{\mathrm{pp}}/\mathrm{d}p_{\mathrm{T}}\mathrm{d}y}, \tag{6.1}$$

where $\langle T_{\mathrm{AA(pA)}} \rangle$ is the nuclear overlap function for the centrality class of Pb–Pb (p–Pb) collisions considered, $\mathrm{d}\sigma_{\mathrm{pp}}/\mathrm{d}p_{\mathrm{T}}$ is the p_{T}-differential production cross section measured in pp collisions (see Eq. 5.1) and $\mathrm{d}N_{\mathrm{AA(pA)}}/\mathrm{d}p_{\mathrm{T}}$ is the p_{T}-differential corrected yield measured in Pb–Pb (p–Pb) collisions, defined as:

$$\frac{\mathrm{d}^2 N_{\mathrm{AA(pA)}}}{\mathrm{d}p_{\mathrm{T}}\mathrm{d}y} = \frac{\frac{1}{2} \cdot f_{\mathrm{prompt}} \cdot N_{\mathrm{raw}}(\mathrm{D} + \overline{\mathrm{D}})|_{|y_{\mathrm{lab}}|<y_{\mathrm{fid}}}}{\Delta p_{\mathrm{T}} \cdot c_{\Delta y} \cdot (\mathrm{Acc} \times \epsilon)_{\mathrm{prompt}} \cdot \mathrm{BR} \cdot N_{\mathrm{ev}}^{\mathrm{norm}}}, \tag{6.2}$$

which is analogous to the cross-section formula (see Eq. 5.1), except for the normalisation $N_{\mathrm{ev}}^{\mathrm{norm}}$, that correspond to the number of triggered events. The rapidity coverage of $\mathrm{d}N_{\mathrm{AA(pA)}}/\mathrm{d}p_{\mathrm{T}}$ in the centre-of-mass frame (y_{cms}) for Pb–Pb collisions coincides with the rapidity coverage in the laboratory frame ($|y_{\mathrm{lab}}| < 0.5$), while for p–Pb collisions is $-0.96 < y_{\mathrm{cms}} < 0.04$, due to the fact that the centre-of-mass frame moves in rapidity by $\Delta y_{\mathrm{cms}} = 0.465$ in the proton direction because of the the beam configuration adopted (4

System	Centrality class	$\langle T_{\mathrm{AA(pA)}} \rangle$ (mb^{-1})	$N_{\mathrm{events}} \times 10^6$	Year
Pb–Pb	0–10%	23.07 ± 0.44	88.7	2018
	30–50%	3.90 ± 0.11	10.4	2015
	60–80%	0.417 ± 0.014	20.8	
p–Pb	0–10%	0.172 ± 0.012	20.8	
	10–20%	0.158 ± 0.006	62.3	
	20–40%	0.137 ± 0.002	62.3	
	40–60%	0.102 ± 0.005	124.6	2016
	60–100%	0.046 ± 0.002	124.6	
			249.2	

Table 6.1: Number of events and average nuclear overlap function for the centrality classes used in the analyses of p–Pb and Pb–Pb collisions taken from Ref. [169].

TeV for protons and 1.58 TeV per nucleon for lead nuclei). This shift in rapidity is taken into account in the pp reference using FONNL calculations, given that the measurement in pp collisions was performed in $|y| < 0.5$.

The letter Q is used instead of R to indicate the centrality-dependent nuclear modification factor measured in p–Pb collisions, owing to the potential biases in the centrality determination introduced in Sec. 3.4.2, that could lead to a Q_{pA} value different from unity also in absence of nuclear effects. For p–Pb collisions, the nuclear modification of the D-meson p_{T} distributions was also studied via the measurement of the central-to-peripheral ratio,

$$Q_{\mathrm{CP}} = \frac{\langle T_{\mathrm{pA}}^{\mathrm{P}} \rangle}{\langle T_{\mathrm{pA}}^{\mathrm{C}} \rangle} \cdot \frac{\mathrm{d}^2 N_{\mathrm{pA}}^{\mathrm{C}} / \mathrm{d}p_{\mathrm{T}} \mathrm{d}y}{\mathrm{d}^2 N_{\mathrm{pA}}^{\mathrm{P}} / \mathrm{d}p_{\mathrm{T}} \mathrm{d}y}, \tag{6.3}$$

where C and P stand for *central* and *peripheral*, respectively. As will be described in Sec. 6.4, this variable is introduced to cancel out some of the systematic uncertainties that are in common among the different centrality classes and hence to improve the precision of the measurement.

The centrality classes defined for the analysis presented in this Chapter and the corresponding average nuclear overlap functions are reported in Table 6.1 [169]. The nuclear overlap function in p–Pb collisions was computed using the hybrid method described in Sec. 3.4.2. For the Q_{CP} the most peripheral class of p–Pb collisions (60–100%) was used for the denominator, while for the numerator the other centrality classes were used.

6.1 Kinematic, topological, and PID selections

The kinematical and topological selection criteria for $\mathrm{D^+}$ and $\mathrm{D_s^+}$ mesons were tuned with the same strategy adopted for the $\mathrm{D_s^+}$ mesons in pp collisions described in Sec. 5.1. The main difference with respect to the analysis performed in pp collisions is the larger

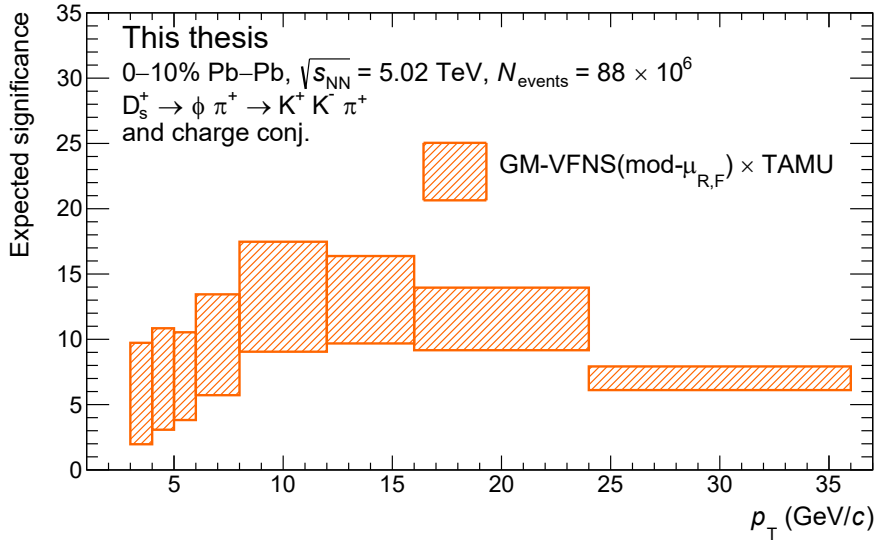

Figure 6.1: Expected significance for the extraction of the D_s^+ signal in the sample of the 10% most central Pb–Pb collisions collected in 2018. The signal is estimated using the GM-VFNS(mod-$\mu_{R,F}$) [81, 82] and TAMU [170] models.

charged-particle multiplicity, which leads to a much larger combinatorial background, especially in central Pb–Pb collisions. Therefore, much stricter selections should be applied in order to achieve a satisfactory statistical significance of the extracted signal and limit the computing resources needed to build and store the candidates. The expected significance was estimated using a fraction of the data for the combinatorial background (selecting candidates in the sidebands of the invariant-mass peak of the signal), and the signal obtained from the selection efficiencies estimated with a MC simulation and a model for the production yield (see Eq. 5.3). Unlike the pp case, model predictions that include nuclear effects have to be used in order to obtain a realistic expected signal.

Figure 6.1 shows the expected statistical significance for the extraction of the D_s^+ signal with the chosen set of selections in the sample of the 10% most central Pb–Pb collisions collected in 2018 as an example. The expected signal was obtained by multiplying the p_T-differential cross section predicted by the GM-VFNS(mod-$\mu_{R,F}$) model for pp collisions [81, 82], scaled by the average nuclear-overlap function $\langle T_{AA} \rangle$ of the 0–10% centrality class, and the R_{AA} from the TAMU model [170]. The coloured band includes the uncertainty on both the model predictions. The amount of combinatorial background was instead estimated from a fraction of the data by fitting the invariant-mass side-band distributions and subsequently scaling the value obtained to get the expectation for the full data sample, as described in Sec. 5.1.

For the analysis of Pb–Pb collisions, the threshold values of the selection variables were tuned for the D_s^+ mesons and for the D^+ mesons in each centrality class independently. For p–Pb collisions instead the combinatorial background does not vary dramatically from central to peripheral collisions and therefore the selection criteria were tuned for

p_{T} (GeV/c)	[1,2]	[2,3]	[3,4]	[4,5]	[5,6]	[6,7]	[7,8]	[8,10]	[10,12]	[12,16]	[16,24]	[24,36]	[36,50]
$\mathrm{D_s^+}$ Pb–Pb 0 – 10%													
ΔM(KK) (MeV/c^2)	-	-	5	5	5	5		5		5	5	5	-
L (μm) >	-	-	500	500	500	500		500		500	500	500	-
$L_{\mathrm{xy}}/\sigma_{\mathrm{xy}}$ >	-	-	9	9	9	8		8		6	6	6	-
σ_{vertex} (μm) <	-	-	200	250	250	250		250		250	350	350	-
$\cos\theta_{\mathrm{p}}$ >	-	-	0.985	0.980	0.980	0.980		0.980		0.980	0.980	0.980	-
$\cos\theta_{\mathrm{p}}^{\mathrm{xy}}$ >	-	-	0.995	0.995	0.990	0.990		0.990		0.980	0.980	0.980	-
$\lvert\cos^3\theta'(\mathrm{K})\rvert$ >	-	-	0.15	0.10	0.05	0.05		0.05		0.00	0.00	0.00	-
$\lvert d_0^{\mathrm{xy}}\rvert$ (μm) <	-	-	70	70	70	70		70		70	70	70	-
$\lvert D_0^{\mathrm{xy}}\rvert$ <	-	-	1.5	2.0	2.0	2.0		2.5		2.5	2.5	2.5	-
$\mathrm{D^+}$ Pb–Pb 0 – 10%													
L (μm) >	-	1200	1300	1300	1300	1400	1400	1400	1400	1600	1800	2000	2000
$L_{\mathrm{xy}}/\sigma_{\mathrm{xy}}$ >	-	15	14	12	12	12	12	12	10	10	10	10	10
σ_{vertex} (μm) <	-	180	200	200	200	200	240	240	240	240	240	340	340
$\cos\theta_{\mathrm{p}}$ >	-	0.998	0.998	0.998	0.997	0.997	0.995	0.992	0.992	0.990	0.990	0.990	0.990
$\cos\theta_{\mathrm{p}}^{\mathrm{xy}}$ >	-	0.999	0.999	0.999	0.998	0.998	0.997	0.994	0.994	0.990	0.990	0.990	0.990
$\lvert d_0^{\mathrm{xy}}\rvert$ (μm) <	-	90	60	60	60	60	60	60	60	60	60	80	80
$\lvert D_0^{\mathrm{xy}}\rvert$ <	-	2.0	2.0	2.0	2.0	2.0	2.0	2.0	2.0	2.0	2.0	2.5	2.5
$\mathrm{D^+}$ Pb–Pb 30 – 50%													
L (μm) >	-	800	1000	1000	1000	1200	1200	1200	1200	1200	1400	1400	-
$L_{\mathrm{xy}}/\sigma_{\mathrm{xy}}$ >	-	12	12	12	12	10	10	10	9	9	8	8	-
σ_{vertex} (μm) <	-	200	220	220	220	220	220	240	240	240	240	340	-
$\cos\theta_{\mathrm{p}}$ >	-	0.996	0.996	0.995	0.995	0.995	0.995	0.990	0.990	0.990	0.980	0.970	-
$\cos\theta_{\mathrm{p}}^{\mathrm{xy}}$ >	-	0.996	0.996	0.995	0.995	0.995	0.995	0.990	0.990	0.990	0.980	0.970	-
$\lvert d_0^{\mathrm{xy}}\rvert$ (μm) <	-	80	60	60	60	60	60	60	60	60	60	60	-
$\lvert D_0^{\mathrm{xy}}\rvert$ <	-	1.5	1.5	2.0	2.0	2.0	2.0	2.0	2.0	2.0	2.5	2.5	-
$\mathrm{D^+}$ Pb–Pb 60 – 80%													
L (μm) >	-	600	600	600	800	1000	1000	1000	1200	1200	1200	-	-
$L_{\mathrm{xy}}/\sigma_{\mathrm{xy}}$ >	-	12	12	11	10	10	10	7	7	6	4	-	-
σ_{vertex} (μm) <	-	280	280	280	280	280	280	280	300	300	340	-	-
$\cos\theta_{\mathrm{p}}$ >	-	0.992	0.992	0.992	0.992	0.990	0.990	0.985	0.985	0.980	0.970	-	-
$\cos\theta_{\mathrm{p}}^{\mathrm{xy}}$ >	-	0.994	0.994	0.994	0.994	0.992	0.992	0.990	0.990	0.985	0.970	-	-
$\lvert d_0^{\mathrm{xy}}\rvert$ (μm) <	-	100	100	100	100	90	80	80	80	80	80	-	-
$\lvert D_0^{\mathrm{xy}}\rvert$ <	-	2.0	2.0	2.0	2.5	2.5	2.5	2.5	2.5	3.0	3.0	-	-
$\mathrm{D^+}$ p–Pb													
L (μm) >	500	600	600	600	600	600	600	800	800	800	1000	-	-
$L_{\mathrm{xy}}/\sigma_{\mathrm{xy}}$ >	10	8	8	8	8	8	8	8	8	7	7	-	-
σ_{vertex} (μm) <	350	350	350	350	350	350	350	350	350	400	400	-	-
$\cos\theta_{\mathrm{p}}$ >	0.992	0.990	0.985	0.985	0.985	0.985	0.985	0.985	0.985	0.980	0.980	-	-
$\cos\theta_{\mathrm{p}}^{\mathrm{xy}}$ >	0.992	0.990	0.985	0.985	0.985	0.985	0.985	0.985	0.985	0.980	0.980	-	-
$\lvert D_0^{\mathrm{xy}}\rvert$ <	100	100	100	100	100	100	100	100	100	100	100	-	-

Table 6.2: Topological and kinematical selections applied to $\mathrm{D_s^+}$ and $\mathrm{D^+}$ candidates in p–Pb and Pb–Pb collisions at $\sqrt{s_{\mathrm{NN}}} = 5.02$ TeV.

the MB sample and applied to all the centrality classes. The chosen selection criteria for each D-meson species, colliding system, and centrality class are reported in Table 6.2 for the p_{T} ranges of the various measurements.

The PID selection strategy applied to further reduce the combinatorial background was different for $\mathrm{D^+}$ and $\mathrm{D_s^+}$ mesons. Given the longer mean proper decay length, the selections based on the displaced decay-vertex topology of $\mathrm{D^+}$ mesons are more effective than for the $\mathrm{D_s^+}$ mesons and therefore a looser PID selection can be applied. Hence, the conservative PID strategy was applied for $\mathrm{D^+}$-meson candidates with $p_{\mathrm{T}} > 2$ GeV/c, while the strong strategy was applied only to the $\mathrm{D^+}$-meson candidates with $1 < p_{\mathrm{T}} < 2$ GeV/c. Given the too large combinatorial background in Pb–Pb collisions, the extraction of $\mathrm{D^+}$ signal in the range $1 < p_{\mathrm{T}} < 2$ GeV/c was not possible. For the $\mathrm{D_s^+}$ mesons instead the strong PID strategy was adopted for candidates having $p_{\mathrm{T}} < 8$ GeV/c, while the conservative PID strategy for $p_{\mathrm{T}} > 8$ GeV/c. This selection strategy allowed for a satisfactory signal extraction down to $p_{\mathrm{T}} = 3$ GeV/c.

6.2 Analysis of $\mathrm{D_s^+}$ mesons in central Pb–Pb collisions

6.2.1 Raw-yield extraction

The raw $\mathrm{D_s^+}$ yields were extracted via fits to the $M(\mathrm{KK}\pi)$ invariant-mass distributions obtained after the application of the selections reported in Sec. 6.1. The signal was modelled with a Gaussian function, while the combinatorial background with an exponential function. As for the analysis in pp collisions, an additional Gaussian term to describe the peak arising from the $\mathrm{D^+} \to \phi\pi^+ \to \mathrm{K^-K^+}\pi^+$ decay was added in the fit function. All the parameters were let free in the fits.

Figure 6.2 shows the fits to the $\mathrm{D_s^+}$-candidate invariant-mass distributions from the lowest (top-left panel) to the highest (bottom-right panel) p_{T} interval of the analysis. The signal-to-background ratio varies from about 0.03 at low p_{T} to a maximum of 1.14 at high p_{T}. The statistical significance was found to be higher than 6 in each p_{T} interval of the analysis.

6.2.2 Acceptance and efficiency corrections

The acceptance-times-efficiency (Acc $\times$ ϵ) factors were computed using the MC simulations described in Sec. 4.3.

The efficiencies were evaluated in a centrality class corresponding to the one used in data in terms of charged-particle multiplicity at mid-rapidity, hence of detector occupancy. The PYTHIA simulation was performed in $p_{\mathrm{T}}^{\mathrm{hard}}$ bins (see Sec. 2.1), to increase the number of generated $\mathrm{D_s^+}$ at high p_{T} and have a sufficient statistical precision. This procedure implies a p_{T} shape harder than the natural one, and therefore a weighting procedure was applied to the p_{T} distribution of $\mathrm{D_s^+}$ mesons in the MC simulation. In particular, the $\mathrm{D_s^+}$-meson p_{T} distribution in the 0–10% centrality class was weighted to reproduce the shape of the p_{T}-differential cross section predicted by FONLL [79, 80] calculations for non-strange D mesons, multiplied by the R_{AA} provided by the TAMU model [170] in the same centrality class. Figure 6.3 shows the (Acc $\times$ ϵ) factors of prompt and feed-down $\mathrm{D_s^+}$

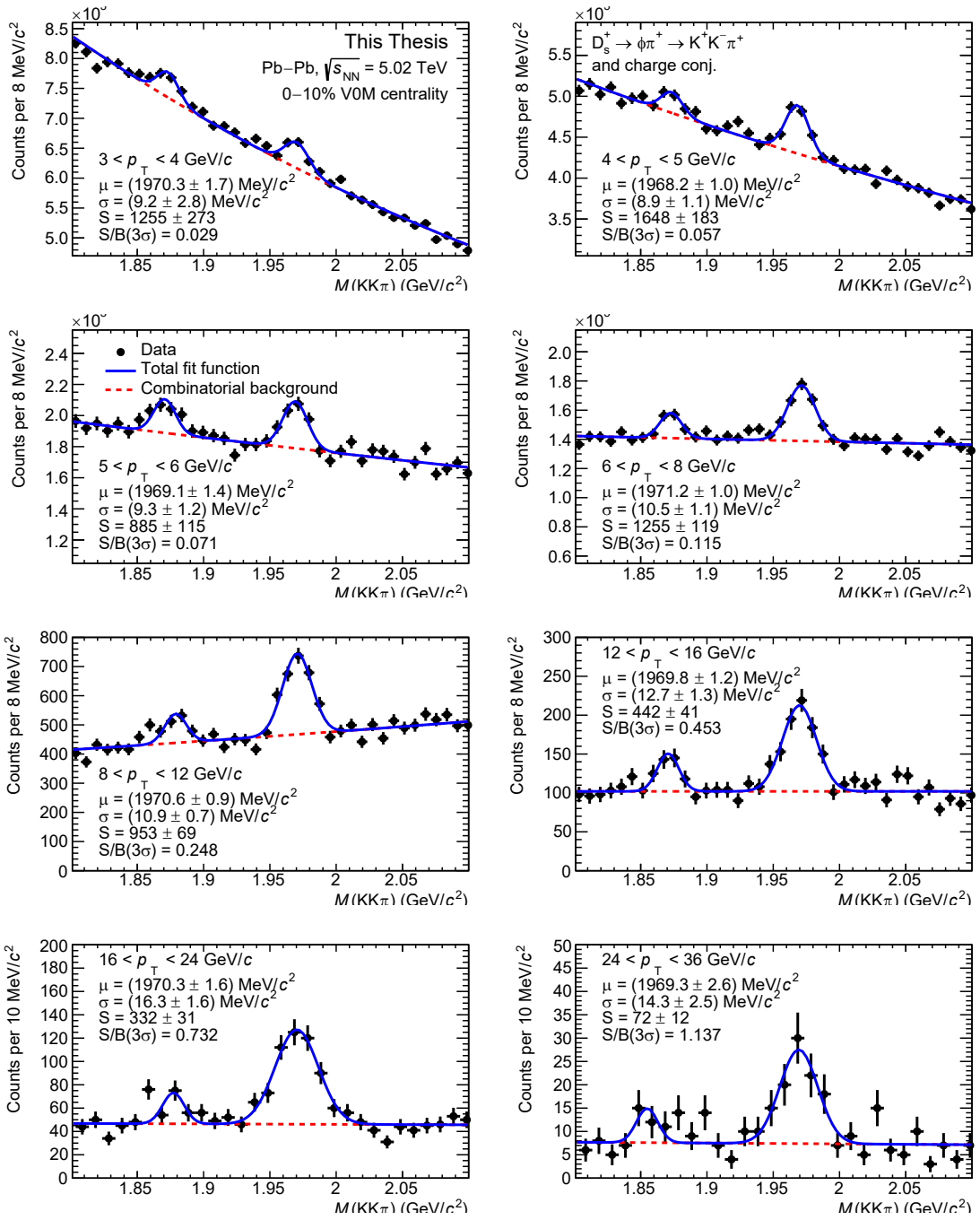

Figure 6.2: Fits to the invariant-mass distributions of D_s^+-meson candidates in the eight p_T intervals of the analysis for the 10% most central Pb–Pb collisions at $\sqrt{s_{NN}} = 5.02$ TeV. The solid blue and the dotted red curves represent the total and the combinatorial-background fit functions, respectively.

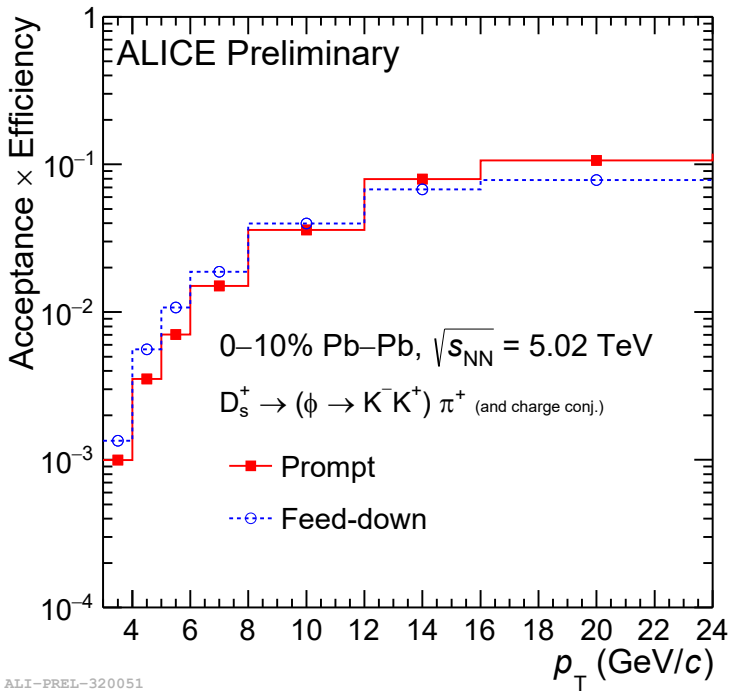

Figure 6.3: Acceptance-times-efficiency factors of prompt and feed-down $\mathrm{D_s^+}$ as a function of p_{T} in the 0–10% most central Pb–Pb collisions at $\sqrt{s_{\mathrm{NN}}} = 50.2$ TeV.

mesons as a function of p_{T}. The efficiency of feed-down $\mathrm{D_s^+}$ mesons is typically similar or even lower than that of prompt D mesons thanks to the selections on the d_0^{xy} and D_0^{xy} variables, that select preferentially prompt D mesons thus reducing the uncertainty on the feed-down subtraction.

6.2.3 Fraction of prompt $\mathrm{D_s^+}$ mesons

The fraction of prompt $\mathrm{D_s^+}$ mesons in the measured raw yield was computed with a similar strategy as the one adopted for the measurement of the prompt $\mathrm{D_s^+}$-meson production in pp collisions:

$$
\begin{aligned}
f_{\mathrm{prompt}} &= 1 - \frac{N_{\mathrm{raw}}^{\text{feed-down}}(\mathrm{D_s^\pm})}{N_{\mathrm{raw}}(\mathrm{D_s^\pm})} = \\
&= 1 - \langle T_{\mathrm{AA}} \rangle \cdot R_{\mathrm{AA}}^{\text{feed-down}} \left(\frac{\mathrm{d}^2\sigma}{\mathrm{d}p_{\mathrm{T}}\mathrm{d}y} \right)_{\text{FONLL, EvtGen}}^{\text{feed-down}} \times \\
&\times \frac{(\mathrm{Acc} \times \epsilon)_{\text{feed-down}} \cdot c_{\Delta y}\ \Delta p_{\mathrm{T}} \cdot \mathrm{BR} \cdot N_{\mathrm{ev}}^{\mathrm{norm}}}{\frac{1}{2} \cdot N_{\mathrm{raw}}(\mathrm{D_s^\pm})} .
\end{aligned}
\tag{6.4}
$$

In addition to Eq. 5.5, the p_{T}-differential cross section of feed-down D mesons is multiplied by the nuclear overlap function, $\langle T_{\mathrm{AA}} \rangle$, and the nuclear modification factor of feed-down D

mesons, $R_{\mathrm{AA}}^{\text{feed-down}}$. Moreover, the integrated luminosity, $\mathcal{L}_{\mathrm{int}}$, is replaced by the number of analysed events, $N_{\mathrm{ev}}^{\mathrm{norm}}$.

The nuclear modification of feed-down D mesons was not measured and therefore a hypothesis on its value was necessary. For the $\mathrm{D_s^+}$ meson in central Pb–Pb collisions the hypothesis $R_{\mathrm{AA}}^{\text{feed-down}} = R_{\mathrm{AA}}^{\text{prompt}}$ was adopted to take into account both the reduced suppression measured by the CMS Collaboration for feed-down J/ψ and $\mathrm{D^0}$ mesons compared to that of prompt D mesons [105, 106, 171], and the enhancement of strange quarks and the possible modification of the charm-quark hadronisation in the medium, which are predicted to lead to a higher $\mathrm{D_s^+}$-meson R_{AA} compared to that of D mesons without strange-quark content [170].

The hypotheses on the nuclear modification factor of feed-down $\mathrm{D_s^+}$ mesons were varied within the model uncertainty bands and the available data uncertainties in order to estimate a systematic uncertainty, as will be discussed in Sec. 6.4.7.

6.2.4 Proton–proton reference

The measurement of the p_{T}-differential production cross section in pp collisions presented in this Thesis (see Chapter 5) was used as pp reference for the measurement of the $\mathrm{D_s^+}$-meson R_{AA} in central Pb–Pb collisions.

Because of the reduced p_{T} coverage of the pp measurement compared to the Pb–Pb one, an extrapolation procedure was adopted to extend the cross section in the p_{T} intervals where the measurement was not available. In particular, the extrapolation consisted in rescaling the FONLL prediction to match the data points in the measured p_{T} interval:

$$(\mathrm{d}\sigma/\mathrm{d}p_{\mathrm{T}})_{\mathrm{extrap}} = \kappa \cdot (\mathrm{d}\sigma/\mathrm{d}p_{\mathrm{T}})_{\mathrm{FONLL}} \tag{6.5}$$

where κ is the factor obtained by fitting the ratio between the measured p_{T}-differential cross section and that predicted by FONLL with a constant function. The uncertainty was estimated as suggested in Ref [172]. The same procedure was therefore repeated by varying (i) the renormalisation (μ_{R}) and factorisation (μ_{F}) scales in the range $0.5 < \mu_{\mathrm{R}}$ (μ_{F})$/\mu_0 < 2$, being μ_0 the default value of μ_{R} and μ_{F} in the central FONLL prediction, (ii) the mass of the charm quark m_{c} between 1.3 and 1.7 GeV/c^2, and (iii) considering the uncertainty on the PDFs. The fits to the data-to-theory ratios for the $\mathrm{D_s^+}$ mesons in pp collisions at $\sqrt{s} = 5.02$ TeV are reported in the left panel of Fig. 6.4. The pp reference with the extrapolated point for the $24 < p_{\mathrm{T}} < 36$ GeV/c interval is shown in the right panel of the same Figure.

The systematic uncertainty was evaluated as the envelope of the values of the κ parameters obtained from the different fits.

6.3 Analysis of $\mathrm{D^+}$ mesons in p–Pb and Pb–Pb collisions

6.3.1 Raw-yield extraction

The raw $\mathrm{D^+}$ yields were extracted via fits to the $M(\mathrm{K}\mathrm{K}\pi)$ invariant-mass distributions obtained after the application of the selections reported in Sec. 6.1. The signal was modelled with a Gaussian function, while the combinatorial background with an exponential

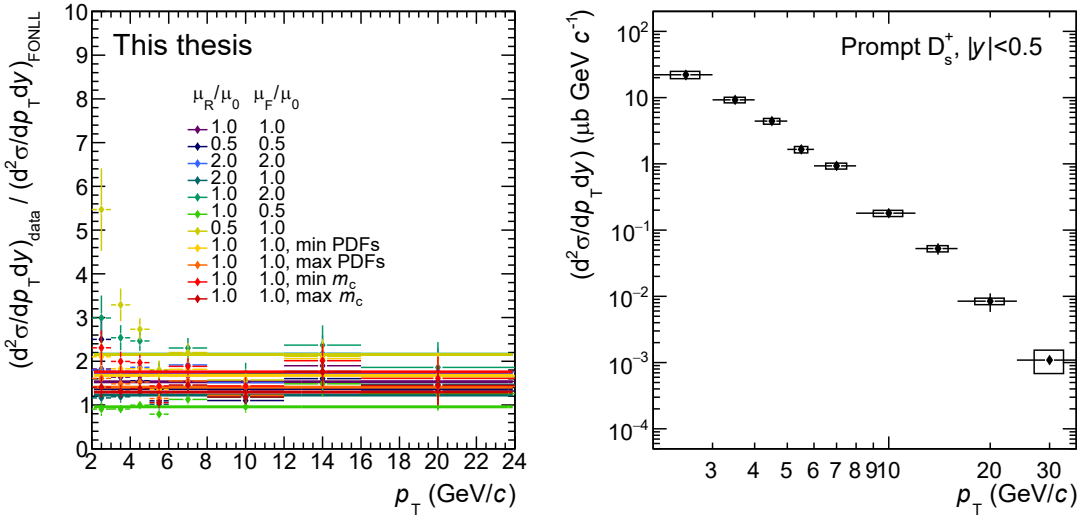

Figure 6.4: Left: ratios of measured p_T-differential cross section of prompt D_s^+ mesons and FONLL prediction with different parameters. The curves represent the linear fits performed to obtain the extrapolated cross section for $24 < p_T < 36$ GeV/c. Right: pp reference for the measurement of the D_s^+-meson R_{AA} in the 10% most central Pb–Pb collisions.

function. All the parameters were let free in the fits, except for the width of the Gaussian describing the D^+ signal in p–Pb collisions, which was fixed to the value extracted from the Minimum Bias sample for each p_T bin to reduce the statistical fluctuations among the centrality classes. The width was not fixed to the centrality-integrated values in Pb–Pb collisions, since the large variation of detector occupancy between peripheral and central Pb–Pb collisions could lead to a different tracking performance and hence to a different p_T (invariant-mass) resolution.

The top panels of Figure 6.5 show three examples of fits to the D^+-candidate invariant-mass distributions in three different p_T interval of the analysis, while the bottom panels show the fits to the D^+-candidate invariant-mass distributions for the transverse-momentum interval $4 < p_T < 5$ GeV/c from peripheral p–Pb collisions (top-left panel) to central Pb–Pb collisions (bottom-right panel).

In Fig. 6.6 the per-event raw yield (left panel), the statistical significance of the extracted signal (middle panel), and the signal-to-background ratio as a function of p_T of D^+ mesons are compared to those of D_s^+ mesons.

The per-event raw yield of D^+ mesons is larger in central and semi-central Pb–Pb collisions than peripheral Pb–Pb and p–Pb collisions despite the tighter selection criteria, due to the sensibly higher production cross section. The per-event raw yield in the 60–80% centrality class of Pb–Pb collisions is similar to that measured in p–Pb collisions, due to an interplay between larger production cross section and lower selection efficiency. A larger D^+-meson raw yield is observed in central compared to peripheral p–Pb collisions,

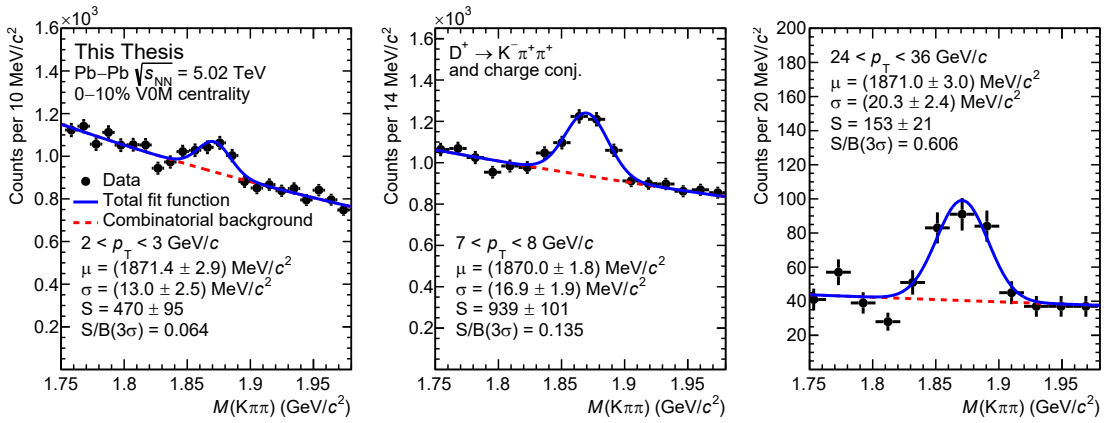

(a) Fits to the invariant-mass distributions of D^+-meson candidates in three different p_T intervals in the 10% most central Pb–Pb collisions at $\sqrt{s_{NN}} = 5.02$ TeV

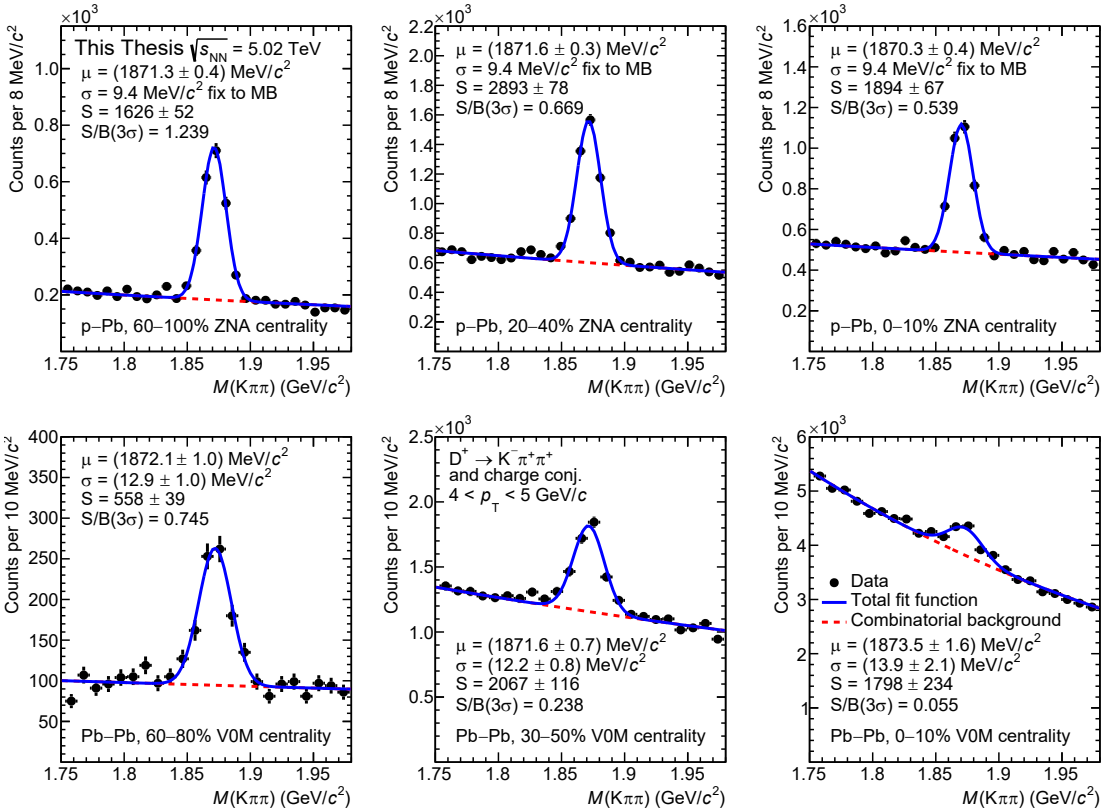

(b) Fits to the invariant-mass distributions of D^+-meson candidates with $4 < p_T < 5$ GeV/c in Pb–Pb and p–Pb collisions at $\sqrt{s_{NN}} = 5.02$ TeV

Figure 6.5: Fits to the invariant-mass distributions of D^+-meson candidates. The solid blue and the dotted red curves represent the total and the combinatorial-background fit functions, respectively.

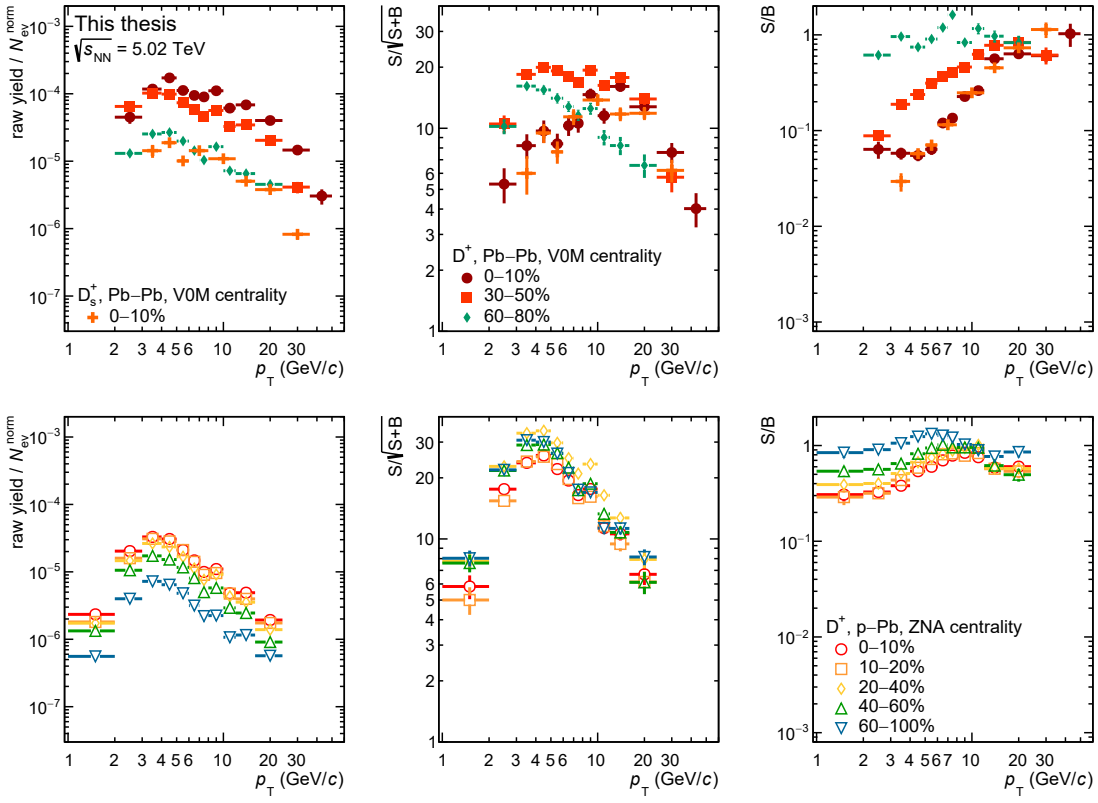

Figure 6.6: Raw yield per event (left panel), statistical significance of the extracted signal (middle panel), and signal-to-background ratio (right panel) of D_s^+ and D^+ mesons in Pb–Pb collisions at $\sqrt{s_{NN}} = 5.02$ TeV (top panels) and D^+ mesons in p–Pb collisions at $\sqrt{s_{NN}} = 5.02$ TeV (bottom panels).

as expected since the same selection criteria are applied in all the centrality classes of p–Pb collisions, and thus the efficiency is similar, while $\langle N_{coll} \rangle$ increases from peripheral to central collisions. The D_s^+ per-event raw yield in central Pb–Pb collisions is significantly smaller than that of D^+ mesons in the same centrality class because of lower production cross section, BR, and selection efficiency.

The statistical significance varies between 4 and 35, depending on the D-meson species, centrality class and p_T interval.

For $p_T < 10$ GeV/c the signal-to-background ratio varies mildly from p–Pb to peripheral Pb–Pb collisions, while decreases significantly in semi-central and central Pb–Pb collisions. For $p_T > 10$ GeV/c instead the signal-to-background ratio is similar for all the D-meson species and centrality classes.

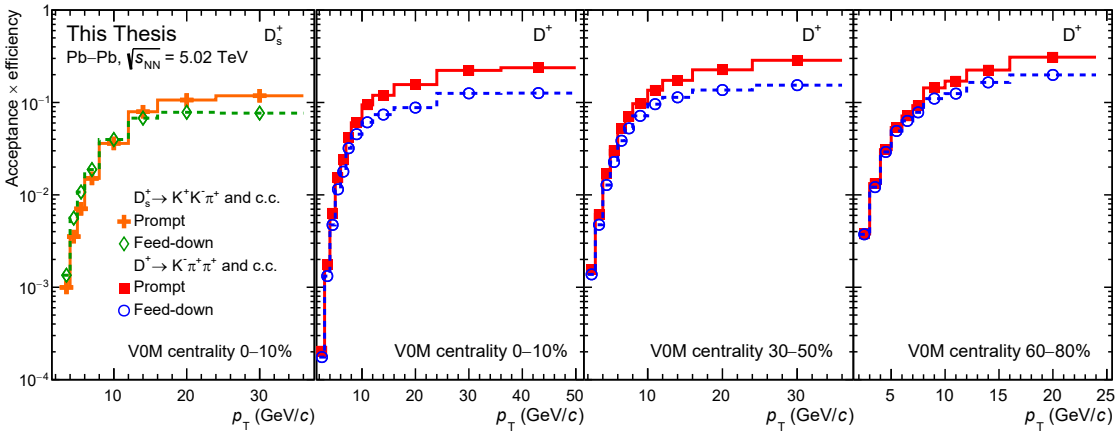

Figure 6.7: Acceptance-times-efficiency factors of prompt and feed-down D_s^+ (left panel) and D^+ (other panels) mesons as a function of p_T for the different centrality classes in Pb–Pb collisions at $\sqrt{s_{NN}} = 5.02$ TeV.

6.3.2 Acceptance and efficiency corrections

The acceptance-times-efficiency (Acc × ϵ) factors of D^+ mesons were computed using the MC simulations described in Sec. 4.3.

As for the D_s^+ mesons (see Sec. 6.2.2), the p_T distributions of D^+ mesons in Pb–Pb collisions were weighted to reproduce the natural ones. For the D^+ mesons in the 0–10% centrality class, the shape of D^0 mesons measured in the same centrality class in finer p_T bins was used. This was justified by the observation of a flat ratio between the p_T-differential yields of D^+ and D^0 mesons from previous measurements [104]. For the 30–50% centrality class, FONLL calculations multiplied by the R_{AA} predicted by the BAMPS model [173] were used, while for the 60–80% centrality class where the R_{AA} is nearly flat, only FONLL calculations were used. Figure 6.7 shows the (Acc × ϵ) factors of D^+ mesons in the centrality classes of the analysis (middle and right panels), compared to those of the D_s^+ mesons in the central collisions (left panel). The efficiency of D^+ mesons increases from central to peripheral Pb–Pb collisions, since more stringent selections are needed in the most central collisions in order to extract the signal. Similarly, the efficiency of D_s^+ mesons is typically lower, since tighter selections are needed to separate the D_s^+ signal from the combinatorial background, owing to their shorter mean proper decay length compared to that of D^+ mesons (see Table 4.2).

For p–Pb collisions, the shape of the D-meson p_T distribution is consistent with the FONLL prediction, which describes the experimental data within the uncertainties [1], therefore the FONLL p_T shape was used. In addition, since the selection efficiency depends on the charged-particle multiplicity, for each centrality class the events in the MC simulation were weighted to reproduce the distribution of the number of tracklets (track-segments reconstructed using the two SPD layers as described in Sec. 3.5), $N_{\text{tracklets}}$,

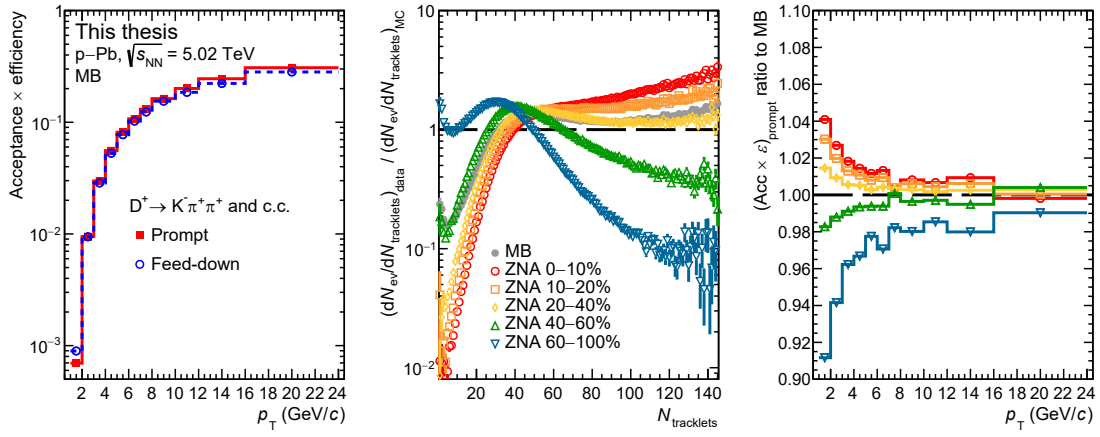

Figure 6.8: Left: (Acc × ϵ) factors of prompt and feed-down D^+ mesons in Minimum Bias p–Pb collisions at $\sqrt{s_{NN}}$ = 5.02 TeV. Middle: ratios of $N_{tracklets}$ distributions in data and in the multiplicity-integrated MC for the different centrality classes defined in the analysis. Right: ratios of (Acc × ϵ) factors for each centrality class with respect to the one for the Minimum Bias sample.

observed in the data for events having at least a D^0-meson candidate in the invariant-mass region of the signal defined as $|M - M(D^0)| < 3\sigma$, where σ is the invariant-mass peak resolution. The requirement of the D-meson candidate was motivated by the fact that events with charm production have on average higher multiplicity than soft events [174]. The (Acc × ϵ) factor of prompt and feed-down D^+ mesons in MB p–Pb collisions is reported in the left panel of Fig. 6.8. The middle panel of the same Figure shows the ratio of the $N_{tracklets}$ distributions in data for each centrality class and that in the MC simulation, while the right panel shows the ratio between the (Acc × ϵ) of prompt D^+ mesons in each centrality class with respect to the one in the MB sample, obtained after the weighting procedure of the $N_{tracklets}$ distribution in the multiplicity-integrated MC simulation. As expected, the efficiency is lower for more peripheral events due to the worse resolution on the determination of the primary-vertex position, given the lower charged-particle multiplicity.

6.3.3 Fraction of prompt D^+ mesons

The fraction of prompt D^+ mesons was calculated using Eq. **??**, where for p–Pb collisions $R_{AA}^{\text{feed-down}}$ was replaced by $Q_{pA}^{\text{feed-down}}$.

For D^+ mesons having $3 < p_T < 24$ GeV/c in the 0–10% and 30–50% centrality classes of Pb–Pb collisions the central hypothesis considered was $R_{AA}^{\text{feed-down}} = 2 \cdot R_{AA}^{\text{prompt}}$, owing to the reduced suppression observed for feed-down J/ψ and D^0 mesons compared to that of prompt D mesons [105, 106, 171]. For $p_T < 3$ GeV/c and $p_T > 24$ GeV/c and for the 60–80% centrality class model calculations predict a smaller difference between the R_{AA} of prompt and feed-down charmed mesons [170, 175] and therefore $R_{AA}^{\text{feed-down}} = 1.5 \cdot R_{AA}^{\text{prompt}}$

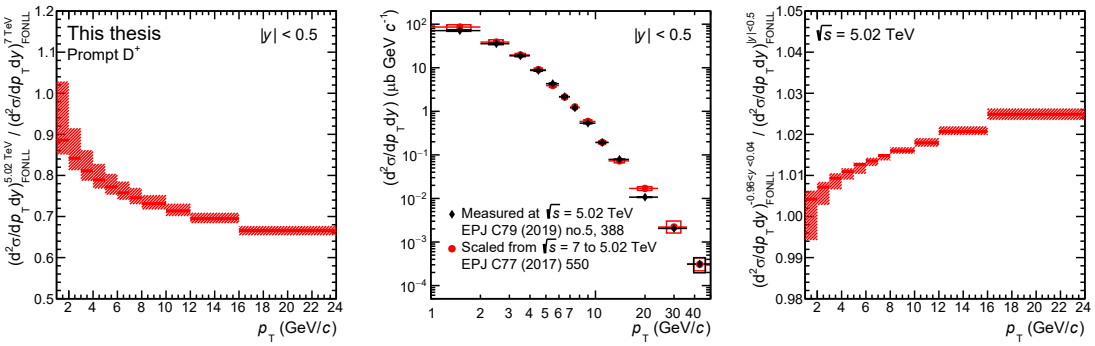

Figure 6.9: Left: Scaling factor for the p_{T}-differential cross section of prompt $\mathrm{D^+}$ mesons at mid rapidity ($|y| < 0.5$) from 7 TeV to 5.02 obtained with FONLL calculations. Middle: Comparison between measured and scaled p_{T}-differential cross section of prompt $\mathrm{D^+}$ mesons in $|y| < 0.5$ at $\sqrt{s} = 5.02$ TeV. Right: scaling factor for the p_{T}-differential cross section of prompt $\mathrm{D^+}$ mesons at $\sqrt{s} = 5.02$ TeV from the rapidity coverage in the centre of mass of pp collisions ($|y| < 0.5$) to that of p–Pb collisions ($-0.96 < y < 0.04$) obtained with FONLL calculations.

was used.

In p–Pb collisions the nuclear modification factor of feed-down $\mathrm{D^+}$ mesons was assumed to be equal to that of prompt mesons, $Q_{\mathrm{pA}}^{\text{feed-down}} = Q_{\mathrm{pA}}^{\text{prompt}}$, on the basis of calculations including the Colour Glass Condensate formalism [176], or the nuclear modification of the PDFs (EPPS09 nPDF [92]), and the measurement of the nuclear modification factor of B mesons performed by the CMS Collaboration [177].

6.3.4 Proton–proton reference

Different pp references where used for the $\mathrm{D^+}$-meson R_{AA} and Q_{pA} measurements, depending on the availability of pp measurements when the different analyses were performed.

The measurement of the p_{T}-differential production cross section in pp collisions at $\sqrt{s} = 7$ TeV published in Ref. [158] scaled to $\sqrt{s} = 5.02$ TeV with the ratio of the FONLL predictions at the two energies was used for the R_{AA} of $\mathrm{D^+}$ mesons with $|y| < 0.5$ in Pb–Pb collisions collected in 2015:

$$(\mathrm{d}\sigma/\mathrm{d}p_{\mathrm{T}})^{5.02\ \mathrm{TeV}}_{\mathrm{scaled}} = \frac{(\mathrm{d}\sigma/\mathrm{d}p_{\mathrm{T}})^{5.02\ \mathrm{TeV}}_{\mathrm{FONLL}}}{(\mathrm{d}\sigma/\mathrm{d}p_{\mathrm{T}})^{7\ \mathrm{TeV}}_{\mathrm{FONLL}}} \cdot (\mathrm{d}\sigma/\mathrm{d}p_{\mathrm{T}})^{7\ \mathrm{TeV}}_{\mathrm{measured}}. \tag{6.6}$$

The left panel of Fig 6.9 shows the scaling factor obtained from FONLL predictions as a function of p_{T}. The uncertainty was estimated as suggested in Ref [172] by varying the renormalisation and factorisation scales, the mass of the charm quark, and considering the uncertainty on the PDFs. The middle panel of the same Figure shows the comparison between the p_{T}-differential production cross section scaled to $\sqrt{s} = 5.02$ TeV with the aforementioned procedure and the one measured at the same centre-of-mass energy by

the ALICE Collaboration [1]. The two highest $p_{\rm T}$ intervals of the pp reference were extrapolated as described for the $\rm D_s^+$ meson in Sec. 6.2.4. The measured cross section was not used since it was not available when the sample of Pb–Pb collisions at $\sqrt{s_{\rm NN}} = 5.02$ TeV collected in 2015 was analysed.

For the $\rm D^+$-meson $Q_{\rm pA}$, the pp reference was extracted from the cross section measured in pp collisions at $\sqrt{s} = 5.02$ TeV with a correction for the rapidity coverage in the centre-of-mass frame of the measurement in p–Pb collisions ($-0.96 < y_{\rm cms} < 0.04$). The rapidity-coverage correction factor is shown in the right panel of Fig. **??** was obtained similarly to the one for the $\sqrt{s}$-scaling, by dividing the $p_{\rm T}$-differential cross sections obtained with FONLL calculations in the two rapidity ranges:

$$(\mathrm{d}\sigma/\mathrm{d}p_{\rm T})^{-0.96<y_{\rm cms}<0.04}_{\rm scaled} = \frac{(\mathrm{d}\sigma/\mathrm{d}p_{\rm T})^{-0.96<y_{\rm cms}<0.04}_{\rm FONLL}}{(\mathrm{d}\sigma/\mathrm{d}p_{\rm T})^{|y_{\rm cms}|<0.5}_{\rm FONLL}} \cdot (\mathrm{d}\sigma/\mathrm{d}p_{\rm T})^{|y_{\rm cms}|<0.5}_{\rm measured}. \tag{6.7}$$

The same procedure adopted for the evaluation of the uncertainty in case of the $\sqrt{s}$-scaling was also applied to the $y_{\rm cms}$-scaling.

6.4 Systematic uncertainties

In this Section, the evaluation of the systematic uncertainties on the measurement of the $R_{\rm AA}(Q_{\rm pA})$ of $\rm D^+$ and $\rm D_s^+$ mesons will be discussed. Most of the sources of systematic uncertainty are in common with those affecting the analysis of the $p_{\rm T}$-differential cross section in pp collisions (see Sec. 5.6), therefore this Section will be focused more on the difference with respect to the pp analysis and on the dependence of the systematic uncertainties on the D-meson species, the collision system, and the centrality class.

6.4.1 Raw-yield extraction

The systematic uncertainty on the raw-yield extraction was estimated with the same multi-trial approach described in Sec. 5.6.1. The fits to the invariant-mass distributions of $\rm D^+$ and $\rm D_s^+$ candidates were repeated with all the possible combinations of the varied fit configurations, which include variations of (i) the functional form used for the description of the combinatorial background (linear, parabolic and exponential), (ii) the lower and the upper invariant-mass fit limits, and (iii) the invariant-mass bin width. The latter variation was performed as a consistency check of the result to ensure that the chosen invariant-mass bin width did not introduce a bias in the measurement, and it was found not to contribute to the overall systematic uncertainty. In addition, the fits were repeated with the Gaussian width and mean of the signal as free parameters and fixed to the values extracted from the MC simulation (from the MB sample) for Pb–Pb (p–Pb) collisions. Finally, to test the stability of the result obtained with the Gaussian-shaped signal, the raw yields were extracted by integrating the invariant-mass distribution after subtracting the background estimated from a fit to the side-bands invariant-mass distribution.

The systematic uncertainty was then evaluated from the RMS of the distribution obtained from the multi-trial technique and the shift of the mean of this distribution with respect to the raw-yield value obtained with the default configuration. The sum

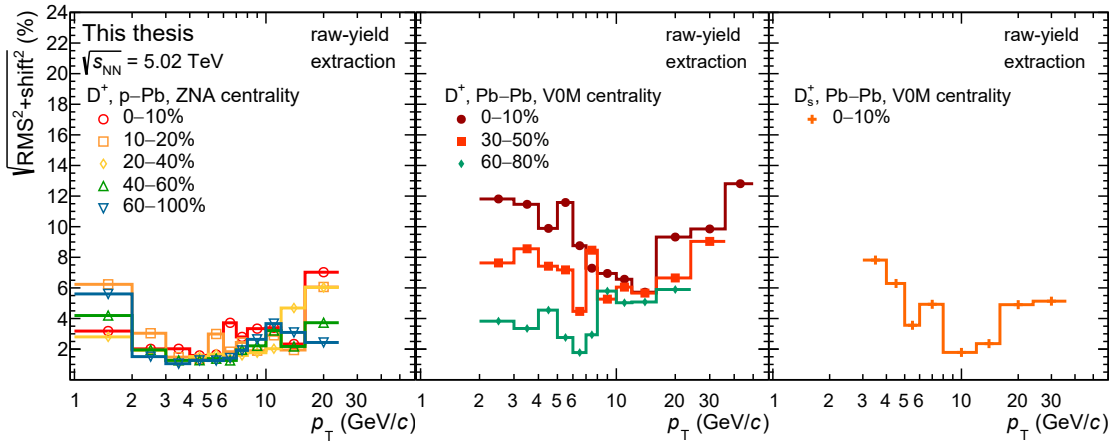

Figure 6.10: Sum in quadrature of RMS and shift with respect to the central value of the raw-yield distributions obtained from the multi-trial technique of D^+ mesons in p–Pb collisions (left panel), D^+ mesons in Pb–Pb collisions (middle panel), and D_s^+ mesons in Pb–Pb collisions (right panel).

in quadrature of RMS and shift is shown in Fig. 6.10 for D^+ mesons in p–Pb collisions (left panel), D^+ mesons in Pb–Pb collisions (middle panel), and D_s^+ mesons in Pb–Pb collisions (right panel). The values obtained in the different centrality classes of p–Pb collisions are similar, with a hint of larger values in the 0–10% and 10–20% centrality classes, as expected because of the smaller signal-to-background ratio compared to that obtained in more peripheral collisions. This hierarchy is more clear for $p_T < 10$ GeV/c in Pb–Pb collisions, where the difference of the signal-to-background can be more than one order of magnitude between central and peripheral collisions (see right panels of Fig. 6.6).

For the Q_{CP} measurement the systematic uncertainty was evaluated with the multi-trial approach on the ratio of the raw yields extracted in the two centrality classes. The fit configurations were varied consistently for the numerator and the denominator, in order to estimate a possible correlation between the uncertainties on the extraction of the two raw yields. Figure 6.11 shows the comparison between the systematic uncertainty evaluated from the distributions of the raw-yield ratios and that obtained from the uncertainties on the raw yields, propagated as uncorrelated. In the case of Q_{CP} between the 0–10% and 60–100% centrality classes, the values obtained with the two methods are similar, indicating that the degree of correlation is small. In the case of 40–60% centrality class as numerator, the values obtained with the evaluation from the ratio is significantly smaller, especially in the intermediate p_T region. This reflects the correlation between the systematic uncertainties on the raw-yield extraction in the two most peripheral classes of the events, which is due to the similar signal-to-background ratio and background shape.

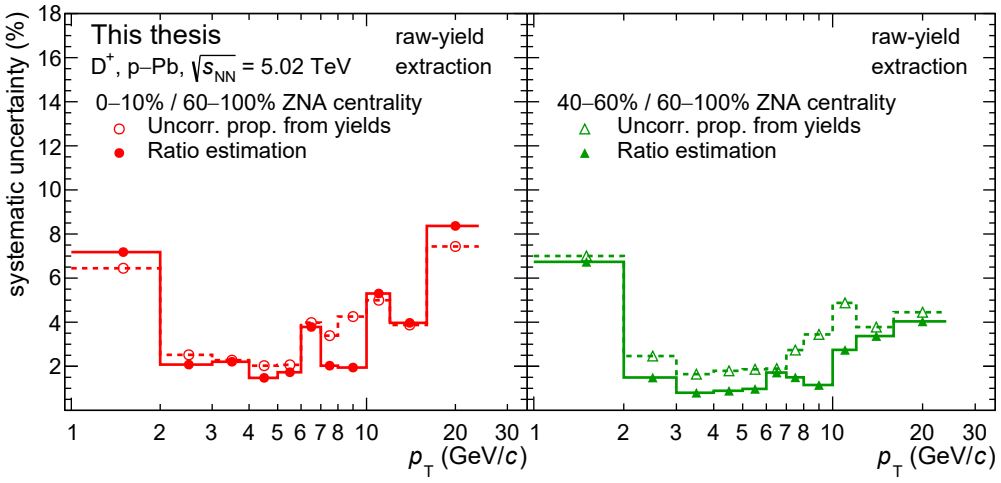

Figure 6.11: Comparison between the systematic uncertainty on the raw-yield extraction for the $Q_{\rm CP}$ computed between the 0–10% and 60–100% centrality classes (left panel) and the 40–60% and 60–100% centrality classes (right panel), evaluated on the ratio of the raw yields in the central and peripheral classes and that obtained by propagating the two uncertainties as uncorrelated.

6.4.2 Topological and kinematical selection efficiency

The uncertainty on the topological and kinematical selection efficiency arises from imperfect descriptions of the selection variables in the MC simulation. It was evaluated by varying the selection criteria as explained in Sec. 5.6.2. The systematic uncertainty was evaluated from the observation of trends of the corrected yields when tightening or releasing a selection, and from the RMS of the distributions of the corrected yields obtained with different selection criteria and the shift of these distributions with respect to the value of corrected yield obtained with the default set of selections. Figure 6.12 shows the sum in quadrature of the RMS and shift of such distributions, for $\rm D^+$ mesons in p–Pb collisions (left panel), $\rm D^+$ mesons in Pb–Pb collisions (middle panel), and $\rm D_s^+$ mesons in Pb–Pb collisions (right panel). The values obtained in p–Pb collisions are similar for all the centrality classes, as expected since the same selection criteria are applied and the efficiency does not vary much with the charged-particle multiplicity. A hierarchy is instead observed for $\rm D^+$ mesons in Pb–Pb collisions, which reflects the tighter selection criteria applied in more central collisions. The same consideration can be applied to the measurement of $\rm D_s^+$ mesons in central Pb–Pb collisions, for which the efficiency is lower than that of $\rm D^+$ mesons in the same centrality class. The increase of the values towards high $p_{\rm T}$ is attributed to the statistical fluctuations given the smaller D-meson yield. Therefore, it was not considered in the assignment of the systematic uncertainty, since a larger systematic uncertainty is not expected at high $p_{\rm T}$, owing to the more released selection criteria.

For the $Q_{\rm CP}$ measurement, the systematic uncertainty on the topological and kinematical selection efficiency was considered as fully correlated among different centrality

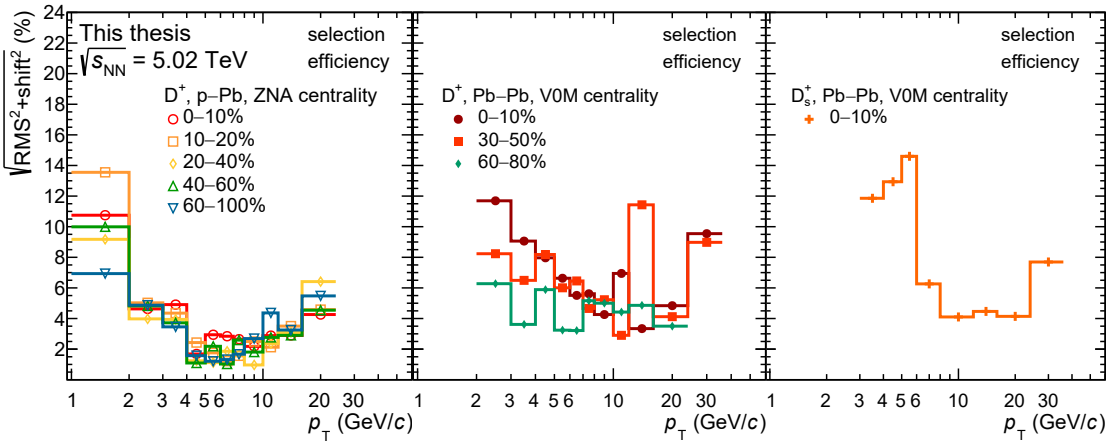

Figure 6.12: Sum in quadrature of RMS and shift with respect to the central value of the distributions of the corrected yields obtained with different selection criteria for D^+ mesons in p–Pb collisions (left panel), D^+ mesons in Pb–Pb collisions (middle panel), and D_s^+ mesons in Pb–Pb collisions (right panel).

classes, considering that for p–Pb collisions the same selections were applied to the D^+-meson candidates and a consistent systematic uncertainty was found in all the centrality classes. The uncertainty was instead considered as fully uncorrelated between the AA (pA) and pp collisions for the computation of the $R_{AA}(Q_{pA})$, given the significantly different selection criteria applied in pp and heavy-ion collisions and that the data samples were collected in different years, with different detector conditions.

6.4.3 PID selection efficiency

The systematic uncertainty on the PID selection efficiency was evaluated with a per-track study, using relatively pure samples of pions and kaons. Pions were selected from K_s^0 and Λ decays, while kaons in the TPC (TOF) were selected applying a tight selection on the PID signal in the TOF (TPC) of $|N_\sigma(K)| < 0.2$, as described in Sec. 5.6.3.

However, for the data sample of Pb–Pb collisions collected in 2018, a discrepancy between the TPC PID efficiency in data and MC simulation up to 5%, 15%, 30% for a $3\,\sigma$, $2\,\sigma$, and $1\,\sigma$ selection, respectively, was observed. This was caused by an imperfect calibration of the expected dE/dx for the different hadron species in the data, which was reflected in a deviation of the N_σ^{TPC} distributions from the Normal distribution. In order to avoid large biases in the D_s^+-meson measurement, a post-calibration procedure was applied to correct the N_σ^{TPC} values. In particular, the distributions obtained from the pure samples of pions and kaons in narrow momentum and pseudorapidity intervals were fitted with a Gaussian function to extract the mean, $\langle N_\sigma^{TPC}\rangle$, and the width, $\sigma(N_\sigma^{TPC})$, of the uncalibrated distributions of pions and kaons. The extracted parameters were then

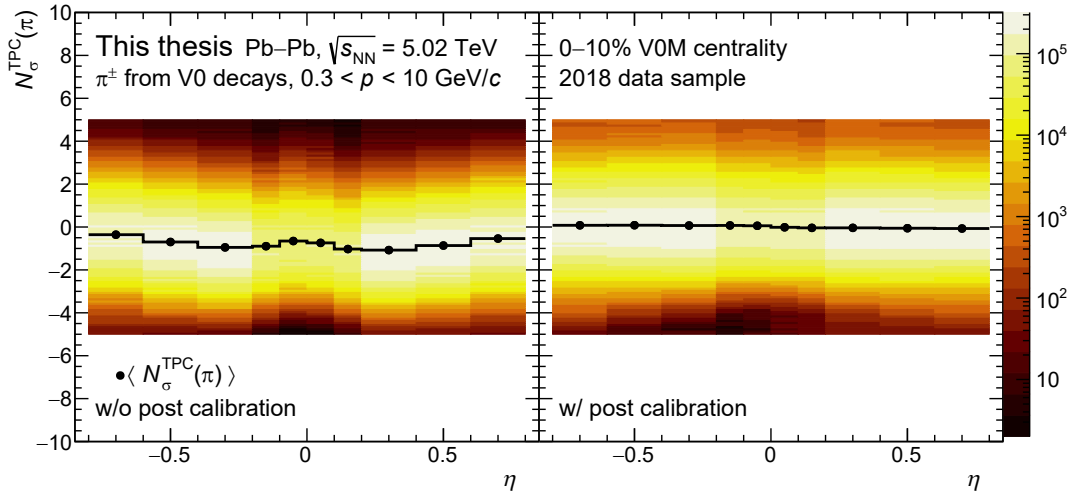

Figure 6.13: $N_{\sigma}^{\mathrm{TPC}}(\pi)$ distribution of pions selected from $\mathrm{K}^0_{\mathrm{s}}$ and Λ decays as a function of pseudorapidity in the sample of Pb–Pb collisions collected in 2018, before and after the post calibration. The black points represent the average $N_{\sigma}^{\mathrm{TPC}}(\pi)$.

used to compute the corrected $N_{\sigma}^{\mathrm{TPC,corr}}$ value for each track as

$$N_{\sigma}^{\mathrm{TPC,corr}}(X) = \frac{N_{\sigma}^{\mathrm{TPC}}(X) - \langle N_{\sigma}^{\mathrm{TPC}}(X)\rangle}{\sigma(N_{\sigma}^{\mathrm{TPC}}(X))}, \tag{6.8}$$

where X stands for a given mass hypothesis, i.e. pion or kaon. Figure 6.13 shows the $N_{\sigma}^{\mathrm{TPC}}(\pi)$ distribution as a function of pseudorapidity before (left panel) and after (right panel) the post-calibration procedure, for a sample of pions selected from $\mathrm{K}^0_{\mathrm{s}}$ and Λ decays in the interval $0.3 < p < 10$ GeV/c, independent of the one used to compute the correction. The mean value of the distribution before the correction is shifted towards negative values, and shows a clear η-dependence. The corrected distribution is constantly centred at zero as a function of η. In the left panel of Fig. 6.14 the data-to-MC ratios of the $N_{\sigma}^{\mathrm{TPC}}(\pi)$ efficiency of pions as a function of p_{T} are reported for a $3\,\sigma$, $2\,\sigma$, and $1\,\sigma$ selection. Before the post calibration the bias is up to 30% for the tightest selection criterion, while the ratios are close to unity after the correction. A similar result was obtained for the kaons.

The residual systematic uncertainty on the selection of pion and kaon tracks was evaluated as the relative difference between the efficiencies of the N_{σ} selection in data and in the MC simulation, and then propagated to the $\mathrm{D}_{\mathrm{s}}^{+}$ mesons using the decay kinematics, as described in Sec. 5.6.3. The right panel of Fig. 6.14 shows the relative systematic uncertainty estimated for $\mathrm{D}_{\mathrm{s}}^{+}$ mesons in Pb–Pb collisions, compared to that estimated for D^{+} mesons in p–Pb and Pb–Pb collisions. In the p_{T} intervals $1 < p_{\mathrm{T}} < 2$ GeV/c for D^{+} mesons in p–Pb collisions and $3 < p_{\mathrm{T}} < 8$ GeV/c for $\mathrm{D}_{\mathrm{s}}^{+}$ mesons in Pb–Pb collisions, where the strong PID strategy is applied, the uncertainty is of the order of 1%, while it is negligible in the remaining p_{T} intervals.

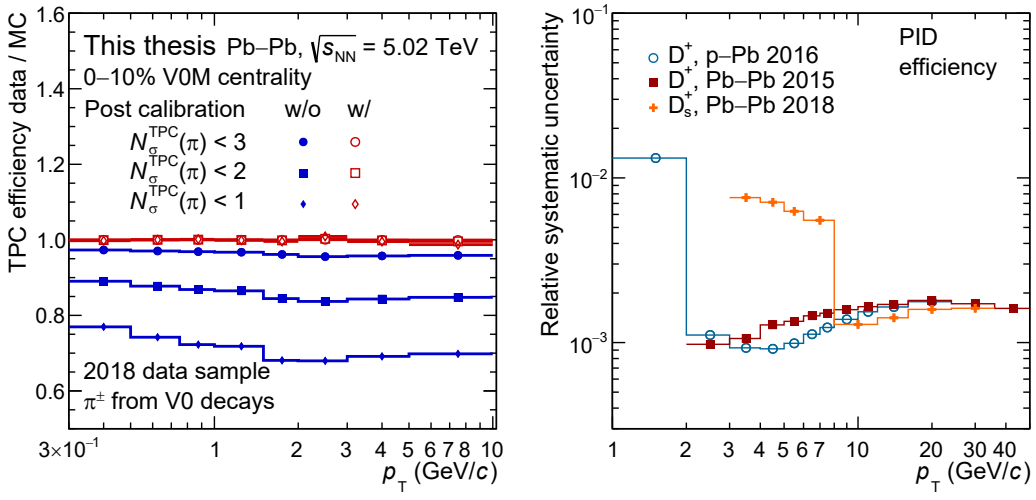

Figure 6.14: Left: data-to-MC ratios of the N_σ^{TPC} selection efficiencies of pions as a function of track p_{T}, before (blue markers) and after (red markers) the post calibration of the N_σ^{TPC}. Right: Relative systematic uncertainty on the PID selection efficiency for D^+ and D_s^+ mesons in p–Pb and Pb–Pb collisions at $\sqrt{s_{\mathrm{NN}}} = 5.02$ TeV. The systematic uncertainty for the D_s^+ meson in the 2018 Pb–Pb data sample was estimated after the post-calibration procedure.

6.4.4 Track-reconstruction efficiency

The systematic uncertainty on the track-reconstruction efficiency was estimated with the same strategy adopted for D_s^+ mesons in pp collisions described in Sec. 5.6.4. It includes the contribution of the track-quality selection efficiencies and the ITS-TPC track-matching efficiency, which are evaluated per track. The two contributions are then propagated to the D_s^+ and D^+ mesons, via the decay kinematics, as done for the systematic uncertainty on the PID selection efficiency.

Figure 6.15 shows the relative uncertainty evaluated for D^+ mesons in p–Pb and Pb–Pb collisions, as well as that for D_s^+ mesons in Pb–Pb collisions. The left panel of the same Figure shows the average p_{T} of the decay tracks as a function of the parent D_s^+- or D^+-meson p_{T}. The decay kinematics of the D^+ and D_s^+ mesons is similar owing to the similar difference between their masses and the sum of the masses of their decay products, and therefore a very similar systematic uncertainty is expected in case of the same per-track uncertainty. The systematic uncertainty for the D_s^+ mesons is however larger because of an imperfect description of the dead zones between TPC sectors in the MC simulation for the Pb–Pb sample collected in 2018, that was estimated to increase by about 7% the systematic uncertainty.

The difference between the systematic uncertainty of D^+ meson in p–Pb and Pb–Pb collisions is mainly due to the different uncertainty due to the ITS-TPC matching efficiency, which is the dominant contribution in case of Pb–Pb collisions.

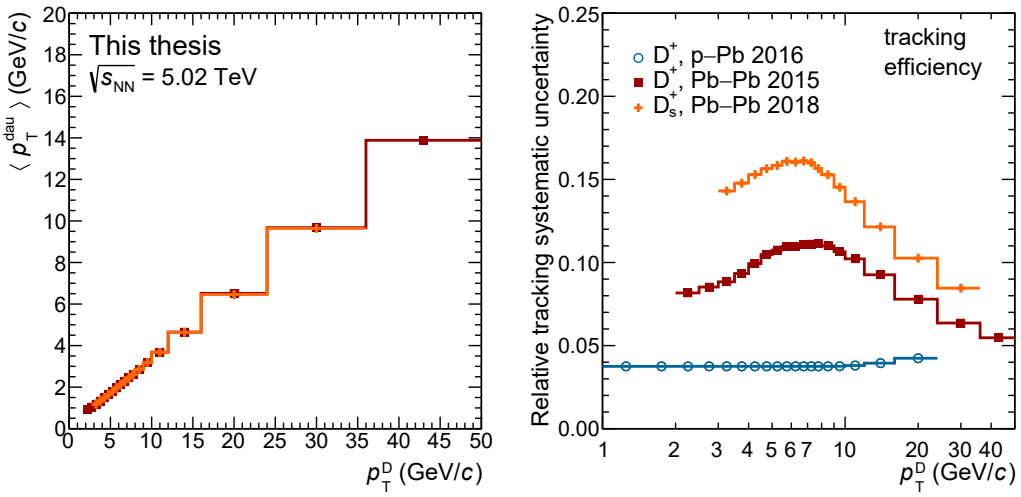

Figure 6.15: Left: average decay-track p_T as a function of D_s^+- or D^+-meson p_T. Right: relative systematic uncertainty on the track-reconstruction efficiency as a function of p_T for D^+ mesons in p–Pb and Pb–Pb collisions at $\sqrt{s_{NN}} = 5.02$ TeV and D_s^+ mesons in Pb–Pb collisions at $\sqrt{s_{NN}} = 5.02$ TeV.

6.4.5 Generated Monte Carlo p_T shape

The systematic uncertainty on the efficiency due to a possible discrepancy between the real and simulated shape of the p_T distribution of D^+ and D_s^+ mesons was estimated by computing the efficiency with alternative p_T shapes.

For the D_s^+ mesons, in addition to the p_T distribution obtained from FONLL calculations, the in-medium effects on the p_T shape were included using the prediction of the R_{AA} from the MC@sHQ+EPOS2 [111] model. Moreover, models implementing an enhanced production of charmed mesons with strange-quark content in the medium, such as TAMU [170], PHSD [178] and CATANIA [115] models, were employed.

The left panel of Fig. 6.16 shows the ratios of the normalised p_T spectra from the these model calculations and the simulation with the p_T^{hard} bins of PYTHIA, which were used to weight the D_s^+-meson efficiency in the 0–10% centrality class. In the right panel of the same Figure, the ratios of the prompt D_s^+-meson efficiency obtained with the alternative p_T shapes and that obtained from FONLL p_T distribution multiplied by the R_{AA} predicted by the TAMU model, which was used as default, are shown.

For D^+ mesons in Pb–Pb collisions, the shape of the p_T distribution provided by FONLL and models including the nuclear modification factor were adopted. The maximum systematic uncertainty assigned to the D^+ mesons is about 10% for 0–10% central collisions in the $2 < p_T < 3$ GeV/c, where the efficiency varies steeply as a function of p_T (see Fig. 6.7), while it decreases down to 0% for $p_T > 5$ GeV/c. For D^+ mesons in p–Pb collisions, the FONLL p_T shape was used instead of the one from PYTHIA and the effect on the efficiency was found to be negligible.

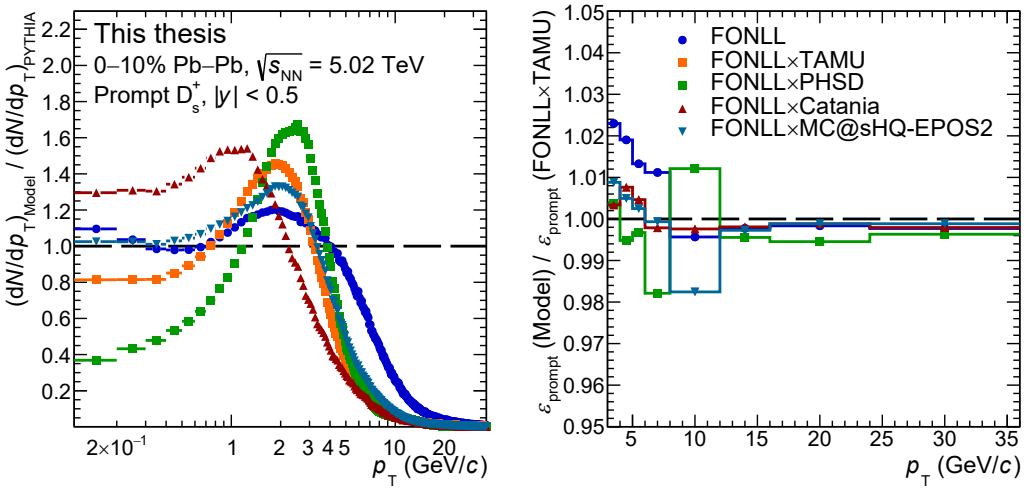

Figure 6.16: Left: ratio between the normalised p_T spectra from the several model calculations to the one from the simulation with the p_T^{hard} bins of PYTHIA. These ratios were used to weight the D_s^+ efficiency. Right: ratio between the efficiency of prompt D_s^+ mesons obtained with the p_T shapes provided by alternative models and that from FONLL calculations multiplied by the R_{AA} from the TAMU model (default).

6.4.6 Generated Monte Carlo multiplicity distribution

For p–Pb collisions, an additional source of systematic uncertainty is related to the weighting procedure of the efficiencies applied in order to reproduce the $N_{tracklets}$ distribution measured in data. In fact, in p–Pb collisions, the efficiency is more sensitive to the multiplicity distribution than the p_T distribution of D mesons, because of the impact of the resolution on the determination of the primary-vertex position.

For the central value of the efficiencies, the weights were obtained from events that have at least a D^0-meson candidate that fulfils the selections and has the invariant mass compatible within 3σ the D^0-meson mass [13] (see Sec. 6.3.2). To test the stability of the efficiency, the weighting procedure was repeated using events with at least a D^0-meson candidate, with no further request on its invariant mass. The left panel of Fig. 6.17 shows the comparison between the default and alternative $N_{tracklets}$ weights for the 0–10% and the 60–100% centrality classes. In the right panel of the same Figure, the effect of the different weights on the efficiency of prompt D^+ mesons is shown. The largest deviation of about 2% is observed at low p_T for peripheral events, where the primary-vertex resolution is poorer because of the reduced charged-particle multiplicity. The difference is smaller for the other centrality classes, and decreases to zero for $p_T > 10$ GeV/c.

The uncertainty due to the possible difference of the charged-particle multiplicity distribution in data and in the $N_{tracklets}$-weighted simulation on the Q_{CP} was estimated via a double ratio of the efficiencies for the central and peripheral classes of events obtained with the default and alternative $N_{tracklets}$ weights. Since the effect was found to be similar in each centrality class, the resulting uncertainty is smaller compared to the one on the

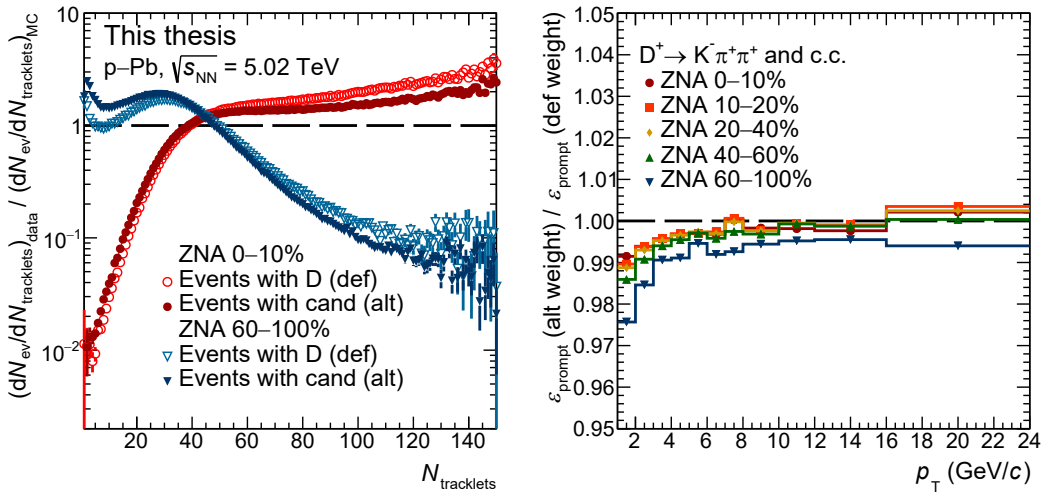

Figure 6.17: Left: comparison of $N_{\text{tracklets}}$ weights obtained from events with at least a D^0 candidate (alternative) and those obtained from events with at least in the signal mass range (default) for the 0–10% and 60–100% centrality classes. Right: ratio of the efficiency for prompt D^+ mesons obtained with the default and alternative $N_{\text{tracklets}}$ weights.

Q_{pA} and, in particular, it was estimated to be about 1% for $p_{\mathrm{T}} < 5$ GeV/c and negligible above.

6.4.7 Beauty feed-down subtraction

The systematic uncertainty on the subtraction of the contribution of D mesons from beauty-hadron decays, performed via the calculation of the f_{prompt} fraction described in Sec. 4.1.1, has two components. The first one was estimated as for pp collisions by varying the parameters of the FONLL prediction (see Sec. 5.5.1). This contribution is fully correlated in pp and p–Pb (Pb–Pb) collisions and therefore almost cancels out in the nuclear modification factor.

The second contribution arises from the assumption on the nuclear modification factor of feed-down D mesons introduced in Sec. 6.3.3 and 6.2.3. It was estimated by varying the hypothesis on $R_{\mathrm{AA}}(Q_{\mathrm{pA}})^{\text{feed-down}}/R_{\mathrm{AA}}(Q_{\mathrm{pA}})^{\text{prompt}}$ within the uncertainties of the models and the measurements used to estimate the central value. In particular, for D^+ mesons in p–Pb collisions it was varied between 0.9 and 1.3 for all the centrality classes but the 40–60% and 60–100% classes, for which the reduced range 0.9-1.1 was used since in these centrality intervals the possible differences of the production mechanisms of prompt and feed-down D mesons with respect to pp collisions are expected to be smaller. For D^+ mesons in Pb–Pb collisions the hypothesis was varied between 1 and 3 (2) in the p_{T} intervals and centrality classes where the central hypothesis was set to 2 (1.5). For $\mathrm{D}_{\mathrm{s}}^+$ mesons the hypothesis was varied between 1/3 and 3. The lower limit was reduced with respect to the D^+ case to take into account that the modification of the hadronisation

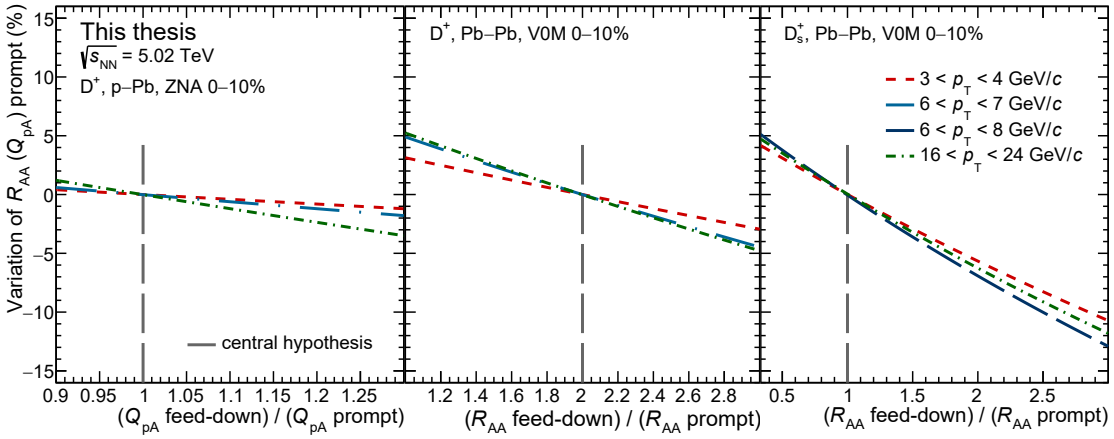

Figure 6.18: Variation of the $R_{\rm AA}$ ($Q_{\rm pA}$) of prompt $\rm D^+$ and $\rm D_s^+$ mesons in three centrality classes and three $p_{\rm T}$ intervals as a function of the variation of the hypothesis on $R_{\rm AA}(Q_{\rm pA})^{\rm feed\text{-}down}/R_{\rm AA}(Q_{\rm pA})^{\rm prompt}$.

mechanism in the medium and the increased abundance of strange quarks could lead to a reduced suppression of prompt $\rm D_s^+$ mesons compared to $\rm D_s^+$ mesons from beauty-hadron decays. Figure 6.18 shows the variation of the $R_{\rm AA}$ ($Q_{\rm pA}$) of prompt $\rm D^+$ and $\rm D_s^+$ mesons in three centrality classes and different $p_{\rm T}$ intervals as a function of the variation of the hypothesis on $R_{\rm AA}(Q_{\rm pA})^{\rm feed\text{-}down}/R_{\rm AA}(Q_{\rm pA})^{\rm prompt}$, which corresponds to the assigned systematic uncertainty. For $\rm D^+$ mesons in p–Pb collisions (left panel), the systematic uncertainty varies between 1.5% and 4%. In Pb–Pb collisions the uncertainty assigned to $\rm D^+$ mesons is between 3% and 8%, while the one assigned to $\rm D_s^+$ mesons ranges from 5% to 18%, depending on $p_{\rm T}$.

6.4.8 Normalisation

The uncertainty on the normalisation of the $p_{\rm T}$-differential corrected yields is due to the uncertainty on the BR of the decay channels used to reconstruct the $\rm D_s^+$ and $\rm D^+$ mesons (see Table 4.2). For Pb–Pb collisions, an additional contribution is given by the uncertainty on the fraction of the hadronic cross section used in the Glauber fit to determine the centrality, which was estimated to be <0.1%, 2% and 3% for the 0–10%, 30–50%, and 60–80% centrality classes, respectively.

The normalisation uncertainty on the nuclear modification factors includes also the uncertainty on the luminosity of the pp reference, which is 2.1% for the cross sections measured at $\sqrt{s} = 5.02$ TeV and 3.5% for that measured at $\sqrt{s} = 7$ TeV and scaled to $\sqrt{s} = 5.02$ TeV using FONLL calculations, and the uncertainty on the $\langle T_{\rm AA}(T_{\rm pA})\rangle$, which are reported in Table 6.1. Since the pp reference is not used in the calculation of the $Q_{\rm CP}$, its normalisation uncertainty is not included, and the uncertainty on the $\langle T_{\rm pA}\rangle$ partially cancels out in the ratio, since it is partially correlated among the different centrality classes of p–Pb collisions. The BR uncertainty cancels out in the nuclear modification

factors, being the same in the numerator and in the denominator.

6.4.9 Summary of systematic uncertainties

The values assigned as systematic uncertainty for each contribution are reported in Table 6.3 and Table 6.4 for the measurement of the $p_{\rm T}$-differential corrected yields of $\rm D_s^+$ and $\rm D^+$ mesons in Pb–Pb collisions at $\sqrt{s_{\rm NN}} = 5.02$ TeV and that of $\rm D^+$ mesons in p–Pb collisions at $\sqrt{s_{\rm NN}} = 5.02$ TeV, respectively. As for the analysis of the $\rm D_s^+$-meson production in pp collisions, the systematic uncertainty on the raw-yield extraction was considered as uncorrelated among the $p_{\rm T}$ intervals, while the uncertainties on the topological, tracking, and PID selection efficiencies correlated.

For the computation of the $R_{\rm AA}$ of $\rm D^+$ and $\rm D_s^+$ mesons and the $Q_{\rm pA}$ of $\rm D^+$ mesons, all the sources of uncertainty were considered uncorrelated among pp and Pb–Pb (p–Pb) collisions, except for the uncertainty on the feed-down subtraction deriving from the variation of the parameters of the FONLL calculation and the uncertainty on the BR, which are fully correlated and hence cancel out in the ratio.

The systematic uncertainties on the $\rm D^+$-meson $Q_{\rm CP}$ are reported in Table 6.5. The uncertainties on the raw-yield extraction and the contribution due to the possible difference of the charged-particle multiplicity distribution in data and in the $N_{\rm tracklets}$-weighted simulation were estimated directly on the ratio to evaluate the degree of correlation, allowing for a partial cancellation. The contribution to the uncertainty related to the feed-down subtraction arising from the hypothesis on the nuclear modification factor of $\rm D^+$ mesons coming from beauty-hadron decays was considered as uncorrelated in each centrality class and therefore added in quadrature in the ratio. The contributions from the topological and kinematical selection, PID, and track-reconstruction efficiency are fully correlated among the different centrality classes of p–Pb collisions and cancels completely in the ratio. Therefore, the overall systematic uncertainty on the $Q_{\rm CP}$ is reduced with respect to that on the $Q_{\rm pA}$.

6.5 Uncertainties on the pp reference

The systematic uncertainties on the pp reference were considered as systematic uncertainties in the computation of the nuclear modification factors. They include (i) the systematic uncertainties of the measurement, (ii) the uncertainty on the $\sqrt{s}$- and $y_{\rm cms}$-scaling, and (iii) the uncertainty on the $p_{\rm T}$-extrapolation procedures. The values for the three pp references are reported in Table 6.6. In the systematic uncertainty on the pp measurement, the uncertainty from the beauty feed-down subtraction due to the FONLL uncertainty is not included, since it cancels out in the nuclear modification factors because it is fully correlated between the measurements in pp and p–Pb (Pb–Pb) collisions.

The statistical uncertainty was propagated to the statistical uncertainty on the nuclear modification factor, summing it in quadrature with the statistical uncertainty of the corrected yield measured in AA (pA) collisions.

p_{T} (GeV/c)	[2,3]	[3,4]	[4,5]	[5,6]	[6,7]	[7,8]	[8,10]	[10,12]	[12,16]	[16,24]	[24,36]	[36,50]
$\mathrm{D_s^+}$ Pb–Pb 0 – 10%												
Raw-yield extraction (%)	-	8.0	8.0	5.0	5.0		3.0	3.0	5.0	5.0	-	
Selection efficiency (%)	-	10.0	10.0	10.0	6.0		5.0	5.0	5.0	5.0	-	
PID efficiency (%)	-	1.0	1.0	1.0	1.0		negl.	negl.	negl.	negl.	-	
Tracking efficiency (%)	-	15.5	16.5	17.0	17.0		17.0	15.0	15.0	11.5	-	
MC p_{T} shape (%)	-	2.0	2.0	2.0	2.0		2.0	negl.	negl.	negl.	-	
Feed-down (FONLL) (%)	-	$^{+2.6}_{-3.2}$	$^{+3.2}_{-4.1}$	$^{+4.3}_{-5.7}$	$^{+2.8}_{-3.6}$		$^{+3.3}_{-4.1}$	$^{+1.8}_{-2.3}$	$^{+2.0}_{-2.3}$	$^{+1.8}_{-1.9}$	-	
Feed-down (R_{AA} hypo) (%)	-	$^{+4.8}_{-11.2}$	$^{+6.3}_{-14.0}$	$^{+8.8}_{-18.4}$	$^{+5.8}_{-13.5}$		$^{+7.4}_{-16.3}$	$^{+4.5}_{-10.8}$	$^{+5.1}_{-12.0}$	$^{+4.9}_{-11.7}$	-	
Branching ratio (%)	-	3.5	3.5	3.5	3.5		3.5	3.5	3.5	3.5	-	
Centrality limit (%)	-	0.1	0.1	0.1	0.1		0.1	0.1	0.1	0.1	-	
$\mathrm{D^+}$ Pb–Pb 0 – 10%												
Raw-yield extraction (%)	12.0	12.0	11.0	11.0	8.0	7.0	6.0	6.0	6.0	8.0	12.0	12.0
Selection efficiency (%)	12.0	12.0	9.0	9.0	8.0	8.0	5.0	5.0	5.0	5.0	5.0	5.0
PID efficiency (%)	negl.	negl.	negl.	negl.	negl.	negl.	negl.	negl.	negl.	negl.	negl.	negl.
Tracking efficiency (%)	8.5	9.0	10.0	11.0	11.0	11.0	11.0	10.0	9.0	8.0	6.5	5.5
MC p_{T} shape (%)	10.0	3.0	1.0	negl.	negl.	negl.	negl.	negl.	negl.	negl.	negl.	negl.
Feed-down (FONLL) (%)	$^{+2.1}_{-2.5}$	$^{+2.4}_{-3.1}$	$^{+2.5}_{-3.4}$	$^{+3.1}_{-4.3}$	$^{+3.1}_{-4.4}$	$^{+3.2}_{-4.4}$	$^{+3.3}_{-4.5}$	$^{+3.6}_{-4.8}$	$^{+3.2}_{-4.1}$	$^{+2.4}_{-3.0}$	$^{+1.8}_{-2.0}$	$^{+1.5}_{-1.6}$
Feed-down (R_{AA} hypo) (%)	$^{+2.7}_{-3.0}$	$^{+4.0}_{-4.3}$	$^{+4.4}_{-4.8}$	$^{+5.6}_{-6.0}$	$^{+5.8}_{-6.2}$	$^{+6.0}_{-6.4}$	$^{+6.5}_{-6.7}$	$^{+7.3}_{-7.5}$	$^{+6.8}_{-6.9}$	$^{+5.6}_{-5.7}$	$^{+3.3}_{-3.4}$	$^{+3.0}_{-3.1}$
Branching ratio (%)	3.1	3.1	3.1	3.1	3.1	3.1	3.1	3.1	3.1	3.1	3.1	3.1
Centrality limit (%)	0.1	0.1	0.1	0.1	0.1	0.1	0.1	0.1	0.1	0.1	0.1	0.1
$\mathrm{D^+}$ Pb–Pb 30 – 50%												
Raw-yield extraction (%)	8.0	8.0	6.0	6.0	4.0	4.0	4.0	4.0	4.0	6.0	8.0	-
Selection efficiency (%)	8.0	8.0	8.0	6.0	5.0	5.0	5.0	5.0	5.0	5.0	5.0	-
PID efficiency (%)	negl.	negl.	negl.	negl.	negl.	negl.	negl.	negl.	negl.	negl.	negl.	-
Tracking efficiency (%)	8.5	9.0	10.0	11.0	11.0	11.0	11.0	10.0	9.0	8.0	6.5	-
MC p_{T} shape (%)	5.0	1.0	negl.	negl.	negl.	negl.	negl.	negl.	negl.	negl.	negl.	-
Feed-down (FONLL) (%)	$^{+2.1}_{-2.5}$	$^{+2.4}_{-3.1}$	$^{+2.4}_{-3.4}$	$^{+2.9}_{-4.2}$	$^{+2.9}_{-4.2}$	$^{+2.9}_{-4.1}$	$^{+3.1}_{-4.3}$	$^{+3.8}_{-5.1}$	$^{+3.3}_{-4.3}$	$^{+2.6}_{-3.2}$	$^{+1.7}_{-2.0}$	-
Feed-down (R_{AA} hypo) (%)	$^{+2.7}_{-3.0}$	$^{+4.0}_{-4.3}$	$^{+4.4}_{-4.8}$	$^{+5.5}_{-6.0}$	$^{+5.7}_{-6.1}$	$^{+5.7}_{-6.1}$	$^{+6.3}_{-6.6}$	$^{+7.9}_{-8.0}$	$^{+7.2}_{-7.3}$	$^{+6.0}_{-6.2}$	$^{+3.2}_{-3.2}$	-
Branching ratio (%)	3.1	3.1	3.1	3.1	3.1	3.1	3.1	3.1	3.1	3.1	3.1	3.1
Centrality limit (%)	2.0	2.0	2.0	2.0	2.0	2.0	2.0	2.0	2.0	2.0	2.0	2.0
$\mathrm{D^+}$ Pb–Pb 60 – 80%												
Raw-yield extraction (%)	4.0	4.0	4.0	3.0	3.0	3.0	5.0	5.0	5.0	6.0	-	-
Selection efficiency (%)	6.0	6.0	5.0	5.0	5.0	5.0	5.0	5.0	5.0	5.0	-	-
PID efficiency (%)	negl.	negl.	negl.	negl.	negl.	negl.	negl.	negl.	negl.	negl.	-	-
Tracking efficiency (%)	8.5	9.0	10.0	11.0	11.0	11.0	11.0	10.0	9.0	8.0	-	-
MC p_{T} shape (%)	4.0	1.0	negl.	negl.	negl.	negl.	negl.	negl.	negl.	negl.	-	-
Feed-down (FONLL) (%)	$^{+2.4}_{-2.8}$	$^{+2.1}_{-2.7}$	$^{+2.3}_{-3.2}$	$^{+2.7}_{-3.9}$	$^{+2.7}_{-3.8}$	$^{+2.6}_{-3.6}$	$^{+2.5}_{-3.4}$	$^{+3.1}_{-4.1}$	$^{+2.9}_{-3.7}$	$^{+2.1}_{-2.6}$	-	-
Feed-down (R_{AA} hypo) (%)	$^{+3.0}_{-3.4}$	$^{+2.9}_{-3.3}$	$^{+3.3}_{-3.9}$	$^{+3.9}_{-4.7}$	$^{+4.0}_{-4.7}$	$^{+3.8}_{-4.5}$	$^{+3.8}_{-4.4}$	$^{+4.8}_{-5.3}$	$^{+4.6}_{-5.0}$	$^{+3.6}_{-3.8}$	-	-
Branching ratio (%)	3.1	3.1	3.1	3.1	3.1	3.1	3.1	3.1	3.1	3.1	-	-
Centrality limit (%)	3.0	3.0	3.0	3.0	3.0	3.0	3.0	3.0	3.0	3.0	-	-

Table 6.3: Summary of relative systematic uncertainties on the p_{T}-differential corrected yields of $\mathrm{D_s^+}$ and $\mathrm{D^+}$ mesons in Pb–Pb collisions at $\sqrt{s_{\mathrm{NN}}} = 5.02$ TeV.

p_{T} (GeV/c)	[1,2]	[2,3]	[3,4]	[4,5]	[5,6]	[6,7]	[7,8]	[8,10]	[10,12]	[12,16]	[16,24]
D^+ p–Pb all centralities											
Selection efficiency (%)	7.0	3.0	3.0	3.0	3.0	3.0	3.0	3.0	3.0	3.0	3.0
PID efficiency (%)	1.5	negl.	negl.	negl.	negl.	negl.	negl.	negl.	negl.	negl.	negl.
Tracking efficiency (%)	3.7	3.7	3.7	3.7	3.7	3.7	3.7	3.7	4.0	4.0	4.0
Feed-down (FONLL) (%)	$^{+1.8}_{-2.1}$	$^{+1.7}_{-2.0}$	$^{+1.5}_{-1.9}$	$^{+1.6}_{-2.2}$	$^{+1.6}_{-2.4}$	$^{+1.8}_{-2.6}$	$^{+1.9}_{-2.7}$	$^{+2.2}_{-3.0}$	$^{+2.5}_{-3.3}$	$^{+2.1}_{-2.7}$	$^{+3.1}_{-3.9}$
Branching ratio (%)	3.1	3.1	3.1	3.1	3.1	3.1	3.1	3.1	3.1	3.1	3.1
$0-10\%$											
Raw-yield extraction (%)	5.0	3.0	2.0	2.0	2.0	3.0	3.0	3.0	3.0	4.0	5.0
$N_{\mathrm{tracklets}}$ distribution (%)	1.0	1.0	1.0	1.0	1.0	1.0	1.0	1.0	negl.	negl.	negl.
Feed-down (Q_{pA} hypo) (%)	$^{+1.9}_{-2.4}$	$^{+1.7}_{-2.3}$	$^{+1.6}_{-2.3}$	$^{+1.6}_{-2.6}$	$^{+1.7}_{-2.8}$	$^{+1.9}_{-3.2}$	$^{+2.0}_{-3.3}$	$^{+2.3}_{-3.8}$	$^{+2.6}_{-4.2}$	$^{+2.3}_{-3.6}$	$^{+3.4}_{-5.3}$
$10-20\%$											
Raw-yield extraction (%)	5.0	3.0	2.0	2.0	2.0	2.0	2.0	2.0	3.0	4.0	5.0
$N_{\mathrm{tracklets}}$ distribution (%)	1.0	1.0	1.0	1.0	1.0	1.0	1.0	1.0	negl.	negl.	negl.
Feed-down (Q_{pA} hypo) (%)	$^{+1.8}_{-2.4}$	$^{+1.7}_{-2.3}$	$^{+1.5}_{-2.3}$	$^{+1.6}_{-2.6}$	$^{+1.7}_{-2.8}$	$^{+1.9}_{-3.2}$	$^{+2.0}_{-3.3}$	$^{+2.2}_{-3.7}$	$^{+2.6}_{-4.2}$	$^{+2.2}_{-3.6}$	$^{+3.3}_{-5.2}$
$20-40\%$											
Raw-yield extraction (%)	5.0	2.0	2.0	2.0	2.0	2.0	2.0	2.0	3.0	4.0	5.0
$N_{\mathrm{tracklets}}$ distribution (%)	1.0	1.0	1.0	1.0	1.0	1.0	1.0	1.0	negl.	negl.	negl.
Feed-down (Q_{pA} hypo) (%)	$^{+1.8}_{-2.4}$	$^{+1.7}_{-2.3}$	$^{+1.5}_{-2.3}$	$^{+1.6}_{-2.6}$	$^{+1.7}_{-2.8}$	$^{+1.9}_{-3.1}$	$^{+2.0}_{-3.3}$	$^{+2.2}_{-3.7}$	$^{+2.6}_{-4.2}$	$^{+2.2}_{-3.6}$	$^{+3.2}_{-5.2}$
$40-60\%$											
Raw-yield extraction (%)	5.0	2.0	2.0	2.0	2.0	2.0	2.0	2.0	3.0	4.0	5.0
$N_{\mathrm{tracklets}}$ distribution (%)	2.0	1.0	1.0	1.0	1.0	1.0	1.0	1.0	negl.	negl.	negl.
Feed-down (Q_{pA} hypo) (%)	$^{+1.9}_{-2.1}$	$^{+1.7}_{-2.0}$	$^{+1.6}_{-2.0}$	$^{+1.6}_{-2.2}$	$^{+1.7}_{-2.4}$	$^{+1.9}_{-2.7}$	$^{+2.0}_{-2.8}$	$^{+2.2}_{-3.1}$	$^{+2.6}_{-3.4}$	$^{+2.2}_{-2.8}$	$^{+3.3}_{-3.9}$
$60-100\%$											
Raw-yield extraction (%)	5.0	2.0	2.0	2.0	2.0	2.0	2.0	2.0	3.0	4.0	5.0
$N_{\mathrm{tracklets}}$ distribution (%)	2.0	1.0	1.0	1.0	1.0	1.0	1.0	1.0	negl.	negl.	negl.
Feed-down (Q_{pA} hypo) (%)	$^{+1.9}_{-2.1}$	$^{+1.7}_{-2.1}$	$^{+1.6}_{-2.0}$	$^{+1.6}_{-2.2}$	$^{+1.7}_{-2.4}$	$^{+1.9}_{-2.7}$	$^{+2.0}_{-2.8}$	$^{+2.2}_{-3.0}$	$^{+2.6}_{-3.5}$	$^{+2.2}_{-2.8}$	$^{+3.3}_{-3.9}$

Table 6.4: Summary of relative systematic uncertainties on the p_{T}-differential corrected yields of D^+ mesons in p–Pb collisions at $\sqrt{s_{\mathrm{NN}}} = 5.02$ TeV.

p_{T} (GeV/c)	[1,2]	[2,3]	[3,4]	[4,5]	[5,6]	[6,7]	[7,8]	[8,10]	[10,12]	[12,16]	[16,24]
$\mathrm{D^+}$ p–Pb $0-10\%/60-100\%$											
Raw-yield extraction (%)	7.0	3.0	2.0	2.0	2.0	2.0	3.0	3.0	4.0	5.0	6.0
$N_{\mathrm{tracklets}}$ distribution (%)	1.0	1.0	1.0	1.0	negl.	negl.	negl.	negl.	negl.	negl.	negl.
Feed-down (Q_{pA} hypo) (%)	$^{+2.6}_{-3.0}$	$^{+2.4}_{-3.1}$	$^{+2.2}_{-3.3}$	$^{+2.2}_{-3.7}$	$^{+2.2}_{-3.7}$	$^{+2.6}_{-4.2}$	$^{+2.8}_{-4.3}$	$^{+3.1}_{-4.8}$	$^{+3.7}_{-5.5}$	$^{+3.1}_{-4.6}$	$^{+4.7}_{-6.5}$
$\mathrm{D^+}$ p–Pb $10-20\%/60-100\%$											
Raw-yield extraction (%)	7.0	3.0	2.0	2.0	2.0	2.0	3.0	3.0	4.0	5.0	6.0
$N_{\mathrm{tracklets}}$ distribution (%)	1.0	1.0	1.0	1.0	1.0	1.0	1.0	1.0	negl.	negl.	negl.
Feed-down (Q_{pA} hypo) (%)	$^{+2.6}_{-3.0}$	$^{+2.4}_{-3.1}$	$^{+2.2}_{-3.3}$	$^{+2.2}_{-3.7}$	$^{+2.2}_{-3.7}$	$^{+2.6}_{-4.2}$	$^{+2.8}_{-4.3}$	$^{+3.1}_{-4.8}$	$^{+3.7}_{-5.5}$	$^{+3.1}_{-4.6}$	$^{+4.7}_{-6.5}$
$\mathrm{D^+}$ p–Pb $20-40\%/60-100\%$											
Raw-yield extraction (%)	7.0	3.0	2.0	2.0	2.0	2.0	3.0	3.0	4.0	5.0	6.0
$N_{\mathrm{tracklets}}$ distribution (%)	1.0	1.0	1.0	1.0	1.0	1.0	1.0	1.0	negl.	negl.	negl.
Feed-down (Q_{pA} hypo) (%)	$^{+2.6}_{-3.0}$	$^{+2.4}_{-3.1}$	$^{+2.2}_{-3.3}$	$^{+2.2}_{-3.7}$	$^{+2.2}_{-3.7}$	$^{+2.6}_{-4.2}$	$^{+2.8}_{-4.3}$	$^{+3.1}_{-4.8}$	$^{+3.7}_{-5.5}$	$^{+3.1}_{-4.6}$	$^{+4.7}_{-6.5}$
$\mathrm{D^+}$ p–Pb $40-60\%/60-100\%$											
Raw-yield extraction (%)	7.0	2.0	2.0	2.0	2.0	2.0	2.0	3.0	3.0	4.0	4.0
$N_{\mathrm{tracklets}}$ distribution (%)	1.0	1.0	1.0	1.0	1.0	1.0	1.0	1.0	negl.	negl.	negl.
Feed-down (Q_{pA} hypo) (%)	$^{+2.7}_{-3.0}$	$^{+2.4}_{-3.0}$	$^{+2.3}_{-2.8}$	$^{+2.3}_{-3.1}$	$^{+2.4}_{-3.4}$	$^{+2.7}_{-3.8}$	$^{+2.8}_{-4.0}$	$^{+3.1}_{-4.2}$	$^{+3.7}_{-4.9}$	$^{+2.8}_{-4.0}$	$^{+4.7}_{-5.5}$

Table 6.5: Summary of relative systematic uncertainties on the Q_{CP} of $\mathrm{D^+}$ mesons in p–Pb collisions at $\sqrt{s_{\mathrm{NN}}} = 5.02$ TeV.

p_{T} (GeV/c)	[1,2]	[2,3]	[3,4]	[4,5]	[5,6]	[6,8]	[7,8]	[8,10]	[10,12]	[12,16]	[16,24]	[24,36]	[36,50]
$\mathrm{D^+}$ 7 TeV													
measurement (%)	13.1	12.8	8.2	8.2	8.7	9.0	9.1	9.0	9.2	9.9	10.0	0	0
$\sqrt{s}$-scaling (%)	3.9	3.4	3.0	2.7	2.4	2.2	2.1	1.9	1.7	1.6	1.7	0	0
extrapolation (%)	0	0	0	0	0	0	0	0	0	0	0	$^{+37.5}_{-27.1}$	$^{+40.8}_{-29.3}$
$\mathrm{D^+}$ 5.02 TeV													
measurement (%)	8.9	7.3	6.8	7.6	7.5	8.0	8.0	8.1	8.7	8.5	9.1	10.5	-
y_{cms}-scaling (%)	1.0	0.4	0.3	0.2	0.2	0.1	0.1	0.1	0.1	0.1	0.1	0.2	-
$\mathrm{D_s^+}$ 5.02 TeV													
measurement (%)	-	12.3	9.2	9.6	10.4	9.9		10.1		10.5	10.7	0	-
extrapolation (%)	-	0	0	0	0	0		0		0	0	$^{+41.5}_{-37.6}$	-

Table 6.6: Summary table of relative systematic uncertainties on the pp references.

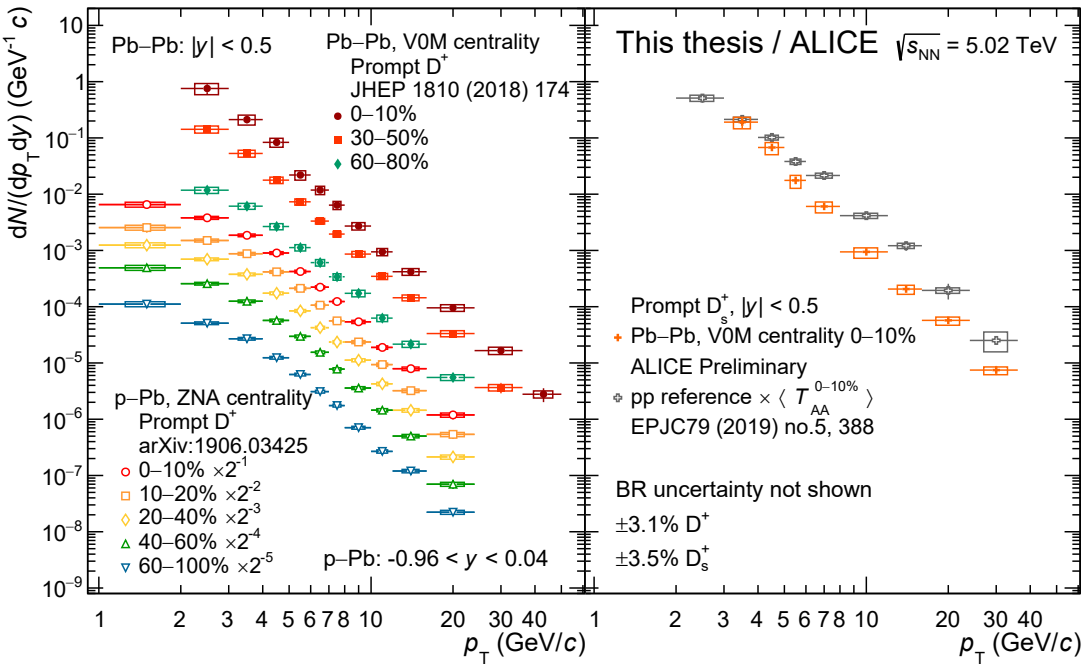

Figure 6.19: Left: p_{T}-differential corrected yields of D^+ mesons in Pb–Pb collisions at $\sqrt{s_{\mathrm{NN}}} = 5.02$ TeV compared to those in p–Pb collisions at the same centre-of-mass energy, rescaled for better visibility. Right: p_{T}-differential corrected yields of $\mathrm{D_s^+}$ mesons in the 10% most central Pb–Pb collisions at $\sqrt{s_{\mathrm{NN}}} = 5.02$ TeV compared to the pp reference scaled by the average nuclear overlap function.

6.6 Results

The left panel of Fig. 6.19 shows the p_{T}-differential corrected yields of prompt D^+ mesons in p–Pb and Pb–Pb collisions at $\sqrt{s_{\mathrm{NN}}} = 5.02$ TeV, for all the centrality classes of the analysis (see Table 6.1). The corrected yields measured in p–Pb collisions have been rescaled to improve the visibility. The right panel of the same Figure shows the p_{T}-differential corrected yield of prompt $\mathrm{D_s^+}$ mesons in the 10% most central Pb–Pb collisions at $\sqrt{s_{\mathrm{NN}}} = 5.02$ TeV, compared to the corresponding p_{T}-differential cross-section measured in pp collisions at the same centre-of-mass energy multiplied by the $\langle T_{\mathrm{AA}} \rangle$ of the same centrality class. The vertical bars represent the statistical uncertainty, while the boxes the total systematic uncertainty, except for the uncertainty on the branching ratio, which is quoted separately.

The nuclear modification factors were computed dividing the p_{T} differential corrected yields by the pp references described in Sec. 6.2.4 and Sec. 6.3.4, and are shown in Fig. 6.20 and Fig. 6.21 for Pb–Pb and p–Pb collisions, respectively. The statistical uncertainties are represented by the vertical bars, while the total systematic uncertainty by the empty boxes. The shaded box around unity represents the relative normalisation uncertainty.

The R_{AA} of prompt D^+ mesons with $p_{\mathrm{T}} > 3{-}4$ GeV/c shows an increasing suppression

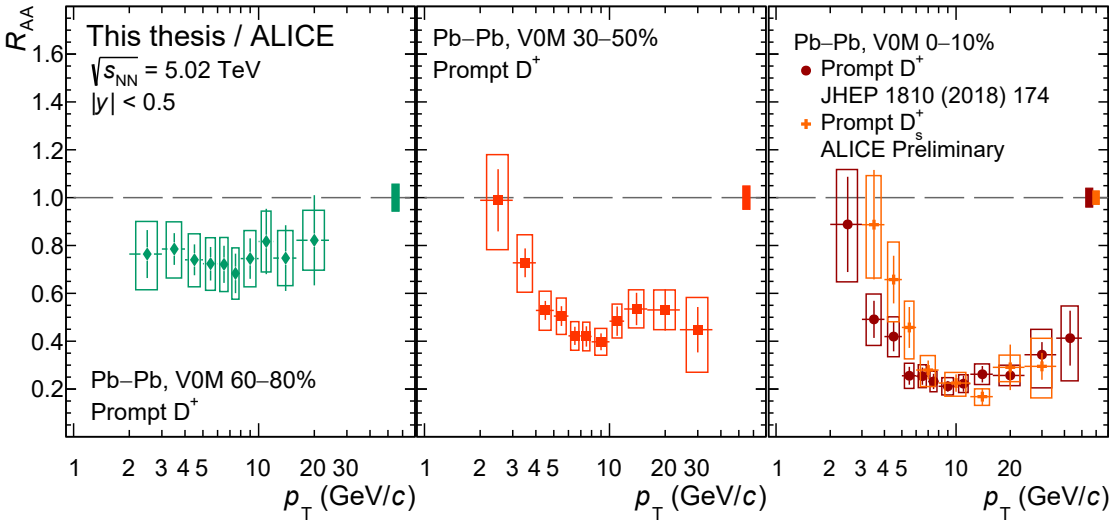

Figure 6.20: R_{AA} of prompt D^+ mesons from 60–80% peripheral (left panel) to 0–10% central (right panel) Pb–Pb collisions at $\sqrt{s_{NN}}$ = 5.02 TeV. The R_{AA} of prompt D_s^+ mesons in the 10% most central Pb–Pb collisions at $\sqrt{s_{NN}}$ = 5.02 TeV is superimposed to that of prompt D^+ mesons in the same centrality interval in the right panel.

from peripheral (60–80%) to central (0–10%) Pb–Pb collisions, while it is compatible within the three centrality classes and with unity for $p_T < 3$ GeV/c. The observed suppression is maximal in the range $6 < p_T < 10$ GeV/c and reaches a factor of about 5 in central collisions. For the 0–10% and 30–50% centrality classes, the R_{AA} rises steeply with decreasing p_T, while it increase slowly for $p_T > 10$ GeV/c. For peripheral collisions it remains nearly flat over the measured p_T range. This strong suppression at intermediated and high p_T indicates that the charm quarks substantially interact with the constituents of the QGP formed in Pb–Pb collisions losing energy.

The prompt D_s^+-meson R_{AA} in the 0–10% centrality class is similar to that of prompt D^+ mesons in the same centrality class for $p_T > 8$ GeV/c, while it is higher for $p_T < 8$ GeV/c, although the experimental points are still compatible within about one standard deviation of the combined statistical and systematic uncertainties. Therefore, no strong conclusion can be drawn on the predicted difference of the R_{AA} of D mesons with and without strange-quark content in presence of hadronisation via charm-quark coalescence in the QGP.

The Q_{pA} of prompt D^+ mesons is compatible with unity for all the centrality classes, with a hint of suppression in the $1 < p_T < 2$ GeV/c interval and a hint of enhancement in the $2 < p_T < 10$ GeV/c interval for the 0–10%, 10–20%, and 20–40% centrality classes. The suppression at low p_T is qualitatively expected from the nuclear modification of the PDFs, in particular from the shadowing effect [179], which is the dominant effect at the LHC energies because of the low values of Bjorken-x.

Figure 6.22 shows the Q_{CP} of prompt D^+ mesons, computed using the p_T-differential corrected yields measured in the 0–10%, 10–20%, 20–40%, and 40–60% centrality classes

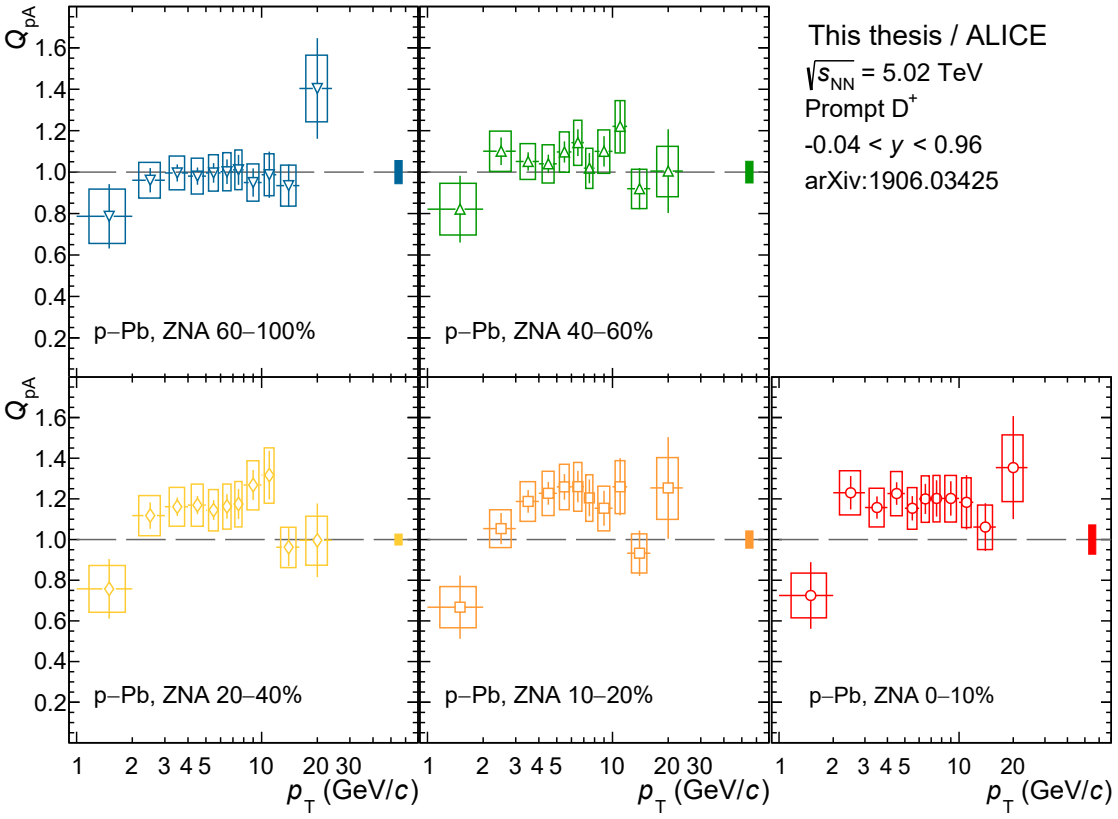

Figure 6.21: Q_{pA} of prompt D^+ mesons as a function of p_{T} from 60–100% peripheral (top-left panel) to central 0–10% (bottom-right panel) p–Pb collisions at $\sqrt{s_{\mathrm{NN}}} = 5.02$ TeV.

as numerators and that in the 60–10% centrality class the denominator. The enhancement in the $3 < p_{\mathrm{T}} < 10$ GeV/c interval seems to be more evident thanks to the reduced uncertainties with respect to those of the Q_{pA} measurement, however the uncertainty on the normalisation still prevents us to draw a firm conclusion on the formation of a high density final state.

6.6.1 Comparison to light-flavour hadrons

The comparison of the nuclear modification factors of open-charm mesons and light-flavour hadrons in Pb–Pb collisions is an important ingredient for the study of the in-medium energy loss properties, in particular for the quark-mass and colour charge dependences.

In order to have a more precise estimation of the nuclear modification factor of open-charm mesons without strange-quark content, the measurements of the D^+-meson R_{AA} presented in this thesis were averaged with those of D^0 and D^{*+} mesons measured in the same data sample, and hence same collision systems and centrality classes. The average was computed by using the inverse of the squared sum of the relative statistical and

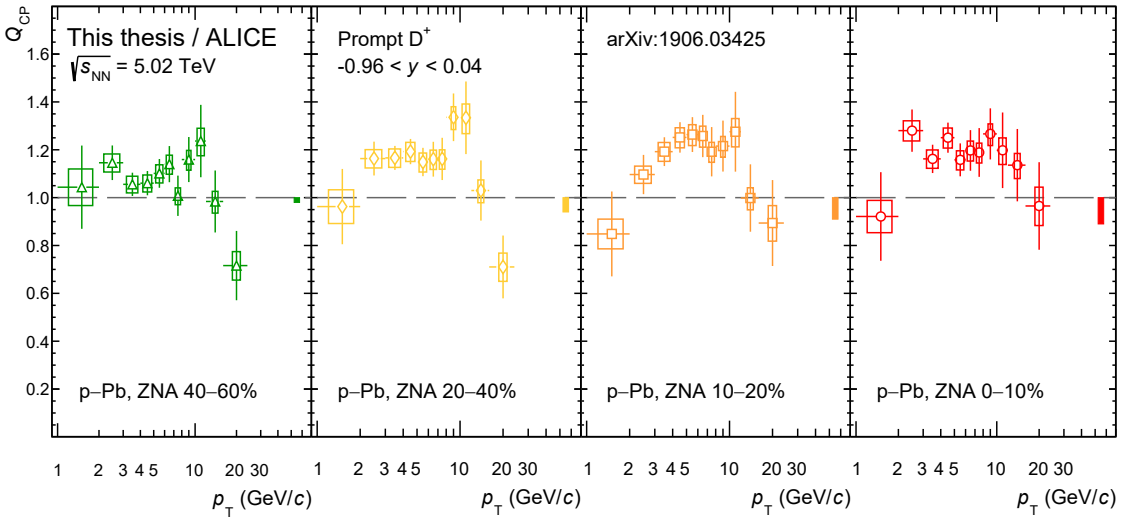

Figure 6.22: Q_{CP} of prompt D^+ mesons in p–Pb collisions at $\sqrt{s_{NN}} = 5.02$ TeV computed using the p_T-differential corrected yields measured in the 0–10%, 10–20%, 20–40%, and 40–60% centrality classes as numerators and that in the 60–100% centrality class as the denominator.

uncorrelated systematic uncertainties as weights. This can be done since it was verified that the measurements of the R_{AA} of prompt D^0, D^+, and D^{*+} mesons were compatible within the experimental uncertainties, as shown in Fig. 6.23 for the measurements in the 0–10% (left panel) and 60–80% (right panel) centrality classes of Pb–Pb collisions at $\sqrt{s_{NN}} = 5.02$ TeV performed with the 2015 data sample [3]. Moreover, the difference in their mass of about 0.3% in case of D^+ and D^0 and 7.5% in case of D^+ and D^{*+} [13] should however lead to a negligible effect.

In the top panels of Fig. 6.24, the average R_{AA} of prompt D^0, D^+, and D^{*+} mesons in the 0–10%, 30–50%, and 60–80% centrality classes of Pb–Pb collisions at $\sqrt{s_{NN}} = 5.02$ TeV, measured with the 2015 data sample [3], is compared to that of charged particles [61], which is dominated by the contribution of charged pions, measured at the same centre-of-mass energy and collision centralities. In the bottom panels of the same Figure, the ratios between the prompt D-meson and charged-particle nuclear modification factors is shown to provide a more quantitative estimation of the difference. In the 0–10% centrality class, the prompt D-meson R_{AA} is higher than that of charged particles of about two standard deviations, including both statistical and systematic uncertainties, in all the p_T intervals in the range $3 < p_T < 8$ GeV/c. The difference is reduced in the 30–50% centrality class and the ratio between the two R_{AA} is close to unity in the 60–80% centrality class. The R_{AA} of prompt D mesons and charged particles is consistent for $p_T > 8$ GeV/c, where the mass of the quark is expected to be less relevant. The difference at low p_T however is not only due to the quark-mass and colour-charge dependences of the in-medium energy loss, but also because of the harder fragmentation function and harder p_T distribution of charm quarks compared to those of light quarks as discussed

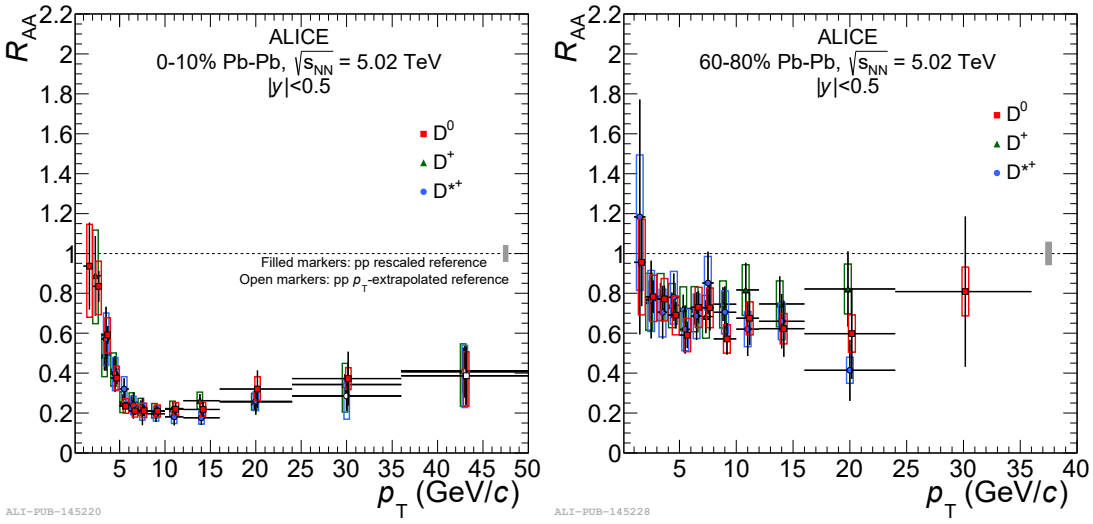

Figure 6.23: Comparison between the $R_{\rm AA}$ of prompt $\rm D^0$, $\rm D^+$ and $\rm D^{*+}$ mesons in Pb–Pb collisions at $\sqrt{s_{\rm NN}} = 5.02$ TeV for the 0–10% (left panel) and 60–80% (right panel) centrality classes. Figures taken from Ref. [3].

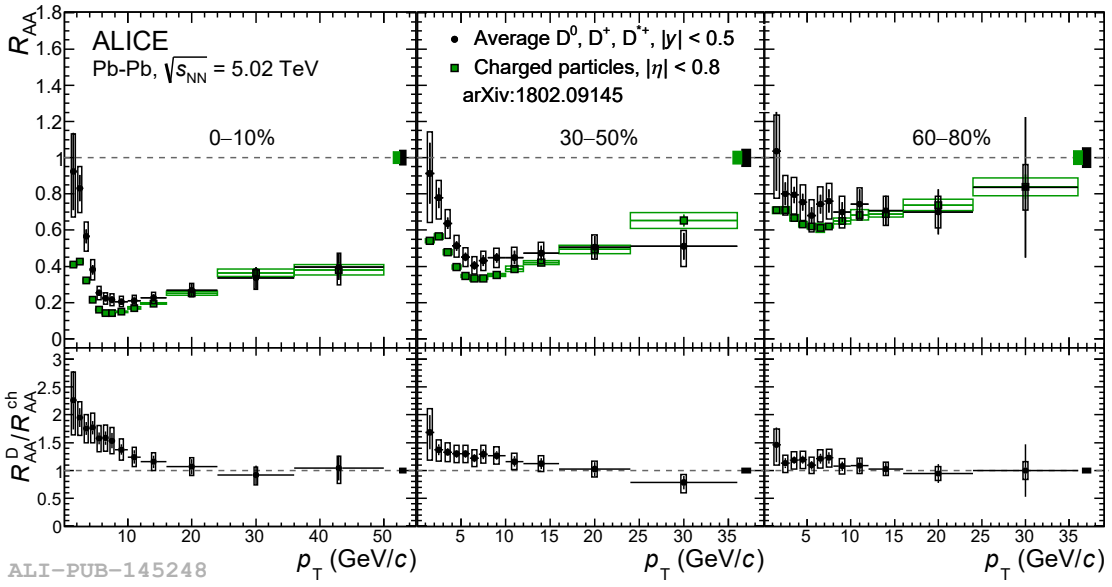

Figure 6.24: Average $R_{\rm AA}$ of prompt $\rm D^0$, $\rm D^+$, and $\rm D^{*+}$ mesons compared to that of charged particles in the 0–10% (left panel), 30–50% (middle panel), and 60–80% (right panel) centrality classes of Pb–Pb collisions at $\sqrt{s_{\rm NN}} = 5.02$ TeV. The bottom panels show the ratio between the $R_{\rm AA}$ of D mesons and that of charged particles. Figure taken from Ref. [3].

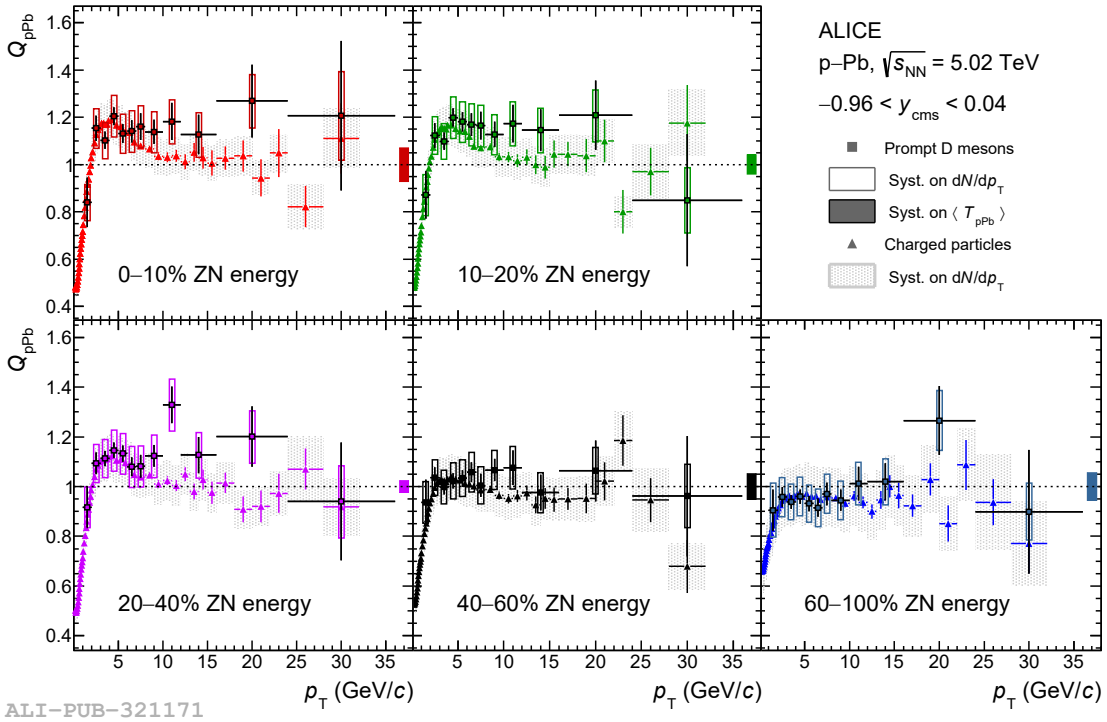

Figure 6.25: Average Q_{pA} of prompt D^0, D^+, and D^{*+} mesons compared to that of charged particles in the 0–10% (top-left panel), 10–20% (top-middle panel), 20–40% (bottom-left panel), 40–60% (bottom-middle panel), and 60–100% (bottom-right panel) centrality classes of p–Pb collisions at $\sqrt{s_{NN}} = 5.02$ TeV. Figure taken from Ref. [2].

in Ref. [180], the different radial flow, and the possible hadronisation via recombination. It has also to be considered the significant contribution to the charged-particle yield up to $p_T \approx 2 - 3$ GeV/c of soft-production processes, which scales with the number of participants instead of the number of binary nucleon–nucleon collisions, leading to a smaller R_{AA} of charged particles compared to that of D mesons.

For a more quantitative interpretation, the comparison between the measured R_{AA} of prompt D mesons and the model predictions is needed. This comparison will be discussed in Chapter 7 together with the same comparison of the D-meson elliptic flow, to provide a more complete view of the data interpretation.

Figures 6.25 and 6.26 show the comparison of the average prompt D-meson and charged-particle Q_{pA} and Q_{CP}, respectively. A similar trend of the nuclear modification factors of prompt D mesons and charged particles is observed in all the centrality classes of p–Pb collisions. In particular, the same suppression of the Q_{pA} for $p_T < 2$ GeV/c and enhancement for $2 < p_T < 10$ GeV/c are observed. Thanks to the reduced uncertainties achieved averaging the measurement of the three non-strange D-meson species, a significance of 3σ for a D-meson Q_{CP} larger than unity is achieved in the 20–40% centrality class in the $2 < p_T < 10$ GeV/c range. Despite the effect seems to be milder in this

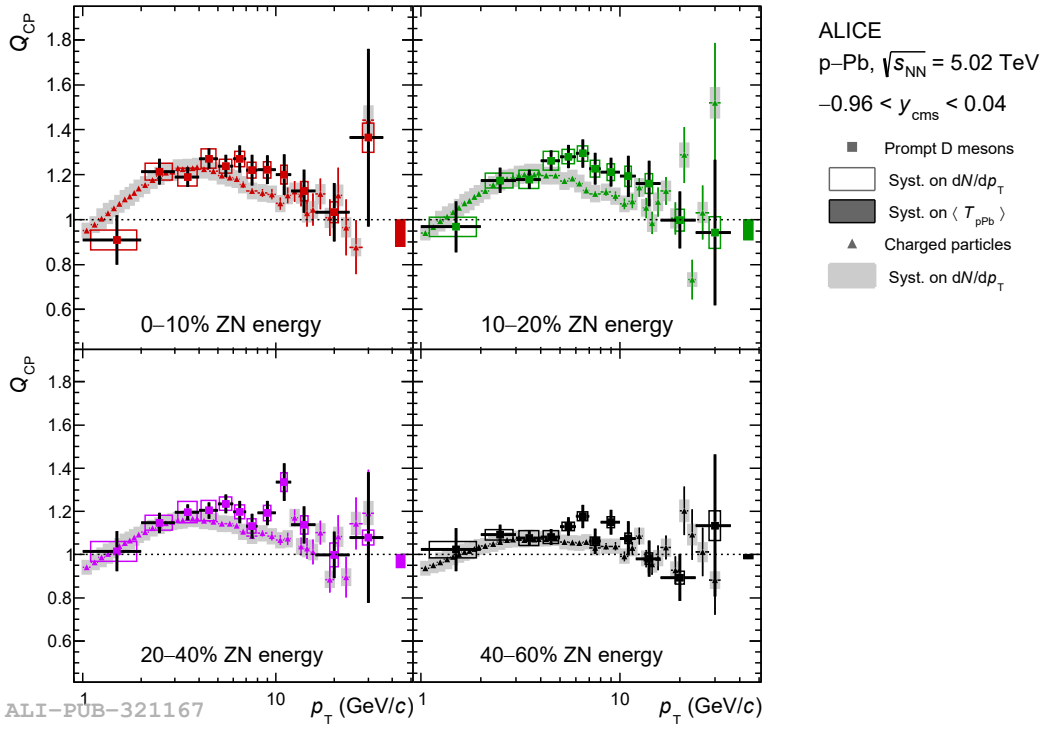

Figure 6.26: Average $Q_{\rm CP}$ of prompt $\rm D^0$, $\rm D^+$, and $\rm D^{*+}$ mesons compared to that of charged particles in the 0–10% (top-left panel), 10–20% (top-right panel), 20–40% (bottom-left panel), and 40–60% (bottom-right panel) centrality classes of p–Pb collisions at $\sqrt{s_{\rm NN}} = 5.02$ TeV. The yields measured in the 60–100% centrality class were used for the denominator. Figure taken from Ref. [2].

centrality class compared to the more central ones, the significance is higher because of the normalisation uncertainty, which is smaller for the 20–40% centrality class due to the reduced separation between the centrality classes used in the calculation of the $Q_{\rm CP}$.

6.6.2 Abundance of strange and non-strange D mesons

The measurement of the abundances of the different D-meson species in Pb–Pb and p–Pb collisions relative to those measured in pp collisions can provide information about the possible modification of the hadronisation mechanism.

The left panel of Fig. 6.27 shows the ratio of the $p_{\rm T}$-differential yields of prompt $\rm D^+$ and $\rm D^0$ mesons measured in the 0–10%, 20–40%, and 60-100% centrality classes of p–Pb collisions and in the 0–10%, 30–50%, and 60–80% centrality classes of Pb–Pb collisions at $\sqrt{s_{\rm NN}} = 5.02$ TeV, compared to the same quantity measured in pp collisions at the same centre-of-mass energy. In the right panel of the same Figure, the $p_{\rm T}$-differential $\rm D_s^+/D^0$ ratio in the 10% most central Pb–Pb collisions is compared to the same ratio measured in pp collisions and reported in Sec. 5.7. The $p_{\rm T}$-differential corrected yields of prompt

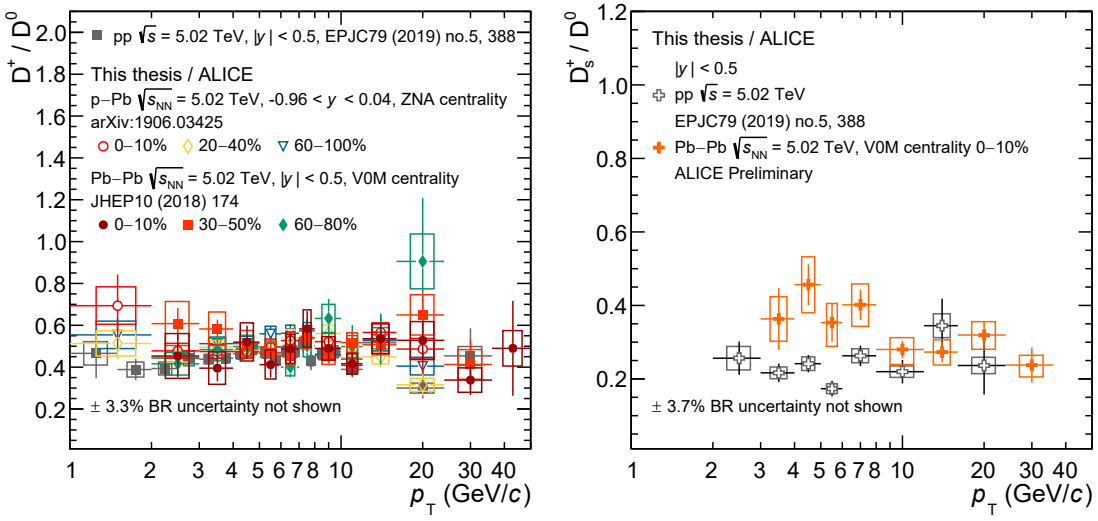

Figure 6.27: Left: D^+/D^0 p_T-differential yield ratios in the 0–10%, 20–40%, and 60–100% centrality classes of p–Pb collisions at $\sqrt{s_{NN}} = 5.02$ TeV and in the 0–10%, 30–50%, and 60–100% centrality classes of Pb–Pb collisions at $\sqrt{s_{NN}} = 5.02$ TeV, compared to the same quantity measured in pp collisions at $\sqrt{s} = 5.02$ TeV taken from Ref. [1]. Right: D_s^+/D^0 p_T-differential yield (cross-section) ratios measured in Pb–Pb (pp) collisions at $\sqrt{s_{NN}}(\sqrt{s}) = 5.02$ TeV.

D^0 mesons were measured using the same data samples adopted for D^+ mesons in this thesis [2, 3]. As for pp collisions (see Sec. 5.7), the systematic uncertainties on the BR, raw-yield extraction, and selection efficiency were propagated as uncorrelated among the different species, while the other sources as fully correlated.

The p_T-differential D^+/D^0 corrected-yield ratios are compatible in each centrality class and collision system considered, indicating no significance modification of the D^0 and D^+ relative abundances.

On the contrary, for the abundance of prompt D_s^+ mesons relative to that of prompt D^0 mesons a hint of difference is observed between the measurements in Pb–Pb and pp collisions. The p_T-differential D_s^+/D^0 ratio was found to be higher in Pb–Pb collisions with respect to pp collisions of about $1.5\sigma - 2\sigma$ for $3 < p_T < 8 - 10$ GeV/c, while compatible within less than 1σ for $p_T > 10$ GeV/c. Albeit the current precision does not allow for a firm conclusion, the observation of a higher D_s^+/D^0 ratio at intermediate p_T in Pb–Pb collisions compared to pp collisions is consistent with a scenario of charm-quark coalescence in a strangeness-rich medium. A preliminary measurement by the STAR Collaboration in Au–Au collisions at $\sqrt{s_{NN}} = 200$ GeV/c seem to indicate a similar enhancement [181]. Moreover, the low-intermediate p_T D_s^+/D^0 ratio is compatible with the p_T-integrated value predicted by the statistical-hadronisation model (SHM) in the grand-canonical ensamble [182].

Figure 6.28 the p_T-differential double ratio of D_s^+/D^0 ratio measured in the 10% most central Pb–Pb collisions and that measured in pp collision compared to the predictions

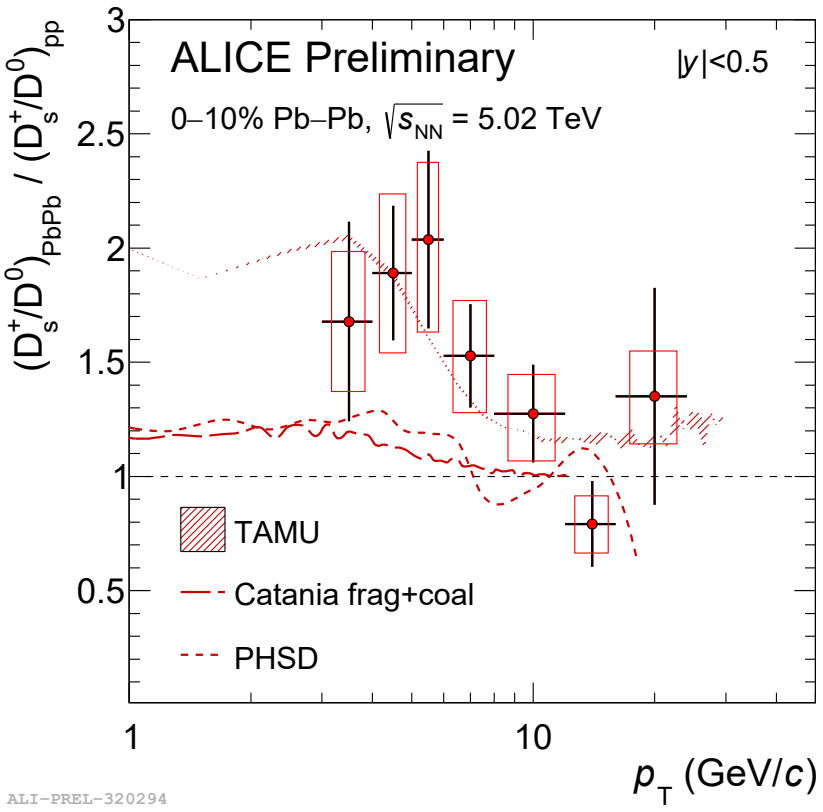

Figure 6.28: Double ratio of p_{T}-differential $\mathrm{D_s^+/D^0}$ ratios measured in the 10% most central Pb–Pb and pp collisions at $\sqrt{s_{\mathrm{NN}}}(\sqrt{s}) = 5.02$ TeV compared to the TAMU [170], CATANIA [115], and PHSD [178] model predictions.

provided by the TAMU [170], CATANIA [115], and PHSD [178] models. An increase of the $\mathrm{D_s^+}$ abundance relative to the non-strange D mesons is expected in the three models for $p_{\mathrm{T}} < 8 - 10$ GeV/c, while it decreases for higher p_{T}, going down to the pp value for the CATANIA and PHSD models. This enhancement is due to the hadronisation via coalescence in the QGP and the different interaction cross section of D mesons with and without strange-quark content in the hadronic phase of the system. The effect predicted by the CATANIA and PHSD models is similar and of the order of 20%, while it is larger for the TAMU model, which predicts and enhancement reaching a factor 2 around 4 GeV/c, similarly to what observed for the central values of the current measurement.

Chapter 7

D^+ elliptic flow in Pb–Pb collisions at $\sqrt{s_{\mathrm{NN}}} = 5.02$ TeV

In this Chapter, the measurement of the elliptic flow coefficient v_2 of prompt D^+ mesons in mid-central Pb–Pb collisions at $\sqrt{s_{\mathrm{NN}}} = 5.02$ TeV is discussed. The analysis was performed with the event-plane (EP) method [183] in the 10–30% and 30–50% centrality classes using the sample of MB Pb–Pb collisions collected in 2015 (see Sec 4.1.1), and it was published in Ref. [4] and in Ref. [5]. The number of analysed events was in this case 20.7×10^6 for each centrality class. The measurement was then improved in the 30–50% centrality class exploiting the sample of Pb–Pb collisions collected in 2018 with the semi-central trigger (see Sec 4.1.1 for details), consisting of 76.7×10^6 events. In this case, the scalar-product (SP) method [184] was adopted and the measurement was approved as preliminary result by the ALICE Collaboration.

7.1 Methods for the measurement of the anisotropic flow

The azimuthal anisotropy in the particle-momentum space is typically expressed in terms of Fourier decomposition with respect to the initial-state symmetry plane angles for the n^{th}-harmonic Ψ_n (see Sec. 1.4.5). The Ψ_n angles are not experimentally accessible but they can be estimated event-by-event via the measurement of the n^{th}-harmonic event-plane angle ψ_n that is built from the so called flow vectors $\boldsymbol{Q}_n$. The $\boldsymbol{Q}_n$-vectors are computed using the measured azimuthal angles of particles produced in the event as

$$\boldsymbol{Q}_n = \sum_{k=1}^{M} w_k e^{in\varphi_k}, \tag{7.1}$$

where the sum runs over all reconstructed tracks in case of the TPC, or segments of detectors with azimuthal segmentation like the V0, PMD or FMD detectors. The angle φ_k is the azimuthal emission angle of the particle or the azimuthal coordinate of the detector element k, respectively. For track-based $\boldsymbol{Q}_n$ vectors, the weights w_k can be unity or a function of φ or p_{T}, that can be useful to correct for a possible non-uniform acceptance of the detector or to enhance the contribution of particles with large anisotropy, improving

the resolution on ψ_n. For segmented detectors w_k is the amplitude of the signal measured in the k^{th} sector. The $\boldsymbol{Q}_n$ vectors are the basic quantity both for the EP and SP methods, which are described in the following sections.

7.1.1 Event-plane method

The EP method relies on the computation of the n^{th}-harmonic event-plane angles ψ_n from the $Q_{n,x}$ and $Q_{n,y}$ components of the $\boldsymbol{Q}_n$ vectors:

$$\psi_n = \frac{1}{n}\tan^{-1}\left(\frac{Q_{n,y}}{Q_{n,x}}\right). \tag{7.2}$$

The v_n coefficients can be then expressed as

$$v_n\{\text{EP}\} = \frac{1}{\mathcal{R}_n}\langle\cos[n(\varphi - \psi_n)]\rangle. \tag{7.3}$$

$\mathcal{R}_n$ is the event-plane resolution that takes into account the difference between true plane defined by the position of the participant nucleons in the initial-state geometry and the event plane estimated from final-state particles. The brackets indicate an average over all the particles and all the events, and φ is the azimuthal angle of the particles. The $\mathcal{R}_n$ resolution depends on the root square of the multiplicity of particles used to estimate ψ_n and on the strength of the average flow for the harmonic n [183]. It assumes zero values in case of a poor reconstruction of ψ_n and it is equal to unity for a perfect reconstruction of ψ_n. If the full event can be divided into two independent sub-events A and B, with corresponding event-plane angles ψ_n^{A} and ψ_n^{B}, with same multiplicity and rapidity coverage, the event-plane resolution for each sub-event can be expressed as

$$\mathcal{R}_n = \sqrt{\langle\cos[n(\psi_n^{\text{A}} - \psi_n^{\text{B}})]\rangle}. \tag{7.4}$$

If it is not possible to split the event in two sub-events with the same multiplicity and rapidity coverage, a method based on three event-plane estimates (A, B, C) is used. In this case, the event-plane resolution of the sub-event A can be obtained as

$$\mathcal{R}_n = \sqrt{\frac{\langle\cos[n(\psi_n^{\text{A}} - \psi_n^{\text{B}})]\rangle\langle\cos[n(\psi_n^{\text{A}} - \psi_n^{\text{C}})]\rangle}{\langle\cos[n(\psi_n^{\text{B}} - \psi_n^{\text{C}})]\rangle}}. \tag{7.5}$$

7.1.2 Scalar-product method

The SP method does not depend on the explicit calculation of the event-plane angle, but it provides the v_n coefficients directly from the correlation of the particle of interest with the $\boldsymbol{Q}_n$-vectors [184]. In particular, with the SP method, the v_n can be computed as

$$v_n\{\text{SP}\} = \frac{\langle \boldsymbol{u}_{n,\text{D}} \cdot \frac{\boldsymbol{Q}^*_{n,\text{A}}}{M_{\text{A}}}\rangle}{\sqrt{\frac{\langle \frac{\boldsymbol{Q}_{n,\text{A}}}{M_{\text{A}}} \cdot \frac{\boldsymbol{Q}^*_{n,\text{B}}}{M_{\text{B}}}\rangle \langle \frac{\boldsymbol{Q}_{n,\text{A}}}{M_{\text{A}}} \cdot \frac{\boldsymbol{Q}^*_{n,\text{C}}}{M_{\text{C}}}\rangle}{\langle \frac{\boldsymbol{Q}_{n,\text{B}}}{M_{\text{B}}} \cdot \frac{\boldsymbol{Q}^*_{n,\text{C}}}{M_{\text{C}}}\rangle}}}, \tag{7.6}$$

where $\boldsymbol{u}_{n,\mathrm{D}} = e^{in\varphi_\mathrm{D}}$ is the D-meson unitary vector, φ_D the azimuthal angle of the D meson, $\boldsymbol{Q}_n^i$ the n^{th}-harmonic flow vector for the sub-event i, and M^i the particle multiplicity in the corresponding sub-event. In case of segmented detectors M^i is the sum of the w_k weights defined in Eq. 7.1. The denominator in Eq. 7.6 is the analogue of the $\mathcal{R}_n$ factor in the EP method (see Eq. 7.5), and therefore it will be addressed as *scalar-product resolution* in the following.

7.2 Q_n-vector calibration

The detectors used in this Thesis to compute the $\boldsymbol{Q}_2$-vectors for the measurement of the D^+-meson v_2 are the TPC and V0 detectors. In particular, six different sub-events were defined using:

1. amplitudes in the V0A detector ($2.8 < \eta < 5.1$)
2. amplitudes in the V0C detector ($-3.7 < \eta < -1.7$)
3. amplitudes in the V0A and V0C detectors (V0M, $2.8 < \eta < 5.1 \cup -3.7 < \eta < -1.7$)
4. tracks of charged particles reconstructed in the full TPC volume ($|\eta| < 0.8$)
5. tracks of charged particles reconstructed in the TPC semi-volume with positive pseudorapidity ($0 < \eta < 0.8$)
6. tracks of charged particles reconstructed in the TPC semi-volume with negative pseudorapidity ($-0.8 < \eta < 0$).

Since there are no preferred orientations of the symmetry planes, the distribution of the event-plane angle ψ_2, and consequently the event-averaged φ-distribution of the emitted particles, are expected to be uniform. However, the measured ψ_2-distribution typically shows a modulation due to detector inefficiencies in the azimuthal direction, which could induce false correlations and bias the final results. Therefore, the $\boldsymbol{Q}_2$-vectors were corrected for the non-uniform acceptance of the detectors used to compute them.

For the V0 detectors a gain equalisation of each channel was applied to correct the raw amplitudes $M_{i,j}$:

$$M_{i,j}^{\mathrm{corr}} = M_{i,j}/\langle M_{i,j}\rangle \cdot M, \tag{7.7}$$

where $\langle M_{i,j}\rangle$ is the average amplitude for the channel corresponding to the i^{th} azimuthal sector and the j^{th} radial ring of the detector over all the events, and M is a gain factor fixed to the multiplicity of the first sector from each ring. In addition, a re-centering procedure was applied to the $\boldsymbol{Q}_2$ vectors, in order to obtain the distributions of the $Q_{2,x}$ and $Q_{2,y}$ components centred at zero:

$$\begin{aligned} Q_{2,x}^{\mathrm{rec}} &= Q_{2,x} - \langle Q_{2,x}\rangle \\ Q_{2,y}^{\mathrm{rec}} &= Q_{2,y} - \langle Q_{2,y}\rangle. \end{aligned} \tag{7.8}$$

These corrections were applied on a run-by-run basis as a function of the collision centrality and the interaction-vertex position along the z direction.

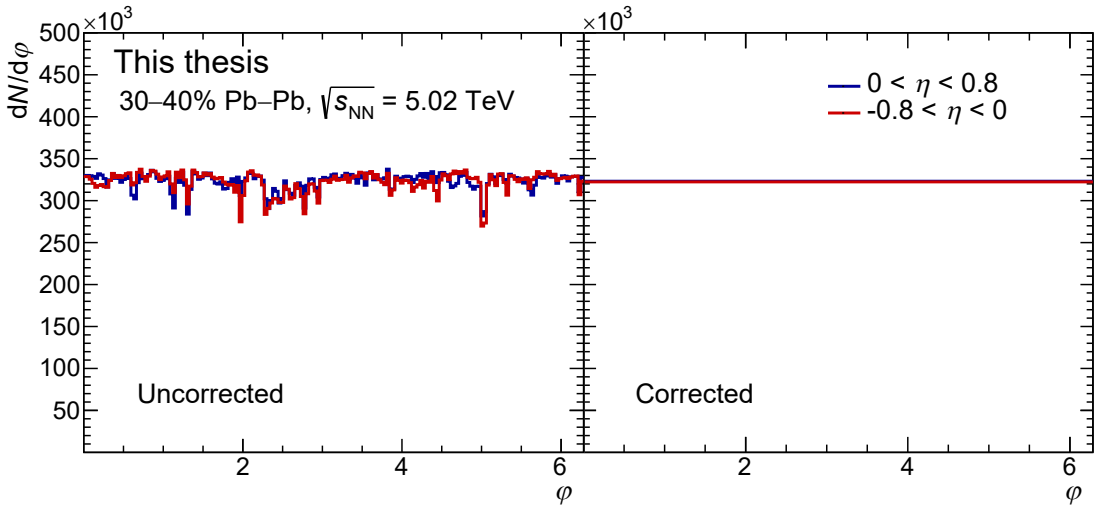

Figure 7.1: φ-distribution of TPC tracks before (left panel) and after (right panel) the correction for the non-uniform acceptance of the TPC detector.

For the TPC-based sub-events the correction was applied in terms of per-track weight w_k (see Eq. 7.1). The weights were computed run-by-run in intervals of collision centrality from the φ distribution of the tracks, as the ratio between the average number of tracks over φ ($\langle N \rangle$) and the value of the measured distribution in the i^{th} φ bin (N^i):

$$w_k^i = \langle N \rangle / N^i. \tag{7.9}$$

In Fig. 7.1 the azimuthal distribution of TPC tracks with $0 < \eta < 0.8$ and $-0.8 < \eta < 0$ in the 30–40% centrality class for one run of the Pb–Pb sample collected in 2018 is shown before and after the weighting correction as an example.

To test the goodness of the calibrations, the flatness of the event-plane-angle distribution was checked and it was found to be flat within 0.1% for the TPC-based ψ_2 angles and 2–3% for the V0-based ψ_2 angles, as shown in Fig. 7.2 for the 30–50% centrality class. The effect on the v_2 measurement of the remaining miscalibration was evaluated as explained in Sec. 7.6.3.

7.3 Sub-event configuration and EP (SP) resolution

The sub-event configurations for the analyses of the 2015 and 2018 data samples are summarised in Table 7.1. In both cases, a pseudorapidity gap of more than 0.9 units ($|\Delta\eta| > 0.9$) between the interval of the measurement of D^+ mesons ($|\eta| < 0.8$) and that of the particles used to compute the main $\boldsymbol{Q}_2$-vectors ($-3.7 < \eta < -1.7$ in case of V0C detector, and $-3.7 < \eta < -1.7 \cup 2.8 < \eta < 5.1$ in case of VOM) ensures the suppression of the contribution of unwanted non-flow correlations to the v_2 measurement. Non-flow correlations are correlations among the emission angles of the particles not induced by the collective expansion of the system, but rather by jet production and particle decays.

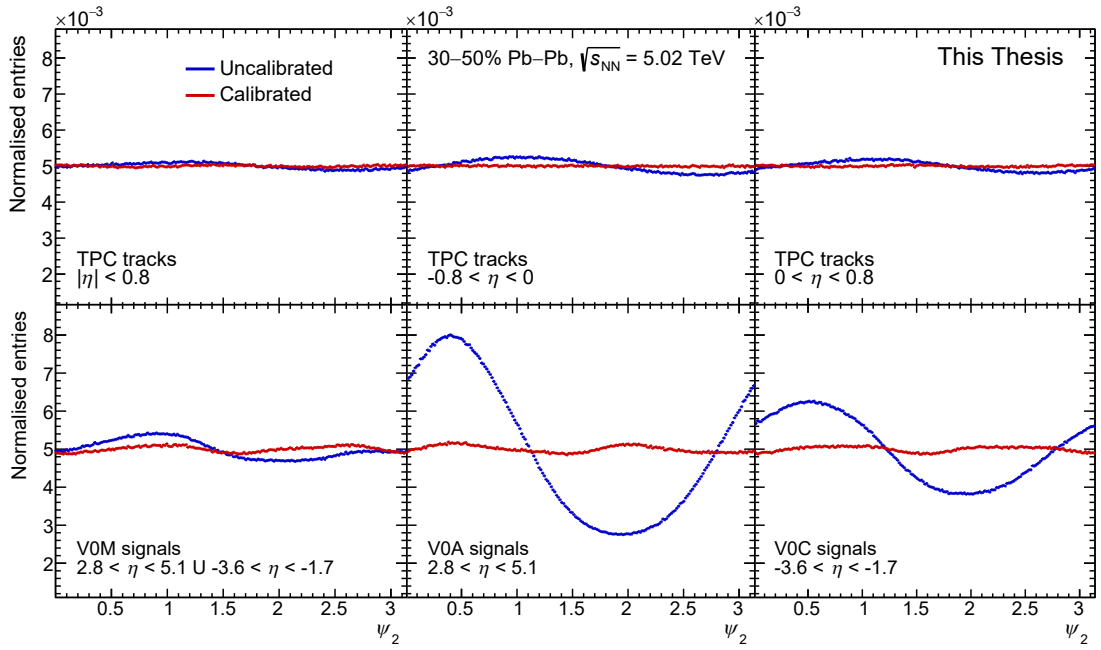

Figure 7.2: Second-harmonic event-plane angle distributions obtained using TPC tracks and V0 signals before and after the $\boldsymbol{Q}_2$-vector calibration for Pb–Pb collisions at $\sqrt{s_{\rm NN}}$ = 5.02 TeV in the 30–50% centrality class.

On the one hand, the combination of V0A and V0C detectors provides a slightly higher resolution $\mathcal{R}_2$ than the V0C detector only. On the other hand, in case of the configuration with the full V0 detector, the null pseudorapidity gap between the two sub-events defined by tracks in the two semi-volumes of the TPC detector can induce a small bias in the estimation of $\mathcal{R}_2$ owing to the possible non-flow correlations. In the left panel of Fig. 7.3 the $\mathcal{R}_2$ factors for the V0C and V0M estimators of the event plane is shown as a function of the centrality percentile, for the two Pb–Pb samples analysed. The $\mathcal{R}_2$ factor increases from central to mid-central collisions because of the increase of the average eccentricity of the events, while its decrease towards more peripheral (50%) collisions is mainly due to the decrease of the particle multiplicity. The values of $\mathcal{R}_2$ for the two detector configurations obtained with the 2015 and 2018 data samples are similar, indicating similar detector conditions during the two periods of data taking. The right panel of Fig. 7.3 shows the SP resolution (denominator of Eq. 7.6) as a function of the

Year	Main sub-event A	Sub-event B	Sub-event C
2015	V0A+V0C signals	TPC tracks $0 < \eta < 0.8$	TPC tracks $-0.8 < \eta < 0$
2018	V0C signals	V0A signals	TPC tracks $\|\eta\| < 0.8$

Table 7.1: Summary table of sub-events used to measure the $\boldsymbol{Q}_2$-vectors.

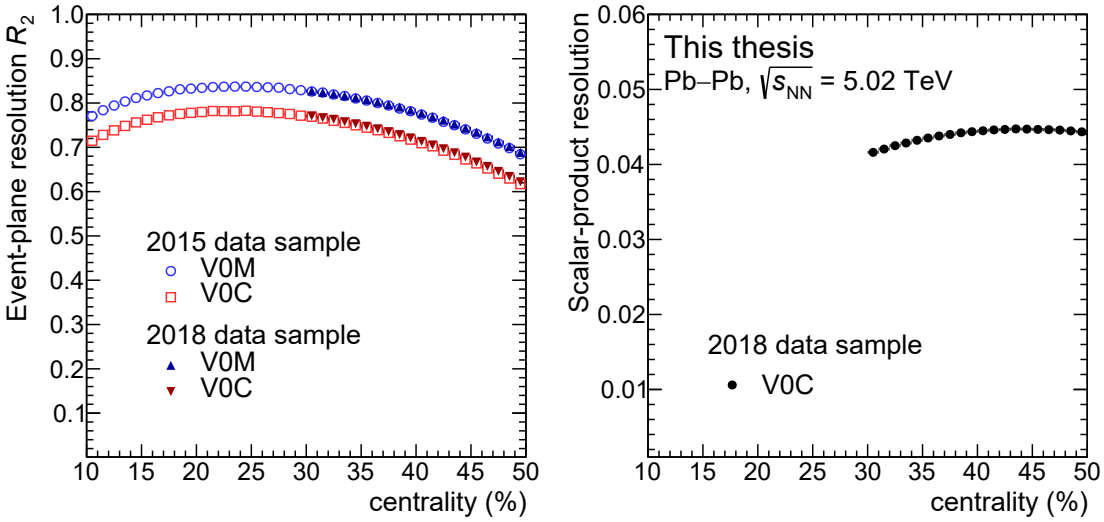

Figure 7.3: Left: event-plane resolution $\mathcal{R}_2$ of V0C and full V0 detectors as a function of the collision centrality for the two data samples of Pb–Pb collisions at $\sqrt{s_{NN}} = 5.02$ TeV analysed. Right: scalar-product resolution of the V0C detector as a function of the collision centrality for the sample of semi-central Pb–Pb collisions at $\sqrt{s_{NN}} = 5.02$ TeV collected in 2018.

collision centrality in the 30–50% centrality class. The SP resolution in this centrality interval has a milder centrality dependence compared to $\mathcal{R}_2$ and the opposite trend, i.e. it increases from more central to more peripheral events.

The corresponding values of EP and SP resolutions for the events integrated in the centrality classes of the analyses are summarised in Table 7.2.

Method	Year	Centrality class	Detector	Resolution
EP	2015	10–30%	V0M	0.8223 ± 0.0001
	2015	30–50%	V0M	0.7708 ± 0.0001
	2018	30–50%	V0M	0.7733 ± 0.0001
	2015	10–30%	V0C	0.7669 ± 0.0001
	2015	30–50%	V0C	0.7077 ± 0.0001
	2018	30–50%	V0C	0.7113 ± 0.0001
SP	2018	30–50%	V0C	0.04391 ± 0.0001

Table 7.2: Event-plane and scalar-product resolutions of V0C and full V0 detectors in the 10–30% and 30–50% centrality classes for the two data samples of Pb–Pb collisions at $\sqrt{s_{NN}} = 5.02$ TeV analysed. Only the statistical uncertainty is reported.

p_T (GeV/c)	[2,3]	[3,4]	[4,5]	[5,6]	[6,7]	[7,8]	[8,10]	[10,12]	[12,16]	[16,24]	[24,36]
$10-30\%$											
L (μm) >	-	1200	1300	1400	1400	1400	1400	1400	1500	1500	-
L_{xy}/σ_{xy} >	-	13	12	12	12	12	10	10	10	10	-
σ_{vertex} (μm) <	-	200	200	200	200	200	220	220	220	220	-
$\cos\theta_p$ >	-	0.997	0.997	0.997	0.997	0.997	0.992	0.992	0.992	0.990	-
$\cos\theta_p^{xy}$ >	-	0.998	0.997	0.997	0.997	0.997	0.992	0.992	0.992	0.990	-
$\lvert d_0^{xy}\rvert$ (μm) <	-	60	60	60	60	60	60	60	60	60	-
$\lvert D_0^{xy}\rvert$ <	-	1.5	2.0	2.0	2.0	2.0	2.0	2.0	2.0	2.0	-
$30-50\%$											
L (μm) >	800	1000	1000	1000	1200	1200	1200	1200	1200	1400	1400
L_{xy}/σ_{xy} >	12	12	12	12	10	10	10	9	9	8	8
σ_{vertex} (μm) <	200	220	220	220	220	220	240	240	240	240	340
$\cos\theta_p$ >	0.996	0.996	0.995	0.995	0.995	0.995	0.990	0.990	0.990	0.980	0.970
$\cos\theta_p^{xy}$ >	0.996	0.996	0.995	0.995	0.995	0.995	0.990	0.990	0.990	0.980	0.970
$\lvert d_0^{xy}\rvert$ (μm) <	80	60	60	60	60	60	60	60	60	60	60
$\lvert D_0^{xy}\rvert$ <	1.5	1.5	2.0	2.0	2.0	2.0	2.0	2.0	2.0	2.5	2.5

Table 7.3: Topological and kinematical selections applied to the D^+ candidates in Pb–Pb collisions at $\sqrt{s_{NN}} = 5.02$ TeV for the measurement of the v_2 in the 10–30% and 30–50% centrality classes.

7.4 D^+-meson v_2 extraction

In this Section the selection criteria used to selected D^+ candidates in the v_2 analysis aimed at improving the signal-to-background and the statistical significance of the measurement are presented. In addition, the techniques used to extract the v_2 coefficient of D^+ mesons with the EP and SP methods are discussed.

7.4.1 D^+-meson topological and kinematical selections

The selections of D^+ candidates were tuned with a strategy similar to the one described in Sec. 5.1 and Sec. 6.1. The topological and kinematical selection criteria applied in the p_T intervals of the measurements for two centrality classes are reported in Table 7.3. Tighter selection criteria were applied in the 10–30% centrality class to reduce the larger combinatorial background arising from the larger charged-particle multiplicity in the 10–30% centrality class compared to that in the 30–50% centrality class. In addition to the topological selections, also the conservative PID selection strategy (see Sec. 4.2.4) was applied to the decay tracks to further reduce the combinatorial background. The same selection criteria were adopted for the analysis of the samples collected in 2015 and 2018.

7.4.2 D^+-meson v_2 extraction with the EP method

The simplest technique to measure the v_n coefficient of D^+ mesons with the EP method is the extraction of the signal from the invariant-mass distributions of the candidates in intervals of $\Delta\varphi = \varphi_{\mathrm{D}} - \psi_n$, where φ_{D} is the azimuthal angle of the reconstructed D^+ meson. The resulting distribution of signal yield as a function of φ can be then fitted with the functional form

$$\frac{\mathrm{d}N(\mathrm{D}^+)}{\mathrm{d}\Delta\varphi} = k \cdot [1 + n v_n \mathcal{R}_n \cos(n\Delta\varphi)], \tag{7.10}$$

where k is a normalisation constant.

In case of relatively rare observables, e.g. D mesons, it could be however not convenient to extract the signal in several $\Delta\varphi$ bins; in this case, an alternative method that requires the extraction of the signal in only two $\Delta\varphi$ intervals, namely *in-plane* and *out-of-plane*, could be adopted. The in-plane and out-of-plane intervals depend on the harmonic and, for example, for the 2$^{\mathrm{nd}}$ harmonic are $\left(-\frac{\pi}{4}, \frac{\pi}{4}\right] \cup \left(\frac{3\pi}{4}, \frac{5\pi}{4}\right]$ and $\left(\frac{\pi}{4}, \frac{3\pi}{4}\right] \cup \left(\frac{5\pi}{4}, \frac{7\pi}{4}\right]$, respectively. The in-plane and out-of-plane yields ($N_{\text{in-plane}}$, $N_{\text{out-of-plane}}$) of D^+ mesons can be the calculated from Eq. 7.10:

$$\begin{aligned} N_{\text{in-plane}} &= k \int_{\text{in-plane}} (1 + n v_n \mathcal{R}_n \cos(n\Delta\varphi)) \mathrm{d}\Delta\varphi = k'(\pi + n^2 v_n \mathcal{R}_n) \\ N_{\text{out-of-plane}} &= k \int_{\text{out-of-plane}} (1 + n v_n \mathcal{R}_n \cos(n\Delta\varphi)) \mathrm{d}\Delta\varphi = k'(\pi - n^2 v_n \mathcal{R}_n) \end{aligned} \tag{7.11}$$

Therefore, the v_n coefficient can be expressed as

$$v_n\{\mathrm{EP}\} = \frac{\pi}{n^2} \frac{1}{\mathcal{R}_n} \frac{N_{\text{in-plane}} - N_{\text{out-of-plane}}}{N_{\text{in-plane}} + N_{\text{out-of-plane}}}. \tag{7.12}$$

However, harmonics different from the n^{th} can contribute to the anisotropy between the in-plane and out-of-plane regions, introducing a bias in the v_n measurement. In the case of the v_2 coefficient, the v_4 and v_8 coefficients, as well as the odd harmonics, induce the same average contribution in the in-plane and out-of-plane yields, leading to an overall null contribution. The sixth and tenth harmonics instead do not cancel completely causing a small bias, that is however negligible owing to the measurement of the v_6 and v_{10} coefficients for light hadrons, which are significantly smaller compared to the v_2 coefficient [185].

Since the event-plane angle is uniformly distributed between 0 and 2π, the reconstruction efficiency of D^+ mesons is not expected to depend on $\Delta\varphi$, except for the possible effect of the different local multiplicity of charged particles in-plane and out-of-plane. However, in Ref. [186] it was verified that the difference in the efficiency introduced by the local charged-particles multiplicity is negligible, and therefore the raw yields of D^+ mesons can be directly used in Eq. 7.12 without applying any efficiency correction.

The in-plane and out-of-plane raw yields for the second-harmonic coefficient v_2 were extracted via fits to the invariant-mass distributions of D^+ candidates obtained in the

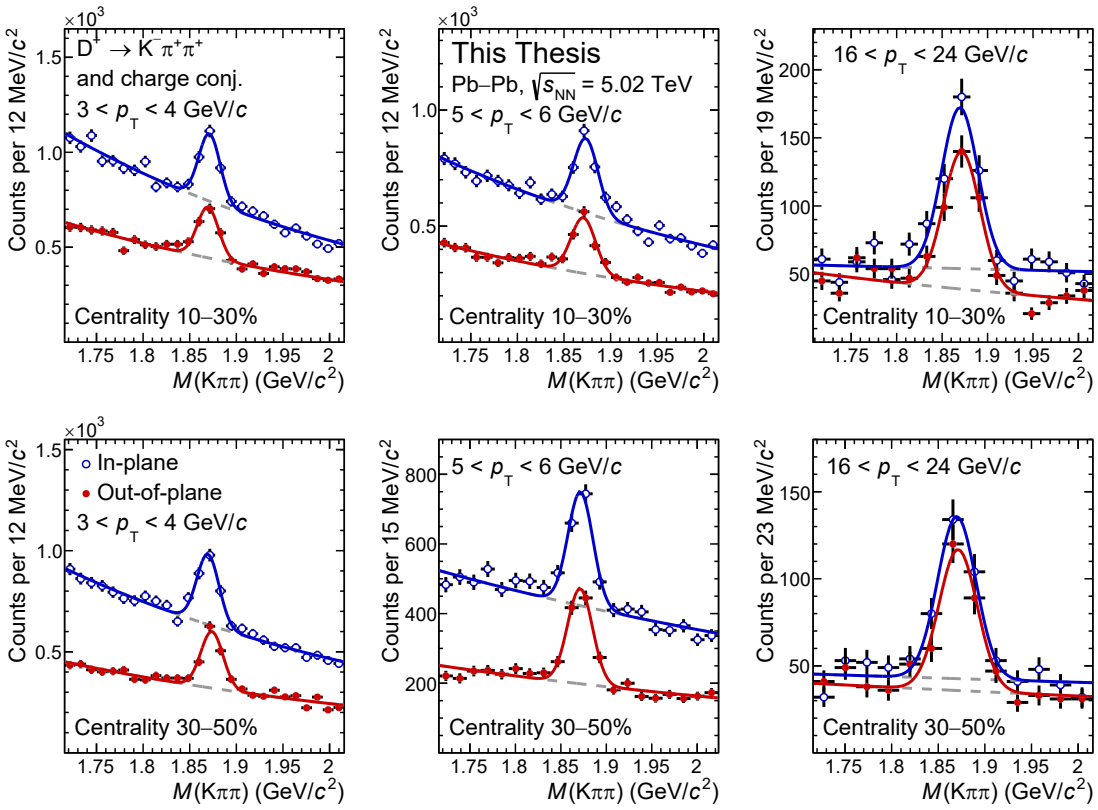

Figure 7.4: Fits to the in-plane and out-of-plane invariant-mass distributions of D^+-meson candidates in the intervals $3 < p_T < 4$ GeV/c, $5 < p_T < 6$ GeV/c, and $16 < p_T < 24$ GeV/c obtained with the sample of Pb–Pb collisions at $\sqrt{s_{NN}} = 5.02$ TeV collected in 2015 in the 10–30% (top panels) and 30–50% (bottom panels) centrality classes. The solid and the dotted curves represent the total and the combinatorial-background fit functions, respectively.

corresponding $\Delta\varphi$ interval. Figure 7.4 shows the fits to the in-plane (in blue) and out-of-plane (in red) invariant-mass distributions of D^+ candidates in the intervals $3 < p_T < 4$ GeV/c, $5 < p_T < 6$ GeV/c, and $16 < p_T < 24$ GeV/c obtained with the sample of Pb–Pb collisions collected in 2015, in the 10–30% (top panels) and 30–50% (bottom panels) centrality classes. The same function, composed of a Gaussian term to describe the signal and an exponential term for the combinatorial background, was utilised both to describe the in-plane and the out-of-plane distributions. The function parameters were let free in the two functions, except for the Gaussian width, which was fixed to the value extracted from the φ-integrated sample, since the invariant-mass resolution was not expected to depend on $\Delta\varphi$. This assumption was verified by repeating the fits leaving the Gaussian width as a free parameter and comparing the values obtained from the in-plane and out-of-plane distributions. Figure 7.4 shows the comparison of the Gaussian width (left panel) and mean (right panel) extracted in the two $\Delta\varphi$ regions. The Gaussian width was found

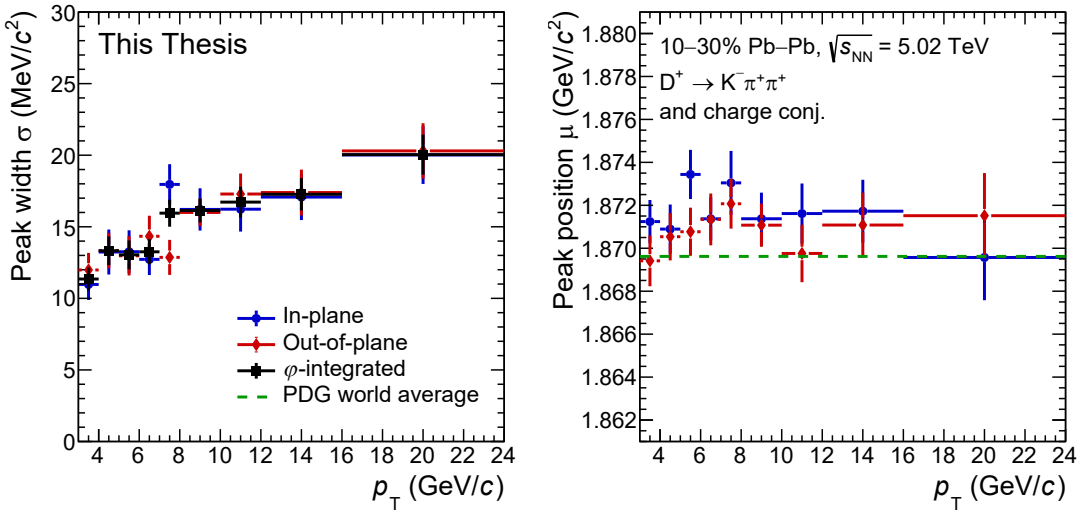

Figure 7.5: Left: Gaussian width extracted from the fits to the in-plane, out-of-plane, and φ-integrated invariant-mass distributions of D^+ candidates. Right: Gaussian mean extracted from the fits to the in-plane and out-of-plane invariant-mass distributions of D^+ candidates compared to the world-average value from the PDG [13].

to be compatible within one standard deviation in the full p_{T} range of the measurement, except for the interval $7 < p_{\mathrm{T}} < 8$ GeV/c, where the two values differ of about $3\,\sigma$, likely due to a statistical fluctuation.

7.4.3 D^+-meson v_2 extraction with the SP method

Since the sample of selected D^+ candidates includes both signal and background, it is not possible to directly extract the v_n of D^+ mesons with the SP method using Eq. 7.6. Hence, the average v_n is evaluated in narrow intervals of invariant mass (M), and expressed as a weighted average of the v_n of the signal (v_n^{sig}) and that of the background (v_n^{bkg}):

$$v_n(M) = \frac{S(M)}{S(M)+B(M)} \cdot v_n^{\mathrm{sig}} + \frac{B(M)}{S(M)+B(M)} \cdot v_n^{\mathrm{bkg}}(M), \tag{7.13}$$

where the weights are given by the relative fraction of signal (S) and background (B) in the invariant-mass interval considered. The v_n of the background can depend on the invariant-mass and therefore it is usually defined as a function of M.

The v_2 of D^+ mesons was then extracted via a simultaneous fit of the invariant-mass and the $v_2(M)$ distributions of D^+ candidates. Figure 7.6 shows the simultaneous fits for D^+ candidates in six p_{T} intervals of the analysis in the 30–50% centrality class obtained from the Pb–Pb sample collected in 2018. The top panels show the fits to the invariant-mass distributions, while the bottom ones to the v_2 as a function of the invariant-mass.

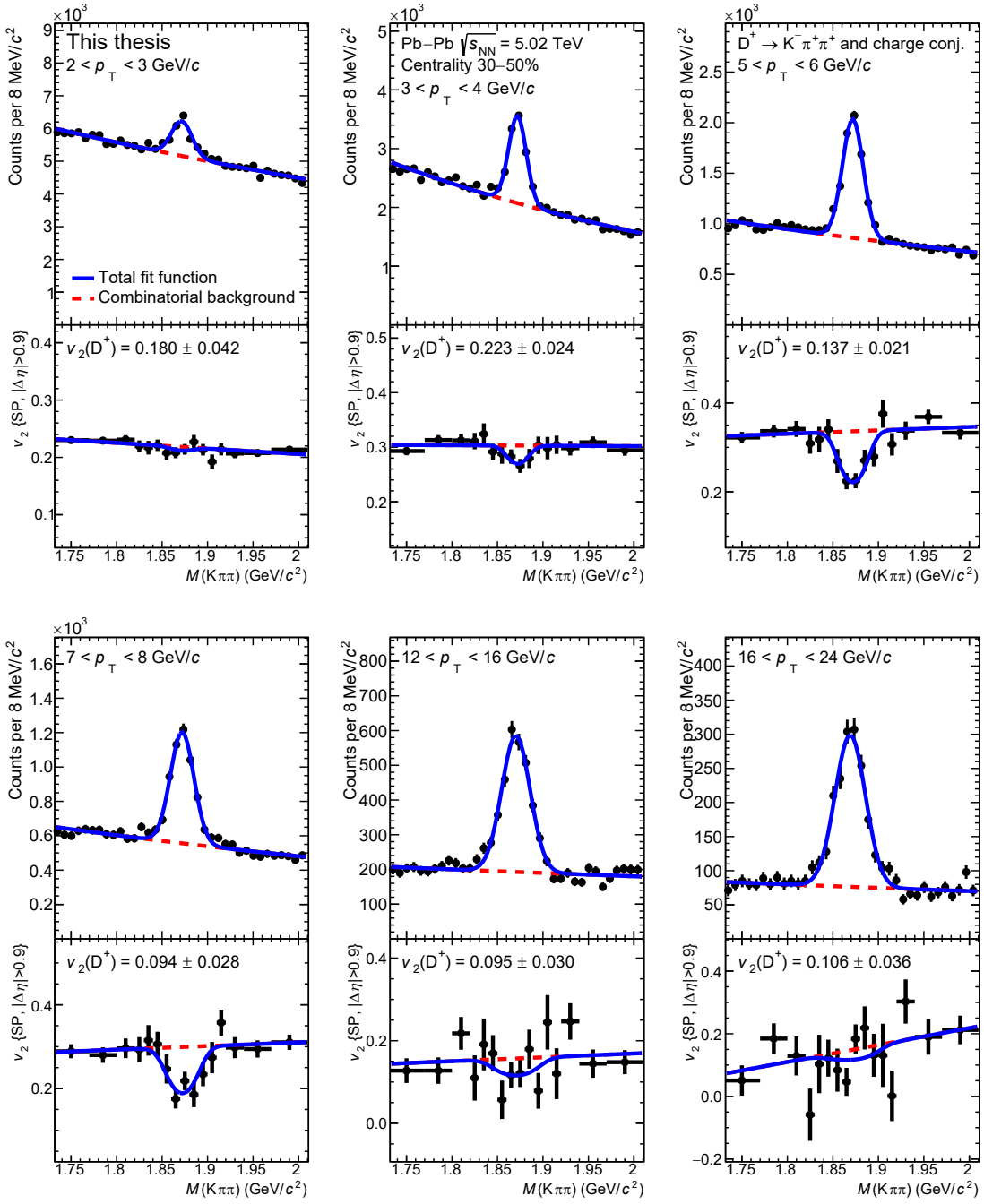

Figure 7.6: Simultaneous fits to the invariant-mass and v_2 vs. invariant-mass distributions of D^+-meson candidates in six p_T intervals of the analysis obtained with the sample of Pb–Pb collisions at $\sqrt{s_{NN}} = 5.02$ TeV collected in 2018. The solid-red and the dotted-blue curves represent the total and the combinatorial-background fit functions, respectively.

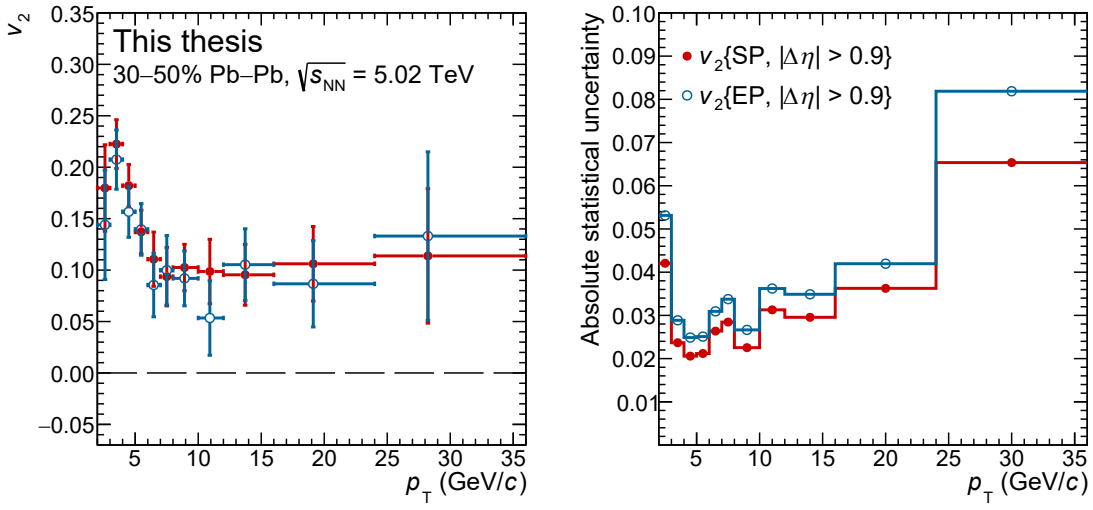

Figure 7.7: D$^+$-meson v_2 measured with the SP and EP methods using the sample of Pb–Pb collisions at $\sqrt{s_{\rm NN}} = 5.02$ TeV collected in 2018 (left panel) and their absolute statistical uncertainty (right panel).

For the $v_2(M)$ distributions a wider binning was used in the side-band regions of the invariant-mass distributions to reduce statistical fluctuations in regions where the number of candidates is small. The fit function adopted for the invariant-mass distribution is the same as the one used for the in-plane and out-of-plane fits (see Sec. 7.4.2), while for the $v_2(M)$ distribution, the function reported in Eq. 7.13 was used, where $v_2^{\rm bkg}$ was parametrised with a linear function of the invariant mass.

As additional cross check, the v_2 coefficient of D$^+$ mesons measured with the SP method was compared with the one measured with the EP method in the same Pb–Pb data sample. The two results were found to be in agreement, as shown in the left panel of Fig. 7.7. In the right panel of the same Figure, the absolute statistical uncertainties obtained with the two methods are also compared. The uncertainty obtained with the SP method is systematically lower of about 10-15%.

7.5 Correction for the fraction of prompt D$^+$ mesons

The sample of D$^+$ candidates used to measure the v_2 contains both prompt and feed-down D$^+$ mesons. Since the v_2 of charm and beauty hadrons is expected to be different [187–190], a correction for the fraction of prompt D$^+$ in the selected sample has to be applied. For this purpose, the measured D$^+$-meson elliptic flow $v_2^{\rm meas}$ was written as a weighted average of the prompt ($v_2^{\rm prompt}$) and feed-down ($v_2^{\rm feed\text{-}down}$) contributions:

$$v_2^{\rm meas} = f_{\rm prompt} \cdot v_2^{\rm prompt} + (1 - f_{\rm prompt}) \cdot v_2^{\rm feed\text{-}down} \tag{7.14}$$

The weight $f_{\rm prompt}$ in the above formula is the fraction of prompt D$^+$ mesons in the sample of selected D$^+$ candidates estimated using (i) the beauty-hadron cross section obtained

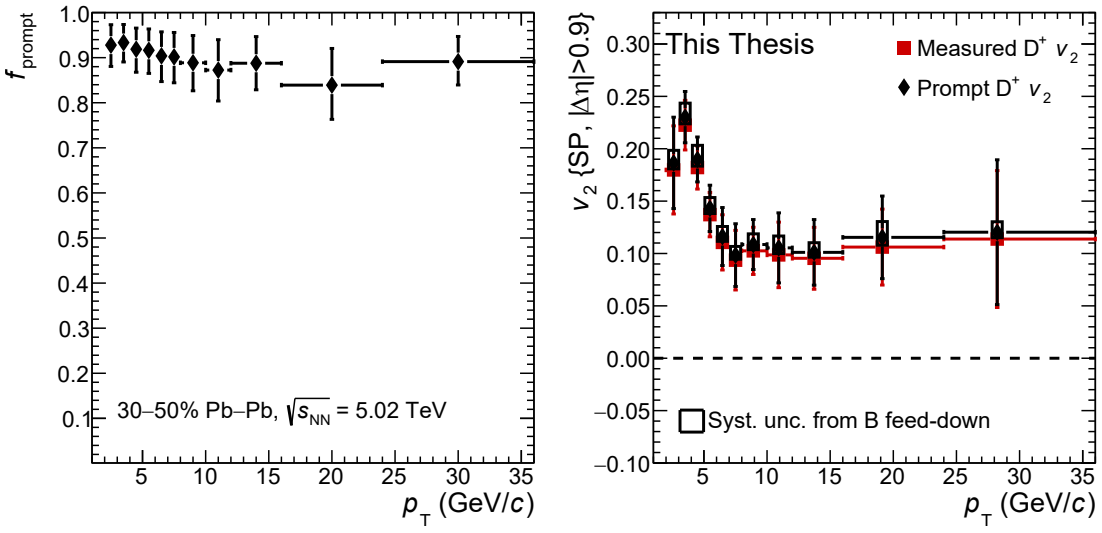

Figure 7.8: Left: fraction of prompt D^+ in the raw yield estimated with the theory-driven method discussed in Sec. 6.3.3. Right: comparison between the measured D^+-meson $v_2\{\mathrm{SP}\}$ and the one corrected for f_{prompt} as a function of p_{T}. The empty boxes represent the systematic uncertainty associated to procedure adopted the feed-down subtraction.

from FONLL calculations [79, 80] and the beauty-hadron $\rightarrow \mathrm{D} + \mathrm{X}$ decay kinematics from the EvtGen package [154], (ii) the acceptance and reconstruction efficiency of feed-down D^+ mesons from the MC simulation (see Sec. 6.3.2), and (iii) an assumption on the R_{AA} of feed-down D^+ mesons, as explained in Sec. 6.3.3. As for the measurement of the D^+-meson R_{AA}, the R_{AA} of feed-down D^+ mesons was assumed to be $R_{\mathrm{AA}}^{\text{feed-down}} = 2R_{\mathrm{AA}}^{\text{prompt}}$ for $3 < p_{\mathrm{T}} < 24$ GeV/c and $R_{\mathrm{AA}}^{\text{feed-down}} = 1.5R_{\mathrm{AA}}^{\text{prompt}}$ in the remaining p_{T} intervals. This hypothesis was varied in the ranges $1 < R_{\mathrm{AA}}^{\text{feed-down}}/R_{\mathrm{AA}}^{\text{prompt}} < 2$ and $1 < R_{\mathrm{AA}}^{\text{feed-down}}/R_{\mathrm{AA}}^{\text{prompt}} < 3$ for the two p_{T} intervals, respectively, as for the R_{AA} analysis (see Sec. 6.4.7). The fraction of prompt D^+ mesons in the 30–50% centrality class obtained with the sample of semi-central Pb–Pb collisions collected in 2018 is shown in the left panel of Fig. 7.8.

An additional assumption was then needed for the v_2 of feed-down D^+ mesons, which was not measured. Considering that the available models [187–190] and the measurement of the non-prompt J/ψ-meson v_2 performed by the CMS Collaboration in Pb–Pb collisions at $\sqrt{s_{\mathrm{NN}}} = 2.76$ TeV [106] indicate that $0 < v_2^{\text{feed-down}} < v_2^{\text{prompt}}$, the v_2 of feed-down D^+ mesons was assumed to be $v_2^{\text{feed-down}} = v_2^{\text{prompt}}/2$. Therefore, the v_2 of prompt D^+ mesons can be obtained from the measured v_2 by inverting Eq. 7.14:

$$v_2^{\text{prompt}} = \frac{2v_2^{\text{meas}}}{1 + f_{\text{prompt}}}. \tag{7.15}$$

In order to estimate a systematic uncertainty on this procedure, the probability distribution of $v_2^{\text{feed-down}}$ was assumed to be uniform between 0 and v_2^{prompt}. Therefore, the

uncertainty associated to $v_2^{\text{feed-down}}$ was evaluated as the standard deviation of a uniform distribution, which in this case corresponds to $v_2^{\text{prompt}}/\sqrt{12}$. Finally, the systematic uncertainty on v_2^{prompt} arising from the subtraction of the feed-down contribution was computed as the envelope of the uncertainties on $v_2^{\text{feed-down}}$ and f_{prompt} (see Sec. 6.4.7). The right panel of Fig. 7.8 shows the comparison between the measured D^+-meson $v_2\{\mathrm{SP}\}$ in the 30–50% centrality class and the same quantity corrected for the fraction of prompt D^+ mesons. The v_2 of prompt D^+ mesons obtained with this procedure results to be 5%-10% higher than the measured v_2 and the systematic uncertainties associated to this correction ranges from 0.001 to 0.015, depending on the centrality class and the p_{T}.

7.6 Systematic uncertainties

In this Section, the sources of systematic uncertainties considered for the measurement of the D^+ v_2 are presented. They include (i) the fitting procedure adopted to extract of the inclusive D^+ v_2, (ii) the determination of the EP (SP) resolution, (iii) the residual miscalibration of the $\boldsymbol{Q}_2$-vectors, and (iv) the subtraction of the feed-down contribution, which was described in Sec. 7.5.

7.6.1 Fitting procedure

The systematic uncertainty on the fitting procedure adopted to extract the D^+-meson v_2 was evaluated both for the EP and the SP methods with a multi-trial approach.

In the case of the EP method, the in-plane and out-of-plane fits were repeated several times with different fit configurations. The background fit function (linear, parabolic, and exponential) and the lower and upper limits of the fit range were varied coherently in the in-plane and out-of-plane fits. The invariant-mass bin width was also varied to cross-check that the value chosen for the central result did not introduce any bias in the measurement. This procedure was performed with the Gaussian width fixed to the value obtained from the φ-integrated invariant-mass distributions. In addition, the result was compared with the one obtained by leaving the Gaussian width as free parameter in the fits and by using the bin-counting method explained in Sec. 5.6.1 for the extraction of the raw yields.

For the SP method, the same fit configurations defined for the EP method were tested. In addition, the simultaneous fits to the v_2 and the invariant-mass distributions were repeated using a linear and a parabolic function to describe the v_2 of the background. The Gaussian width of the D^+ peak was always left as a free parameter in the fit, and the bin-counting method could not be applied.

For each trial the D^+-meson v_2 was extracted and the residual with respect to the central value ($\Delta v_2 = v_2 - v_2^{\text{ref}}$) was computed. The trials in which at least one fit had a reduced χ^2 larger than 2 were rejected. The absolute systematic uncertainty was evaluated considering the RMS and the shift from zero of the Δv_2 distributions obtained from the multi-trial study. The left panel of Fig. 7.9 shows an example of $\Delta v_2\{\mathrm{SP}\}$ distribution obtained with the sample of semi-central Pb–Pb collisions at $\sqrt{s_{\mathrm{NN}}} = 5.02$ TeV collected in 2018, for D^+ mesons with $3 < p_{\mathrm{T}} < 4$ GeV/c. The distributions corresponding to the trials with v_2^{bkg} parametrised with a linear and parabolic functions depicted in blue

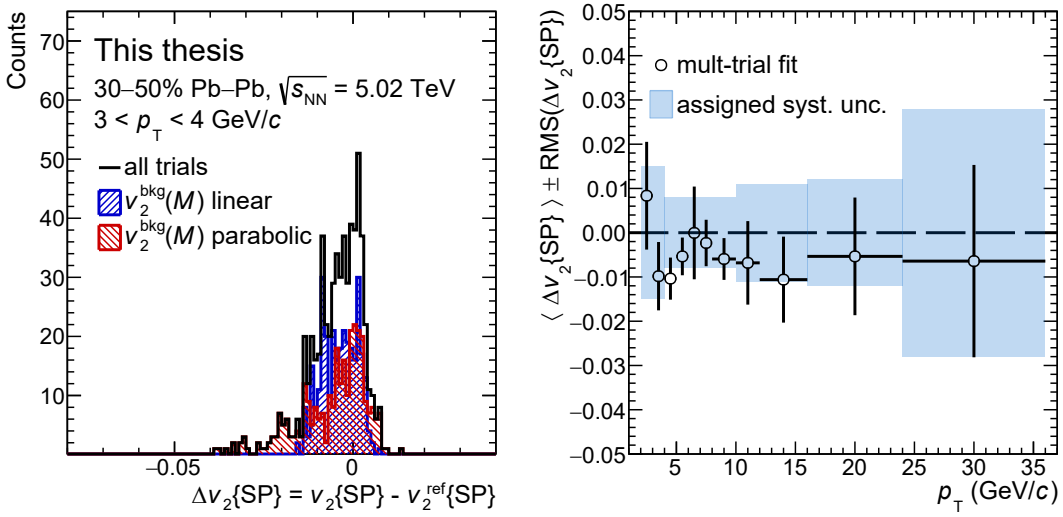

Figure 7.9: Left: distributions of $v_2\{\mathrm{SP}\}$ residuals obtained with the multi-trial study performed on the sample of semi-central Pb–Pb collisions at $\sqrt{s_{\mathrm{NN}}} = 5.02$ TeV collected in 2018 for the trials with the $v_2^{\mathrm{bkg}}(M)$ parametrised with a first-order polynomial (blue), second-order polynomial (red), and for all the trials (black) in the interval $3 < p_{\mathrm{T}} < 4$ GeV/c. Right: mean ± RMS of the residual distributions as a function of p_{T}. The blue band represents the assigned systematic uncertainty.

and red, respectively, are superimposed to the distribution of all the trials depicted in black. The distribution for the trials with the parabolic function has a larger tail towards negative values, which causes a systematic shifts the mean value of the total distribution. The same behaviour was observed for most of the p_{T} intervals of the analysis, as reported in the right panel of Fig. 7.9, where the mean of the residual distributions is shown as a function of p_{T}. The vertical bars represent the RMS of the distributions, while the blue band the assigned absolute systematic uncertainty, which ranges from 0.008 to 0.028 depending on p_{T}.

The values obtained for the SP method was compared to those obtained with the EP method using the same Pb–Pb sample, in order to avoid differences due to statistical fluctuations and not due to the method itself. The left panel of Fig. 7.10 shows the residuals distributions for the trials withGaussian width of D^+ candidates in-plane and out-of-plane fixed to the values obtained from the φ-integrated fits (blue), as free parameters (red), and by extracting the in-plane and out-of-plane raw yields with a bin-counting method (green). In the right panel of the same Figure, the mean ± RMS of each distribution are compared to those obtained for the SP method as a function of p_{T}. The values obtained with the Gaussian width fixed in the in-plane and out-of-plane fits are similar to those obtained with the SP method, while a less stable fit result is obtained in case of widths as free parameters in the fits or in case of the bin-counting method, due to the introduction of more degrees of freedom.

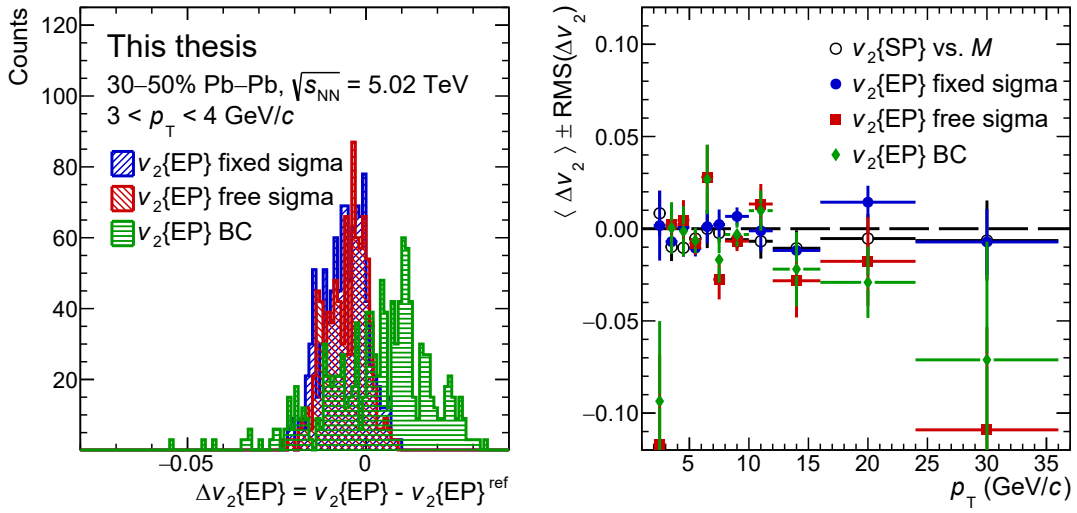

Figure 7.10: Left: distributions of $v_2\{EP\}$ residuals obtained with the multi-trial study performed on the sample of semi-central Pb–Pb collisions at $\sqrt{s_{NN}} = 5.02$ TeV collected in 2018 for the trials with Gaussian width of D^+ candidates in-plane and out-of-plane fixed to the values obtained from the φ-integrated fits (blue), as free parameters (red), and by extracting the in-plane and out-of-plane raw yields with a bin-counting (BC) method (green). Right: mean ± RMS of the residual distributions as a function of p_T compared to that obtained for the SP method.

7.6.2 EP and SP resolutions

The systematic uncertainty on the EP and SP resolutions include two sources. The first one is due to the centrality dependence of the EP or SP resolution within the relatively wide centrality interval of the analysis, while the second one is due to the possible non-flow correlations among the sub-events used to compute the resolution.

The first contribution was estimated by computing the (EP) SP resolution as an average of the resolutions obtained in narrower centrality intervals, weighted by the D^+-meson raw yields measured in the corresponding centrality intervals. The left panel of Fig. 7.11 shows the SP resolution (black full circles) and the D^+-meson raw yields (red open circles) obtained with the sample of semi-central Pb–Pb collisions collected in 2018 as a function of the collision centrality. It is clear from this Figure that the yield of D^+ mesons used to measure the v_2 is maximum for more central events, for which the SP resolution is minimum. Therefore, a systematic of 0.5% was assigned based on the relative difference of the SP resolution obtained with the weighted average to the one obtained considering all the events in the 30–50% centrality class. The same procedure was applied for the EP resolution, for which a 1% uncertainty was evaluated in both the 10–30% and 30–50% centrality classes, owing to the more pronounced centrality dependence of the EP resolution compared to the SP resolution.

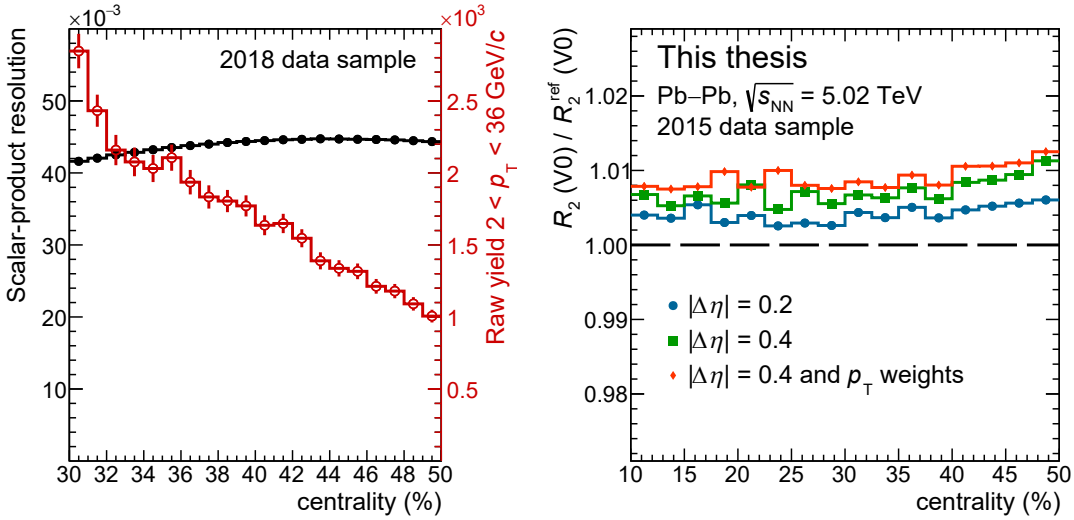

Figure 7.11: Left: SP resolution (black full circles) and D^+-meson raw yields (red open circles) obtained with the sample of semi-central Pb–Pb collisions collected in 2018 as a function of the collision centrality. Right: ratio of EP resolution of the V0 detector obtained with the pseudorapidity gaps between the TPC-based sub-events compared to the one default one (R_2^{ref}).

The contribution to the systematic uncertainty due to the possible non-flow correlations among the sub-events used for the EP resolution was estimated by varying the sub-events based on TPC tracks used to compute the $\mathcal{R}_2$ of the V0 detector (see Sec. 7.3). In particular, a pseudorapidiy gap of $|\Delta\eta| = 0.2$ and $|\Delta\eta| = 0.4$ was introduced between the sub-events defined with the tracks measured in the two semi-volumes of the TPC, in contrast to the $|\Delta\eta| = 0$ gap between the default TPC sub-events. In addition, in case of $|\Delta\eta| = 0.4$ the $\boldsymbol{Q}_2$-vectors of the TPC sub-events were also computed using the inverse of the track p_{T} as weight (see Eq. 7.1). The ratios between the V0 EP resolution obtained with the alternative sub-events and the default one (R_2^{ref}) are shown in the right panel of Fig. 7.11. The V0 EP resolution increases of about 1% when enlarging the pseudorapidity gap and applying the p_{T} weights to the $\boldsymbol{Q}_2$-vectors up to about 1%, almost independently of the collision centrality. Therefore, an additional 1% systematic uncertainty was assigned both to the 10–30% and 30–50% centrality classes to account for possible non-flow correlations among the different sub-events. For the analysis with the SP method no systematic uncertainty was assigned, because of the different sub-event configuration adopted (see Sec. 7.3) which ensures a $|\Delta\eta| > 0.9$ among all the sub-events, implying the suppression of the non-flow correlations.

7.6.3 Residual miscalibration of the $\boldsymbol{Q}_2$-vectors

As discussed in Sec. 7.2, the residual miscalibration in the correction of the non-uniform acceptance of the detectors can induce a systematic bias due to false correlations.

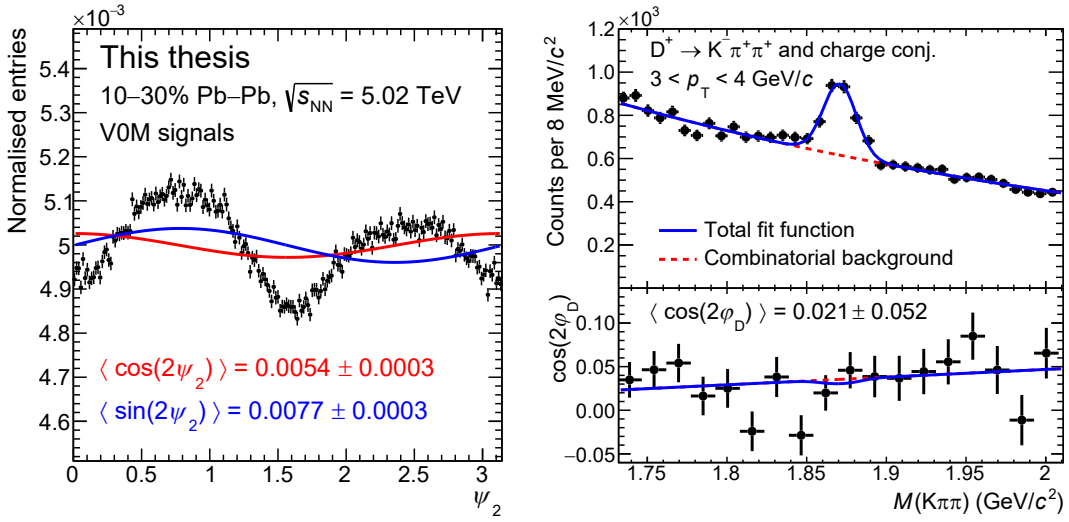

Figure 7.12: Left: fits to the ψ_2 distribution obtained with the V0 detector performed to extract $\langle\cos(2\psi_2)\rangle$ and $\langle\sin(2\psi_2)\rangle$. Right: simultaneous fit of $\langle\cos(2\varphi_{\mathrm{D}})\rangle$ as a function of the invariant-mass and the invariant-mass distribution of D^+ candidates with $3 < p_{\mathrm{T}} < 4$ GeV/c in the 10–30% centrality class obtained using the sample of Pb–Pb collisions collected in 2015.

In particular, considering the expression of the v_2 with the EP method of Eq. 7.3, and that $\cos(2\Delta\varphi)$ can be decomposed in terms of the azimuthal angle φ_{D} and the EP angle ψ_2^{V0},

$$\cos(2\Delta\varphi) = \cos[2(\varphi_{\mathrm{D}} - \psi_2^{\mathrm{V0}})] = \cos(2\varphi_{\mathrm{D}})\cos(2\psi_2^{\mathrm{V0}}) + \sin(2\varphi_{\mathrm{D}})\sin(2\psi_2^{\mathrm{V0}}), \tag{7.16}$$

a non-zero product of $\langle\cos(\sin)(2\varphi_{\mathrm{D}})\rangle$ and $\langle\cos(\sin)(2\psi_2^{\mathrm{V0}})\rangle$, would lead to a bias in the D^+-meson v_2 measurement. Therefore, the $\langle\cos(2\psi_2^{\mathrm{V0}})\rangle$ and $\langle\sin(2\psi_2^{\mathrm{V0}})\rangle$ factors have been extracted by fitting the event-plane distributions with the functions

$$\begin{aligned} f(\psi_2^{\mathrm{V0}}) &= N(1 + p_0 \cdot \cos(2\psi_2^{\mathrm{V0}})) \\ f'(\psi_2^{\mathrm{V0}}) &= N'(1 + p_1 \cdot \sin(2\psi_2^{\mathrm{V0}})), \end{aligned} \tag{7.17}$$

where N and N' are normalisation factors, while $p_0 = \langle\cos(2\psi_2^{\mathrm{V0}})\rangle$ and $p_1 = \langle\sin(2\psi_2^{\mathrm{V0}})\rangle$. The left panel of Fig. 7.12 shows the fits to the ψ_2^{V0} distribution for the 10–30% centrality class obtained with the sample of Pb–Pb collisions collected in 2015. The values of $\langle\cos(2\psi_2)\rangle$ and $\langle\sin(2\psi_2)\rangle$ were found to be of the order of 0.005.

Then, the $\langle\cos(2\varphi_{\mathrm{D}})\rangle$ and $\langle\sin(2\varphi_{\mathrm{D}})\rangle$ factors were extracted from a simultaneous fit of the invariant-mass distribution and the distribution of $\cos(2\varphi_{\mathrm{D}})$ ($\sin(2\varphi_{\mathrm{D}})$) as a function of the invariant-mass, as shown in the right panel of Fig. 7.12 for D^+-meson candidates with $3 < p_{\mathrm{T}} < 4$ GeV/c in the 10–30% centrality class.

The left panel of Fig. 7.13 shows the bias for the analysis with the EP method in 10–30% and 30–50% centrality classes, computed using Eq. 7.16, where the sines and cosines

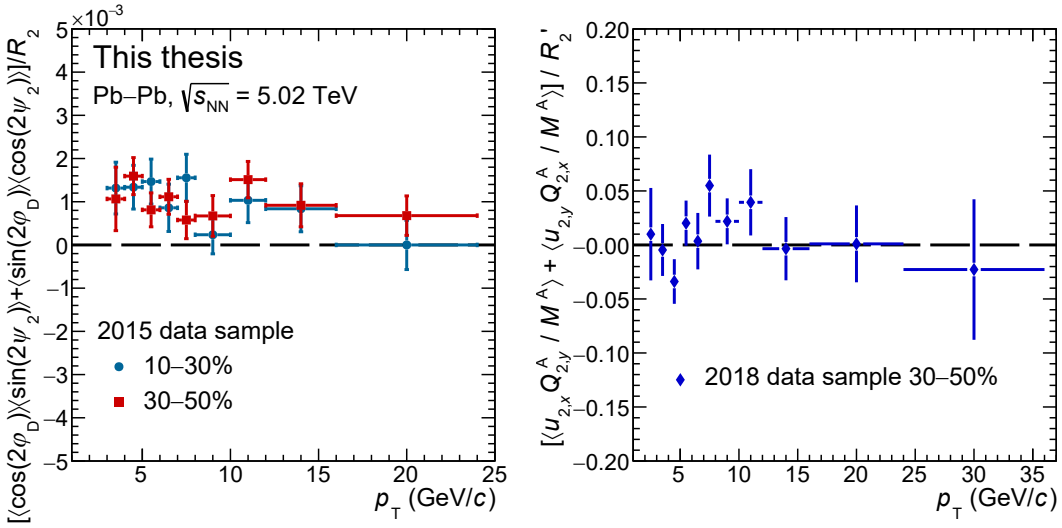

Figure 7.13: Bias from residual miscalibration of the $\boldsymbol{Q}_2$ vectors for the analyses with the EP (left panel) and SP (right panel) methods as a function of p_{T}.

were replaced by their average values, divided by $\mathcal{R}_2$. The bias is almost independent of p_{T} and of the order of 10^{-3}, which is negligible compared to the other sources of systematic uncertainty that affect the v_2 measurement.

For the measurement of the v_2 with SP method, the effect of the residual miscalibration was checked by computing the product of the x component of the unitary vector $\boldsymbol{u}_{2,\mathrm{D}}$ with the y component of the main $\boldsymbol{Q}_2$-vector (obtained from V0C signals) and the opposite one:

$$\begin{aligned} u_{2,\mathrm{D},x} \cdot Q^{\mathrm{V0C}}_{2,y} &= \cos(2\varphi_{\mathrm{D}}) \cdot Q^{\mathrm{V0C}}_{2,y} \\ u_{2,\mathrm{D},y} \cdot Q^{\mathrm{V0C}}_{2,x} &= \sin(2\varphi_{\mathrm{D}}) \cdot Q^{\mathrm{V0C}}_{2,x} \end{aligned} \tag{7.18}$$

These two products are expected to be zero in case of calibrated $\boldsymbol{Q}_2$ vectors for symmetry reasons. The average values of the products reported in Eq. 7.18 were extracted via the simultaneous fits of the invariant-mass distribution of D^+ candidates and their distribution in invariant-mass intervals. The sum of the average value of the two products divided by the SP resolution is reported as a function of p_{T} in the right panel of Fig. 7.13. It was found to be consistent with zero within uncertainties, confirming that the effect of the residual miscalibration of the $\boldsymbol{Q}_2$-vectors on the measurement of the D^+-meson v_2 with the SP is negligible.

7.6.4 Summary of systematic uncertainties

The values assigned as systematic uncertainty for each non-negligible contribution are reported in Table 7.4 for the measurements of the D^+-meson v_2 with the EP and SP methods. The systematic uncertainties on the fit procedure and the feed-down subtraction are quoted as absolute uncertainties, while that on the EP and SP resolutions

p_T (GeV/c)	[2,3]	[3,4]	[4,5]	[5,6]	[6,7]	[7,8]	[8,10]	[10,12]	[12,16]	[16,24]	[24,36]
EP 10 – 30%											
M and v_2 fits	-	0.020	0.020	0.020	0.015	0.015	0.015	0.015	0.015	0.015	-
Feed-down	-	$^{+0.008}_{-0.004}$	$^{+0.007}_{-0.003}$	$^{+0.010}_{-0.005}$	$^{+0.010}_{-0.005}$	$^{+0.009}_{-0.004}$	$^{+0.001}_{-0.002}$	$^{+0.002}_{-0.001}$	$^{+0.006}_{-0.003}$	$^{+0.006}_{-0.003}$	-
EP resolution	2.0%										
EP 30 – 50%											
M and v_2 fits	0.035	0.025	0.015	0.015	0.015	0.015	0.012	0.012	0.015	0.025	-
Feed-down	$^{+0.007}_{-0.003}$	$^{+0.007}_{-0.003}$	$^{+0.014}_{-0.006}$	$^{+0.008}_{-0.004}$	$^{+0.012}_{-0.006}$	$^{+0.010}_{-0.005}$	$^{+0.012}_{-0.006}$	$^{+0.012}_{-0.005}$	$^{+0.003}_{-0.001}$	$^{+0.007}_{-0.003}$	-
EP resolution	2.0%										
SP 30 – 50%											
M and v_2 fits	0.015	0.015	0.008	0.008	0.008	0.008	0.008	0.011	0.011	0.012	0.028
Feed-down	$^{+0.012}_{-0.006}$	$^{+0.013}_{-0.006}$	$^{+0.013}_{-0.006}$	$^{+0.010}_{-0.005}$	$^{+0.010}_{-0.005}$	$^{+0.008}_{-0.004}$	$^{+0.010}_{-0.005}$	$^{+0.011}_{-0.005}$	$^{+0.009}_{-0.005}$	$^{+0.015}_{-0.007}$	$^{+0.010}_{-0.005}$
SP resolution	0.5%										

Table 7.4: Summary of systematic uncertainties on the measurement of the D^+-meson v_2 in Pb–Pb collisions at $\sqrt{s_{NN}} = 5.02$ TeV. The uncertainties on the fitting procedure and feed-down subtraction are quoted as absolute uncertainties, while that on the EP (SP) resolution as relative uncertainty.

as relative uncertainty. The systematic uncertainties estimated for the two analyses performed with the EP and SP methods are similar in magnitude, even if the systematic uncertainty related to the fit procedure is slightly lower for the measurement with the SP method. This is partly due to the method itself as discussed in Sec. 7.6.1, but it could also suggest that the estimation of this systematic uncertainty partially suffers from statistical fluctuations with the statistical uncertainty, owing to the larger data sample used for the analysis performed with the SP method. However, in both cases the assigned systematic uncertainty is smaller than the statistical one, which is the dominant source of uncertainty of the measurement. Finally, the uncertainty on the resolution is lower for the SP method thanks to (i) the milder dependence on the centrality of the SP resolution compared to that of the EP resolution and (ii) the different configuration of sub-events adopted (see Sec. 7.3), which suppressed the non-flow correlations. However, the different sub-event configuration had also the effect of reducing the resolution, increasing the statistical uncertainty on the measurement.

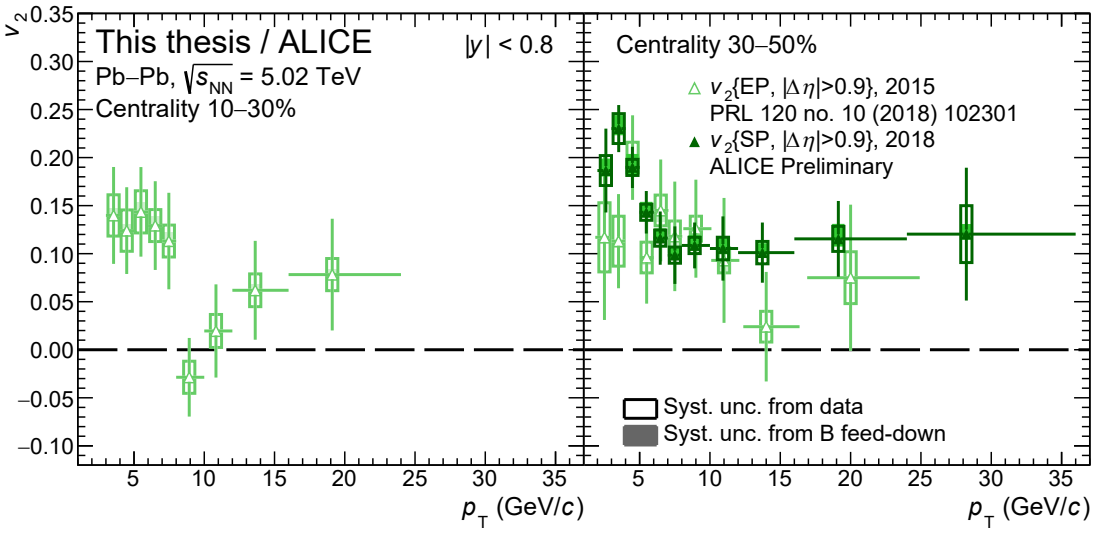

Figure 7.14: Prompt D^+-meson v_2 as a function of p_T for Pb–Pb collisions at $\sqrt{s_{NN}} = 5.02$ TeV in the 10–30% (left panel) and 30–50% (right panel) centrality classes. For the 30–50% centrality class, the measurements performed with the EP and SP methods are compared.

7.7 Results

In Fig. 7.14, the v_2 coefficients of prompt D^+ mesons measured with the EP method in the 10–30% (left panel) centrality class and with the EP (2015 sample) and SP (2018 sample) methods in the 30–50% (right panel) centrality class, are reported as a function of p_T. The data points along the x-axis are positioned at the average p_T of the reconstructed D^+ mesons, which was computed as the average of the p_T distribution of candidates with $|M - M(D^+)| < 3\sigma$, after subtracting the distribution of the background candidates estimated from the side bands ($|M - M(D^+)| > 4\sigma$).

The v_2 in the two centrality classes is similar in magnitude and shows a maximum value of about 0.15 (0.2) for the 10–30% (30–50%) centrality class around 3–5 GeV/c. It decreases for higher p_T and reaches an almost constant value of about 0.1 for $p_T >$ 7 GeV/c. The v_2 measured in the 30–50% centrality class with the two methods are compatible within uncertainties, and the one measured with the SP method has statistical uncertainties reduced of about a factor 2 thanks to the larger data sample used for the analysis.

The v_2 of D^+ mesons was found to be compatible to those of D^0 and D^{*+} mesons [4, 5], as expected from the valence-quark content of the three D-meson species and their small difference in mass. Figure 7.15 shows the comparison of the prompt D^0, D^+, and D^{*+} meson v_2 measured with the EP method in the 10–30% centrality class in Pb–Pb collisions at $\sqrt{s_{NN}} = 5.02$ TeV. Therefore, to improve the precision of the measurement, the v_2 coefficients of the three D-meson species measured in the same centrality class and with the same method were averaged. The inverse of the squared absolute statistical

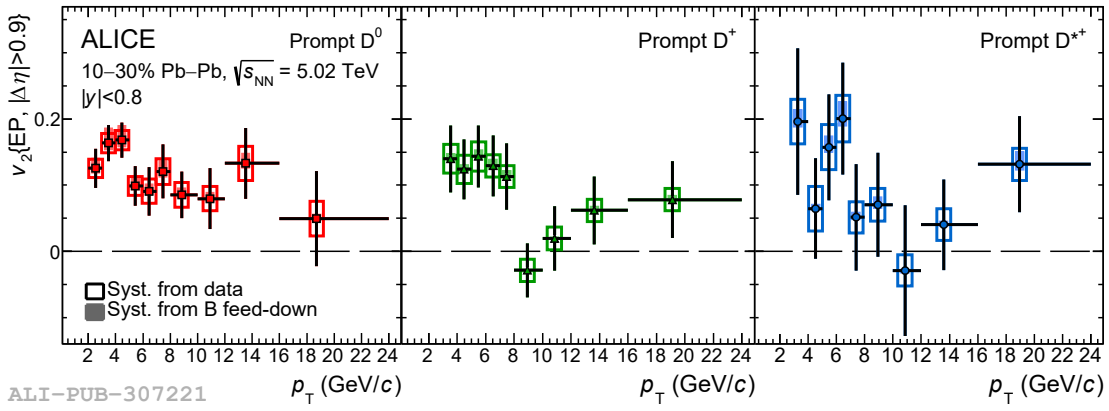

Figure 7.15: Comparison of prompt D^0 (left panel), D^+ (middle panel), and D^{*+} (right panel) v_2 measured with the EP method in the 10–30% centrality class in Pb–Pb collisions at $\sqrt{s_{NN}} = 5.02$ TeV. Figure taken from Ref. [5].

uncertainties were used as weights in the average procedure.

7.7.1 Comparison to light-flavour hadrons and hidden-charm mesons

The average prompt D^0, D^+, and D^{*+} v_2 measured with the SP method in the 30–50% centrality class using the sample of semi-central collisions collected in 2018 is compared in the right panel of Fig. 7.16 to the charged-pion v_2 [52] (for $p_T < 15$ GeV/c), the charged-particle v_2 [185] (for $p_T > 15$ GeV/c) at mid-rapidity, and to the v_2 of inclusive J/ψ mesons at forward rapidity [191], measured at the same energy and in the same centrality class. For all the measurements the SP method was used, with a pseudorapidity gap of $|\Delta\eta| > 2$ and $|\Delta\eta| > 1$ for charged pions (particles) and J/ψ mesons, respectively. An ordering with the mass of the meson species, $v_2(J/\psi) < v_2(D) < v_2(\pi^{\pm})$, is observed for $p_T < 3 - 4$ GeV/c. At intermediate p_T the D-meson and charged-pion v_2 become compatible, but still higher than that of J/ψ mesons. This observation is consistent with a scenario in which a significant fraction of charm quarks hadronise via recombination with light quarks from the medium, leading to an increase of the D-meson v_2 in the intermediate p_T range [112, 192, 193]. However, it has also to be considered that the comparison between the D and the J/ψ mesons could be influenced by the non-negligible fraction of J/ψ mesons coming from beauty-hadron decays (about 10%–20% in the considered p_T range [194]). For $p_T > 6 - 8$ GeV/c all the considered v_2 coefficients converge, indicating that the path-length dependence of parton in-medium energy loss governs the azimuthal anisotropy at high p_T.

The mass ordering of the v_2 at low p_T is observed also for light-flavour hadrons and is described by hydrodynamical calculations [52]. In this Thesis, the mass ordering observed for charged pions, D mesons, and J/ψ mesons was compared to the one predicted by the Blast-Wave model [39, 195, 196]. The Blast-Wave model describes the p_T distributions at the kinetic freeze-out of particles produced from a source in thermal equilibrium which

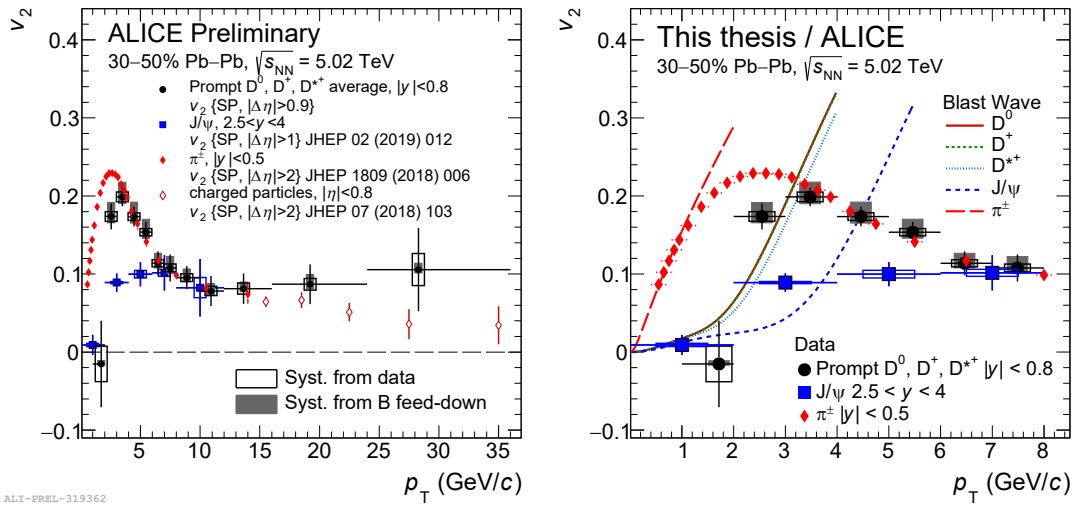

Figure 7.16: Left: comparison among the v_2 coefficients of average prompt D^0, D^+, and D^{*+} mesons, charged pions [52] (for $p_\mathrm{T} < 15$ GeV/c), charged particles [185] (for $p_\mathrm{T} > 15$ GeV/c) at mid-rapidity, and inclusive J/ψ mesons at forward rapidity [191] for Pb–Pb collisions at $\sqrt{s_\mathrm{NN}} = 5.02$ TeV in the 30–50% centrality class. Right: zoom of the left panel in $0 < p_\mathrm{T} < 8$ GeV/c, with the Blast-Wave prediction from the combined fit of p_T distributions and v_2 of charged pions, kaons, and protons (see text for details) superimposed.

undergoes a collective radial expansion. It is valid for low p_T spectra and v_2 coefficients ($p_\mathrm{T} < 1.5-2$ GeV/c for light hadrons), where a hydrodynamic description can be applied. In this description, the thermalised matter is approximated by a boosted Boltzmann distribution, and freezes out instantaneously (*Cooper-Frye* prescription). The Cooper-Frye freeze-out spectrum of hadrons can be then expressed as [39]

$$\frac{\mathrm{d}N}{\mathrm{d}y\mathrm{d}m_\mathrm{T}^2\mathrm{d}\varphi_\mathrm{p}} \sim \int_0^{2\pi} d\varphi_\mathrm{s} K_1[\beta_\mathrm{T}(\varphi_\mathrm{s})] e^{\alpha_\mathrm{T}(\varphi_\mathrm{s})\cos(\varphi_\mathrm{s}-\varphi_\mathrm{p})}, \tag{7.19}$$

where $m_\mathrm{T} = \sqrt{p_\mathrm{T}^2 + m^2}$ is the transverse mass of the hadron with mass m, while φ_s and φ_p are the azimuthal angles in the coordinate and momentum spaces, respectively. Moreover, K_1 is a modified Bessel function of the second kind, and $\beta_\mathrm{T} = \frac{m_\mathrm{T}}{T_\mathrm{fo}}\cosh(\rho(\varphi_\mathrm{s}))$ and $\alpha_\mathrm{T} = \frac{p_\mathrm{T}}{T_\mathrm{fo}}\sinh(\rho(\varphi_\mathrm{s}))$ depend on the kinetic freeze-out temperature T_fo and the radial rapidity $\rho(\varphi_\mathrm{s})$, parametrised as $\rho_0 + \rho_a\cos(\varphi_\mathrm{s})$.

The v_2 coefficient can be then obtained as the average of $\cos(2\varphi_\mathrm{p})$ with the spectrum of Eq. 7.19. However, a further parameter s_2 was introduced by the STAR Collaboration [196], which takes into account the anisotropic shape of the source in coordinate space, to better describe the data. With this additional term, the v_2 in the Blast-Wave model reads

$$v_2(p_\mathrm{T}) = \frac{\int_0^{2\pi}\mathrm{d}\varphi_\mathrm{s}\cos(2\varphi_\mathrm{s})K_1[\beta_\mathrm{T}]I_2[\alpha_\mathrm{T}][1+2s_2\cos(2\varphi_\mathrm{s})]}{\int_0^{2\pi}\mathrm{d}\varphi_\mathrm{s}K_1[\beta_\mathrm{T}]I_0[\alpha_\mathrm{T}][1+2s_2\cos(2\varphi_\mathrm{s})]}, \tag{7.20}$$

BW parameters	T_{fo}(MeV)	ρ_0	ρ_a	s_2
30–50% centrality	110 ± 4	0.74 ± 0.4	0.0434 ± 0.0006	0.0948 ± 0.0013

Table 7.5: Blast-Wave parameters extracted from the combined fit of p_T distributions and v_2 of charged pions, kaons, and protons (see text for details) in the 30–50% centrality class for Pb–Pb collisions at $\sqrt{s_{NN}} = 5.02$ TeV.

where I_0 and I_2 are two Bessel functions of the first kind.

In order to fix the Blast-Wave parameters and obtain a prediction for the v_2 of D and J/ψ mesons, a simultaneous fit to the measured p_T distributions and v_2 coefficients of charged pions, kaons, and protons in the 30–50% centrality class in Pb–Pb collisions at $\sqrt{s_{NN}} = 5.02$ TeV was performed in this Thesis. The v_2 data were taken from Ref. [52], while for the p_T distributions the measurements published in Ref. [116] were used. The p_T ranges adopted for the fits were $0.5 < p_T < 1$ GeV/c, $0.2 < p_T < 1.2$ GeV/c, and $0.3 < p_T < 1.7$ GeV/c, for pions, kaons, and protons respectively, as done in Ref. [197] to obtain the prediction for the deuteron v_2 in Pb–Pb collisions at $\sqrt{s_{NN}} = 2.76$ TeV. The parameters extracted from the simultaneous fit are reported in Table 7.5. As shown in the right panel of Fig. 7.16, the mass ordering observed in data is qualitatively described by the Blast-Wave model. A large separation is obtained between pions and D mesons and between D and J/ψ mesons. As expected, the curves for D^0, D^+, and D^{*+} mesons are close to each other, given the small difference among the masses of the three D-meson species. Nevertheless, the Blast-Wave prediction seems to underestimate the v_2 of D and J/ψ mesons for $2 < p_T < 3$ GeV/c. At higher p_T the Blast-Wave model is not expected to describe the D-meson and J/ψ-meson v_2, since a hydrodynamical description cannot be applied.

7.7.2 Comparison of D-meson v_2 and R_{AA} to theoretical models

The prompt D^0, D^+, and D^{*+} average v_2 presented in this Chapter and the R_{AA} presented in Chapter 6 were compared to predictions of theoretical models based on pQCD calculations of high-p_T parton energy loss, that are valid at high p_T, and models which implement the charm-quark transport in a hydrodynamically expanding medium, based on Boltzmann, Langevin, or Fokker-Planck equations, which include energy loss and flow effects and provide predictions down to $p_T = 0$.

Figure 7.17 shows the comparison of the prompt D^0, D^+, and D^{*+} average R_{AA} in the 0–10% centrality class (top panels) and v_2{SP} in the 30–50% centrality class (bottom panels) to the transport (left panels) and pQCD-based energy-loss (right panels) model predictions. The theoretical uncertainties, when available, are displayed with a coloured band or a double line. Among the transport models, the MC@sHQ+EPOS2 [190], PHSD [178], LBT [198], LIDO [114], $BAMPS_{el+rad}$ [173], and DAB-MOD(M&T) [199] calculations include charm-quark interactions with the medium constituents via both collisional (elastic) and radiative (gluon radiation) processes. In the TAMU [170, 200],

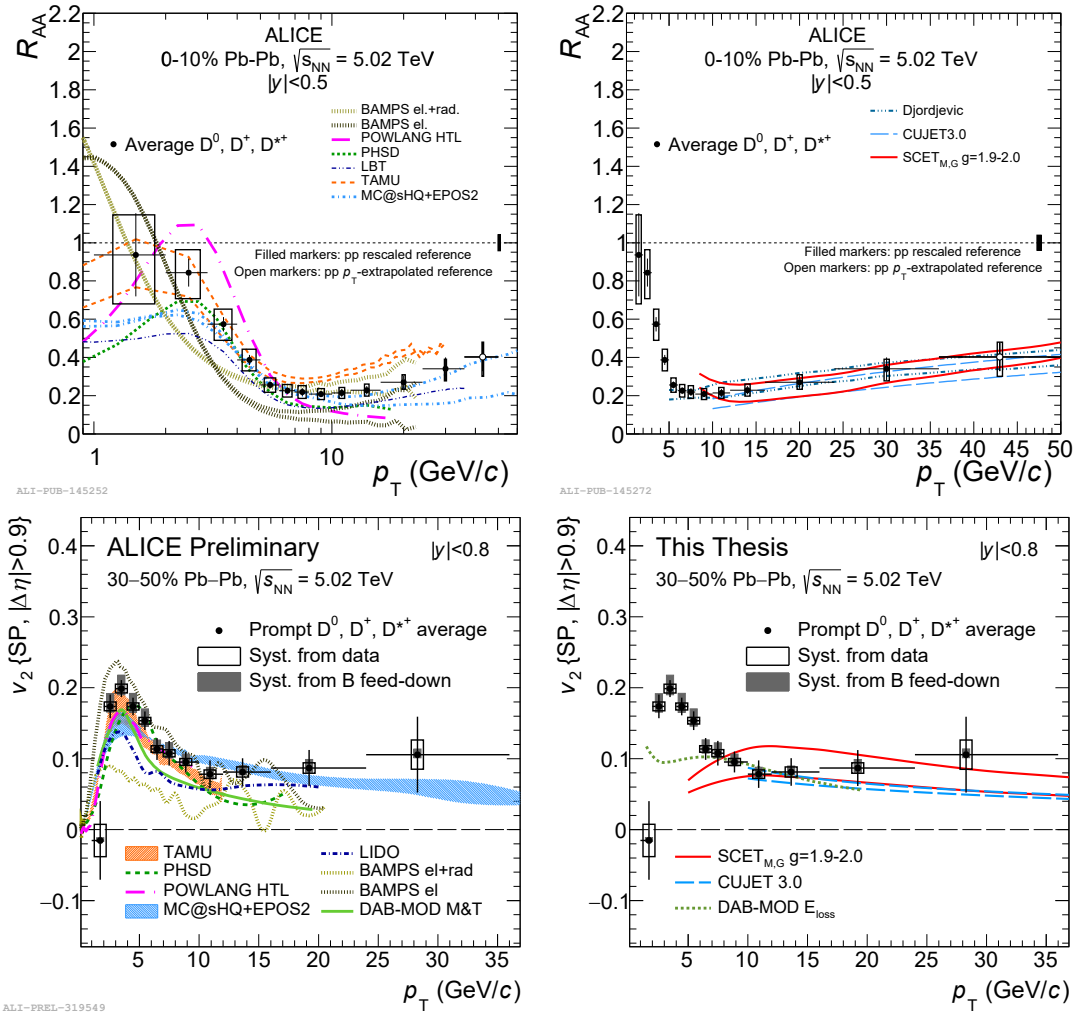

Figure 7.17: Top: prompt D^0, D^+, and D^{*+} average R_{AA} in the 0–10% centrality class measured with the sample of Pb–Pb collisions at $\sqrt{s_{NN}} = 5.02$ TeV collected in 2015 compared to transport (left panel) and pQCD-inspired (right panel) models. Figures taken from Ref. [3]. Bottom: prompt D^0, D^+, and D^{*+} average $v_2\{SP\}$ in the 30–50% centrality class measured with the sample of Pb–Pb collisions at $\sqrt{s_{NN}} = 5.02$ TeV collected in 2018 compared to transport (left panel) and pQCD-inspired (right panel) models.

POWLANG [201], and BAMPS_{el} [173] models only the collisional processes are implemented. All the considered pQCD-based energy-loss models (i.e. DJORDJEVIC [180], CUJET3.0 [202], SCET_{MG} [203], and DAB-MOD(E_{loss}) [199] models) include radiative energy-loss processes, while only DJORDJEVIC, CUJET3.0, and DAB-MOD(E_{loss}) [199] calculations include also collisional processes. A positive v_2 in these calculations arises from the path-length dependent energy loss. A nuclear modification of the PDFs is included in all the

models but BAMPS and CUJET3.0. The hadronisation of the charm quark via coalescence, in addition to the independent fragmentation mechanism, is implemented in the TAMU, MC@SHQ+EPOS2, PHSD, POWLANG, LBT, LIDO, and DAB-MOD(M&T) models.

Most of the models based on the charm-quark transport in a hydrodynamically expanding medium fairly reproduce the measured R_{AA} and the v_2 for $p_T \lesssim 10$ GeV/c. For the BAMPS model, a worse description of the R_{AA} is obtained when only the collisional energy-loss processes are included ($BAMPS_{el}$), while it improves with the introduction of radiative processes ($BAMPS_{el+rad}$). However, $BAMPS_{el+rad}$ underestimates the measured v_2 of about a factor two in $2 < p_T < 10$ GeV/c. This indicates that the elastic collisions are more efficient in producing a positive v_2, and moreover that the charm-quark coalescence with light quarks from the medium, not implemented in BAMPS, is necessary to describe the v_2 at low p_T. The TAMU model overestimates the R_{AA} for $p_T > 5-6$ GeV/c owing to the absence of radiative energy loss. In the same p_T interval the PHSD and POWLANG models predict a R_{AA} lower than the measured one, which could be attributed by different transport coefficients and different implementations of the medium and the interactions of the charm quark in the medium. The missing implementation of radiative energy-loss processes seems not to influence the v_2 prediction of the TAMU and POWLANG models, which is probably compensated by the effect of the hadronisation via charm-quark coalescence. The DAB-MOD model is closer to the data for $p_T < 6$ GeV/c in case of Langevin transport (DAB-MOD(M&T)) and for $p_T > 6$ GeV/c in case of energy-loss based model. For $p_T > 10$ GeV/c, where radiative energy loss is expected to be the dominant interaction mechanism, the v_2 and the R_{AA} are also reproduced by the DJORDJEVIC, CUJET3.0, $SCET_{MG}$, and MC@SHQ+EPOS2 models.

From the comparison to the model predictions, it emerges that (i) the radiative energy loss is needed for the description of the D-meson R_{AA} at high p_T, (ii) the collisional interactions seem to be the dominant effect at low p_T, and (iii) the inclusion of the hadronisation via coalescence is needed to describe the low p_T v_2. Therefore, the comparison between the data and the models provide insights into the main features of the interaction of the charm quarks with the QGP, however due to the different implementations, the transport coefficients of the various models differ from each other. Hence, in recent years a systematic study of the theoretical models and the dependence of the predictions from the different assumptions and initial conditions has been performed, with the aim of achieving a common determination of the transport coefficients [204, 205].

Chapter 8

D^+ event-shape engineering studies in Pb–Pb collisions at $\sqrt{s_{\mathrm{NN}}} = 5.02$ TeV

In this Chapter, the measurements of the elliptic flow v_2 and the p_{T}-differential yields of D^+ mesons in mid-central Pb–Pb collisions with the event-shape engineering (ESE) technique [206] is discussed. This technique is based on the classification of the events, belonging to the same centrality interval, according to the average flow of soft particles. Since hydrodynamical calculations show a linear correlation between the v_2 (v_3) and the corresponding initial eccentricity ϵ_2 (ϵ_3) [207–209], the ESE technique provides a tool to select events with different initial geometrical shape, and therefore to study the interplay between the initial eccentricity of the nucleus–nucleus collisions and the subsequent evolution of the system. This technique was previously applied to the light-flavour sector [210, 211] and for the search of the Chiral Magnetic Effect [212, 213].

The ESE technique was applied for the first time to the heavy-flavour sector to study the correlation between the flow of soft and hard hadrons in the analyses presented in this Thesis, of which I was the main developer. This was performed by measuring the ratios of v_2 and p_{T}-differential yields of prompt D^+ mesons in events classified based on the average elliptic flow of soft particles (*ESE-selected*) and those measured in the full (*unbiased*) sample,

$$R_{\mathrm{ESE}}^{X} = \frac{X(\text{ESE-selected})}{X(\text{unbiased})}, \tag{8.1}$$

where X can be either the v_2 or the p_{T}-differential yields of D^+ mesons. In case of v_2, the measurement of the numerator and denominator are provided separately and the ratio is computed after averaging the results of the D^+ mesons with those of the other non-strange D-meson species, while for the p_{T}-differential yields from the D^+-meson yield, the ratio is computed directly, allowing for a partial cancellation of the systematic uncertainties.

As for the v_2 measurements presented in Chapter 7, the analysis was performed in the 10–30% and 30–50% centrality classes using the sample of MB Pb–Pb collisions at $\sqrt{s_{\mathrm{NN}}} = 5.02$ TeV collected in 2015, and it was improved in the 30–50% centrality class with the sample of semi-central Pb–Pb collisions at the same centre-of-mass energy

collected in 2018 (see Sec 4.1.1). The measurement of the D^+-meson v_2 with the 2015 (2018) data sample was performed with the EP (SP) method [183, 184]. The results obtained with the 2015 data sample were published in Ref. [5], while those obtained with the 2018 data sample were approved as preliminary results by the ALICE Collaboration.

8.1 The event-shape engineering selection

For the samples of Pb–Pb collisions at $\sqrt{s_{\mathrm{NN}}} = 5.02$ TeV adopted for the analyses presented in this Chapter, the events were selected as described in Sec. 4.1.1. The centrality classes were 10–30% and 30–50% for the sample of Pb–Pb collisions collected in 2015 and 30–50% for the sample collected in 2018. The number of selected events in each centrality class was 20.7×10^6 and 76.7×10^6 for the samples collected in 2015 and 2018, respectively.

Beside the centrality selection, the events were also classified according to the average elliptic flow, estimated with the magnitude of the 2^{nd}-harmonic reduced flow vector q_2 [184, 214], defined as

$$q_2 = |\boldsymbol{Q}_2|/\sqrt{M}, \tag{8.2}$$

where $\boldsymbol{Q}_2$ is the 2^{nd}-harmonic flow vector introduced in Eq. 7.1 and M is the particle multiplicity (number of tracks or sum of the signal-amplitudes used in the q_2 calculation). The denominator in Eq. 8.2 is needed to compensate the increase of $|\boldsymbol{Q}_2|$ with $\sqrt{M}$ in case of null elliptic flow.

The q_2 factor was measured both with charged-particle tracks having $|\eta| < 0.8$ and $0.2 < p_{\mathrm{T}} < 5$ GeV/c reconstructed in the TPC (q_2^{TPC}) and with V0A signal amplitudes (q_2^{V0A}). On the one hand, the large charged-particle multiplicity at mid-rapidity and the good φ resolution of the TPC detector guarantee a good sensitivity of q_2 in discriminating eccentric from isotropic events. On the other hand, the overlap between the pseudorapidity intervals defined for the measurement of the D^+-meson candidates and q_2^{TPC} could lead to a bias in the measurement due to non-flow correlations and autocorrelations. The latter were partially removed by excluding the decay tracks of D^+-meson candidates from the q_2 calculation, but some residual non-flow correlations could still be included. The suppression of the non-flow correlations could be ensured by the pseudorapidity gap of 2 units between the D^+-meson candidates and q_2^{V0A}. In this case however, a reduced discriminating power was obtained, because of the lower charged-particle multiplicity at forward rapidity and the coarse segmentation of the V0A detector leading to a worse φ resolution compared to the TPC detector. A detailed comparison between the two q_2 estimators will be discussed in Sec. 8.5.

Figure 8.1 shows the q_2^{TPC} (left panel) and q_2^{V0A} (right panel) distributions as a function of the collision centrality, for the 10–50% centrality interval. The average q_2, depicted with the black-dotted line, is around 2-2.5 for q_2^{TPC} and 2.5-3 for q_2^{V0A}, with a maximum around 25% of centrality in both cases. The q_2 distributions are broad and reach values larger than three times the average value, indicating that the fluctuations in the initial geometry are relevant.

Since the q_2 distributions are not constant as a function of centrality, a selection on a fixed value of q_2 would unbalance the centrality and multiplicity distributions, introducing

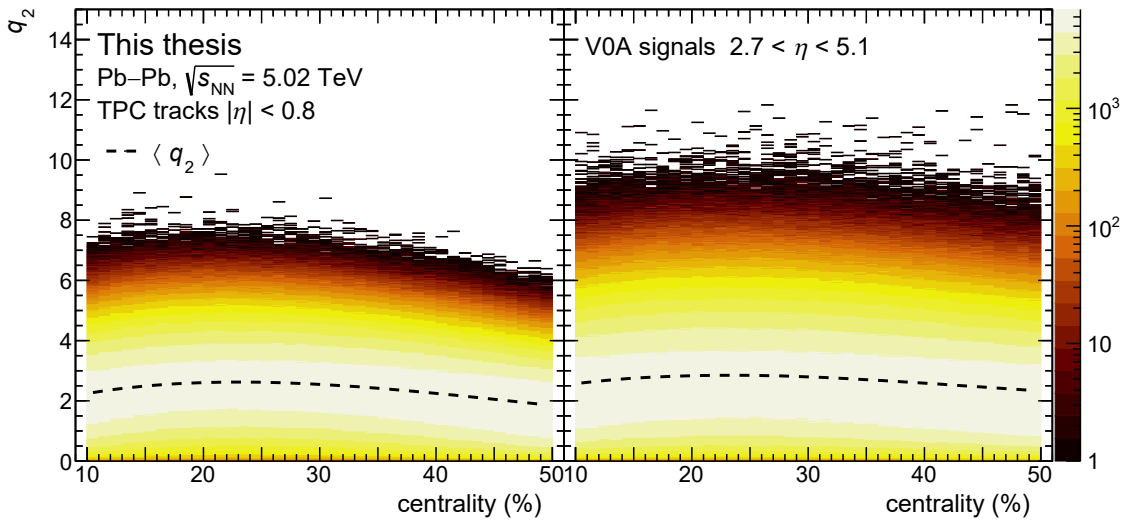

Figure 8.1: Distribution of q_2^{TPC} (left panel) and q_2^{V0A} (right panel) as a function of centrality in Pb–Pb collisions at $\sqrt{s_{\mathrm{NN}}} = 5.02$ TeV. The black dotted lines represent the average q_2 as a function of the collision centrality.

a bias in the measurement. For this reason, the ESE selection was performed in narrow centrality intervals. In particular, q_2 percentiles ($q_2^{\%}$) were defined in 1%-wide centrality intervals from the q_2-integral distribution, normalised between 0 and 100,

$$q_2^{\%}(q_2) = \frac{\int_0^{q_2} \frac{\mathrm{d}N}{\mathrm{d}q_2'} \mathrm{d}q_2'}{\int_0^{\infty} \frac{\mathrm{d}N}{\mathrm{d}q_2'} \mathrm{d}q_2'} \cdot 100, \tag{8.3}$$

where $\mathrm{d}N/\mathrm{d}q_2$ is the q_2 distribution evaluated in each 1%-wide centrality interval.

The left panel of Fig. 8.2 shows the integral distributions of q_2^{TPC} and q_2^{V0A} for the 20–21% and 49–50% centrality intervals. They were interpolated with a cubic spline to avoid biases induced by the finite binning of the distribution and obtain a smooth curve. The right panel of the same Figure shows the q_2^{TPC} and q_2^{V0A} percentile distributions. Thanks to the aforementioned procedure they were found to be flat within 0.1%.

The events in each centrality class were then divided in two classes of q_2, one corresponding to more isotropic events and another corresponding to more eccentric events. For the sample of Pb–Pb collisions collected in 2015, two ESE-selected classes were defined, corresponding to the 60% of the events with smallest and q_2 and the 20% with the largest q_2. In the analysis of the 2018 sample, thanks to the larger dataset, a wider separation could be applied between the two q_2 classes, by selecting the 20% of the events with largest and smallest q_2. These q_2 classes will be addressed as *small-q_2* and *large-q_2* in the following Sections. In case of no ESE selection, the term *unbiased* will be used.

The distribution of the centrality percentiles defined by the V0M signal amplitudes in the 20% small-q_2 and 20% large-q_2 classes defined for the data sample of Pb–Pb collisions collected in 2018 are shown in Fig. 8.3. Both the distributions of the events selected

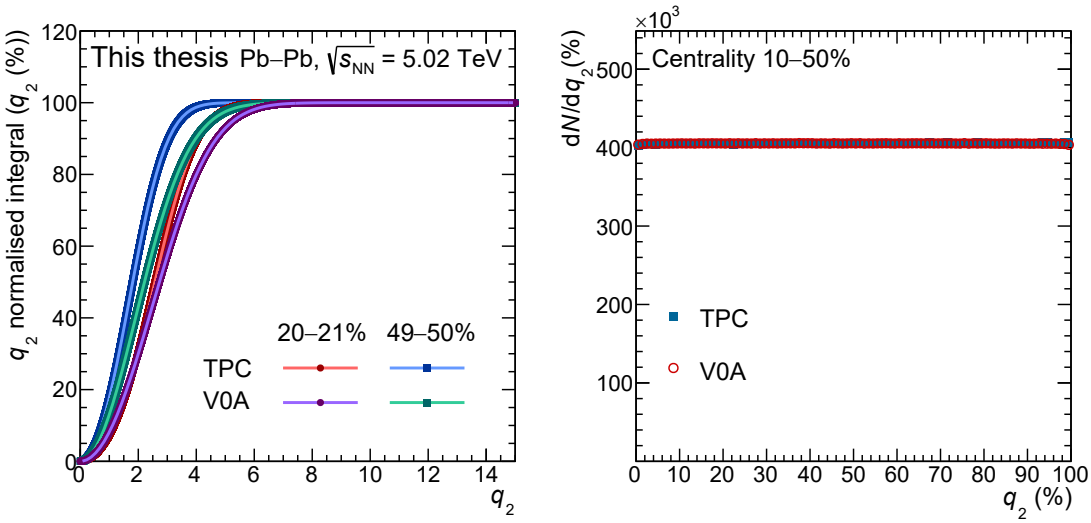

Figure 8.2: Left: integral distributions of q_2^{TPC} and q_2^{V0A} for the 20–21% and 49–50% centrality intervals in Pb–Pb collisions at $\sqrt{s_{NN}} = 5.02$ TeV. The lines represent the cubic spline interpolation of the distributions. Right: q_2^{TPC} and q_2^{V0A} percentile distributions for the 10–50% centrality interval.

with q_2^{TPC} (left panel) and q_2^{V0A} (right panel) were found to be flat within 0.5% in the centrality interval of the analysis, as expected from the procedure adopted for the selection described above.

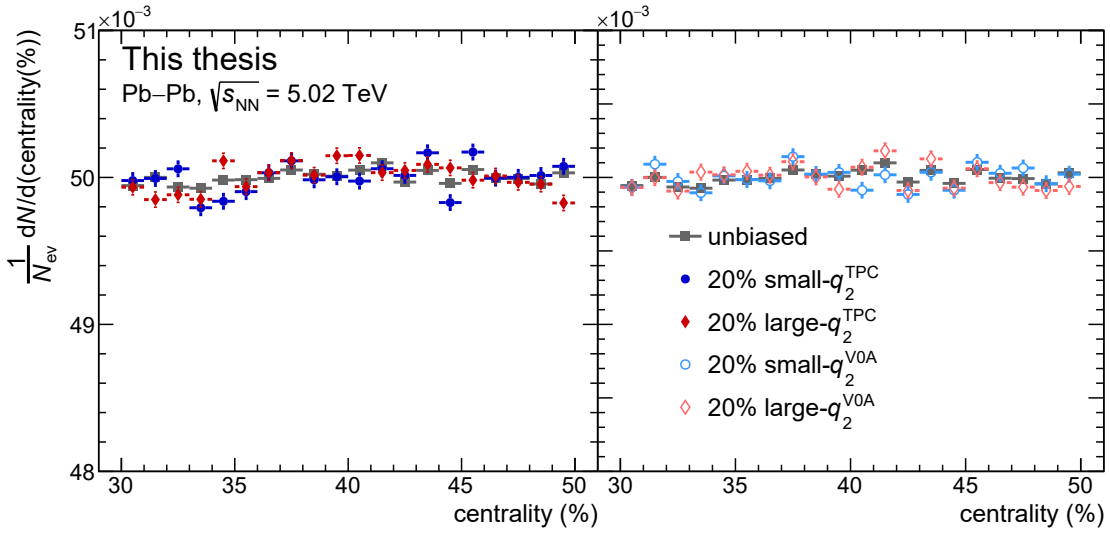

Figure 8.3: Centrality distributions for the 20% small(large)-q_2^{TPC} (left panel) and small(large)-q_2^{V0A} (right panel) in Pb–Pb collisions at $\sqrt{s_{NN}} = 5.02$ TeV.

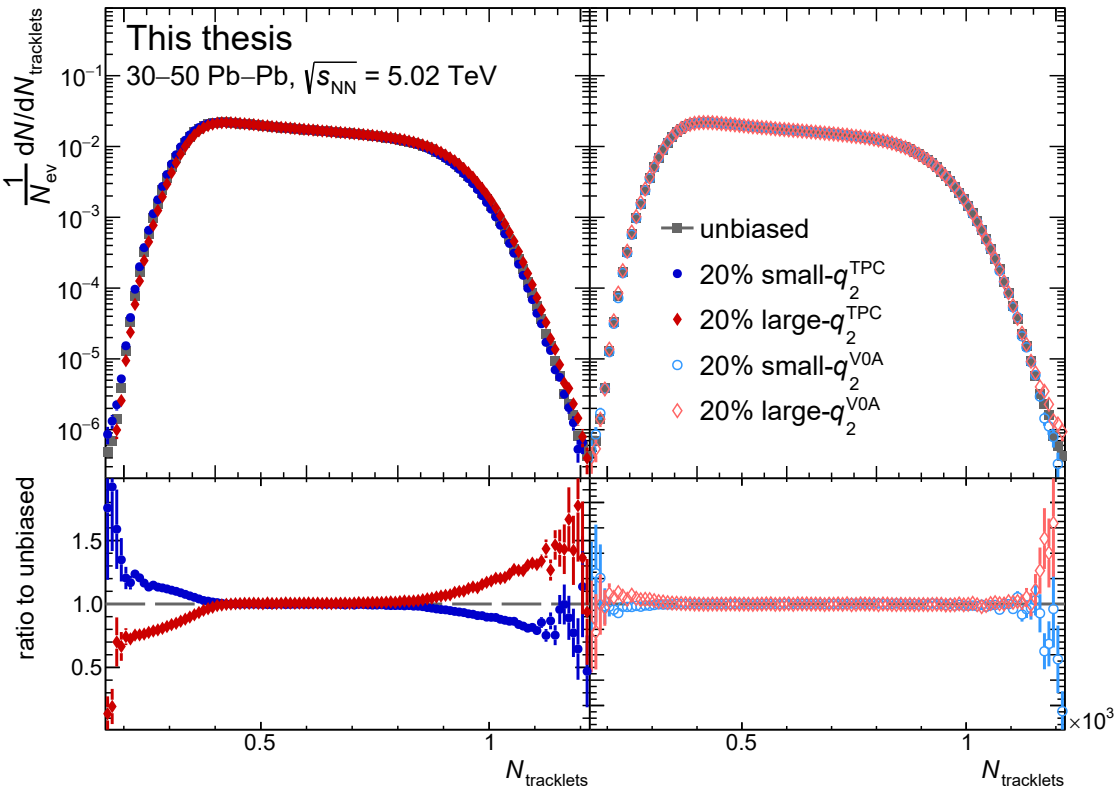

Figure 8.4: Top: $N_{\text{tracklets}}$ distributions for the 20% small(large)-q_2^{TPC} (left panel) and small(large)-q_2^{V0A} (right panel) in Pb–Pb collisions at $\sqrt{s_{\text{NN}}} = 5.02$ TeV. Bottom: ratios of the $N_{\text{tracklets}}$ in the ESE-selected and the unbiased samples.

In addition, since the observables measured in the ESE-selected samples depend on the charged-particle multiplicity, it was verified that the $N_{\text{tracklets}}$ distributions were not significantly modified in the ESE-selected samples with respect to those in the unbiased sample. The top panels of Fig. 8.4 show the $N_{\text{tracklets}}$ distributions for the same classes of events. In the bottom panels, the ratios of such distributions and the one obtained in the unbiased sample are reported. The ratios for the q_2^{V0A}-selected classes are nearly flat at one, while a deviation from unity is observed for the ratios of the q_2^{TPC}-selected classes. However, this deviation is relevant for $N_{\text{tracklets}} < 400$ and $N_{\text{tracklets}} > 900$, where the distribution decreases steeply, and therefore it is expected not to introduce a large bias. The effect of the difference in the $N_{\text{tracklets}}$ distributions was evaluated for the systematic uncertainties and will be discussed in Sec. 8.6.3.

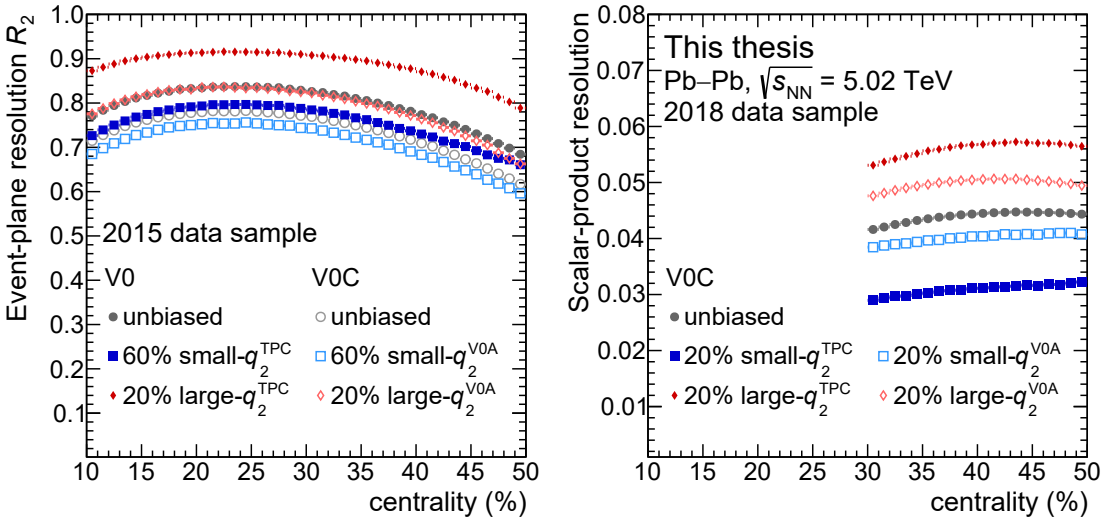

Figure 8.5: Left: EP resolution $\mathcal{R}_2$ of the V0M and V0C detectors obtained with the sample of Pb–Pb collisions collected in 2015 for the unbiased and the ESE-selected classes. Right: SP resolution of the V0C detectors obtained with the sample of semi-central Pb–Pb collisions collected in 2018 for the unbiased and the ESE-selected classes.

8.2 Sub-event configuration and EP (SP) resolution

The sub-events used for the measurement of the D^+ v_2 in the ESE-selected classes are those reported in Sec. 7.2. In particular, they were defined using either the charged-particle tracks reconstructed with the TPC detector, or signals in the V0A and V0C detectors. For both the analyses of the 2015 and 2018 data samples, three sub events were adopted. The same $\boldsymbol{Q}_2$-vector calibration procedure adopted for the measurement of the unbiased v_2 was also applied for the measurements of the v_2 with the ESE technique.

For the analysis of the sample of MB Pb–Pb collisions collected in 2015, the EP method was used. For the classes of events selected with q_2^{TPC}, the sub-event configuration adopted was the same as the one for unbiased v_2 measurement, i.e. correlating charged particles reconstructed in the V0M detector and in the semi-volumes of the TPC detector with positive ($0 < \eta < 0.8$) and negative ($-0.8 < \eta < 0$) pseudorapidity. For the q_2^{V0A}-based selection, only the V0C detector was used for the main EP angle, to avoid the overlap with the pseudorapidity region used for the ESE selection. Hence, in this case the other two sub-events were defined by the V0A signals and the charged-particle tracks reconstructed in the full TPC volume ($|\eta| < 0.8$). The left panel of Fig. 8.5 shows the EP resolution $\mathcal{R}_2$ as a function of the collisions centrality obtained with Eq. 7.5 for the different sub-event configurations and the ESE-selected classes defined. As already observed for the analysis of the unbiased v_2, $\mathcal{R}_2$ is higher for the EP angle measured with the V0M detector compared to the V0C detector, because of the larger particle multiplicity. Moreover, the values of $\mathcal{R}_2$ are higher(lower) in the large(small)-q_2 class with respect to that evaluated for the unbiased sample with the corresponding sub-event

configuration, since $\mathcal{R}_2$ depends linearly on the average v_2 of the events ($\mathcal{R}_2 \propto v_2\sqrt{M}$).

For the analysis of the sample of semi-central Pb–Pb collisions collected in 2018, the SP method was used. The main $\boldsymbol{Q}_2$ vector was determined with V0C signals, while the V0A signals and the charged-particle tracks reconstructed in the full TPC volume ($|\eta| < 0.8$) were used for the definition of the other two sub-events. The same configuration was used for the unbiased, q_2^{TPC}-selected, and q_2^{V0A}-selected classes. The SP resolution (denominator in Eq. 7.6) is reported in the right panel of Fig. 8.5 as a function of the collision centrality, for the unbiased and ESE-selected classes. As for the $\mathcal{R}_2$ factor, also the SP resolution is higher(lower) in the large(small)-q_2 class of events compared to the unbiased sample. Moreover, the variation of the resolution in the q_2^{TPC}-selected classes is larger than the one observed for the q_2^{V0A}-selected classes, because of the better eccentricity discriminating power of q_2^{TPC} compared to q_2^{V0A}. The same holds also for the EP resolution, despite it is less clear from the left panel of Fig. 8.5 because of the different sub-event configuration adopted for the classes of events based on the q_2^{TPC} and q_2^{V0A} selection.

The values of EP and SP resolutions for the centrality and ESE-selected classes defined for the analyses of the D^+-meson v_2 with the samples of Pb–Pb collisions collected in 2015 and 2018 are reported in Table 8.1.

8.3 Signal extraction

In this section, the extraction of the D^+-meson signal for the measurements of the p_{T}-differential yields and the v_2 coefficient is discussed. For each centrality class, the D^+-meson candidates were selected both in the unbiased and in the ESE-selected samples by applying the same selection criteria reported in Sec. 7.4.1. A reduced p_{T} range, $3 < p_{\mathrm{T}} < 24$ GeV/c, and wider p_{T} intervals compared to the analysis of the unbiased D^+-meson v_2, i.e. 3–4, 4–6, 6–8, 8–12, 12–16, and 16–24 GeV/c, were defined due to the reduced size of the data sample after the ESE selection.

8.3.1 D^+-meson p_{T}-differential yields

The D^+-meson raw yields for the measurement of the ratios between the p_{T}-differential yields in the ESE-selected and the unbiased samples were extracted from the invariant-mass distributions of D^+-meson candidates obtained in each class of events. Figure 8.6 shows the fits to the invariant-mass distributions of D^+-meson candidates with $3 < p_{\mathrm{T}} < 4$ GeV/c in the 30–50% centrality class obtained with the sample of Pb–Pb collisions collected in 2018. The unbiased distribution is reported in the top-left panel, the distributions for the q_2^{TPC}-selected classes are reported in the top-middle and top-right panels, while those for the the q_2^{V0A}-selected classes are reported in the bottom panels. As for the analyses presented in Chapters 6 and 7, the signal was modelled with a Gaussian and the background with an exponential function. The width of the Gaussian function in the ESE-selected samples was fixed to the value extracted from the fit to the unbiased distributions, since the invariant-mass resolutions was not expected to depend on q_2. The signal-to-background ratio ranged from 0.2 to 0.8 and from 0.3 to 1.2 in the 10–30% and 30–50% centrality classes, respectively. The statistical significance of the extracted signal

Method	Year	Centrality class	Detector for ψ_2	ESE class	Resolution
EP	2015	10–30%	V0M	unbiased	0.8223 ± 0.0001
				small-q_2^{TPC}	0.7809 ± 0.0001
				large-q_2^{TPC}	0.9058 ± 0.0001
			V0C	unbiased	0.7669 ± 0.0001
				small-q_2^{V0A}	0.7390 ± 0.0001
				large-q_2^{V0A}	0.8223 ± 0.0001
		30–50%	V0M	unbiased	0.7708 ± 0.0001
				small-q_2^{TPC}	0.7301 ± 0.0001
				large-q_2^{TPC}	0.8646 ± 0.0001
			V0C	unbiased	0.7077 ± 0.0001
				small-q_2^{V0A}	0.6822 ± 0.0001
				large-q_2^{V0A}	0.7597 ± 0.0001
SP	2018	30–50%	V0C	unbiased	0.04391 ± 0.0001
				small-q_2^{TPC}	0.0309 ± 0.0001
				large-q_2^{TPC}	0.0561 ± 0.0001
				small-q_2^{V0A}	0.0402 ± 0.0001
				large-q_2^{V0A}	0.0498 ± 0.0001

Table 8.1: Event-plane and scalar-product resolutions of V0C and v0M detectors in the 10–30% and 30–50% centrality classes for the two data samples of Pb–Pb collisions at $\sqrt{s_{NN}} = 5.02$ TeV analysed. Only the statistical uncertainty is reported.

was found to be between 8 and 28 (10 and 55) for the sample of Pb–Pb collisions collected in 2015 (2018). The values of signal-to-background ratio and significance were found to be similar in the small-q_2 and large-q_2 samples.

8.3.2 D^+-meson v_2

The D^+-meson v_2 with the EP method was computed from the measured anisotropy between the in-plane and out-of-plane raw yields, using Eq. 7.12. Figure 8.7 shows the fits to the in-plane and out-of-plane invariant-mass distributions of D^+-meson candidates with $4 < p_T < 6$ GeV/c performed to extract the in-plane and out-of-plane raw yields in the 10–30% centrality class for the sample of Pb–Pb collisions collected in 2015. The invariant-mass distributions for the unbiased and q_2^{TPC}-selected samples obtained with

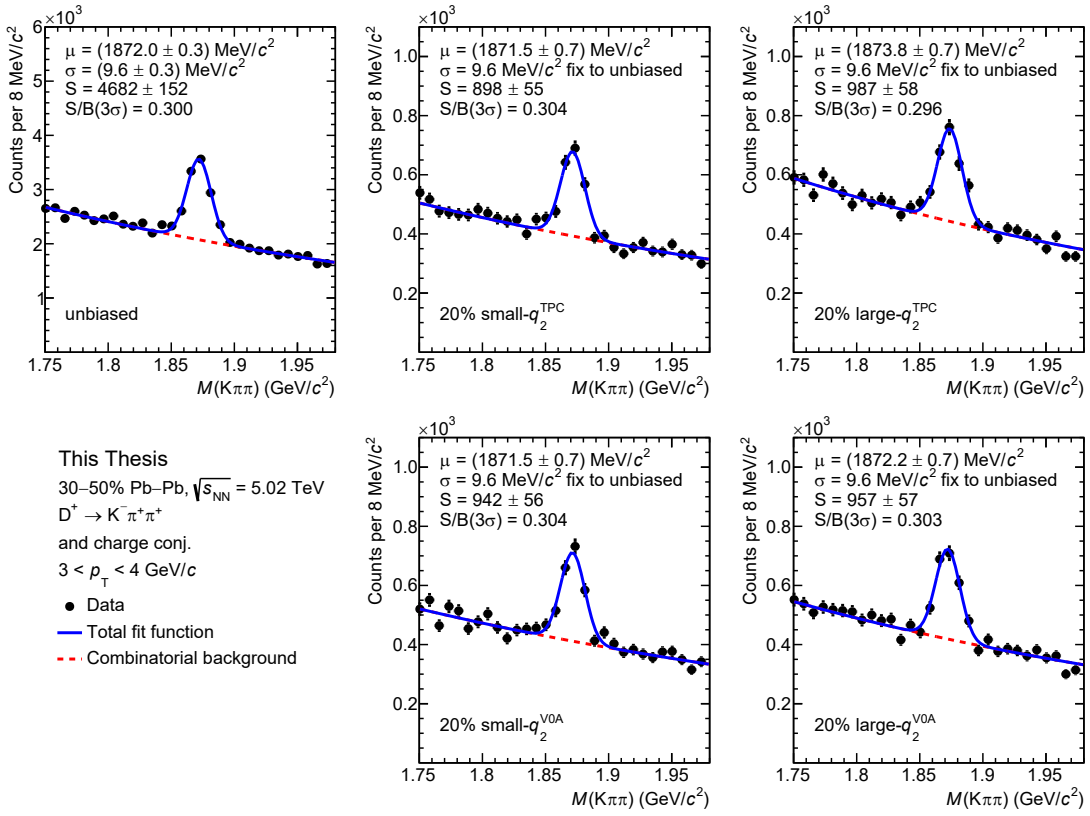

Figure 8.6: Fits to the invariant-mass distributions of D^+-meson candidates with $3 < p_{\mathrm{T}} < 4$ GeV/c in the 30–50% centrality class obtained with the sample of Pb–Pb collisions collected in 2018. The top left panel shows the distribution for the unbiased sample, the middle-top and right-top panels the distributions for the q_2^{TPC}-selected classes, and the bottom panels for the q_2^{V0A}-selected classes. The solid blue and the dotted red curves represent the total and the combinatorial-background fit functions, respectively.

the V0M EP angle are reported in the top row, while those for the unbiased and q_2^{V0A}-selected samples obtained with the V0C EP angle in the bottom row. Also in this case, the signal was modelled with a Gaussian and the background with an exponential function. The Gaussian width was fixed to the one extracted from the distributions integrated over φ and q_2, where the signal has higher statistical significance. The signal-to-background ratio ranged between 0.2 and 1.0, while the statistical significance between 5 and 21.

The analysis of the 2018 data sample was carried out with the SP method. In this case, the D^+-meson v_2 was extracted via a simultaneous fit of the invariant-mass distributions and of candidate v_2 as a function of invariant-mass. The fit function adopted for the $v_2(M)$ distribution was Eq. 7.13, where the v_2 of the background was parametrised with a linear function of the invariant mass. Figure 8.8 shows the simultaneous fits for the $4 < p_{\mathrm{T}} < 6$ GeV/c range. The left panels show the simultaneous fits to the distributions in the q_2^{TPC}-selected samples, while the right panels those to the distributions in the

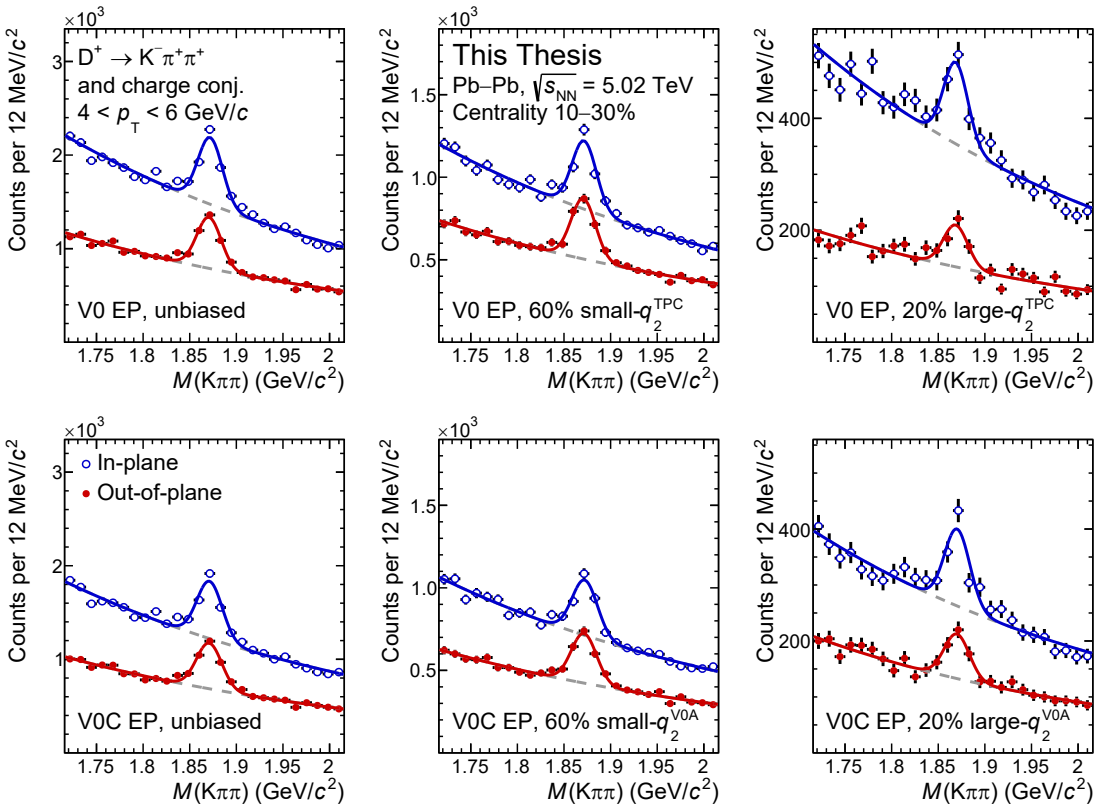

Figure 8.7: Fits to the in-plane (open symbols) and out-of-plane (closed symbols) invariant-mass distributions of D^+-meson candidates with $4 < p_T < 6$ GeV/c in the 10–30% centrality class obtained with the sample of Pb–Pb collisions at $\sqrt{s_{NN}} = 5.02$ TeV collected in 2015. The top panels show the distributions for the unbiased and q_2^{TPC}-selected classes obtained with the V0M EP. The bottom panels show the distributions for the unbiased and q_2^{V0A}-selected classes obtained with the V0C EP. The solid and the dotted curves represent the total and the combinatorial-background fit functions, respectively.

q_2^{V0A}-selected samples. The simultaneous fit of the invariant-mass distribution and v_2 as a function of the invariant-mass in the unbiased sample is superimposed in both panels for comparison. The invariant-mass distributions (top panels) were scaled by the number of events in the corresponding sample to improve the visibility.

8.4 Dependence of efficiency on ESE selection

The ratios of p_T-differential yields of D^+ mesons in the ESE-selected and unbiased samples were computed using the raw yields divided by the number of events in the corresponding sample without applying any efficiency correction, under the assumption

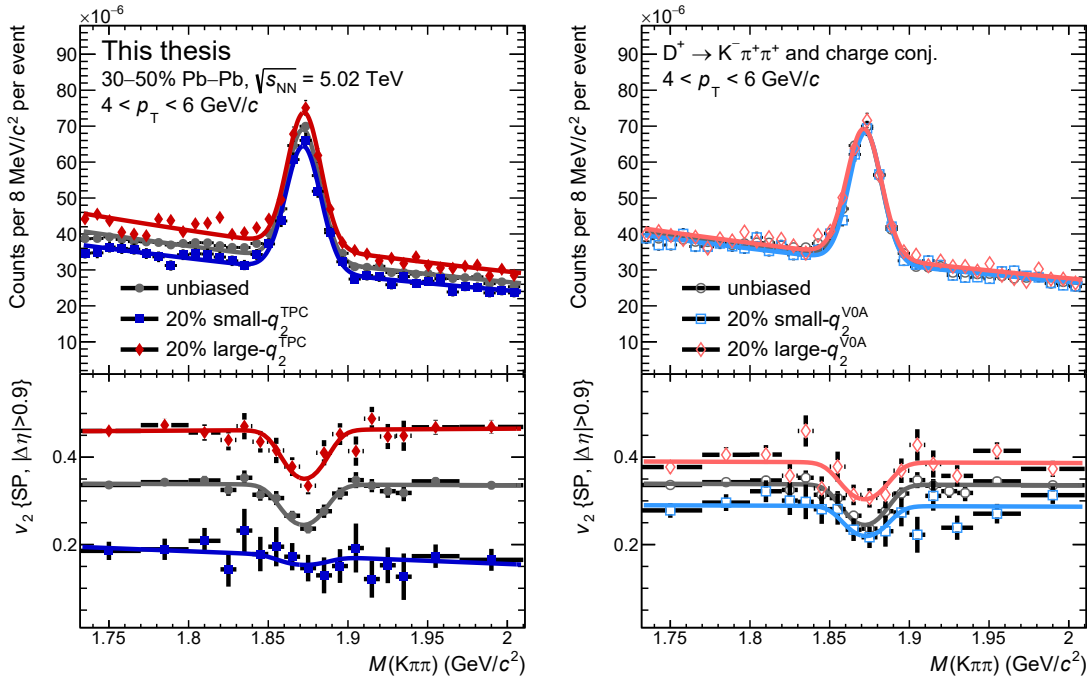

Figure 8.8: Simultaneous fits to the invariant-mass distributions and v_2 vs. invariant-mass distributions of D^+-meson candidates with $4 < p_T < 6$ GeV/c in the 30–50% centrality class for the unbiased, q_2^{TPC}-selected (left panel) and q_2^{V0A}-selected (right panel) classes obtained with the sample of Pb–Pb collisions at $\sqrt{s_{NN}} = 5.02$ TeV collected in 2018. The invariant-mass distributions were scaled by the number of events in the corresponding sample to improve the visibility.

that the reconstruction and selection efficiencies are the same in the ESE-selected and unbiased samples.

In order to verify this assumption, the efficiency was studied as a function of the azimuthal angle and the charged-particle multiplicity using the MC simulation described in Sec. 4.3.

As shown in the top-left panel of Fig. 8.9, the reconstruction efficiency of D^+ mesons depends on the azimuthal angle φ, owing to the non-uniform acceptance of the SPD detector. Therefore, the φ distribution of D^+ mesons in the MC simulation was weighted to reproduce the φ distribution of D^+ mesons observed in data. The φ distributions for the ESE-selected and unbiased samples were obtained by extracting the raw yields in intervals of φ. These distributions are not flat in φ because of the reconstruction efficiency, which depends on the azimuthal angle. The modification of the shape of the φ distribution in the ESE-selected samples was then computed as the ratio of these raw yields. The ratios were computed to factorise the φ dependence of the efficiency and to be sensitive to possible modifications of the φ distributions. These ratios were then fitted with a sinusoidal function to reduce the fluctuations, as shown in the top-middle

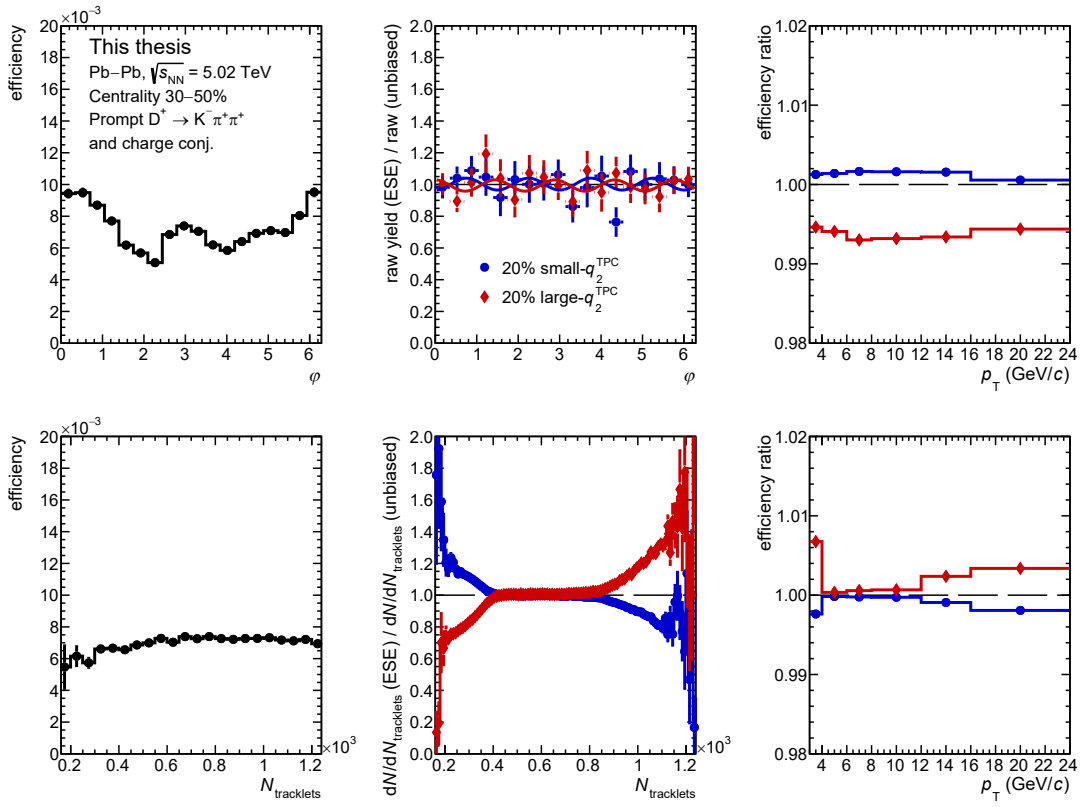

Figure 8.9: Top: reconstruction efficiency of D^+ mesons as a function of the azimuthal angle φ (left panel), φ-weights for the q_2^{TPC} selected samples (middle panel), and ratio of efficiency computed with and without φ-weights (right panel). Bottom: reconstruction efficiency of D^+ mesons as a function of $N_{tracklets}$ (left panel), $N_{tracklets}$-weights for the q_2^{TPC} selected samples (middle panel), and ratio of efficiency computed with and without $N_{tracklets}$-weights (right panel).

panel of Fig. 8.9 for the 20% small-q_2^{TPC} and 20% large-q_2^{TPC} classes. The functions obtained with this procedure were used to weight the φ distributions of D^+ mesons in the MC simulation. The effect of the φ-weights on the efficiency for the same ESE-selected samples is depicted in the top-right panel of Fig. 8.9. The efficiency was found to be less than 1% higher(lower) in the small(large)-q_2^{TPC} class. However, the effect was found to be small compared to the magnitude of the uncertainties on the measurement and therefore considered as negligible.

A similar strategy was adopted for the dependence of the efficiency on the charged-particle multiplicity. As discussed in Sec. 8.1, the selection of the events with the q_2 percentiles calibrated in 1%-wide centrality bins ensures to avoid large biases in the multiplicity distributions of the ESE-selected classes. Nevertheless, in case of q_2^{TPC}-based selection, a residual difference of the $N_{tracklets}$ distributions with respect to the unbiased one was observed. Hence, the ratio of the $N_{tracklets}$ distributions in the ESE-selected

and unbiased samples (see bottom-middle panel of Fig. 8.9) were used to weight the MC simulation. The bottom-right panel of Fig. 8.9 shows the ratio of the efficiencies obtained with the weighted and unweighted simulation. Also in this case, the effect was found to be smaller than 1% (0.5%) for $3 < p_{\mathrm{T}} < 4$ GeV/c ($p_{\mathrm{T}} > 4$ GeV/c) and hence negligible compared to the uncertainties, as expected by the mild dependence of the efficiency as a function of $N_{\mathrm{tracklets}}$ (bottom-left panel of Fig. 8.9) and the fact that the deviation from unity of the weights starts to be relevant where the $N_{\mathrm{tracklets}}$ distribution decreases steeply.

8.5 Non-flow contamination and q_2 selectivity

The effect of the non-flow correlations and the autocorrelations in the ESE-selected v_2 measurement was investigated by comparing the results obtained with the q_2^{TPC}-based and q_2^{V0A}-based selections.

However, the two results cannot be directly compared because of the different selectivity of q_2^{TPC} and q_2^{V0A}, owing to the different φ resolution and the different charged-particle multiplicity in the pseudorapidity intervals covered by the two detectors. Hence, the selectivity of q_2^{TPC} was artificially decreased to match the selectivity of q_2^{V0A} by rejecting randomly 85% of the tracks used in the q_2^{TPC} calculation and obtain a test sample with a selectivity similar to that of q_2^{V0A} and the same non-flow correlations of the q_2^{TPC}-based measurements. This fraction was tuned with a MC simulation produced with AMPT [215] as event generator and GEANT3 for the propagation of the particles through the detector. The top panels of Fig. 8.10 show the reconstructed q_2 percentile (q_2^{reco} (%)) as a function of the generated q_2 percentile (q_2^{gen} (%)). The three different configurations, i.e. q_2^{TPC}, q_2^{TPC} with 85% of tracks randomly rejected, and q_2^{V0A}, are shown in the left, middle, and right panels, respectively. The generated q_2 was computed using the generated primary charged particles (i.e. charged particles not produced by strange-hadron decays or by the interaction with the detector material) in the pseudorapidity coverage of the corresponding detector. The percentiles were calibrated independently for the generated and reconstructed q_2 with the procedure described in Sec. 8.1. A narrow correlation between the reconstructed and generated q_2 is obtained in case of q_2^{TPC}, while a broader correlation in case of random track rejection and q_2^{V0A}. In the bottom panels of the same Figure, the q_2^{gen} percentile distributions obtained selecting the 20% of the events with smallest and largest q_2^{reco} are shown. As a consequence of the correlation degree, the two distributions are separated in case of q_2^{TPC}, while they are distributed over the full q_2^{gen} percentile range in case of the random track rejection and q_2^{V0A}. The distributions obtained by randomly rejecting tracks in the reconstructed q_2^{TPC} calculation and with the q_2^{V0A}-based selection are similar, suggesting a similar selectivity of the two eccentricity estimators.

The D^+-meson v_2 was then measured, selecting the 20% of the events with largest q_2 and the 20% of the events with smallest q_2 for the three configurations. Fig. 8.11 shows the comparison of the effect of the different ESE selections on the D^+-meson $v_2\{\mathrm{SP}\}$ obtained with the sample of semi-central Pb–Pb collisions collected in 2018 in the 30–50% centrality class. The separation between the measurements in the small-q_2^{TPC} and large-q_2^{TPC} samples is reduced in the case of the random track rejection with

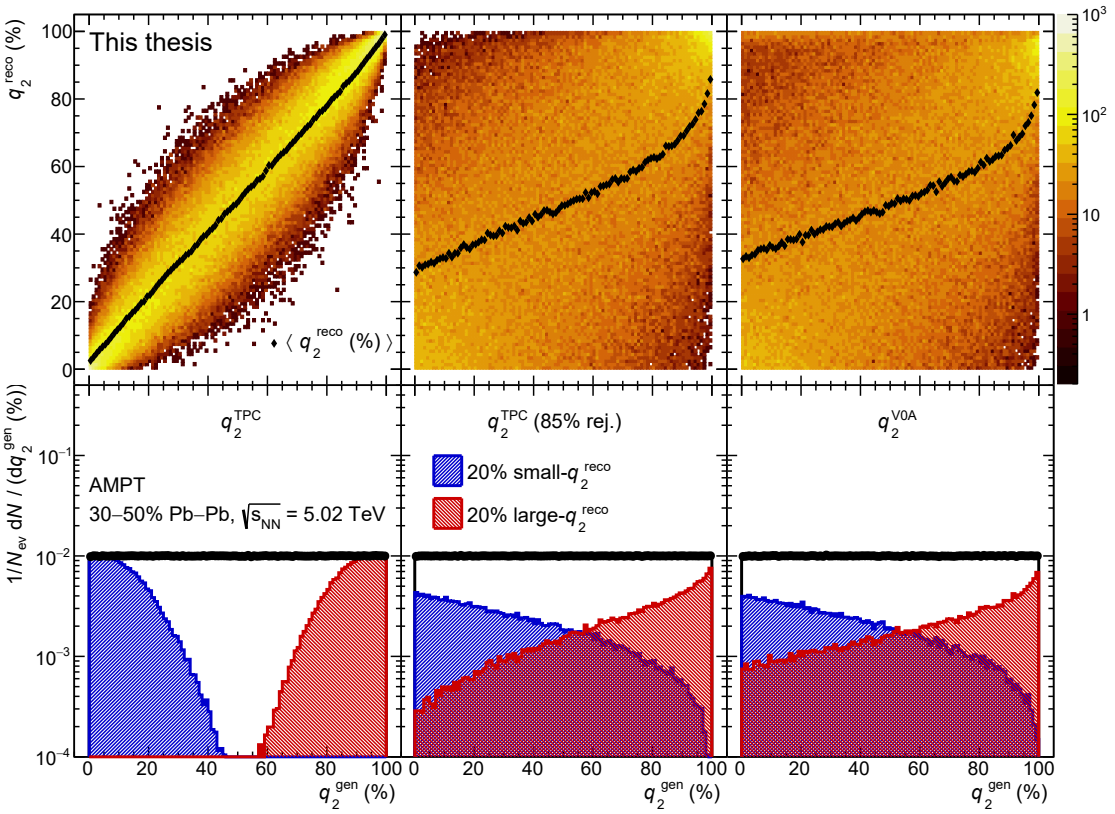

Figure 8.10: Top: reconstructed q_2 percentile ($q_2^{\rm reco}$ (%)) as a function of the generated q_2 percentile ($q_2^{\rm gen}$ (%)) for the TPC (left panel) detector, TPC detector rejecting 85% of the tracks randomly (middle panel) and V0A (right panel) detector, obtained with a MC simulation produced with the AMPT event generator [215]. Bottom: effect of the $q_2^{\rm reco}$ selection on the $q_2^{\rm gen}$ distributions for the TPC (left panel) detector, TPC detector rejecting 85% of the tracks randomly (middle panel) and V0A (right panel) detector.

respect to the default configuration, as expected from the reduced selectivity of $q_2^{\rm TPC}$. The results obtained with the $q_2^{\rm V0A}$-based selection are similar to those obtained with the reduced selectivity of $q_2^{\rm TPC}$, although they are compatible with both $q_2^{\rm TPC}$-based measurements. This observation suggests that the detector resolution and the charged-particle multiplicity is relevant for the effectiveness of the ESE selection and that the current statistical precision is not enough to draw a firm conclusion on the effect of the possible contribution of non-flow correlations in the $q_2^{\rm TPC}$-based measurements.

8.6 Systematic uncertainties

In this Section, the estimation of the systematic uncertainties on the measurements of the D^+-meson v_2 and the ratios of $p_{\rm T}$-differential yields with the ESE technique is

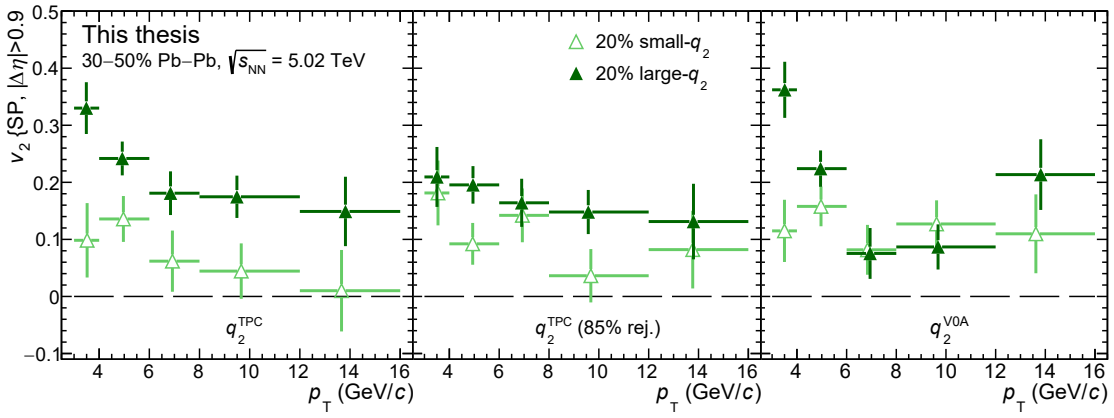

Figure 8.11: Comparison between the D^+-meson $v_2\{SP\}$ in the the 30–50% centrality class measured in the two ESE-selected samples obtained by computing q_2 with all the TPC tracks (left panel), rejecting 85% of the TPC tracks randomly (middle panel), and V0A signals (right panel).

presented. Since several sources of systematic uncertainty are in common with the analyses presented in Sec. 6.4 and 7.6, in this Section a particular focus will be given to the difference with respect to the studies carried out for the R_{AA} and v_2 analyses, and to the sources which are specific to the measurements with the ESE technique.

8.6.1 Fitting procedure

The systematic uncertainty on the fitting procedure was evaluated with a multi-trial approach both for the ratios of p_T-differential yields and for the v_2.

For the ratios of p_T-differential yields in the ESE-selected and unbiased samples, the same strategy adopted for the evaluation of the signal-extraction uncertainty in the measurement of the Q_{CP} in p–Pb collisions (see Sec. 6.4.1) was used. For each trial, the fit configurations were varied consistently for the extraction of the D^+-meson raw yield in the ESE-selected (numerator) and unbiased (denominator) samples, and the ratio of the two raw yield values was computed. The same variations of fit configurations described in Sec. 6.4.1 were tested. The left panel of Fig. 8.12 shows the distribution of the ratio of raw yields extracted in the 20% small-q_2^{V0A} and unbiased classes for candidates having $3 < p_T < 4$ GeV/c in the sample of semi-central Pb–Pb collisions collected in 2018. The distributions obtained by extracting the signal with a bin-counting (BC) method are also displayed in the Figure. The central value of the measurement is represented by the black dotted line. The systematic uncertainty was then evaluated as the sum in quadrature of the RMS and the shift with respect to the central value of the distribution of the raw-yield ratio. With this procedure, the correlation between the systematic uncertainties on the raw yields extracted in the ESE-selected and unbiased samples was taken into account. In particular, the two uncertainties were found to be mostly correlated, as shown in the right panel of Fig. 8.12, where the sum in quadrature of the RMS and the shift of the

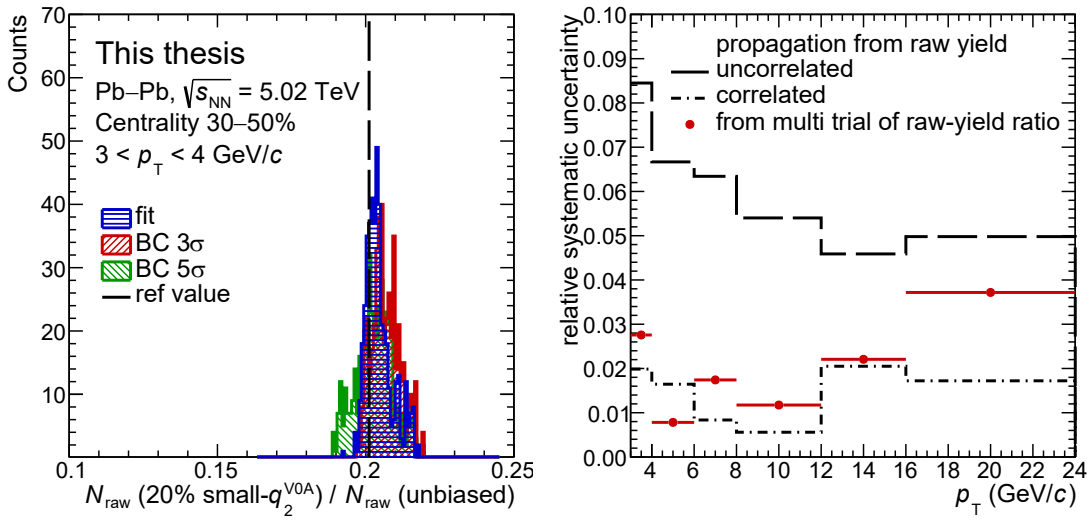

Figure 8.12: Left: distributions of raw-yield ratios in the 20% small-$q_2^{\rm V0A}$ and unbiased samples obtained with the multi-trial study from the fit and the bin-counting (BC) methods in the interval $3 < p_{\rm T} < 4$ GeV/c for the sample of semi-central Pb–Pb collisions at $\sqrt{s_{\rm NN}} = 5.02$ TeV collected in 2018. Right: systematic uncertainty evaluated from the RMS and the shift of the raw-yield ratio distribution compared to the one obtained by propagating the systematic uncertainties on the numerator and denominator as fully uncorrelated and fully correlated.

raw-yield ratio distribution as a function of $p_{\rm T}$ is compared to the systematic uncertainty that would be obtained by propagating the systematic uncertainties on the numerator and the denominator as fully uncorrelated or fully correlated between each other.

For the D$^+$-meson v_2, a similar approach was used. For each fit configuration, the D$^+$-meson v_2 and its residual with respect to the central value were computed as done for the unbiased v_2 analysis (see Sec. 7.6.1). In addition, to evaluate the degree of correlation, the same fit configurations were used for the measurement of the v_2 in the ESE-selected and unbiased samples. The top-left panel of Fig. 8.13 shows the residual of the v_2 measured in the 20% large-$q_2^{\rm TPC}$ sample as a function of that in the unbiased sample for the interval $6 < p_{\rm T} < 8$ GeV/c. The residuals in the two classes of events were found to be mostly uncorrelated. In order to investigate further this behaviour, the ratio of the $v_2\{\rm SP\}$ in the 20% large-$q_2^{\rm TPC}$ and in the unbiased samples, obtained with the same fit configuration was computed. As reported in the top-right panel of Fig. 8.13, the ratio is almost constant when the v_2 of the background is parametrised with a linear function of the invariant-mass, while it shows larger variations when the parabolic function is used. In the bottom panel of the same Figure, the systematic uncertainty on the $v_2\{\rm SP\}$ ratio, estimated independently for the linear and parabolic v_2 background functions as the sum in quadrature of the RMS and the shift with respect to the central value of the $v_2\{\rm SP\}$ ratio distribution, is compared to those obtained from the propagation of the uncertainties on the numerator and denominator as fully

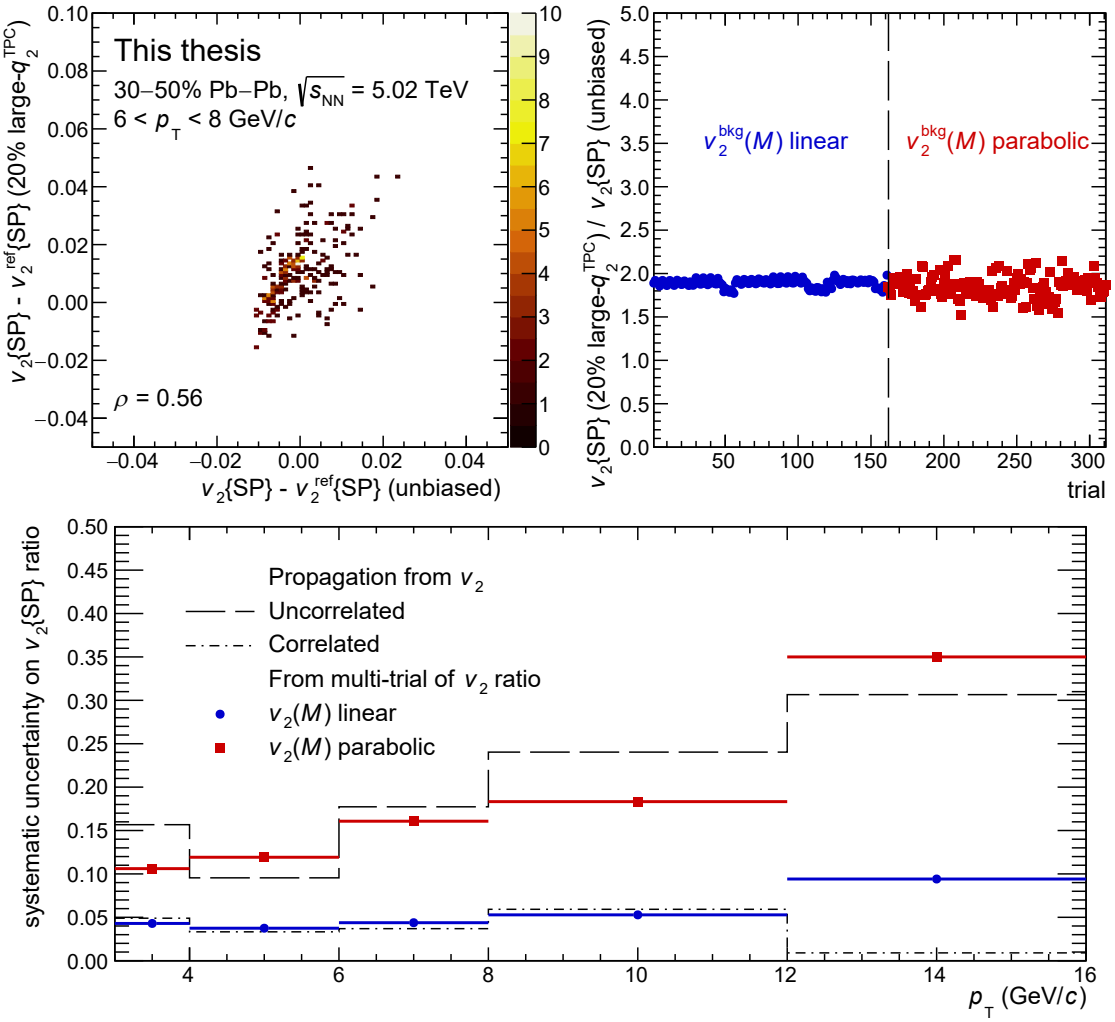

Figure 8.13: Top: correlation between the $v_2\{\mathrm{SP}\}$ residuals (left panel) and ratio of $v_2\{\mathrm{SP}\}$ coefficients (right panel) in the 20% large-q_2^{TPC} and unbiased classes obtained with the multi-trial study for the sample of semi-central Pb–Pb collisions at $\sqrt{s_{\mathrm{NN}}} = 5.02$ TeV collected in 2018. Bottom: systematic uncertainty on the ratio of $v_2\{\mathrm{SP}\}$ coefficients in the 20% large-q_2^{TPC} and unbiased classes from the multi-trial fits compared to the one obtained by propagating the systematic uncertainties on the numerator and denominator as fully uncorrelated and fully correlated.

correlated and fully uncorrelated. In the case of the linear background function, the uncertainty is closer to the correlated case, while it is nearly uncorrelated in case of parabolic background function. This observation suggests that a possible difference in the v_2 shape of the background could have a different impact on the measurements in the ESE-selected and unbiased v_2 measurements, and therefore the systematic uncertainty on the fitting procedure was considered as uncorrelated between the different event classes.

Since the estimate of the systematic uncertainty for the ESE-selected samples is more delicate due to the reduced size of the data sample which could imply the introduction statistical fluctuations in the evaluation of the uncertainty, the values estimated for the unbiased sample were also assigned to the measurements in the ESE-selected samples. The uncertainties were then propagated as uncorrelated in the ratios between the ESE-selected and unbiased v_2, in light of the studies presented in this Section.

8.6.2 EP and SP resolutions

The systematic uncertainty on the EP and SP resolutions in the ESE-selected samples includes three contributions. The first two contributions are (i) the possible effect due to non-flow correlations among the sub-events used in the resolution computation and (ii) the centrality dependence of the EP and SP resolutions. These two contributions are in common for the ESE-selected and unbiased samples and were discussed in Sec. 7.6.2. The third contribution is instead only present for the ESE-selected samples and it is due to autocorrelations originated by the usage of the same sub-events in the q_2 and EP (SP) resolution computation.

This latter contribution was estimated by computing the EP (SP) resolution with an alternative method, under the assumption that the correlation between the main sub-event (A) and the sub-event used for the q_2 calculation (B) is the same in the ESE-selected and unbiased samples.

For the EP method, the ratio of the $\chi_2^i = \langle \cos[2(\psi_2^i - \Psi_2)] \rangle$ variables is assumed to be equal in the ESE-selected and unbiased samples,

$$r = \left. \frac{\chi_2^{\mathrm{A}}}{\chi_2^{\mathrm{B}}} \right|_{\mathrm{ESE}} = \left. \frac{\chi_2^{\mathrm{A}}}{\chi_2^{\mathrm{B}}} \right|_{\mathrm{unbiased}}, \tag{8.4}$$

where χ_2^{A} and χ_2^{B} can be obtained from the EP resolution for the sub-event A [183] by inverting the equation

$$R_2^{\mathrm{A}}(\chi_2^{\mathrm{A}}) = \frac{\sqrt{\pi/2}}{2} \cdot \chi_2^{\mathrm{A}} \cdot e^{-\frac{(\chi_2^{\mathrm{A}})^2}{4}} \cdot \left[I_0\left(\frac{(\chi_2^{\mathrm{A}})^2}{4}\right) + I_1\left(\frac{(\chi_2^{\mathrm{A}})^2}{4}\right) \right], \tag{8.5}$$

being I_0 and I_1 two Bessel functions of the first kind. The EP resolution of the sub-event A for the ESE-selected samples can be obtained using Eq. 8.6 as

$$R_2^{\mathrm{A}}|_{\mathrm{ESE}} = R_2^{\mathrm{A}}(\chi_2^{\mathrm{A}}|_{\mathrm{ESE}}) = R_2^{\mathrm{A}}(\chi_2^{\mathrm{B}}|_{\mathrm{ESE}} \cdot r), \tag{8.6}$$

where r is computed using Eq. 8.4 and the χ_2 functions obtained from the unbiased sample. The top panels of Fig. 8.14 shows the EP resolution for the q_2^{TPC}-selected classes (left panel) and the q_2^{V0A}-selected classes (right panel) computed with the default and alternative methods as a function of the collision centrality. The sub-event A was the V0M detector for the q_2^{TPC}-selected classes, while the V0C detector for the q_2^{V0A}-selected classes. For the sub-event B, the tracks reconstructed in the TPC detector having $0 < \eta < 0.8$ were used in case of q_2^{TPC}, while the V0A in case of q_2^{V0A}. In the bottom panel of the same Figure, the ratios between the EP resolutions computed with the alternative and default

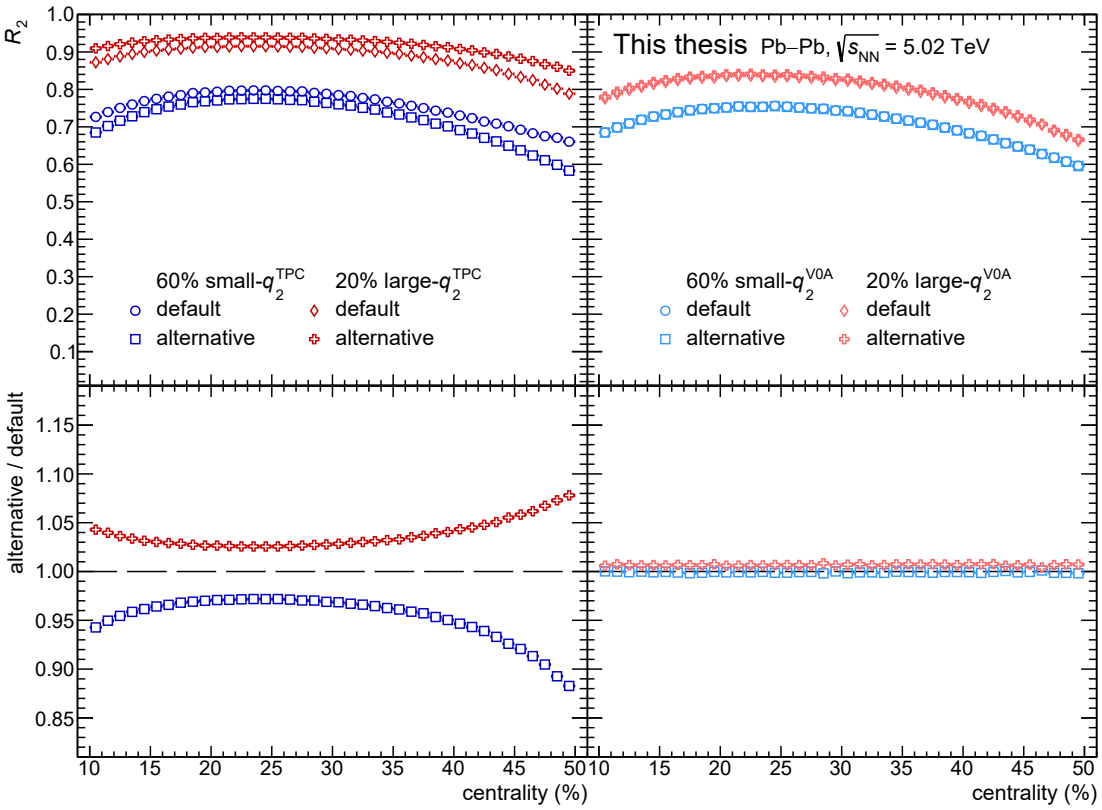

Figure 8.14: Comparison between the EP resolutions obtained with the 2015 Pb–Pb data sample for the q_2^{TPC}-selected (left panel) and q_2^{V0A}-selected (right panel) classes computed with the default and alternative methods (see text for the details) as a function of the collision centrality. The ratios between the EP resolutions computed with the alternative and default methods are displayed in the bottom panels.

methods are shown. The discrepancy between the two methods is sizeable for the sub-event configuration adopted for the q_2^{TPC}-selected classes, leading to 3% (5%) systematic uncertainty for the EP resolution integrated in the 10–30% (30–50%) centrality class, for both the ESE-selected samples. For the q_2^{V0A}-selected samples the difference between the two methods is considerably smaller, and therefore a 1% was assigned for the large-q_2^{V0A} sample, which is negligible compared to the other sources of systematic uncertainty.

A similar approach was used for the SP resolution. In particular, the ratio of the scalar products between the $\boldsymbol{Q}_2$-vectors of for main sub-event (A) and the sub-event used for the q_2 calculation (B) and between the sub-event used for the q_2 calculation and the third one (C) was assumed to be equal for the ESE-selected and unbiased samples:

$$r' = \frac{\langle \frac{\boldsymbol{Q}^*_{2,\mathrm{A}}}{M_{\mathrm{A}}} \cdot \frac{\boldsymbol{Q}_{2,\mathrm{B}}}{M_{\mathrm{B}}} \rangle}{\langle \frac{\boldsymbol{Q}^*_{2,\mathrm{B}}}{M_{\mathrm{B}}} \cdot \frac{\boldsymbol{Q}_{2,\mathrm{C}}}{M_{\mathrm{C}}} \rangle}\Bigg|_{\mathrm{ESE}} = \frac{\langle \frac{\boldsymbol{Q}^*_{2,\mathrm{A}}}{M_{\mathrm{A}}} \cdot \frac{\boldsymbol{Q}_{2,\mathrm{B}}}{M_{\mathrm{B}}} \rangle}{\langle \frac{\boldsymbol{Q}^*_{2,\mathrm{B}}}{M_{\mathrm{B}}} \cdot \frac{\boldsymbol{Q}_{2,\mathrm{C}}}{M_{\mathrm{C}}} \rangle}\Bigg|_{\mathrm{unbiased}} \tag{8.7}$$

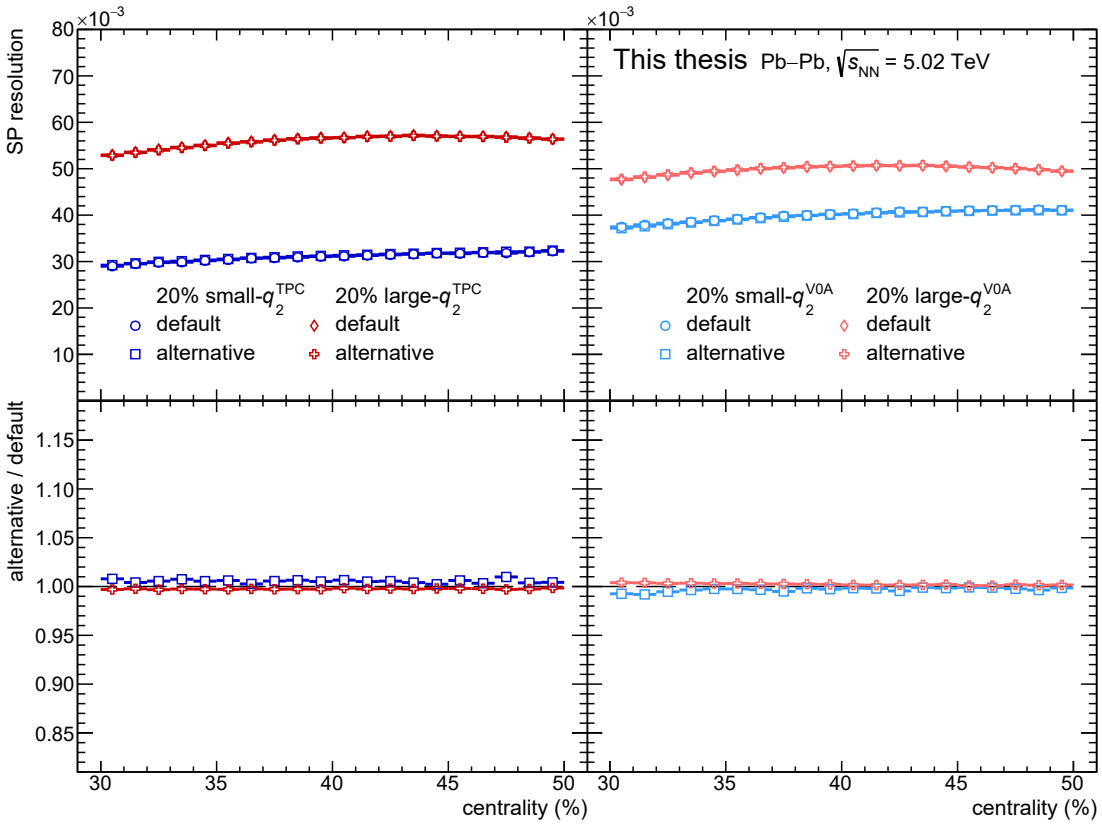

Figure 8.15: Comparison between the SP resolutions obtained with the 2018 Pb–Pb data sample for the q_2^{TPC}-selected (left panel) and q_2^{V0A}-selected (right panel) classes computed with the default and alternative methods (see text for the details) as a function of the collision centrality. The ratios between the SP resolutions computed with the alternative and default methods are displayed in the bottom panels.

The SP resolution of the sub-event A for the ESE-selected samples can be then expressed as

$$R_2'^{\mathrm{A}} = \sqrt{\langle \frac{\boldsymbol{Q}^*_{2,\mathrm{A}}}{M_{\mathrm{A}}} \cdot \frac{\boldsymbol{Q}_{2,\mathrm{C}}}{M_{\mathrm{C}}} \rangle \cdot r'} \tag{8.8}$$

where r' was computed using Eq. 8.4 and the $\boldsymbol{Q}_2$-vectors obtained from the unbiased sample. The comparisons between the SP resolutions computed with the alternative and default methods are reported in the top panels of Fig. 8.15. In the bottom panels of the same Figure, the ratios between the two methods are reported. In this case the systematic uncertainty was estimated to be 0.5% for each ESE-selected sample.

8.6.3 Multiplicity bias in ESE-selected classes

As discussed in Sec. 8.1, a different multiplicity distribution in the ESE-selected an unbiased samples would introduce a bias in the measurements. Apart from the variation

of the reconstruction efficiency, which was found to be negligible (see Sec. 8.4), a bias would arise from the multiplicity dependence of the observables (yields and v_2) studied with the ESE technique. To evaluate the magnitude of this bias, a fast MC simulation was adopted.

The inputs of the fast MC simulation were (i) the $N_{\text{tracklets}}$ distributions in the unbiased and ESE-selected samples, (ii) the distribution of $N_{\text{tracklets}}$ as a function of the collision centrality for the full sample, and (iii) a parametrisation of the observables as a function of the collision centrality. Since the measurement of the D-meson v_2 as a function of centrality was not available, the v_2 of the charged particles taken from Ref. [216] was used. The data points were interpolated with a cubic spline, as shown in the top-left panel of Fig. 8.16. For the p_{T}-differential yields, the D^+ raw yields were extracted in 1%-wide centrality bins for the p_{T} intervals of the analysis and were fitted with a second-order polynomial, as shown in the bottom-left panel of the same Figure. The raw yields were adopted instead the corrected yields, since it was verified that the efficiency does not depend on the collision centrality for the 30–50% centrality class.

For the fast MC simulation, a value of $N_{\text{tracklets}}$ was extracted randomly from the corresponding distributions for the unbiased and ESE-selected samples. For each $N_{\text{tracklets}}$, a centrality value was extracted from the centrality distribution, obtained from the two-dimensional centrality vs. $N_{\text{tracklets}}$ correlation. Finally, the v_2 and the raw yield for the corresponding centrality were computed from the aforementioned parameterisations. This procedure was repeated 10^6 times, and for each time a v_2 and raw yield distribution was filled. The middle panels of Fig. 8.16 show the distributions obtained for the v_2 in the 30–50% centrality class (top panel) and the raw yield in the same centrality class in the $4 < p_{\text{T}} < 6$ GeV/c interval (bottom panel), for the unbiased, and 20% small-q_2^{TPC}, and 20% large-q_2^{TPC} samples. The bias due to the different multiplicity distribution was then evaluated as the ratio between the mean value of the v_2 (raw yield) distributions in the ESE-selected and unbiased samples. The top-right panel of Fig. 8.16 shows the bias for the v_2 in the 10–30% and 30–50% centrality classes. The bottom-right panel of the same Figure shows the bias for the raw yields in the 30–50% centrality class as a function of p_{T}. In both cases the effect was found to be smaller than 1% and therefore it was considered as negligible compared to the other sources of systematic uncertainty.

8.6.4 Beauty feed-down subtraction

The contribution to the v_2 due to the D^+ mesons from beauty-hadron decays in the ESE-selected samples was subtracted with the same strategy adopted for the unbiased measurement (see Sec. 7.5). In particular, the measured v_2 was expressed as a linear combination of the v_2 of prompt and feed-down D^+ mesons, as reported in Eq. 7.14, where the v_2 of feed-down D^+ mesons was assumed to be half of that of prompt D^+ mesons. The two contributions were weighted by the fraction of prompt D^+ mesons in the raw yield, estimated using the feed-down D^+ meson cross section from FONLL calculations and the EvtGen package, and an assumption on the R_{AA} of feed-down D^+ mesons, as described in Sec. 6.3.3.

The systematic uncertainty associated to the beauty feed-down subtraction was also estimated with the same procedure adopted for the unbiased v_2 measurement. It was

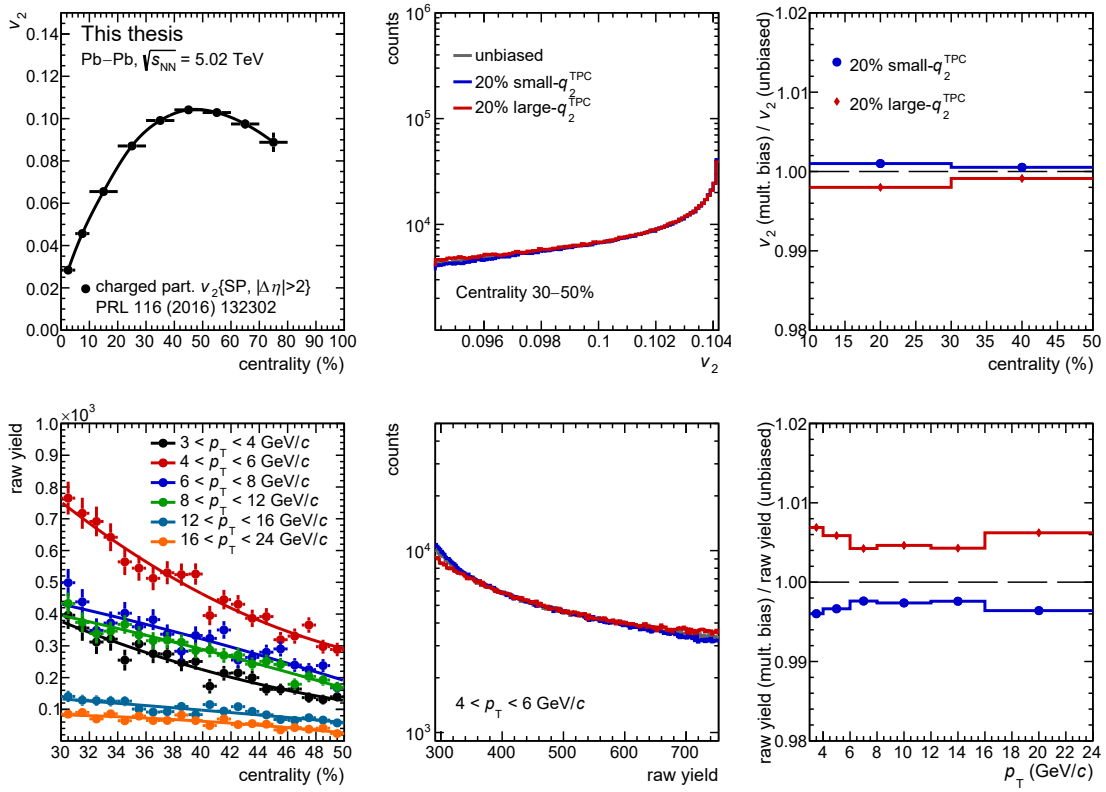

Figure 8.16: Top: charged-particle v_2 used as input for the shape of v_2 as a function of the collision centrality (left panel), distribution of v_2 obtained from the fast MC simulation for the 30–50% centrality class (middle panel), and ratio of the average v_2 for the ESE-selected and unbiased samples obtained from the fast simulation for the 10–30% and 30–50% centrality classes (right panel). Bottom: D^+-meson raw yields as a function of the collision centrality for different p_T intervals (left panel), distribution of raw yields obtained from the fast MC simulation for the 30–50% centrality class and $4 < p_T < 6$ GeV/c interval (middle panel), and ratio of the average raw yield as a function of p_T for the ESE-selected and unbiased samples obtained from the fast simulation for the 30–50% centrality classes (right panel).

estimated by varying (i) the renormalisation and factorisation scales and the charm-quark mass in the FONLL calculations, (ii) the hypothesis on the R_{AA} of feed-down D^+ mesons as reported in Sec. 6.4.7, and (iii) the assumption on the v_2 of feed-down D^+ mesons considering one standard deviation of a probability distribution uniformly distributed between 0 and the v_2 of prompt D^+ mesons.

This source of systematic uncertainty was considered as fully correlated in the ESE-selected and unbiased samples, both for the ratio of v_2 and for that between the p_T-differential yields.

8.6.5 Summary of systematic uncertainties

The values assigned as systematic uncertainty to the v_2 measurements for each non-negligible contribution are summarised in Table 8.2. The systematic uncertainties on the fit procedure and the feed-down subtraction are reported as absolute values, while those on the EP (SP) resolution as relative values. The systematic uncertainties evaluated for each centrality class, ESE-selected sample, and measurement method are similar in magnitude. The systematic uncertainty on the EP resolution is larger in case of q_2^{TPC} because of the autocorrelation between the sub-events used in the q_2 and $\mathcal{R}_2$ computation. The uncertainty relative to the feed-down subtraction procedure is typically larger in the large-q_2 samples compared to the small-q_2 samples, since it depends on the magnitude of the v_2. As already observed for the analysis of the unbiased v_2 (see Sec. 7.6.4), the uncertainty on the fitting procedure is slightly smaller in case measurement with the SP method, probably because the evaluation of this source of systematic uncertainty for the EP method is more sensitive to statistical fluctuations (see Sec. 7.6.1).

The values assigned as systematic uncertainty to the ratios of p_{T}-differential yields in the ESE-selected and unbiased samples are reported in Table 8.3. The only non-negligible source of systematic uncertainty that does not completely cancel out in the ratio is the one related to the raw-yield extraction, which is however smaller compared to the statistical uncertainty.

8.7 Results

Figure 8.17 shows the prompt D^+-meson v_2 as a function of p_{T} measured in the ESE-selected and unbiased samples, in Pb–Pb collisions at $\sqrt{s_{\mathrm{NN}}} = 5.02$ TeV. The data points along the x-axis are positioned at the average p_{T} of the reconstructed D^+ mesons, which was computed as the average of the p_{T} distribution of candidates with $|M - M(\mathrm{D}^+)| < 3\sigma$, after subtracting the distribution of the background candidates estimated from the side bands, as for the analysis of the unbiased v_2. In the left column, the results obtained in the q_2^{TPC}-selected classes are displayed, while in the right column there are those in the q_2^{V0A}-selected classes. The measurements with the EP method performed with the sample of MB Pb–Pb collisions collected in 2015 are shown in the top and middle rows for the 10–30% and the 30–50% centrality classes, respectively. These results were published in Ref. [5]. The measurements with the SP method performed using the sample of semi-central Pb–Pb collisions collected in 2018 in the 30–50% centrality class are shown in the bottom row. These measurements were approved as preliminary results by the ALICE Collaboration.

The v_2 measured in the small(large)-q_2 classes of events was found to be lower (higher) than that measured in the unbiased sample, indicating a positive correlation between the elliptic flow of the D mesons and that of the bulk of light-flavour particles. The separation between the measurements in the large-q_2 and small-q_2 samples is reduced for the q_2^{V0A}-selected classes compared to that observed for the q_2^{TPC}-selected classes, mainly due to the lower selectivity of q_2^{V0A}, and in addition to the suppression of possible non-flow contributions.

p_T (GeV/c)		[3,4]	[4,6]	[6,8]	[8,12]	[12,16]
EP 10 – 30%						
M and v_2 fits	all ESE classes	-	0.020	0.015	0.015	-
Feed-down	small-q_2^{TPC}	-	$^{+0.004}_{-0.002}$	$^{+0.007}_{-0.003}$	$^{+0.002}_{-0.004}$	-
	large-q_2^{TPC}	-	$^{+0.018}_{-0.009}$	$^{+0.013}_{-0.006}$	$^{+0.004}_{-0.002}$	-
	small-q_2^{V0A}	-	$^{+0.004}_{-0.002}$	$^{+0.002}_{-0.001}$	$^{+0.001}_{-0.001}$	-
	large-q_2^{V0A}	-	$^{+0.016}_{-0.008}$	$^{+0.013}_{-0.006}$	$^{+0.005}_{-0.003}$	-
EP resolution	small-q_2^{TPC}			5.0%		
	large-q_2^{TPC}			5.0%		
	small-q_2^{V0A}			1.0%		
	large-q_2^{V0A}			2.0%		
EP 30 – 50%						
M and v_2 fits	all ESE classes	0.025	0.015	0.015	0.012	-
Feed-down	small-q_2^{TPC}	$^{+0.005}_{-0.003}$	$^{+0.007}_{-0.003}$	$^{+0.009}_{-0.004}$	$^{+0.009}_{-0.004}$	-
	large-q_2^{TPC}	$^{+0.011}_{-0.005}$	$^{+0.020}_{-0.009}$	$^{+0.023}_{-0.011}$	$^{+0.024}_{-0.012}$	-
	small-q_2^{V0A}	$^{+0.009}_{-0.004}$	$^{+0.010}_{-0.005}$	$^{+0.012}_{-0.006}$	$^{+0.007}_{-0.003}$	-
	large-q_2^{V0A}	$^{+0.013}_{-0.006}$	$^{+0.021}_{-0.010}$	$^{+0.001}_{-0.002}$	$^{+0.005}_{-0.002}$	-
EP resolution	small-q_2^{TPC}			7.0%		
	large-q_2^{TPC}			7.0%		
	small-q_2^{V0A}			1.0%		
	large-q_2^{V0A}			2.0%		
SP 30 – 50%						
M and v_2 fits	all ESE classes	0.015	0.008	0.008	0.011	0.011
Feed-down	small-q_2^{TPC}	$^{+0.006}_{-0.003}$	$^{+0.010}_{-0.005}$	$^{+0.005}_{-0.003}$	$^{+0.005}_{-0.002}$	$^{+0.001}_{-0.001}$
	large-q_2^{TPC}	$^{+0.020}_{-0.010}$	$^{+0.018}_{-0.009}$	$^{+0.016}_{-0.008}$	$^{+0.018}_{-0.009}$	$^{+0.014}_{-0.007}$
	small-q_2^{V0A}	$^{+0.007}_{-0.003}$	$^{+0.012}_{-0.006}$	$^{+0.007}_{-0.003}$	$^{+0.013}_{-0.006}$	$^{+0.011}_{-0.005}$
	large-q_2^{V0A}	$^{+0.022}_{-0.010}$	$^{+0.017}_{-0.008}$	$^{+0.007}_{-0.003}$	$^{+0.009}_{-0.004}$	$^{+0.021}_{-0.010}$
SP resolution	small-q_2^{TPC}			1.0%		
	large-q_2^{TPC}			1.0%		
	small-q_2^{V0A}			1.0%		
	large-q_2^{V0A}			1.0%		

Table 8.2: Summary of systematic uncertainties on the measurement of the D^+-meson v_2 with the ESE technique in Pb–Pb collisions at $\sqrt{s_{NN}} = 5.02$ TeV. The uncertainties on the fitting procedure and feed-down subtraction are quoted as absolute uncertainties, while that on the EP (SP) resolution as relative uncertainty.

p_{T} (GeV/c)		[3,4]	[4,6]	[6,8]	[8,12]	[12,16]	[16,24]
$10-30\%$ (2015)							
Raw-yield extraction (%)	small-q_2^{TPC}	-	5	2	2	3	-
	large-q_2^{TPC}	-	4	2	2	4	-
	small-q_2^{V0A}	-	5	2	2	3	-
	large-q_2^{V0A}	-	4	2	2	4	-
$30-50\%$ (2015)							
Raw-yield extraction (%)	small-q_2^{TPC}	3	2	2	2	2	-
	large-q_2^{TPC}	5	4	2	3	4	-
	small-q_2^{V0A}	3	2	2	2	2	-
	large-q_2^{V0A}	5	4	2	3	4	-
$30-50\%$ (2018)							
Raw-yield extraction (%)	small-q_2^{TPC}	4	1	1	1	3	4
	large-q_2^{TPC}	3	1	1	1	3	3
	small-q_2^{V0A}	3	1	1	1	2	3
	large-q_2^{V0A}	3	1	1	1	3	4

Table 8.3: Summary of relative systematic uncertainties on the measurement of the ratios of D^+-meson p_{T}-differential yields in the ESE-selected and unbiased samples in Pb–Pb collisions at $\sqrt{s_{\mathrm{NN}}} = 5.02$ TeV.

Figure 8.18 shows the ratios of the p_{T}-differential yields of prompt D^+ mesons measured in the ESE-selected and unbiased samples, in Pb–Pb collisions at $\sqrt{s_{\mathrm{NN}}} = 5.02$ TeV. The results obtained with the q_2^{TPC}-selected classes are displayed in the right column, while those in the q_2^{V0A}-selected classes in the left column. The measurements performed using the sample of MB Pb–Pb collisions collected in 2015 and published in Ref. [5] are shown in the top and middle rows for the 10–30% and the 30–50% centrality classes, respectively. The measurements performed with the sample of semi-central Pb–Pb collisions collected in 2018 and approved as preliminary results by the ALICE Collaboration in the 30–50% centrality class are shown in the bottom row. The statistical uncertainty on the ratio was obtained by propagating the statistical uncertainties from the raw yields extracted in the ESE-selected and unbiased samples, taking into account the degree of correlation due to the intersection between the two samples.

The ratios of the p_{T}-differential yields were found to be compatible with unity. A hint of larger p_{T}-differential yields higher in the large-q_2^{TPC} class compared to those in the small-q_2^{TPC} class was observed in the $3 < p_{\mathrm{T}} < 12$ GeV/c range for the 30–50% centrality class in both the analyses of the 2015 and 2018 Pb–Pb data samples. This observation is

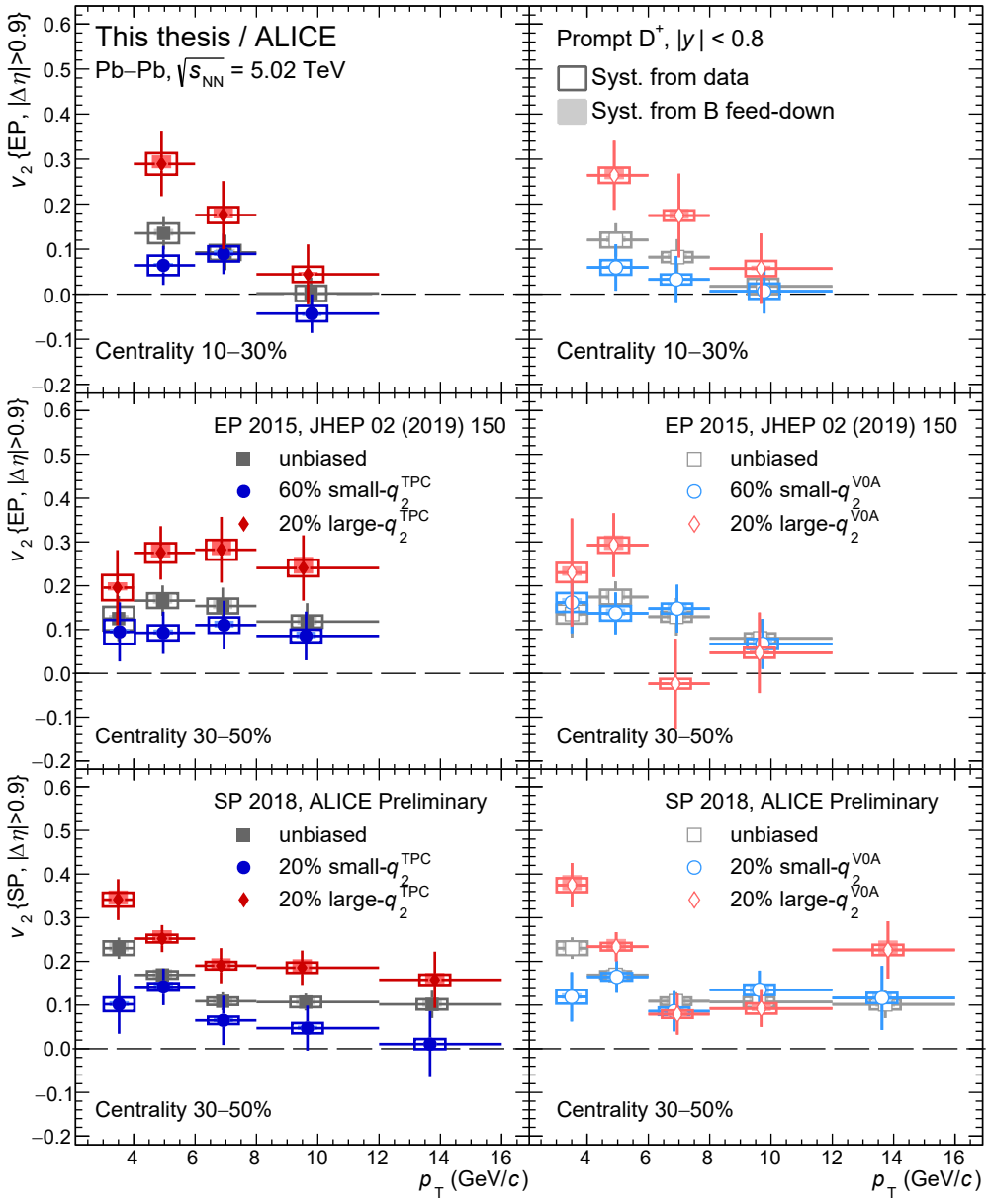

Figure 8.17: Prompt D^+-meson v_2 as a function of p_T measured with the ESE technique in Pb–Pb collisions at $\sqrt{s_{NN}} = 5.02$ TeV. The measurements with the EP method performed with the sample of MB Pb–Pb collisions collected in 2015 are reported in the top (middle) row for the 10–30% (30–50%) centrality class, those with the SP method with the sample of semi-central Pb–Pb collisions collected in 2018 for the 30–50% centrality class in the bottom row.

consistent with the measurement of light-flavour hadrons, which is understood in terms

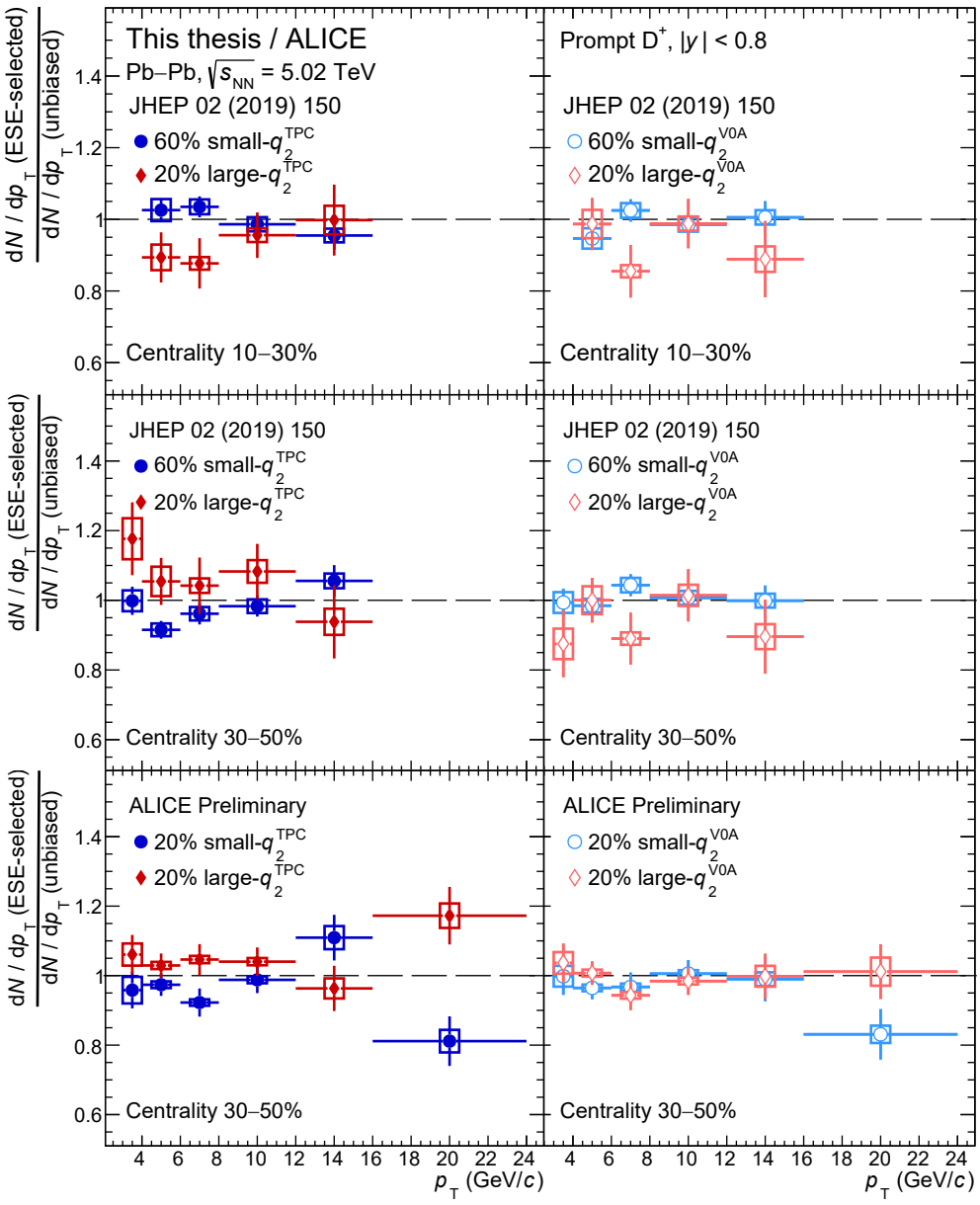

Figure 8.18: Ratios of prompt D^+-meson p_T-differential yields in the ESE-selected and unbiased samples in Pb–Pb collisions at $\sqrt{s_{NN}} = 5.02$ TeV. The measurements performed with the sample of MB Pb–Pb collisions collected in 2015 are reported in the top (middle) row for the 10–30% (30–50%) centrality class, those with the sample of semi-central Pb–Pb collisions collected in 2018 for the 30–50% centrality class in the bottom row.

of correlation between radial and elliptic flow, induced by a larger initial density in more anisotropic events. However, the effect was found at most 5% for pions with $p_T \approx 4$ GeV/c

in semi-central Pb–Pb collisions at $\sqrt{s_{NN}} = 2.76$ TeV [210], which is of the order of the current statistical uncertainties of the D^+-meson measurements.

8.7.1 Comparison to light-flavour hadrons

The effect of the ESE selection on the D-meson v_2 was compared to that of light-flavour hadrons. For this comparison, the average of the v_2 coefficients of prompt D^0, D^+, and D^{*+} mesons was computed by using the inverse of the squared absolute statistical uncertainty as weight.

The measurements in the q_2^{V0A}-classes were used, to avoid the contributions of non-flow correlations and autocorrelations, that are larger in case of light-flavour hadrons, because of their larger abundance.

Figure 8.19 shows the comparison between the $v_2\{SP\}$ of prompt D mesons and that for charged particles, obtained in the unbiased (top-left panel) and in the 20% large-q_2^{V0A} (top-right panel) samples. In both the ESE-selected and unbiased samples, the D-meson and charged-particle $v_2\{SP\}$ coefficients are similar in magnitude for $p_T > 3$ GeV/c, while the prompt D-meson $v_2\{SP\}$ is lower than that of charged particles for lower p_T. The ratio between the $v_2\{SP\}$ in the large-q_2^{V0A} and unbiased samples is shown in the bottom-left panel of the same Figure. For the ratio of the average D-meson $v_2\{SP\}$, the statistical uncertainty was propagated taking into account the degree of correlation between the measurements in the ESE-selected and the unbiased samples. For the systematic uncertainties, the contribution of the fitting procedure was considered as uncorrelated as discussed in Sec. **??**, while those of the SP resolution and the beauty feed-down subtraction as fully correlated. The ratios of $v_2\{SP\}$ in the ESE-selected and unbiased sample were found to be flat as a function of p_T, confirming that the usage of q_2^{V0A} ensures the selection of a global property of the events, and similar in magnitude. However, the ratio of the average D-meson $v_2\{SP\}$ was found to be also compatible with unity, given the reduced sensitivity of q_2^{V0A} and the current statistical precision of the measurement.

8.7.2 Comparison to model predictions

The measurement of the D-meson v_2 in the ESE-selected samples and the ratios of p_T-differential yields were compared to theoretical models implementing the charm-quark transport in an hydrodynamically expanding medium. The measurements in the q_2^{TPC}-classes were used, to reduce as much as possible the detector effects, which are not included in the model predictions. In particular, the LIDO [114] and DAB-MOD [199] models classify the events according to the q_2 computed with generated particles, while in the POWLANG [188] model the eccentricity is used. Also in this case, the measurements of prompt D^0, D^+, and D^{*+} mesons were averaged to improve the statistical precision.

Figure 8.20 shows the average $v_2\{SP\}$ of prompt D^0, D^+, and D^{*+} mesons in the 20% small-q_2^{TPC} (top-left panel), 20% large-q_2^{TPC}(top-middle panel), and unbiased samples (top-right panel), compared to the POWLANG, LIDO, and DAB-MOD model predictions. The DAB-MOD and LIDO models underestimate the D-meson v_2 in the large-q_2^{TPC} class of events, while they reproduce that in the small-q_2^{TPC} sample. On the contrary, the

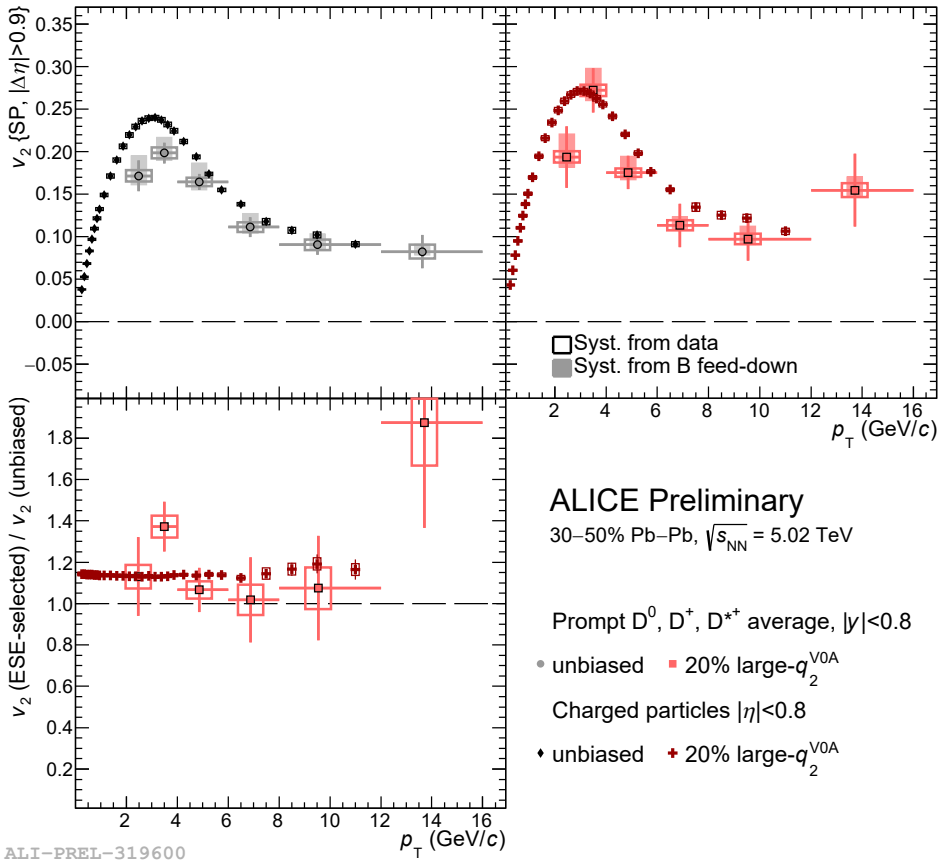

Figure 8.19: Top: prompt D^0, D^+, and D^{*+} average $v_2\{SP\}$ as a function of p_T for the sample of Pb–Pb collisions at $\sqrt{s_{NN}} = 5.02$ TeV collected in 2018, in the unbiased (left panel) and 20% large-q_2^{V0A} (right panel) samples, in the 30–50% centrality class. The charged-particle $v_2\{SP\}$ obtained at the same energy, centrality classes and ESE-selected samples are superimposed for comparison. Bottom: ratio of the measured $v_2\{SP\}$ in the large-q_2 sample to the one obtained from the unbiased sample.

POWLANG model reproduces the v_2 in the large-q_2^{TPC} class of events and underestimates that in the small-q_2^{TPC} class. In particular, a better description of the measured data is obtained by the prediction that makes use of the transport parameters obtained with the weak-coupling calculations with Hard-Thermal-Loop (HTL) resummation of medium effects, rather than those extracted from lattice QCD (lQCD) simulations [201, 217].

The ratios of the $v_2\{SP\}$ in the ESE-selected and unbiased samples are shown in the bottom-left and bottom-middle panels of Fig. 8.20 for the small-q_2^{TPC} and large-q_2^{TPC} classes of events, respectively. The measured ratios and those predicted by the various models are nearly flat as a function of p_T. In addition, the predictions provided by the same model with different transport coefficients (i.e. POWLANG HTL and POWLANG lQCD, or DAB-MOD(M&T) and DAB-MOD(E_{loss})) give consistent predictions, indicating that the

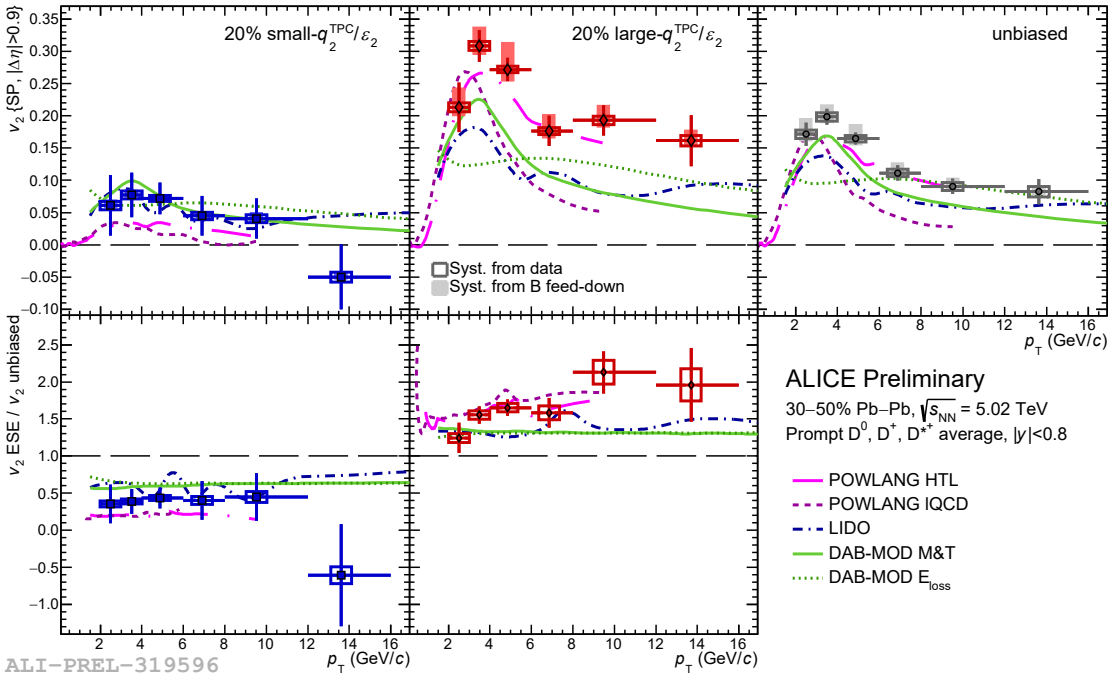

Figure 8.20: Top: prompt D^0, D^+, and D^{*+} average $v_2\{SP\}$ as a function of p_T for the sample of Pb–Pb collisions at $\sqrt{s_{NN}} = 5.02$ TeV collected in 2018, in the 20% small-q_2^{TPC} (left panel), 20% large-q_2^{TPC} (middle panel), and unbiased (right panel) samples, in the 30–50% centrality class. Bottom: ratio of the measured $v_2\{SP\}$ in the ESE-selected classes to the one obtained from the unbiased sample. The data points are compared to model predictions based on the charm-quark transport in an hydrodynamically expanding medium.

effect of the ESE selection is more related to the initial geometry rather than the dynamic evolution of the heavy quarks in the medium.

Figure 8.21 shows the average of the ratio of prompt D^0, D^+, and D^{*+} p_T-differential yields in the 20% small(large)-q_2^{TPC} and the unbiased samples compared to the predictions provided by the POWLANG model. A hardening (softening) of the p_T distributions is predicted by the POWLANG model in the large(small)-q_2^{TPC} class of events, due to the correlation between the radial and the elliptic flow. The effect predicted for the small-q_2^{TPC} describes the measurement, while the one in the large-q_2^{TPC} seems to be overestimated, especially in case of HTL transport coefficients. Unlike the modification of the v_2 in the ESE-selected samples, the modification of the p_T-differential yields is sensitive to the variation of the transport coefficients. Therefore, these measurements with the unbiased v_2 and R_{AA} have the potential to set constraints to model predictions based on the charm-quark transport in the medium, which need several ingredients, such as the initial geometry, the flow of the underlying medium, the transport coefficients, and the hadronisation mechanisms in the medium, to be compared with the measurements and

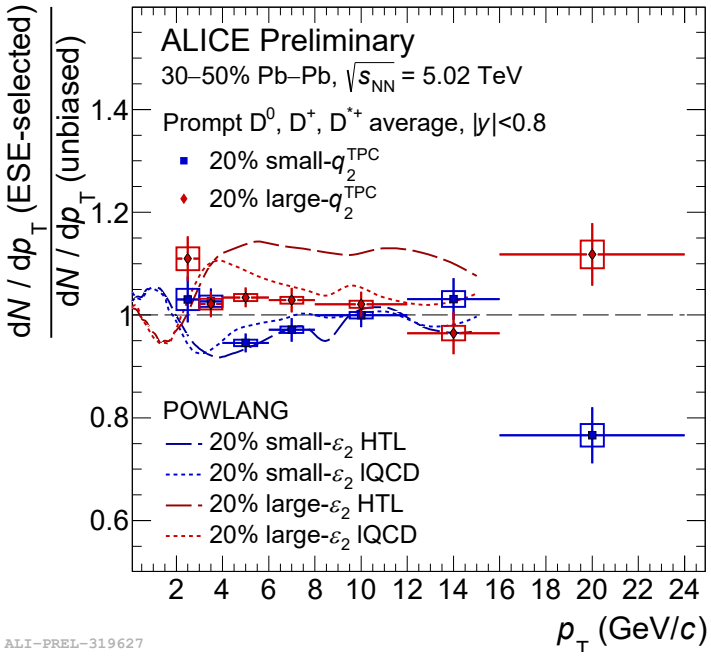

Figure 8.21: Average of the ratio of prompt D^0, D^+, and D^{*+} p_T-differential yields in the q_2^{TPC}-selected samples to those in the unbiased sample in the 30–50% centrality class, obtained with the sample of Pb–Pb collisions at $\sqrt{s_{NN}}$ = 5.02 TeV collected in 2018. The data points are compared to the POWLANG predictions obtained with two sets of transport coefficients.

extract information about the properties of the QGP.

Chapter 9

Conclusions and perspectives

In this Thesis, the measurements of the production of D^+ and D_s^+ mesons in pp, p–Pb and Pb–Pb collisions were presented. The analyses were performed via the reconstruction of the displaced decay-vertex topologies $\mathrm{D}^+ \to \mathrm{K}^-\pi^+\pi^+$ and $\mathrm{D}_\mathrm{s}^+ \to \phi\pi^+ \to \mathrm{K}^-\mathrm{K}^+\pi^+$ at mid rapidity.

The measurement of the p_T-differential production cross section of prompt D_s^+ mesons in pp collisions at $\sqrt{s} = 5.02$ TeV is more differential and has an extended p_T coverage with respect with the previous measurement at $\sqrt{s} = 7$ TeV [158]. The production cross section is found to be described by perturbative QCD calculations and the abundance of D_s^+ mesons compared to the D meson without strange-quark content is compatible with that measured at e^+e^- colliders, indicating that the charm-quark hadronisation mechanism is not significantly modified.

The nuclear modification factor of prompt D_s^+ mesons measured in the 10% most central Pb–Pb collisions at $\sqrt{s_\mathrm{NN}} = 5.02$ TeV has statistical uncertainties reduced down to a factor 3 compared to the previous measurement at the same energy [3]. The central values of the R_AA are systematically higher then those measured for prompt D^+ mesons for $p_\mathrm{T} \lesssim 8$ GeV/c, as expected in case of charm-quark hadronisation via coalescence in a strangeness rich medium. However, the two measurements are still compatible within uncertainties. The R_AA of prompt D^+ mesons, averaged with that of prompt D^0 and D^{*+} mesons, in central (0–10%) Pb–Pb collisions is higher than that of charged particles by more than $2\,\sigma$ in each p_T interval of the measurement for $p_\mathrm{T} < 8$ GeV/c. This difference is reduced in semi-central (30–50%) collisions and is almost vanished in peripheral (60–80%) collisions. The multiplicity-dependent nuclear modification factor Q_pA of prompt D^+ mesons is compatible with unity, with a hint of increasing enhancement from peripheral to central collisions, in the $2 < p_\mathrm{T} < 10$ GeV/c interval, which suggests the presence of radial flow in p–Pb collisions. This enhancement has a significance of about $3\,\sigma$ in the 20–40% centrality class when the average central-to-peripheral ratio of D^+, D^0, and D^{*+} mesons is considered.

The elliptic flow of prompt D^+ mesons was measured in semi-central Pb–Pb collisions at $\sqrt{s_\mathrm{NN}} = 5.02$ TeV with the event-plane and scalar-product methods. It was found to be positive and similar in magnitude in the 10–30% and 30–50% centrality classes. The average prompt D-meson v_2 was found to be lower (similar) to that of charged pions for

$p_{\rm T} < 3$ GeV/c ($p_{\rm T} > 3$ GeV/c) and higher than that of J/ψ mesons for $p_{\rm T} < 6$ GeV/c. This observation is consistent with the scaling of the v_2 with the mass of the meson species observed for light-flavour hadrons below 3 GeV/c [52], and with the increase of the D-meson v_2 due to the hadronisation via recombination of the charm quarks with the flowing light-flavour quarks [113].

The elliptic flow and the $p_{\rm T}$-differential yields of prompt $\rm D^+$ mesons were also investigated for the first time with the event-shape engineering (ESE) technique. The v_2 is found to be higher (lower) in the events with larger-than average (smaller-than-average) q_2, confirming a correlation between the D-meson azimuthal anisotropy and the collective expansion of the bulk matter. The ratios of the $p_{\rm T}$-differential yields measured in the ESE-selected and unbiased samples are compatible with unity, with a hint of increase in the $3 < p_{\rm T} < 12$ GeV/c range for the 30–50% centrality class. This increase could be understood in terms of correlation between radial and elliptic flow, induced by a larger initial density in case of more anisotropic events.

The results presented in this Thesis contribute to give insights into the production of charm mesons and its modification in the hot medium created in heavy-ion collisions. Although in recent years the understanding of the interaction of the charm quark with the QGP made important progresses, the current precision of the measurements does not allow for drawing final conclusions on some relevant aspects, such as the enhancement of the $\rm D_s^+$-meson production in heavy-ion collisions. For this reason, great effort is devoted to improve these measurements in the future, both from the point of view of the analysis methods and the detector performances. In the following sections, the perspectives of improvement provided by the application of machine-learning techniques to the measurement of $\rm D_s^+$ mesons in central Pb–Pb collisions, and by the upgrade of the ALICE detector for the LHC Run3 to the ESE measurements are briefly discussed.

9.1 Improvements in the $\rm D_s^+$-meson measurement with machine-learning techniques

The term *machine learning* (ML) comprehends a vast landscape of algorithms which can "learn" to perform a task without being explicitly programmed. They have a huge range of applications from speech recognition to image generation. The application of ML methods in high-energy physics has become increasingly popular in recent years, mostly for classification and regression problems, but also for simulation and event reconstruction [218, 219].

A ML technique was employed in this Thesis to improve the extraction of the $\rm D_s^+$-meson signal in central Pb–Pb collisions. For this purpose, a *supervised* model was adopted. Supervised algorithms learn how to correctly classify the data starting from a set of examples of which the belonging class is known (*training* sample), and are therefore interesting for the separation of the signal from the background candidates. The output of a supervised model is a *score* evaluated from the instance properties, normally called *features*. This score is a numerical value related to the instance probability of belonging to the different classes. In particular, the algorithm included in the category of the *Boosted Decision Trees* [220] provided by the `XGBoost` library [221, 222], was used.

As a first step, $\mathrm{D_s^+}$-meson candidates were selected applying loose pre-selection criteria on the decay-vertex topology and the conservative PID strategy described in Sec. 4.2.4. The training of the ML algorithm was then performed with a sample of prompt $\mathrm{D_s^+}$ mesons obtained from a MC simulation produced as described in Sec. 4.3 for the signal, and a sample of $\mathrm{D_s^+}$-meson candidates in the sidebands of the the invariant-mass distribution, away from the $\mathrm{D^+}$ and $\mathrm{D_s^+}$ peaks ($M - M(\mathrm{D_s^+}) > 4\sigma$ or $M(\mathrm{D^+}) - M > 4\sigma$), for the background. The topological variables used for the training were (i) the decay length, (ii) the normalised decay length in the transverse plane, (iii) the cosine of the pointing angle in the transverse plane, (iv) the dispersion of the tracks at the decay vertex, (v) the maximum normalised difference between the measured and the expected daughter-track impact parameters in the transverse plane, (vi) the difference between the invariant mass of the kaon pair and the ϕ-meson mass, and (vii) the cubic cosine of the angle between one of the kaons and the pion in the $\mathrm{K^+K^-}$ rest frame (see Sec 4.2.2 for more details). The PID information was also exploited by including for each decay track the variables

$$N_{\sigma}^{\mathrm{comb}}(\pi,\mathrm{K}) = \begin{cases} |N_{\sigma}^{\mathrm{TPC}}(\pi,\mathrm{K})| & \text{tracks with only TPC} \\ |N_{\sigma}^{\mathrm{TOF}}(\pi,\mathrm{K})| & \text{tracks with only TOF} \\ \frac{1}{\sqrt{2}}\sqrt{(N_{\sigma}^{\mathrm{TPC}}(\pi,\mathrm{K}))^2 + (N_{\sigma}^{\mathrm{TOF}}(\pi,\mathrm{K}))^2} & \text{tracks with TPC and TOF} \end{cases}$$

This was done to retain the number of variables used in the training and to account for tracks that do not have hits in the TOF detector.

The performance of the trained model was evaluated by considering the area under the *Receiver Operating Characteristic* (ROC) curve. The ROC curve is obtained by the signal selection efficiency as a function of the background selection efficiency, evaluated on a *test* sample independent of the training sample, for various threshold settings on the model output. The area under the ROC curve can assume values that range from 0.5, which corresponds to a random classification, to 1, which is obtained in case of perfect discrimination between signal and background. The ROC curve for the model trained for prompt $\mathrm{D_s^+}$ mesons with $2 < p_{\mathrm{T}} < 3$ GeV/c in the 0–10% most central Pb–Pb collisions is shown in the left panel of Fig. 9.1. The area under the curve was obtained to be 0.971, indicating a good performance of the ML model. The signal and background efficiencies obtained with a set of selections defined with the standard strategy, tuned to optimise the statistical significance as described in Sec. 6.1, are compared to the ROC curve in the Figure inset. For the same signal efficiency, the selection performed with the ML model provides a background efficiency which is more than 5 times smaller.

The optimal selection on the score of the ML was evaluated with a procedure similar to the one adopted for the standard selection strategy (Sec. 6.1). The invariant-mass distributions of real $\mathrm{D_s^+}$ candidates obtained with the standard and the ML-based selections are compared in the right panel of Fig. 9.1. While in case of standard selection the peak of the $\mathrm{D_s^+}$ meson is not visible, in case of ML-based selection a statistical significance of 7.3 ± 0.1 is obtained.

This selection strategy opens the possibility to extend the measurement of the $\mathrm{D_s^+}$

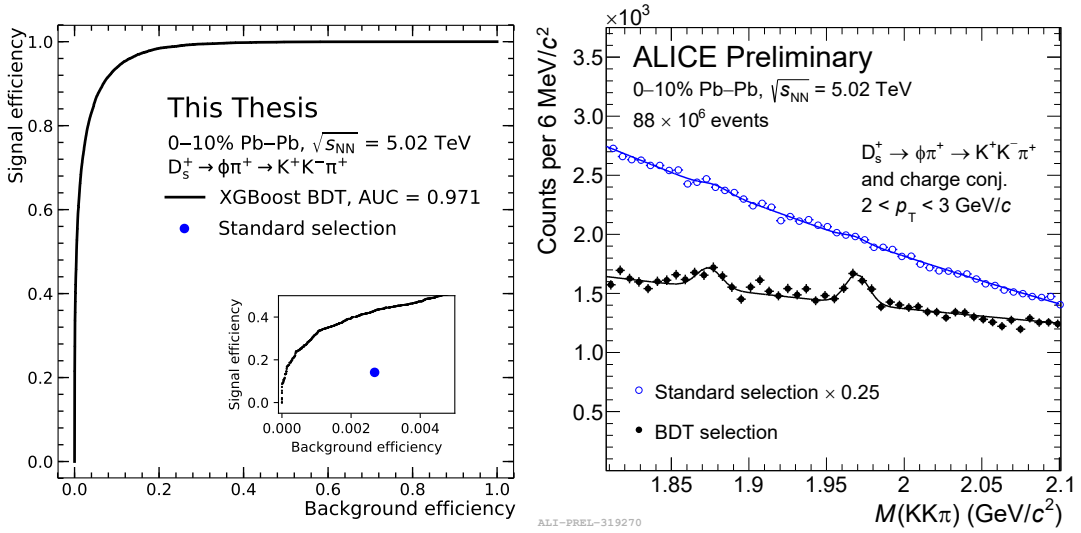

Figure 9.1: Left: ROC curve obtained for the ML model trained for the selection of prompt D_s^+ mesons with $2 < p_T < 3$ GeV/c in the 10% most central Pb–Pb collisions at $\sqrt{s_{NN}} = 5.02$ TeV. The inset shows the comparison with the signal and background efficiencies obtained with the standard analysis. Right: comparison of the $M(KK\pi)$ distribution of D_s^+-meson candidates having $2 < p_T < 3$ GeV/c obtained with the standard and ML-based selections. Figure taken from the ALICE figure repository ©.

meson down to lower p_T, as well as to significantly improve the statistical precision of the measurement in the current p_T range covered by the standard analysis. For this reason, this analysis technique is under study and will be applied for the publication of the results on the D_s^+-meson production in Pb–Pb collisions at $\sqrt{s_{NN}} = 5.02$ TeV performed on the data sample collected in 2018.

9.2 Improvements in the ESE measurements with the upgraded Inner Tracking System

The ALICE Collaboration is preparing a major upgrade of the experimental apparatus, planned for installation in the second long LHC shutdown in 2020, which will also involve the Inner Tracking System [223, 224]. The main goals of the upgrade of the ALICE ITS are an improved reconstruction of primary and secondary vertices and an improved performance in the tracking of low-momentum particles.

The central part of the upgraded ALICE ITS is the pixel chip. The most challenging requirements for the detector design are the high spatial resolution and the extremely low material budget, in particular for the inner layers. These requirements led to the choice of Monolithic Active Pixel Sensors (MAPS) [224]. Hence, the six ITS layers of the current setup will be replaced with seven concentric barrel layers of silicon MAPS detectors with radii between 22 mm for the innermost and 400 mm for the outermost

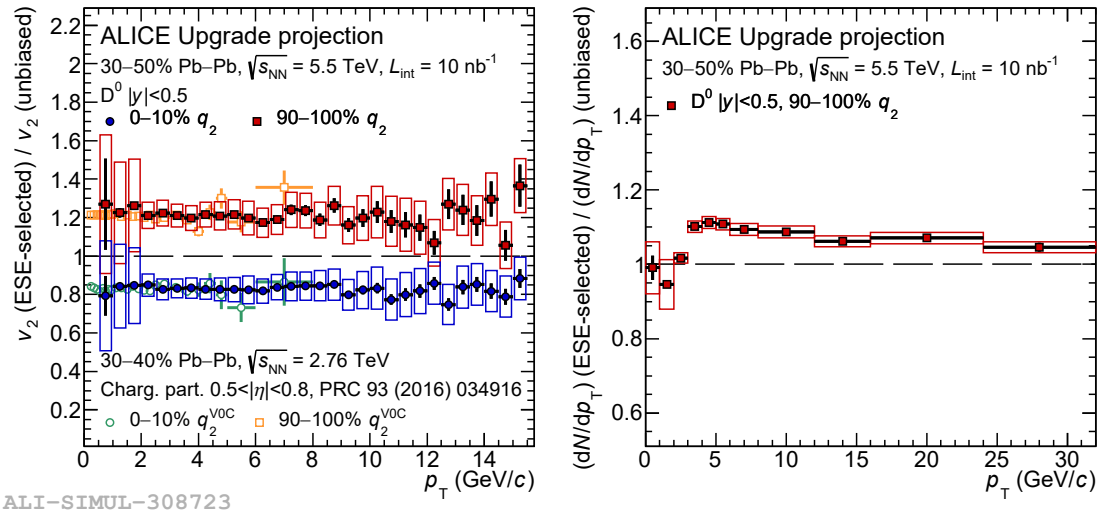

Figure 9.2: Left: projection of the expected ratio of D^0-meson v_2 in the 10% large-q_2 and small-q_2 samples to the unbiased one as a function of p_T for the 30–50% centrality class. The modification of the D^0-meson v_2 was assumed to be equal to that measured for the charged particles in Pb–Pb collisions at $\sqrt{s_{NN}} = 2.76$ TeV in the 30–40% centrality class, which is superimposed for comparison [210]. Right: projection of the expected ratio of D^0-meson p_T-differential yield in the 10% large-q_2 sample with respect to the unbiased one, estimated considering the prediction provided by the POWLANG model [188]. Figure taken from Ref. [6].

layer. The pixel size of the new sensors will be 30 μm x 30 μm, compared to 50 μm x 425 μm of the current pixel detector. The material budget will be reduced down to 0.3% X_0 in the innermost and $\sim$ 0.9% X_0 in the outer and middle layers compared to 1.14% X_0 per layer in the current SPD detector. As a consequence of this upgrade, the impact-parameter resolution will improve by a factor 3 (5) in the $r\varphi$ (z) direction [224], implying a large improvement in the measurement of heavy-flavour hadrons.

As an example, in this Thesis the expected performance of the ESE measurements for the D^0 meson in Pb–Pb collisions at $\sqrt{s_{NN}} = 5.5$ TeV with $\mathcal{L}_{int} = 10$ nb^{-1} was evaluated. The expected statistical precision for the measurement of the D^0 meson p_T-differential yields and v_2 in the 10% of the events with largest (smallest) elliptic flow of the bulk, quantified through the magnitude of the so-called reduced flow vector q_2, was obtained by scaling the expected uncertainty on the unbiased measurements taken from Ref. [224], considering the percentage of events in the ESE-selected classes and the modification of the observable. The systematic uncertainty was assumed to be the same as the one estimated for the unbiased measurements.

For the v_2, the modification was assumed to be equal to that of charged particles measured by the ALICE in Pb–Pb collisions at $\sqrt{s_{NN}} = 2.76$ TeV in the 30–40% centrality class [210] using the V0C detector to compute the q_2 estimator. On the one hand it

represents an unfavourable scenario for the sensitivity of the ESE selection (see Sec. 8.5 for more details), on the other hand a forward-rapidity estimator for q_2 would suppress unwanted non-flow correlations and autocorrelations, giving the possibility to measure the same observables for soft and hard probes and hence have a more direct comparison. In the left panel of Fig. 9.2, the prospects for the measurement of the ratio between the ESE-selected and unbiased v_2 of prompt D^0 mesons are compared to the current measurement of the charged particles. Despite the assumed reduced sensitivity of q_2, the expected precision of the measurement will be sufficient to measure a modification of the D^0-meson v_2, removing the effects induced by non-flow correlations. The precision at intermediate p_T is expected to be better than 5% and thus it will provide the possibility to resolve a possible difference of a few percent in the response of the v_2 to the ESE selection between the D^0 mesons and the light hadrons.

The right panel of Fig. 9.2 shows the expected ratio between the p_T-differential yields of D^0 mesons in the 10% large-q_2 and unbiased samples. In this case, the modification of the p_T-differential yields was estimated considering the prediction provided by the POWLANG model [188]. The expected performance will provide a sensitivity of a few percent for the modification of the D-meson p_T spectra in events with small (large) initial geometrical anisotropy, opening the way for precise studies on the interplay between the initial geometrical anisotropy (the collective flow of the bulk) and the heavy-flavour radial flow and energy loss.

Bibliography

[1] **ALICE** Collaboration, S. Acharya *et al.*, "Measurement of D^0 , D^+ , D^{*+} and D_s^+ production in pp collisions at $\sqrt{s}$ = 5.02 TeV with ALICE," *Eur. Phys. J.* **C79** no. 5, (2019) 388, arXiv:1901.07979 [nucl-ex].

[2] **ALICE** Collaboration, S. Acharya *et al.*, "Measurement of prompt D^0, D^+, D^{*+}, and D_s^+ production in p–Pb collisions at $\sqrt{s_\mathrm{NN}}$ = 5.02 TeV," *JHEP* **12** (2019) 092, arXiv:1906.03425 [nucl-ex].

[3] **ALICE** Collaboration, S. Acharya *et al.*, "Measurement of D^0, D^+, D^{*+} and D_s^+ production in Pb-Pb collisions at $\sqrt{s_\mathrm{NN}}$ = 5.02 TeV," *JHEP* **10** (2018) 174, arXiv:1804.09083 [nucl-ex].

[4] **ALICE** Collaboration, S. Acharya *et al.*, "D-meson azimuthal anisotropy in midcentral Pb-Pb collisions at $\sqrt{\mathbf{s}_\mathrm{NN}}$ = **5.02** TeV," *Phys. Rev. Lett.* **120** no. 10, (2018) 102301, arXiv:1707.01005 [nucl-ex].

[5] **ALICE** Collaboration, S. Acharya *et al.*, "Event-shape engineering for the D-meson elliptic flow in mid-central Pb-Pb collisions at $\sqrt{s_\mathrm{NN}}$ = 5.02 TeV," *JHEP* **02** (2019) 150, arXiv:1809.09371 [nucl-ex].

[6] Z. Citron *et al.*, "Future physics opportunities for high-density QCD at the LHC with heavy-ion and proton beams," in *HL/HE-LHC Workshop: Workshop on the Physics of HL-LHC, and Perspectives at HE-LHC Geneva, Switzerland, June 18-20, 2018*. 2018. arXiv:1812.06772 [hep-ph].

[7] F. Karsch, "Lattice simulations of the thermodynamics of strongly interacting elementary particles and the exploration of new phases of matter in relativistic heavy ion collisions," *J. Phys. Conf. Ser.* **46** (2006) 122–131, arXiv:hep-lat/0608003 [hep-lat].

[8] W. Florkowski, R. Ryblewski, N. Su, and K. Tywoniuk, "Strong-coupling effects in a plasma of confining gluons," *Nucl. Phys.* **A956** (2016) 669–672, arXiv:1512.06402 [hep-ph].

[9] **Wuppertal-Budapest** Collaboration, S. Borsanyi, Z. Fodor, C. Hoelbling, S. D. Katz, S. Krieg, C. Ratti, and K. K. Szabo, "Is there still any T_c mystery in lattice QCD? Results with physical masses in the continuum limit III," *JHEP* **09** (2010) 073, arXiv:1005.3508 [hep-lat].

[10] A. Bazavov *et al.*, "The chiral and deconfinement aspects of the QCD transition," *Phys. Rev.* **D85** (2012) 054503, arXiv:1111.1710 [hep-lat].

[11] Ian J R Aitchison and Anthony J.G. Hey, *Gauge theories in particle physics*. CRC Press, 4th ed. ed., 2012.

[12] S. Bethke, "Experimental tests of asymptotic freedom," *Prog. Part. Nucl. Phys.* **58** (2007) 351–386, arXiv:hep-ex/0606035 [hep-ex].

[13] **Particle Data Group** Collaboration, M. Tanabashi *et al.*, "Review of Particle Physics," *Phys. Rev.* **D98** no. 3, (2018) 030001.

[14] K. G. Wilson, "Confinement of Quarks," *Phys. Rev.* **D10** (1974) 2445–2459. [,319(1974)].

[15] H. Caines, "The Search for Critical Behavior and Other Features of the QCD Phase Diagram - Current Status and Future Prospects," *Nucl. Phys.* **A967** (2017) 121–128.

[16] N. Cabibbo and G. Parisi, "Exponential Hadronic Spectrum and Quark Liberation," *Phys. Lett.* **59B** (1975) 67–69.

[17] F. Karsch and E. Laermann, "Thermodynamics and in medium hadron properties from lattice QCD," arXiv:hep-lat/0305025 [hep-lat].

[18] G. Baym, T. Hatsuda, T. Kojo, P. D. Powell, Y. Song, and T. Takatsuka, "From hadrons to quarks in neutron stars: a review," *Rept. Prog. Phys.* **81** no. 5, (2018) 056902, arXiv:1707.04966 [astro-ph.HE].

[19] M. G. Alford, "Color superconducting quark matter," *Ann. Rev. Nucl. Part. Sci.* **51** (2001) 131–160, arXiv:hep-ph/0102047 [hep-ph].

[20] M. G. Alford, A. Schmitt, K. Rajagopal, and T. Schäfer, "Color superconductivity in dense quark matter," *Rev. Mod. Phys.* **80** (2008) 1455–1515, arXiv:0709.4635 [hep-ph].

[21] **HotQCD** Collaboration, A. Bazavov *et al.*, "Equation of state in (2+1)-flavor QCD," *Phys. Rev.* **D90** (2014) 094503, arXiv:1407.6387 [hep-lat].

[22] J. D. Bjorken, "Highly Relativistic Nucleus-Nucleus Collisions: The Central Rapidity Region," *Phys. Rev.* **D27** (1983) 140–151.

[23] A. Tawfik and A. G. Shalaby, "Balance Function in High-Energy Collisions," *Adv. High Energy Phys.* **2015** (2015) 186812.

[24] M. L. Miller, K. Reygers, S. J. Sanders, and P. Steinberg, "Glauber modeling in high energy nuclear collisions," *Ann. Rev. Nucl. Part. Sci.* **57** (2007) 205–243, arXiv:nucl-ex/0701025 [nucl-ex].

[25] **ALICE** Collaboration, J. Adam *et al.*, "Centrality dependence of the charged-particle multiplicity density at midrapidity in Pb-Pb collisions at $\sqrt{s_{\rm NN}} = 5.02$ TeV," *Phys. Rev. Lett.* **116** no. 22, (2016) 222302, arXiv:1512.06104 [nucl-ex].

[26] **NA35** Collaboration, J. Baechler *et al.*, "Strangeness enhancement in central S + S collisions at 200-GeV/nucleon," *Nucl. Phys.* **A525** (1991) 221C–226C.

[27] **WA97** Collaboration, E. Andersen *et al.*, "Strangeness enhancement at mid-rapidity in Pb Pb collisions at 158-A-GeV/c," *Phys. Lett.* **B449** (1999) 401–406.

[28] **NA57** Collaboration, F. Antinori *et al.*, "Study of the production of strange and multi-strange particles in lead lead interactions at the CERN SPS: The NA57 experiment," *Nucl. Phys.* **A681** (2001) 165–173.

[29] J. Rafelski and B. Muller, "Strangeness Production in the Quark - Gluon Plasma," *Phys. Rev. Lett.* **48** (1982) 1066. [Erratum: Phys. Rev. Lett.56,2334(1986)].

[30] O. Kaczmarek and F. Zantow, "Static quark anti-quark interactions in zero and finite temperature QCD. I. Heavy quark free energies, running coupling and quarkonium binding," *Phys. Rev.* **D71** (2005) 114510, arXiv:hep-lat/0503017 [hep-lat].

[31] **STAR** Collaboration, G. Agakishiev *et al.*, "Strangeness Enhancement in Cu+Cu and Au+Au Collisions at $\sqrt{s_{NN}} = 200$ GeV," *Phys. Rev. Lett.* **108** (2012) 072301, arXiv:1107.2955 [nucl-ex].

[32] **ALICE** Collaboration, B. B. Abelev *et al.*, "Multi-strange baryon production at mid-rapidity in Pb-Pb collisions at $\sqrt{s_{NN}} = 2.76$ TeV," *Phys. Lett.* **B728** (2014) 216–227, arXiv:1307.5543 [nucl-ex]. [Erratum: Phys. Lett.B734,409(2014)].

[33] **ALICE** Collaboration, J. Adam *et al.*, "Enhanced production of multi-strange hadrons in high-multiplicity proton-proton collisions," *Nature Phys.* **13** (2017) 535–539, arXiv:1606.07424 [nucl-ex].

[34] T. Sjöstrand, S. Ask, J. R. Christiansen, R. Corke, N. Desai, P. Ilten, S. Mrenna, S. Prestel, C. O. Rasmussen, and P. Z. Skands, "An Introduction to PYTHIA 8.2," *Comput. Phys. Commun.* **191** (2015) 159–177, arXiv:1410.3012 [hep-ph].

[35] C. Bierlich and J. R. Christiansen, "Effects of color reconnection on hadron flavor observables," *Phys. Rev.* **D92** no. 9, (2015) 094010, arXiv:1507.02091 [hep-ph].

[36] T. Pierog, I. Karpenko, J. M. Katzy, E. Yatsenko, and K. Werner, "EPOS LHC: Test of collective hadronization with data measured at the CERN Large Hadron Collider," *Phys. Rev.* **C92** no. 3, (2015) 034906, arXiv:1306.0121 [hep-ph].

[37] F. Beutler, A. Andronic, P. Braun-Munzinger, K. Redlich, and J. Stachel, "The Canonical partition function for relativistic hadron gases," *Eur. Phys. J.* **C67** (2010) 439–444, arXiv:0910.1697 [hep-ph].

[38] **ALICE** Collaboration, B. Abelev *et al.*, "Pion, Kaon, and Proton Production in Central Pb–Pb Collisions at $\sqrt{s_{NN}} = 2.76$ TeV," *Phys. Rev. Lett.* **109** (2012) 252301, arXiv:1208.1974 [hep-ex].

[39] E. Schnedermann, J. Sollfrank, and U. W. Heinz, "Thermal phenomenology of hadrons from 200-A/GeV S+S collisions," *Phys. Rev.* **C48** (1993) 2462–2475, arXiv:nucl-th/9307020 [nucl-th].

[40] **STAR** Collaboration, B. I. Abelev *et al.*, "Systematic Measurements of Identified Particle Spectra in pp, d^+ Au and Au+Au Collisions from STAR," *Phys. Rev.* **C79** (2009) 034909, arXiv:0808.2041 [nucl-ex].

[41] **PHENIX** Collaboration, S. S. Adler *et al.*, "Identified charged particle spectra and yields in Au+Au collisions at S(NN)**1/2 = 200-GeV," *Phys. Rev.* **C69** (2004) 034909, arXiv:nucl-ex/0307022 [nucl-ex].

[42] **ALICE** Collaboration, B. B. Abelev *et al.*, "Multiplicity Dependence of Pion, Kaon, Proton and Lambda Production in p-Pb Collisions at $\sqrt{s_{NN}} = 5.02$ TeV," *Phys. Lett.* **B728** (2014) 25–38, arXiv:1307.6796 [nucl-ex].

[43] **CMS** Collaboration, S. Chatrchyan *et al.*, "Study of the Production of Charged Pions, Kaons, and Protons in pPb Collisions at $\sqrt{s_{NN}} =$ 5.02 TeV," *Eur. Phys. J.* **C74** no. 6, (2014) 2847, arXiv:1307.3442 [hep-ex].

[44] **ALICE** Collaboration, J. Adam *et al.*, "Multiplicity dependence of charged pion, kaon, and (anti)proton production at large transverse momentum in p-Pb collisions at $\sqrt{s_{\rm NN}} = 5.02$ TeV," *Phys. Lett.* **B760** (2016) 720–735, arXiv:1601.03658 [nucl-ex].

[45] K. Werner, F.-M. Liu, and T. Pierog, "Parton ladder splitting and the rapidity dependence of transverse momentum spectra in deuteron-gold collisions at RHIC," *Phys. Rev.* **C74** (2006) 044902, arXiv:hep-ph/0506232 [hep-ph].

[46] **CMS** Collaboration, V. Khachatryan *et al.*, "Evidence for collectivity in pp collisions at the LHC," *Phys. Lett.* **B765** (2017) 193–220, arXiv:1606.06198 [nucl-ex].

[47] **ATLAS** Collaboration, G. Aad *et al.*, "Observation of Long-Range Elliptic Azimuthal Anisotropies in $\sqrt{s}$ =13 and 2.76 TeV pp Collisions with the ATLAS Detector," *Phys. Rev. Lett.* **116** no. 17, (2016) 172301, arXiv:1509.04776 [hep-ex].

[48] **ALICE** Collaboration, B. Abelev *et al.*, "Long-range angular correlations on the near and away side in p-Pb collisions at $\sqrt{s_{NN}} = 5.02$ TeV," *Phys. Lett.* **B719** (2013) 29–41, arXiv:1212.2001 [nucl-ex].

[49] **CMS** Collaboration, S. Chatrchyan *et al.*, "Observation of Long-Range Near-Side Angular Correlations in Proton-Lead Collisions at the LHC," *Phys. Lett.* **B718** (2013) 795–814, arXiv:1210.5482 [nucl-ex].

[50] **ATLAS** Collaboration, G. Aad *et al.*, "Observation of Associated Near-Side and Away-Side Long-Range Correlations in $\sqrt{s_{NN}}$=5.02 TeV Proton-Lead Collisions with the ATLAS Detector," *Phys. Rev. Lett.* **110** no. 18, (2013) 182302, arXiv:1212.5198 [hep-ex].

[51] S. Voloshin and Y. Zhang, "Flow study in relativistic nuclear collisions by Fourier expansion of Azimuthal particle distributions," *Z. Phys.* **C70** (1996) 665–672, arXiv:hep-ph/9407282 [hep-ph].

[52] **ALICE** Collaboration, S. Acharya *et al.*, "Anisotropic flow of identified particles in Pb-Pb collisions at $\sqrt{s}_{\rm NN} = 5.02$ TeV," *JHEP* **09** (2018) 006, arXiv:1805.04390 [nucl-ex].

[53] D. Molnar and S. A. Voloshin, "Elliptic flow at large transverse momenta from quark coalescence," *Phys. Rev. Lett.* **91** (2003) 092301, arXiv:nucl-th/0302014 [nucl-th].

[54] C. Gale, S. Jeon, B. Schenke, P. Tribedy, and R. Venugopalan, "Event-by-event anisotropic flow in heavy-ion collisions from combined Yang-Mills and viscous fluid dynamics," *Phys. Rev. Lett.* **110** no. 1, (2013) 012302, arXiv:1209.6330 [nucl-th].

[55] **PHENIX** Collaboration, C. Aidala *et al.*, "Creation of quark-gluon plasma droplets with three distinct geometries," *Nature Phys.* **15** no. 3, (2019) 214–220, arXiv:1805.02973 [nucl-ex].

[56] B. Schenke and S. Schlichting, "3D glasma initial state for relativistic heavy ion collisions," *Phys. Rev.* **C94** no. 4, (2016) 044907, arXiv:1605.07158 [hep-ph].

[57] M. Mace, V. V. Skokov, P. Tribedy, and R. Venugopalan, "Hierarchy of Azimuthal Anisotropy Harmonics in Collisions of Small Systems from the Color Glass Condensate," *Phys. Rev. Lett.* **121** no. 5, (2018) 052301, arXiv:1805.09342 [hep-ph]. [Erratum: Phys. Rev. Lett.123,no.3,039901(2019)].

[58] P. Bozek and W. Broniowski, "Correlations from hydrodynamic flow in p-Pb collisions," *Phys. Lett.* **B718** (2013) 1557–1561, arXiv:1211.0845 [nucl-th].

[59] G.-Y. Qin and B. Müller, "Elliptic and triangular flow anisotropy in deuteron-gold collisions at $\sqrt{s_{NN}} = 200$ GeV at RHIC and in proton-lead collisions at $\sqrt{s_{NN}} = 5.02$ TeV at the LHC," *Phys. Rev.* **C89** no. 4, (2014) 044902, arXiv:1306.3439 [nucl-th].

[60] M. Habich, J. L. Nagle, and P. Romatschke, "Particle spectra and HBT radii for simulated central nuclear collisions of C + C, Al + Al, Cu + Cu, Au + Au, and Pb + Pb from $\sqrt{s} = 62.4$ - 2760 GeV," *Eur. Phys. J.* **C75** no. 1, (2015) 15, arXiv:1409.0040 [nucl-th].

[61] **ALICE** Collaboration, S. Acharya *et al.*, "Transverse momentum spectra and nuclear modification factors of charged particles in pp, p-Pb and Pb-Pb collisions at the LHC," *JHEP* **11** (2018) 013, arXiv:1802.09145 [nucl-ex].

[62] **ALICE** Collaboration, J. Adam *et al.*, "Measurement of jet suppression in central Pb-Pb collisions at $\sqrt{s_{\rm NN}} = 2.76$ TeV," *Phys. Lett.* **B746** (2015) 1–14, arXiv:1502.01689 [nucl-ex].

[63] **ATLAS** Collaboration, G. Aad *et al.*, "Measurements of the Nuclear Modification Factor for Jets in Pb+Pb Collisions at $\sqrt{s_{\rm NN}} = 2.76$ TeV with the ATLAS Detector," *Phys. Rev. Lett.* **114** no. 7, (2015) 072302, arXiv:1411.2357 [hep-ex].

[64] **CMS** Collaboration, V. Khachatryan *et al.*, "Measurement of inclusive jet cross sections in *pp* and PbPb collisions at $\sqrt{s_{NN}} = 2.76$ TeV," *Phys. Rev.* **C96** no. 1, (2017) 015202, arXiv:1609.05383 [nucl-ex].

[65] **CMS** Collaboration, V. Khachatryan *et al.*, "Charged-particle nuclear modification factors in PbPb and pPb collisions at $\sqrt{s_{\rm N\,N}} = 5.02$ TeV," *JHEP* **04** (2017) 039, arXiv:1611.01664 [nucl-ex].

[66] **ALICE** Collaboration, J. Adam *et al.*, "Direct photon production in Pb-Pb collisions at $\sqrt{s_{\rm NN}} = 2.76$ TeV," *Phys. Lett.* **B754** (2016) 235–248, arXiv:1509.07324 [nucl-ex].

[67] **ATLAS** Collaboration, G. Aad *et al.*, "Centrality, rapidity and transverse momentum dependence of isolated prompt photon production in lead-lead collisions at $\sqrt{s_{\rm NN}} = 2.76$ TeV measured with the ATLAS detector," *Phys. Rev.* **C93** no. 3, (2016) 034914, arXiv:1506.08552 [hep-ex].

[68] **ATLAS** Collaboration, G. Aad *et al.*, "Measurement of Z boson Production in Pb+Pb Collisions at $\sqrt{s_{NN}} = 2.76$ TeV with the ATLAS Detector," *Phys. Rev. Lett.* **110** no. 2, (2013) 022301, arXiv:1210.6486 [hep-ex].

[69] **CMS** Collaboration, S. Chatrchyan *et al.*, "Study of W boson production in PbPb and *pp* collisions at $\sqrt{s_{NN}} = 2.76$ TeV," *Phys. Lett.* **B715** (2012) 66–87, arXiv:1205.6334 [nucl-ex].

[70] **CMS** Collaboration, S. Chatrchyan *et al.*, "Measurement of isolated photon production in *pp* and PbPb collisions at $\sqrt{s_{NN}} = 2.76$ TeV," *Phys. Lett.* **B710** (2012) 256–277, arXiv:1201.3093 [nucl-ex].

[71] M. Xie, S.-Y. Wei, G.-Y. Qin, and H.-Z. Zhang, "Extracting jet transport coefficient via single hadron and dihadron productions in high-energy heavy-ion collisions," *Eur. Phys. J.* **C79** no. 7, (2019) 589, arXiv:1901.04155 [hep-ph].

[72] F. Prino and R. Rapp, "Open Heavy Flavor in QCD Matter and in Nuclear Collisions," *J. Phys.* **G43** no. 9, (2016) 093002, arXiv:1603.00529 [nucl-ex].

[73] M. L. Mangano, "Two lectures on heavy quark production in hadronic collisions," *Proc. Int. Sch. Phys. Fermi* **137** (1998) 95–137, arXiv:hep-ph/9711337 [hep-ph].

[74] J. Pumplin, D. R. Stump, J. Huston, H. L. Lai, P. M. Nadolsky, and W. K. Tung, "New generation of parton distributions with uncertainties from global QCD analysis," *JHEP* **07** (2002) 012, arXiv:hep-ph/0201195 [hep-ph].

[75] S. Dulat, T.-J. Hou, J. Gao, M. Guzzi, J. Huston, P. Nadolsky, J. Pumplin, C. Schmidt, D. Stump, and C. P. Yuan, "New parton distribution functions from a global analysis of quantum chromodynamics," *Phys. Rev.* **D93** no. 3, (2016) 033006, arXiv:1506.07443 [hep-ph].

[76] **NNPDF** Collaboration, R. D. Ball *et al.*, "Parton distributions from high-precision collider data," *Eur. Phys. J.* **C77** no. 10, (2017) 663, arXiv:1706.00428 [hep-ph].

[77] V. G. Kartvelishvili, A. K. Likhoded, and V. A. Petrov, "On the Fragmentation Functions of Heavy Quarks Into Hadrons," *Phys. Lett.* **78B** (1978) 615–617.

[78] G. Altarelli and G. Parisi, "Asymptotic Freedom in Parton Language," *Nucl. Phys.* **B126** (1977) 298–318.

[79] M. Cacciari, M. Greco, and P. Nason, "The P(T) spectrum in heavy flavor hadroproduction," *JHEP* **05** (1998) 007, arXiv:hep-ph/9803400 [hep-ph].

[80] M. Cacciari, S. Frixione, N. Houdeau, M. L. Mangano, P. Nason, and G. Ridolfi, "Theoretical predictions for charm and bottom production at the LHC," *JHEP* **10** (2012) 137, arXiv:1205.6344 [hep-ph].

[81] M. Benzke, M. V. Garzelli, B. Kniehl, G. Kramer, S. Moch, and G. Sigl, "Prompt neutrinos from atmospheric charm in the general-mass variable-flavor-number scheme," *JHEP* **12** (2017) 021, arXiv:1705.10386 [hep-ph].

[82] G. Kramer and H. Spiesberger, "Study of heavy meson production in p-Pb collisions at $\sqrt{s}$= 5.02 TeV in the general-mass variable-flavour-number scheme," *Nucl. Phys.* **B925** (2017) 415–430, arXiv:1703.04754 [hep-ph].

[83] I. Helenius and H. Paukkunen, "Revisiting the D-meson hadroproduction in general-mass variable flavour number scheme," *JHEP* **05** (2018) 196, arXiv:1804.03557 [hep-ph].

[84] **LHCb** Collaboration, R. Aaij *et al.*, "Measurement of B meson production cross-sections in proton-proton collisions at $\sqrt{s} = 7$ TeV," *JHEP* **08** (2013) 117, arXiv:1306.3663 [hep-ex].

[85] R. Maciuła and A. Szczurek, "Production of Λ_c baryons at the LHC within the k_T-factorization approach and independent parton fragmentation picture," *Phys. Rev.* **D98** no. 1, (2018) 014016, arXiv:1803.05807 [hep-ph].

[86] T. Sjostrand, S. Mrenna, and P. Z. Skands, "PYTHIA 6.4 Physics and Manual," *JHEP* **05** (2006) 026, arXiv:hep-ph/0603175 [hep-ph].

[87] G. Marchesini, B. R. Webber, G. Abbiendi, I. G. Knowles, M. H. Seymour, and L. Stanco, "HERWIG: A Monte Carlo event generator for simulating hadron emission reactions with interfering gluons. Version 5.1 - April 1991," *Comput. Phys. Commun.* **67** (1992) 465–508.

[88] S. Frixione, P. Nason, and G. Ridolfi, "A Positive-weight next-to-leading-order Monte Carlo for heavy flavour hadroproduction," *JHEP* **09** (2007) 126, arXiv:0707.3088 [hep-ph].

[89] S. Frixione and B. R. Webber, "Matching NLO QCD computations and parton shower simulations," *JHEP* **06** (2002) 029, arXiv:hep-ph/0204244 [hep-ph].

[90] N. Armesto, "Nuclear shadowing," *J. Phys.* **G32** (2006) R367–R394, arXiv:hep-ph/0604108 [hep-ph].

[91] K. Rith, "Present Status of the EMC effect," *Subnucl. Ser.* **51** (2015) 431–449, arXiv:1402.5000 [hep-ex].

[92] K. J. Eskola, H. Paukkunen, and C. A. Salgado, "EPS09: A New Generation of NLO and LO Nuclear Parton Distribution Functions," *JHEP* **04** (2009) 065, arXiv:0902.4154 [hep-ph].

[93] K. J. Eskola, P. Paakkinen, H. Paukkunen, and C. A. Salgado, "EPPS16: Nuclear parton distributions with LHC data," *Eur. Phys. J.* **C77** no. 3, (2017) 163, arXiv:1612.05741 [hep-ph].

[94] N. Carrer and A. Dainese, "Charm and beauty production at LHC," in *ALICE: Physics performance report, volume II*, B. Alessandro, F. Antinori, J. A. Belikov, C. Blume, A. Dainese, P. Foka, P. Giubellino, B. Hippolyte, C. Kuhn, G. Martinez, *et al.*, eds., pp. 1768–1783. 2006. arXiv:hep-ph/0311225 [hep-ph]. http://cdsweb.cern.ch/search.py?sysno=002388104CER.

[95] A. M. Sickles, "Possible Evidence for Radial Flow of Heavy Mesons in d+Au Collisions," *Phys. Lett.* **B731** (2014) 51–56, arXiv:1309.6924 [nucl-th].

[96] D. Antreasyan, J. W. Cronin, H. J. Frisch, M. J. Shochet, L. Kluberg, P. A. Piroue, and R. L. Sumner, "Production of Hadrons at Large Transverse Momentum in 200-GeV, 300-GeV and 400-GeV p p and p n Collisions," *Phys. Rev.* **D19** (1979) 764–778.

[97] **PHENIX** Collaboration, A. Adare *et al.*, "Spectra and ratios of identified particles in Au+Au and d+Au collisions at $\sqrt{s_{NN}} = 200$ GeV," *Phys. Rev.* **C88** no. 2, (2013) 024906, arXiv:1304.3410 [nucl-ex].

[98] A. Beraudo, A. De Pace, M. Monteno, M. Nardi, and F. Prino, "Heavy-flavour production in high-energy d-Au and p-Pb collisions," *JHEP* **03** (2016) 123, arXiv:1512.05186 [hep-ph].

[99] Y. Xu, S. Cao, G.-Y. Qin, W. Ke, M. Nahrgang, J. Auvinen, and S. A. Bass, "Heavy-flavor dynamics in relativistic p-Pb collisions at $\sqrt{S_{NN}} = 5.02$ TeV," *Nucl. Part. Phys. Proc.* **276-278** (2016) 225–228, arXiv:1510.07520 [nucl-th].

[100] G. D. Moore and D. Teaney, "How much do heavy quarks thermalize in a heavy ion collision?," *Phys. Rev.* **C71** (2005) 064904, arXiv:hep-ph/0412346 [hep-ph].

[101] S. Cao, G.-Y. Qin, and S. A. Bass, "Heavy-quark dynamics and hadronization in ultrarelativistic heavy-ion collisions: Collisional versus radiative energy loss," *Phys. Rev.* **C88** (2013) 044907, arXiv:1308.0617 [nucl-th].

[102] C. A. Salgado and U. A. Wiedemann, "Calculating quenching weights," *Phys. Rev.* **D68** (2003) 014008, arXiv:hep-ph/0302184 [hep-ph].

[103] M. Djordjevic and M. Gyulassy, "Where is the charm quark energy loss at RHIC?," *Phys. Lett.* **B560** (2003) 37–43, arXiv:nucl-th/0302069 [nucl-th].

[104] **ALICE** Collaboration, J. Adam *et al.*, "Transverse momentum dependence of D-meson production in Pb-Pb collisions at $\sqrt{s_{\rm NN}} = 2.76$ TeV," *JHEP* **03** (2016) 081, arXiv:1509.06888 [nucl-ex].

[105] **ALICE** Collaboration, J. Adam *et al.*, "Centrality dependence of high-p_T D meson suppression in Pb-Pb collisions at $\sqrt{s_{\rm NN}} = 2.76$ TeV," *JHEP* **11** (2015) 205, arXiv:1506.06604 [nucl-ex]. [Addendum: JHEP06,032(2017)].

[106] **CMS** Collaboration, V. Khachatryan *et al.*, "Suppression and azimuthal anisotropy of prompt and nonprompt J/ψ production in PbPb collisions at $\sqrt{s_{\rm NN}} = 2.76$ TeV," *Eur. Phys. J.* **C77** no. 4, (2017) 252, arXiv:1610.00613 [nucl-ex].

[107] E. Braaten and M. H. Thoma, "Energy loss of a heavy quark in the quark - gluon plasma," *Phys. Rev.* **D44** no. 9, (1991) R2625.

[108] S. Peigne and A. V. Smilga, "Energy losses in a hot plasma revisited," *Phys. Usp.* **52** (2009) 659–685, arXiv:0810.5702 [hep-ph]. [Usp. Fiz. Nauk179,697(2009)].

[109] S. Peigne and A. Peshier, "Collisional energy loss of a fast heavy quark in a quark-gluon plasma," *Phys. Rev.* **D77** (2008) 114017, arXiv:0802.4364 [hep-ph].

[110] **ALICE** Collaboration, K. Aamodt *et al.*, "Two-pion Bose-Einstein correlations in central Pb-Pb collisions at $\sqrt{s_{NN}} = 2.76$ TeV," *Phys. Lett.* **B696** (2011) 328–337, arXiv:1012.4035 [nucl-ex].

[111] M. Nahrgang, J. Aichelin, P. B. Gossiaux, and K. Werner, "Influence of hadronic bound states above T_c on heavy-quark observables in Pb + Pb collisions at at the CERN Large Hadron Collider," *Phys. Rev.* **C89** no. 1, (2014) 014905, arXiv:1305.6544 [hep-ph].

[112] A. Beraudo, A. De Pace, M. Monteno, M. Nardi, and F. Prino, "Development of heavy-flavour flow-harmonics in high-energy nuclear collisions," *JHEP* **02** (2018) 043, arXiv:1712.00588 [hep-ph].

[113] M. Nahrgang, J. Aichelin, S. Bass, P. B. Gossiaux, and K. Werner, "Elliptic and triangular flow of heavy flavor in heavy-ion collisions," *Phys. Rev.* **C91** no. 1, (2015) 014904, arXiv:1410.5396 [hep-ph].

[114] W. Ke, Y. Xu, and S. A. Bass, "Linearized Boltzmann-Langevin model for heavy quark transport in hot and dense QCD matter," *Phys. Rev.* **C98** no. 6, (2018) 064901, arXiv:1806.08848 [nucl-th].

[115] S. Plumari, V. Minissale, S. K. Das, G. Coci, and V. Greco, "Charmed Hadrons from Coalescence plus Fragmentation in relativistic nucleus-nucleus collisions at RHIC and LHC," *Eur. Phys. J.* **C78** no. 4, (2018) 348, arXiv:1712.00730 [hep-ph].

[116] **ALICE** Collaboration, S. Acharya *et al.*, "Production of charged pions, kaons and (anti-)protons in Pb-Pb and inelastic pp collisions at $\sqrt{s_{\rm NN}} = 5.02$ TeV," arXiv:1910.07678 [nucl-ex].

[117] **ALICE** Collaboration, S. Acharya *et al.*, "J/ψ elliptic flow in Pb-Pb collisions at $\sqrt{s_{\rm NN}} = 5.02$ TeV," *Phys. Rev. Lett.* **119** no. 24, (2017) 242301, arXiv:1709.05260 [nucl-ex].

[118] **ALICE** Collaboration, J. Adam *et al.*, "J/ψ suppression at forward rapidity in Pb-Pb collisions at $\sqrt{\mathbf{s}_{\rm NN}} = \mathbf{5.02}$ TeV," *Phys. Lett.* **B766** (2017) 212–224, arXiv:1606.08197 [nucl-ex].

[119] **ALICE** Collaboration, S. Acharya *et al.*, "$\Lambda_{\rm c}^{+}$ production in pp collisions at $\sqrt{s} = 7$ TeV and in p-Pb collisions at $\sqrt{s_{\rm NN}} = 5.02$ TeV," *JHEP* **04** (2018) 108, arXiv:1712.09581 [nucl-ex].

[120] A. Beraudo *et al.*, "Extraction of Heavy-Flavor Transport Coefficients in QCD Matter," *Nucl. Phys.* **A979** (2018) 21–86, arXiv:1803.03824 [nucl-th].

[121] L. Evans and P. Bryant, "LHC Machine," *JINST* **3** (2008) S08001.

[122] **ATLAS** Collaboration, G. Aad *et al.*, "Observation of a new particle in the search for the Standard Model Higgs boson with the ATLAS detector at the LHC," *Phys. Lett.* **B716** (2012) 1–29, arXiv:1207.7214 [hep-ex].

[123] **CMS** Collaboration, S. Chatrchyan *et al.*, "Observation of a new boson at a mass of 125 GeV with the CMS experiment at the LHC," *Phys. Lett.* **B716** (2012) 30–61, arXiv:1207.7235 [hep-ex].

[124] "CERN technology department. the LHC underground facilities, 2015." http://te-epc-lpc.web.cern.ch/te-epc-lpc/machines/lhc.

[125] **ALICE** Collaboration, K. Aamodt *et al.*, "The ALICE experiment at the CERN LHC," *JINST* **3** (2008) S08002.

[126] **ALICE** Collaboration, B. B. Abelev *et al.*, "Performance of the ALICE Experiment at the CERN LHC," *Int. J. Mod. Phys.* **A29** (2014) 1430044, arXiv:1402.4476 [nucl-ex].

[127] J. Alme *et al.*, "The ALICE TPC, a large 3-dimensional tracking device with fast readout for ultra-high multiplicity events," *Nucl. Instrum. Meth.* **A622** (2010) 316–367, arXiv:1001.1950 [physics.ins-det].

[128] **ALICE** Collaboration, K. Aamodt *et al.*, "Alignment of the ALICE Inner Tracking System with cosmic-ray tracks," *JINST* **5** (2010) P03003, arXiv:1001.0502 [physics.ins-det].

[129] **ALICE** Collaboration, J. Adam *et al.*, "Determination of the event collision time with the ALICE detector at the LHC," *Eur. Phys. J. Plus* **132** no. 2, (2017) 99, arXiv:1610.03055 [physics.ins-det].

[130] **ALICE** Collaboration, B. Abelev *et al.*, "Centrality determination of Pb-Pb collisions at $\sqrt{s_{NN}} = 2.76$ TeV with ALICE," *Phys. Rev.* **C88** no. 4, (2013) 044909, arXiv:1301.4361 [nucl-ex].

[131] **ALICE** Collaboration, B. Abelev *et al.*, "Directed Flow of Charged Particles at Midrapidity Relative to the Spectator Plane in Pb-Pb Collisions at $\sqrt{s_{NN}}$=2.76 TeV," *Phys. Rev. Lett.* **111** no. 23, (2013) 232302, arXiv:1306.4145 [nucl-ex].

[132] "AliRoot." http://alice-offline.web.cern.ch.

[133] R. Brun and F. Rademakers, "ROOT: An object oriented data analysis framework," *Nucl. Instrum. Meth.* **A389** (1997) 81–86.

[134] "ROOT." https://root.cern.ch.

[135] X.-N. Wang and M. Gyulassy, "HIJING: A Monte Carlo model for multiple jet production in p p, p A and A A collisions," *Phys. Rev.* **D44** (1991) 3501–3516.

[136] J. Ranft, "The Dual parton model at cosmic ray energies," *Phys. Rev.* **D51** (1995) 64–84.

[137] R. Brun, F. Bruyant, F. Carminati, S. Giani, M. Maire, A. McPherson, G. Patrick, and L. Urban, "GEANT Detector Description and Simulation Tool,".

[138] **GEANT4** Collaboration, S. Agostinelli *et al.*, "GEANT4: A Simulation toolkit," *Nucl. Instrum. Meth.* **A506** (2003) 250–303.

[139] A. Ferrari, P. R. Sala, A. Fasso, and J. Ranft, "FLUKA: A multi-particle transport code (Program version 2005),".

[140] "Worldwide lhc computing grid." http://wlcg.web.cern.ch.

[141] **ALICE** Collaboration, P. Saiz, L. Aphecetche, P. Buncic, R. Piskac, J. E. Revsbech, and V. Sego, "AliEn - ALICE environment on the GRID," *Nucl. Instrum. Meth.* **A502** (2003) 437–440.

[142] **ALICE** Collaboration, J. Adam *et al.*, "Centrality dependence of particle production in p-Pb collisions at $\sqrt{s_{\rm NN}}$= 5.02 TeV," *Phys. Rev.* **C91** no. 6, (2015) 064905, arXiv:1412.6828 [nucl-ex].

[143] F. Sikler, "Centrality control of hadron nucleus interactions by detection of slow nucleons," arXiv:hep-ph/0304065 [hep-ph].

[144] R. Fruhwirth, "Application of Kalman filtering to track and vertex fitting," *Nucl. Instrum. Meth.* **A262** (1987) 444–450.

[145] L. Rolandi, W. Riegler, and W. Blum, *Particle Detection with Drift Chambers*, vol. -1. 01, 2008.

[146] E. Bruna, A. Dainese, M. Masera, and F. Prino, "Vertex reconstruction for proton-proton collisions in ALICE,". https://cds.cern.ch/record/1225497.

[147] P. Z. Skands, "Tuning Monte Carlo Generators: The Perugia Tunes," *Phys. Rev.* **D82** (2010) 074018, arXiv:1005.3457 [hep-ph].

[148] **ALICE** Collaboration, J. Adam *et al.*, "D-meson production in p-Pb collisions at $\sqrt{s_{\rm NN}}$ =5.02 TeV and in pp collisions at $\sqrt{s}$ =7 TeV," *Phys. Rev.* **C94** no. 5, (2016) 054908, arXiv:1605.07569 [nucl-ex].

[149] **ALICE Collaboration** Collaboration, "ALICE 2017 luminosity determination for pp collisions at $\sqrt{s}$ = 5 TeV,". http://cds.cern.ch/record/2648933.

[150] **CLEO** Collaboration, J. P. Alexander *et al.*, "Absolute Measurement of Hadronic Branching Fractions of the D(s)+ Meson," *Phys. Rev. Lett.* **100** (2008) 161804, arXiv:0801.0680 [hep-ex].

[151] **LHCb** Collaboration, R. Aaij *et al.*, "Prompt charm production in pp collisions at sqrt(s)=7 TeV," *Nucl. Phys.* **B871** (2013) 1–20, arXiv:1302.2864 [hep-ex].

[152] **LHCb** Collaboration, R. Aaij *et al.*, "Measurements of prompt charm production cross-sections in pp collisions at $\sqrt{s}$ = 13 TeV," *JHEP* **03** (2016) 159, arXiv:1510.01707 [hep-ex]. [Erratum: JHEP05,074(2017)].

[153] **LHCb** Collaboration, R. Aaij *et al.*, "Measurements of prompt charm production cross-sections in pp collisions at $\sqrt{s}$ = 5 TeV," *JHEP* **06** (2017) 147, arXiv:1610.02230 [hep-ex].

[154] D. J. Lange, "The EvtGen particle decay simulation package," *Nucl. Instrum. Meth.* **A462** (2001) 152–155.

[155] R. Barlow and C. Beeston, "Fitting using finite monte carlo samples," *Computer Physics Communications* **77** no. 2, (1993) 219 – 228. http://www.sciencedirect.com/science/article/pii/001046559390005W.

[156] A. M. Barbano, "Prompt D_s^+ meson production in pp, p-Pb and Pb-Pb collisions at LHC with ALICE," Dec, 2018. http://cds.cern.ch/record/2309930. Presented 23 Jan 2018.

[157] **ALICE** Collaboration, B. Abelev *et al.*, "D_s^+ meson production at central rapidity in proton–proton collisions at $\sqrt{s} = 7$ TeV," *Phys. Lett.* **B718** (2012) 279–294, arXiv:1208.1948 [hep-ex].

[158] **ALICE** Collaboration, S. Acharya *et al.*, "Measurement of D-meson production at mid-rapidity in pp collisions at $\sqrt{s} = 7$ TeV," *Eur. Phys. J.* **C77** no. 8, (2017) 550, arXiv:1702.00766 [hep-ex].

[159] **ALEPH** Collaboration, R. Barate *et al.*, "Study of charm production in Z decays," *Eur. Phys. J.* **C16** (2000) 597–611, arXiv:hep-ex/9909032 [hep-ex].

[160] E. Braaten, K.-m. Cheung, S. Fleming, and T. C. Yuan, "Perturbative QCD fragmentation functions as a model for heavy quark fragmentation," *Phys. Rev.* **D51** (1995) 4819–4829, arXiv:hep-ph/9409316 [hep-ph].

[161] **CLEO** Collaboration, M. Artuso *et al.*, "Charm meson spectra in e^+e^- annihilation at 10.5-GeV c.m.e.," *Phys. Rev.* **D70** (2004) 112001, arXiv:hep-ex/0402040 [hep-ex].

[162] **Belle** Collaboration, R. Seuster *et al.*, "Charm hadrons from fragmentation and B decays in e+ e- annihilation at s**(1/2) = 10.6-GeV," *Phys. Rev.* **D73** (2006) 032002, arXiv:hep-ex/0506068 [hep-ex].

[163] **BaBar** Collaboration, B. Aubert *et al.*, "Measurement of D_s^+ and D_s^{*+} production in B meson decays and from continuum e^+e^- annihilation at $\sqrt{s} = 10.6$ GeV," *Phys. Rev.* **D65** (2002) 091104, arXiv:hep-ex/0201041 [hep-ex].

[164] L. Gladilin, "Fragmentation fractions of c and b quarks into charmed hadrons at LEP," *Eur. Phys. J.* **C75** no. 1, (2015) 19, arXiv:1404.3888 [hep-ex].

[165] J. R. Christiansen and P. Z. Skands, "String Formation Beyond Leading Colour," *JHEP* **08** (2015) 003, arXiv:1505.01681 [hep-ph].

[166] L. A. Harland-Lang, A. D. Martin, P. Motylinski, and R. S. Thorne, "Parton distributions in the LHC era: MMHT 2014 PDFs," *Eur. Phys. J.* **C75** no. 5, (2015) 204, arXiv:1412.3989 [hep-ph].

[167] P. Skands, S. Carrazza, and J. Rojo, "Tuning PYTHIA 8.1: the Monash 2013 Tune," *Eur. Phys. J.* **C74** no. 8, (2014) 3024, arXiv:1404.5630 [hep-ph].

[168] **CMS** Collaboration, A. M. Sirunyan *et al.*, "Production of Λ_c^+ baryons in proton-proton and lead-lead collisions at $\sqrt{s_{\mathrm{NN}}} = 5.02$ TeV," arXiv:1906.03322 [hep-ex].

[169] **ALICE Collaboration** Collaboration, "Centrality determination in heavy ion collisions,". https://cds.cern.ch/record/2636623.

[170] M. He, R. J. Fries, and R. Rapp, "Heavy Flavor at the Large Hadron Collider in a Strong Coupling Approach," *Phys. Lett.* **B735** (2014) 445–450, arXiv:1401.3817 [nucl-th].

[171] **CMS** Collaboration, A. M. Sirunyan *et al.*, "Studies of Beauty Suppression via Nonprompt D^0 Mesons in Pb-Pb Collisions at $Q^2 = 4$ GeV^2," *Phys. Rev. Lett.* **123** no. 2, (2019) 022001, arXiv:1810.11102 [hep-ex].

[172] R. Averbeck, N. Bastid, Z. C. del Valle, P. Crochet, A. Dainese, and X. Zhang, "Reference Heavy Flavour Cross Sections in pp Collisions at $\sqrt{s} = 2.76$ TeV, using a pQCD-Driven $\sqrt{s}$-Scaling of ALICE Measurements at $\sqrt{s} = 7$ TeV," arXiv:1107.3243 [hep-ph].

[173] J. Uphoff, O. Fochler, Z. Xu, and C. Greiner, "Elastic and radiative heavy quark interactions in ultra-relativistic heavy-ion collisions," *J. Phys.* **G42** no. 11, (2015) 115106, arXiv:1408.2964 [hep-ph].

[174] **LEBC-EHS** Collaboration, M. Aguilar-Benitez *et al.*, "Comparative Properties of 400-GeV/c Proton - Proton Interactions With and Without Charm Production," *Z. Phys.* **C41** (1988) 191.

[175] M. Djordjevic and M. Djordjevic, "Predictions of heavy-flavor suppression at 5.1 TeV Pb + Pb collisions at the CERN Large Hadron Collider," *Phys. Rev.* **C92** no. 2, (2015) 024918, arXiv:1505.04316 [nucl-th].

[176] F. Gelis, E. Iancu, J. Jalilian-Marian, and R. Venugopalan, "The Color Glass Condensate," *Ann. Rev. Nucl. Part. Sci.* **60** (2010) 463–489, arXiv:1002.0333 [hep-ph].

[177] **CMS** Collaboration, V. Khachatryan *et al.*, "Study of B Meson Production in p+Pb Collisions at $\sqrt{s_{NN}} = 5.02$ TeV Using Exclusive Hadronic Decays," *Phys. Rev. Lett.* **116** no. 3, (2016) 032301, arXiv:1508.06678 [nucl-ex].

[178] T. Song, H. Berrehrah, D. Cabrera, W. Cassing, and E. Bratkovskaya, "Charm production in Pb + Pb collisions at energies available at the CERN Large Hadron Collider," *Phys. Rev.* **C93** no. 3, (2016) 034906, arXiv:1512.00891 [nucl-th].

[179] **European Muon** Collaboration, J. J. Aubert *et al.*, "The ratio of the nucleon structure functions $F2_n$ for iron and deuterium," *Phys. Lett.* **123B** (1983) 275–278.

[180] M. Djordjevic, "Heavy flavor puzzle at LHC: a serendipitous interplay of jet suppression and fragmentation," *Phys. Rev. Lett.* **112** no. 4, (2014) 042302, arXiv:1307.4702 [nucl-th].

[181] **STAR** Collaboration, L. Zhou, "$D_s^{\pm}$ meson production in Au+Au collisions at $\sqrt{s_{NN}} = 200$ GeV in STAR," *J. Phys. Conf. Ser.* **779** no. 1, (2017) 012028.

[182] A. Andronic, P. Braun-Munzinger, K. Redlich, and J. Stachel, "Statistical hadronization of charm in heavy ion collisions at SPS, RHIC and LHC," *Phys. Lett.* **B571** (2003) 36–44, arXiv:nucl-th/0303036 [nucl-th].

[183] A. M. Poskanzer and S. A. Voloshin, "Methods for analyzing anisotropic flow in relativistic nuclear collisions," *Phys. Rev.* **C58** (1998) 1671–1678, arXiv:nucl-ex/9805001 [nucl-ex].

[184] S. A. Voloshin, A. M. Poskanzer, and R. Snellings, "Collective phenomena in non-central nuclear collisions," *Landolt-Bornstein* **23** (2010) 293–333, arXiv:0809.2949 [nucl-ex].

[185] **ALICE** Collaboration, S. Acharya *et al.*, "Energy dependence and fluctuations of anisotropic flow in Pb-Pb collisions at $\sqrt{s_{\rm NN}} = 5.02$ and 2.76 TeV," *JHEP* **07** (2018) 103, arXiv:1804.02944 [nucl-ex].

[186] **ALICE** Collaboration, B. B. Abelev *et al.*, "Azimuthal anisotropy of D meson production in Pb-Pb collisions at $\sqrt{s_{\rm NN}} = 2.76$ TeV," *Phys. Rev.* **C90** no. 3, (2014) 034904, arXiv:1405.2001 [nucl-ex].

[187] J. Uphoff, O. Fochler, Z. Xu, and C. Greiner, "Open Heavy Flavor in Pb+Pb Collisions at $\sqrt{s} = 2.76$ TeV within a Transport Model," *Phys. Lett.* **B717** (2012) 430–435, arXiv:1205.4945 [hep-ph].

[188] A. Beraudo, A. De Pace, M. Monteno, M. Nardi, and F. Prino, "Event-shape engineering and heavy-flavour observables in relativistic heavy-ion collisions," *Eur. Phys. J.* **C79** no. 6, (2019) 494, arXiv:1812.08337 [physics.data-an].

[189] V. Greco, H. van Hees, and R. Rapp, "Heavy-quark kinetics at RHIC and LHC," in *Nuclear physics. Proceedings, 23rd International Conference, INPC 2007, Tokyo, Japan, June 3-8, 2007*. 2007. arXiv:0709.4452 [hep-ph].

[190] J. Aichelin, P. B. Gossiaux, and T. Gousset, "Radiative and Collisional Energy Loss of Heavy Quarks in Deconfined Matter," *Acta Phys. Polon.* **B43** (2012) 655–662, arXiv:1201.4192 [nucl-th].

[191] **ALICE** Collaboration, S. Acharya *et al.*, "Study of J/ψ azimuthal anisotropy at forward rapidity in Pb-Pb collisions at $\sqrt{s_{\rm NN}} = 5.02$ TeV," *JHEP* **02** (2019) 012, arXiv:1811.12727 [nucl-ex].

[192] V. Greco, C. M. Ko, and R. Rapp, "Quark coalescence for charmed mesons in ultrarelativistic heavy ion collisions," *Phys. Lett.* **B595** (2004) 202–208, arXiv:nucl-th/0312100 [nucl-th].

[193] D. Molnar, "Charm elliptic flow from quark coalescence dynamics," *J. Phys.* **G31** (2005) S421–S428, arXiv:nucl-th/0410041 [nucl-th].

[194] **ALICE** Collaboration, J. Adam *et al.*, "Inclusive, prompt and non-prompt J/ψ production at mid-rapidity in Pb-Pb collisions at $\sqrt{s_{\rm NN}} = 2.76$ TeV," *JHEP* **07** (2015) 051, arXiv:1504.07151 [nucl-ex].

[195] P. J. Siemens and J. O. Rasmussen, "Evidence for a blast wave from compress nuclear matter," *Phys. Rev. Lett.* **42** (1979) 880–887.

[196] **STAR** Collaboration, C. Adler *et al.*, "Identified particle elliptic flow in Au + Au collisions at s(NN)**(1/2) = 130-GeV," *Phys. Rev. Lett.* **87** (2001) 182301, arXiv:nucl-ex/0107003 [nucl-ex].

[197] **ALICE** Collaboration, S. Acharya *et al.*, "Measurement of deuteron spectra and elliptic flow in Pb–Pb collisions at $\sqrt{s_{\rm NN}} = 2.76$ TeV at the LHC," *Eur. Phys. J.* **C77** no. 10, (2017) 658, arXiv:1707.07304 [nucl-ex].

[198] S. Cao, T. Luo, G.-Y. Qin, and X.-N. Wang, "Heavy and light flavor jet quenching at RHIC and LHC energies," *Phys. Lett.* **B777** (2018) 255–259, arXiv:1703.00822 [nucl-th].

[199] R. Katz, C. A. G. Prado, J. Noronha-Hostler, J. Noronha, and A. A. P. Suaide, "DAB-MOD sensitivity study of heavy flavor R_{AA} and azimuthal anisotropies based on beam energy, initial conditions, hadronization, and suppression mechanisms," arXiv:1906.10768 [nucl-th].

[200] M. He and R. Rapp, "Hadronization and Charm-Hadron Ratios in Heavy-Ion Collisions," arXiv:1905.09216 [nucl-th].

[201] A. Beraudo, A. De Pace, M. Monteno, M. Nardi, and F. Prino, "Heavy flavors in heavy-ion collisions: quenching, flow and correlations," *Eur. Phys. J.* **C75** no. 3, (2015) 121, arXiv:1410.6082 [hep-ph].

[202] J. Xu, J. Liao, and M. Gyulassy, "Bridging Soft-Hard Transport Properties of Quark-Gluon Plasmas with CUJET3.0," *JHEP* **02** (2016) 169, arXiv:1508.00552 [hep-ph].

[203] Z.-B. Kang, F. Ringer, and I. Vitev, "Effective field theory approach to open heavy flavor production in heavy-ion collisions," *JHEP* **03** (2017) 146, arXiv:1610.02043 [hep-ph].

[204] S. Cao *et al.*, "Toward the determination of heavy-quark transport coefficients in quark-gluon plasma," *Phys. Rev.* **C99** no. 5, (2019) 054907, arXiv:1809.07894 [nucl-th].

[205] Y. Xu *et al.*, "Resolving discrepancies in the estimation of heavy quark transport coefficients in relativistic heavy-ion collisions," *Phys. Rev.* **C99** no. 1, (2019) 014902, arXiv:1809.10734 [nucl-th].

[206] J. Schukraft, A. Timmins, and S. A. Voloshin, "Ultra-relativistic nuclear collisions: event shape engineering," *Phys. Lett.* **B719** (2013) 394–398, arXiv:1208.4563 [nucl-ex].

[207] U. Heinz and R. Snellings, "Collective flow and viscosity in relativistic heavy-ion collisions," *Ann. Rev. Nucl. Part. Sci.* **63** (2013) 123–151, arXiv:1301.2826 [nucl-th].

[208] J. Noronha-Hostler, L. Yan, F. G. Gardim, and J.-Y. Ollitrault, "Linear and cubic response to the initial eccentricity in heavy-ion collisions," *Phys. Rev.* **C93** no. 1, (2016) 014909, arXiv:1511.03896 [nucl-th].

[209] F. G. Gardim, F. Grassi, M. Luzum, and J.-Y. Ollitrault, "Characterizing the hydrodynamic response to the initial conditions," *Nucl. Phys.* **A904-905** (2013) 503c–506c, arXiv:1210.8422 [nucl-th].

[210] **ALICE** Collaboration, J. Adam *et al.*, "Event shape engineering for inclusive spectra and elliptic flow in Pb-Pb collisions at $\sqrt{s_{\rm NN}} = 2.76$ TeV," *Phys. Rev.* **C93** no. 3, (2016) 034916, arXiv:1507.06194 [nucl-ex].

[211] **ATLAS** Collaboration, G. Aad *et al.*, "Measurement of the correlation between flow harmonics of different order in lead-lead collisions at $\sqrt{s_{NN}}$=2.76 TeV with the ATLAS detector," *Phys. Rev.* **C92** no. 3, (2015) 034903, arXiv:1504.01289 [hep-ex].

[212] **ALICE** Collaboration, S. Acharya *et al.*, "Constraining the magnitude of the Chiral Magnetic Effect with Event Shape Engineering in Pb-Pb collisions at $\sqrt{s_{\rm NN}}$ = 2.76 TeV," *Phys. Lett.* **B777** (2018) 151–162, arXiv:1709.04723 [nucl-ex].

[213] **CMS** Collaboration, A. M. Sirunyan *et al.*, "Constraints on the chiral magnetic effect using charge-dependent azimuthal correlations in *p*Pb and PbPb collisions at the CERN Large Hadron Collider," *Phys. Rev.* **C97** no. 4, (2018) 044912, arXiv:1708.01602 [nucl-ex].

[214] **STAR** Collaboration, C. Adler *et al.*, "Elliptic flow from two and four particle correlations in Au+Au collisions at s(NN)**(1/2) = 130-GeV," *Phys. Rev.* **C66** (2002) 034904, arXiv:nucl-ex/0206001 [nucl-ex].

[215] Z.-W. Lin, C. M. Ko, B.-A. Li, B. Zhang, and S. Pal, "A Multi-phase transport model for relativistic heavy ion collisions," *Phys. Rev.* **C72** (2005) 064901, arXiv:nucl-th/0411110 [nucl-th].

[216] **ALICE** Collaboration, J. Adam *et al.*, "Anisotropic flow of charged particles in Pb-Pb collisions at $\sqrt{s_{\rm NN}} = 5.02$ TeV," *Phys. Rev. Lett.* **116** no. 13, (2016) 132302, arXiv:1602.01119 [nucl-ex].

[217] D. Banerjee, S. Datta, R. Gavai, and P. Majumdar, "Heavy Quark Momentum Diffusion Coefficient from Lattice QCD," *Phys. Rev.* **D85** (2012) 014510, arXiv:1109.5738 [hep-lat].

[218] A. Radovic, M. Williams, D. Rousseau, M. Kagan, D. Bonacorsi, A. Himmel, A. Aurisano, K. Terao, and T. Wongjirad, "Machine learning at the energy and intensity frontiers of particle physics," *Nature* **560** no. 7716, (2018) 41–48.

[219] K. Albertsson *et al.*, "Machine Learning in High Energy Physics Community White Paper," *J. Phys. Conf. Ser.* **1085** no. 2, (2018) 022008, arXiv:1807.02876 [physics.comp-ph].

[220] S. B. Kotsiantis, "Decision trees: a recent overview," *Artificial Intelligence Review* **39** no. 4, (Apr, 2013) 261–283. https://doi.org/10.1007/s10462-011-9272-4.

[221] T. Chen and C. Guestrin, "XGBoost: A scalable tree boosting system," in *Proceedings of the 22Nd ACM SIGKDD International Conference on Knowledge Discovery and Data Mining*, KDD '16, pp. 785–794. ACM, New York, NY, USA, 2016. http://doi.acm.org/10.1145/2939672.2939785.

[222] "XGBoost." https://xgboost.readthedocs.io/en/latest.

[223] L. Musa, "Conceptual Design Report for the Upgrade of the ALICE ITS," Tech. Rep. CERN-LHCC-2012-005. LHCC-G-159, CERN, Geneva, Mar, 2012. https://cds.cern.ch/record/1431539.

[224] **ALICE** Collaboration, B. Abelev *et al.*, "Technical Design Report for the Upgrade of the ALICE Inner Tracking System," *J. Phys.* **G41** (2014) 087002.

This Ph.D. thesis has been typeset by means of the TEX-system facilities. The typesetting engine was pdfLATEX. The document class was `toptesi`, by Claudio Beccari, with option `tipotesi=scudo`. This class is available in every up-to-date and complete TEX-system installation.